UNIVERSIDADE FEDERAL DE SANTA CATARINA
CENTRO DE CIÊNCIAS FÍSICAS E MATEMÁTICAS
PROGRAMA DE PÓS-GRADUAÇÃO EM FÍSICA

Muryel Guolo Pereira

The Circumnuclear Region and Long-Term Variability of the Active Nucleus in NGC 2992

Florianópolis
2021

Muryel Guolo Pereira

The Circumnuclear Region and Long-Term Variability of the Active Nucleus in NGC 2992

Dissertação submetida ao Programa de Pós-Graduação em Física da Universidade Federal de Santa Catarina para a obtenção do título de Mestre em Física.
Supervisor: Prof. Dr. Daniel Ruschel Dutra

Florianópolis
2021

Ficha de identificação da obra elaborada pelo autor,
através do Programa de Geração Automática da Biblioteca Universitária da UFSC.

Guolo-Pereira, Muryel
The Circumnuclear Region and Long-Term Variability of the Active Nucleus in NGC 2992 / Muryel Guolo-Pereira ; orientador, Daniel Ruschel Dutra, 2021.
143 p.

Dissertação (mestrado) - Universidade Federal de Santa Catarina, Centro de Ciências Físicas e Matemáticas, Programa de Pós-Graduação em Física, Florianópolis, 2021.

Inclui referências.

1. Física. 2. Astrofísica. 3. Galáxias. 4. Nucleos Ativos de Galáxias. I. Ruschel Dutra, Daniel . II. Universidade Federal de Santa Catarina. Programa de Pós-Graduação em Física. III. Título.

Muryel Guolo Pereira

The Circumnuclear Region and Long-Term Variability of the Active Nucleus in NGC 2992

O presente trabalho em nível de mestrado foi avaliado e aprovado por banca examinadora composta pelos seguintes membros:

Prof^{a}. Dra. Natalia Vale Asari
Universidade Federal de Santa Catarina

Prof. Dr. Rogério Riffel
Universidade Federal do Rio Grande do Sul

Prof. Dr. Tiago Vecchi Ricci
Universidade Federal da Fronteira Sul

Certificamos que esta é a **versão original e final** do trabalho de conclusão que foi julgado adequado para obtenção do título de Mestre em Física.

Documento assinado digitalmente
Ivan Helmuth Bechtold
Data: 18/05/2021 14:42:04-0300
CPF: 895.230.409-87
Verifique as assinaturas em https://v.ufsc.br

Coordenação do Programa de Pós-Graduação

Documento assinado digitalmente
Daniel Ruschel Dutra
Data: 18/05/2021 13:18:47-0300
CPF: 011.099.190-77
Verifique as assinaturas em https://v.ufsc.br

Prof. Dr. Daniel Ruschel Dutra
Orientador

Florianópolis, 2021.

AGRADECIMENTOS

Primeiramente, aos meus pais, que mesmo com todos os sacrifícios nescessários, sempre fizeram de tudo para que eu tivesse uma educação de qualidade, e que apesar de não entenderem muito bem o meu trabalho, sempre me apoiaram incondicionalmente nas minhas decisões e escolhas.

Ao meu orientador, Daniel, por ter me aceito como aluno de Iniciação Científica ainda em 2017 e depois como seu primeiro aluno de mestrado, pelo empenho e companheirismo nesses anos de orientação que foram essenciais na minha formação como aluno e profissional.

Aos professores do Departamento de Física e do Grupo de Astrofísica da UFSC pela formação que me foi dada, em especial ao Cid pela oportunidade de participar do grupo logo no meu primeiro ano na UFSC e pelo apoio nas aplicações para o doutorado.

Aos meus colaboradores pelas contribuições nos artigos que levaram a essa dissertação, em especial à Thaisa e ao Jaderson, pelas discussões e o apoio nas aplicações para o doutorado.

Aos grandes amigos que a física da UFSC me deu e que levarei para a vida toda: Kevin, Hamilton, Café, João, Chico e Hélcio.

Aos membros da banca, Natália, Rogério e Tiago, por aceitarem avaliar este trabalho.

Ao CNPq pelo suporte financeiro.

A minha noiva, Jéssica, por estar comigo nos altos e baixos dessa trajetória, e me apoiar em todos os momentos. A vida ainda nos reserva muitas conquistas!

RESUMO

Núcleos Galácticos Ativos (*AGN*) são regiões compactas no centro de galáxias capazes de gerar grandes quantidades de energia, de tal forma que não podem ser explicadas por fusão termonuclear pelas estrelas da galáxia, mas sim por acreção de matéria por um buraco negro supermassivo. Além de serem laboratórios para o estudo de física em condições extremas, acredita-se que *AGNs* são fundamentais para o entendimento da evolução das galáxias. Nesta dissertação apresentamos uma análise espacial e temporal do *AGN* presente na galáxia Seyfert em interação NGC 2992 usando observações em diferentes comprimentos de onda. Primeiramente, utilizando dados de Espectroscopia de Campo Integral do Telescópio Gemini, fomos capazes de resolver espacialmente as populações estelares, os mecanismos de ionização e a cinemática do gás ionizado. Utilizando síntese de populações estelares, nós mostramos que a população estelar é principalmente composta por estrelas velhas e ricas em metais, mas também por uma fração considerável, de até 30% da luz, por estrelas jovens e pobres em metais. A cinemática da Região de Linhas Estreitas (*NLR*) apresenta duas principais componentes: uma do gás orbitando o disco da galáxia e outra por uma ejeção (*outflow*) de gás, relacionada à emissão em rádio. Mostramos que apesar de a ionização pelo AGN ser o principal dos mecanismos, ionização por estrelas jovens e por choques também contribuem para as razões de linhas encontradas. Depois, apresentamos uma análise do histórico do espectro de emissão da galáxia em raios-X e no óptico. Mostramos que ela apresenta várias transições em sua classificação Seyfert, do tipo 2 para tipos intermediários, perdendo e readquirindo sua Linha de Emissão Larga (*BEL*) em Hα diversas vezes, portanto classificando-o como um '*Changing Look*' *AGN*. Em raios-X, a fonte apresenta grande variabilidade com sua luminosidade corrigida por absorção variando por um fator de ~ 35. Mostramos que a presença (e o fluxo) da *BEL* em Hα está diretamente correlacionada com a taxa de acreção: com um valor mínimo $2.0^{+2.0}_{-1.3}$% na razão de Eddington sendo necessário para a detecção da componente larga. Dois cenários são possíveis para explicar as transições de clasificação: o aumento (diminuição) da luminosidade do contínuo do AGN, que aumenta (diminui) a quantidade de fótons disponíveis para excitar o gás na Região de Linhas Largas (*BLR*), ou o desaparecimento da estrutura da *BEL* em si ocorre quando a baixa taxa de acreção não é capaz de suportar a taxa de fluxo de nuvens necessária. Este trabalho evidencia o papel das galáxias próximas no estudo dos fenômenos *AGNs*, nos quais as estruturas da escala parsec podem ser resolvidas e observações públicas em múltiplos comprimentos de onda e épocas estão disponíveis.
Palavras-chave: Astrofísica. Galáxias. Nucleos Galácticos Ativos.

ABSTRACT

Active Galactic Nuclei (AGN) are compact regions at the center of galaxies that can generate large amounts of energy, such that it can not be explained by thermonuclear fusion in stars, but instead by accretion of matter onto a supermassive black hole (SMBH). Besides being a laboratory to study Physics in extreme conditions, AGNs are also believed to be fundamental for understanding galaxies' evolution. This dissertation presents a multi-wavelength spatial and temporal analysis of the AGN in the interacting Seyfert galaxy NGC 2992. First, using data taken with Gemini Multi-Object Spectrographs (GMOS), with the Integral Field Unit mode, from the inner 1.1 kiloparsecs of the galaxy, we were able to spatially resolve the stellar populations, the ionization mechanism, and kinematics of ionized gas. From full spectral synthesis, we found that the stellar population is primarily composed of old metal-rich stars with a smaller, but considerable, contributing of up to 30% of the light, from young and metal-poor populations. The Narrow Line Region kinematics presents two main components: one from gas orbiting the galaxy disk and another from a blueshifted outflow, correlated with the radio emission. We show that even though the primary ionization mechanism is the AGN radiation, ionization by young stars and shocks may also contribute to the emission line ratios found. Later, we present an analysis of the historical X-rays and optical spectra of the galaxy. We show that the nucleus of the galaxy presents multiple Seyfert type transitions from type 2 to intermediate-type, losing and regaining its Hα Broad Emission Line (BEL) recurrently, hence being a 'Changing Look' AGN. In X-rays, the source shows large intrinsic variability with the absorption corrected 2-10 keV luminosity varying by a factor of ~ 35. We show that the presence (and flux) of the Hα BEL is directly correlated with the accretion rate: a minimum Eddington ratio ($\lambda_{Edd} = L_{bol}/L_{Edd}$) value of $2.0^{+2.0}_{-1.3}$% is necessary for the broad line detection. Two possible scenarios for type transitions are still open: either there is a dimming (brightening) of the AGN continuum luminosity, which reduces (increases) the supply of ionizing photons available to excite the gas in the Broad Line Region (BLR), or the disappearance of the BLR structure itself occurs as the low accretion efficiency is not able to sustain the required cloud flow rate. This work evidences the role of the nearby galaxies in the study of the AGN phenomena, in which the parsec scale structures can be resolved and public multi-wavelength and multi-epoch observations are available.

Keywords: Astrophysics. Galaxies. Active Galactic Nuclei.

RESUMO EXPANDIDO

Introdução

A interpretação de que os objetos luminosos e distantes descobetos por Schmidt (1963) eram buracos negros super massivos (*SMBH*) no centro de galáxias foi primeiramente dada por Lynden-Bell (1969). Nesse modelo, quando matéria da galáxia hospedeira perde momento angular e é transportada para sua região nuclear, seu *SMBH* pode começar um processo conhecido como acreção, através do qual um disco (de acreção) é formado. O material no disco de acreção irradia energia devido às altas temperaturas atingidas pelo efeito da viscosidade do mesmo (SHAKURA; SUNYAEV, 1973). Esse processo define a existência dos chamados Núcleos Galácticos Ativos (*AGN*), onde energia potencial gravitacional do material é transformada em energia térmica e radiação, dessa forma o *AGN* é capaz de influenciar o meio interestelar da sua galáxia hospedeira.

Além de serem laboratórios para o estudo da física em condições extremas, o paradigma teórico atual de evolução das galáxias não somente atribui um papel fundamental aos *AGNs* na evolução de suas galáxias hospedeiras, mas também que ambas evoluções, dos *SMBHs* e das partes centrais (bojos) das galáxias, sejam reguladas pelos mesmos processos. Tal co-evolução é suportada observacionalmente pela existência de correlações fortes entre suas propriedades, por exemplo, a correlação entre a massa dos *SMBHs* (M_{BH}) e a dispersão de velocidades das estrelas do bojos, σ_* (e.g., FERRARESE; MERRITT, 2000; GULTEKIN et al., 2009). Esse cenário se fortalece devido ao fato que ambos o crescimento dos *SMBHs* (medido pela taxa de acreção) e o das galáxias (medido pela taxa de formação estelar) são similares na história do universo (BULLOCK; BOYLAN-KOLCHIN, 2017), ambos com máximo em *redshift* (z) $\sim$ 2.

Objetivos

Embora o efeito dos *AGNs* em suas galáxias tenha sido maior no universo distante, as infraestruturas observacionais disponíveis atualmente não conseguem atingir as resoluções da ordem de parsecs necessárias para resolver espacialmente as estruturas internas das galáxias em altos *redshifts*. Nesse sentido, o estudo de análogos locais ainda é necessário para o completo entendimento do fenômeno dos *AGNs*, particularmente para estudo de sua variabilidade, devido ao fato de essas galáxias estarem sendo observadas por diversos instrumentos de diversos comprimentos de onda, a décadas. Neste trabalho, analisamos tanto as propriedades espaciais da região nuclear da galáxia Seyfert em interação NGC 2992, quanto sua variabilidade de longo período.

Metodologia

Para resolver espacialmente as propriedades da região circum-nuclear da galáxia utilizamos dados de Espectroscopia de Campo Integral obtidos com Telescópio Gemini Sul. Aplicamos síntese de populações estelares, para recuperar a história de formação estelar da galáxia, além disso, modelamos as linhas de emissão mais proeminentes a fim de estudar a cinemática e os mecanismo de ionização do gás da galáxia. A análise da variabilidade da galáxia se deu

pela revisão de toda a literatura sobre a fonte, incluindo todos os espectros ópticos e em raio-X publicados, do final dos anos 1970 até os mais recentes, focando na correlação entre a presença/ausência de *BEL* em Hα e a luminosidade em raios-X (usada como um indicador da taxa de acreção do *SMBH*).

Resultados e Discussão

Nesse trabalho conseguimos mostrar que a emissão do contínuo da região circum-nuclear embora dominada por estrelas velhas e ricas em metais, têm uma fração considerável de luz emitida por estrelas jovens e pobres em metais, o que pode indicar um surto de formação estelar causado pela interação de NGC 2992 com sua companheira NGC 2993. Mostramos que a Região de Linhas Estreitas (*NLR*) apresenta duas componentes cinemáticas, uma que é bem descrita pelo gás orbitando o disco da galáxia em órbitas Keplerianas, e outra devido a ejeção (*outflow*) de gás, possivelmente relacionada com a emissão em rádio da galáxia. Mostramos ainda que a galáxia possui diferentes mecanismos de ionização, e que embora a ionização pelo *AGN* seja a dominante no kiloparsec central, ionização por estrelas jovens e por choques também contribuem para as razões de linhas encontradas. Em maiores escalas, a dominância do *AGN* deve diminuir em relação aos outros dois mecanismos. O estudo da variabilidade revelou que a fonte apresenta várias transições em sua classificação espectral, de Seyfert do tipo 2 para tipo intermediário, perdendo e readquirindo sua *BEL* em Hα em um período de alguns anos, portanto sendo classificado como um *'Changing Look' AGN* (*CL-AGN*). Em raios-X a fonte também apresenta alta variabilidade, com sua luminosidade intrínseca na banda 2-10 keV variando por um fator maior que 30, de 4.9×10^{41} *erg s*$^{-1}$até 1.7×10^{43} *erg s*$^{-1}$. Mostramos que a presença e o fluxo da componente larga da linha em Hα está diretamente correlacionada com a luminosidade em raios-X: um valor mínimo de $L_{2-10} \approx 4\times10^{41}$ *erg s*$^{-1}$é necessário para detecção da componente. Valor esse que se traduz a uma razão de Eddington ($L_{bol}/L_{Edd} = \lambda_{Edd}$) de $2.0^{+2.0}_{-1.3}$%, se supormos $M_{BH} = 3\times10^7\ M_\odot$. A detecção da componente larga em Hβ só é possível a taxas de acreção ainda maiores, $\lambda_{Edd} \approx$ 5-8%. Dois cenários para as transições são possíveis: o aumento (diminuição) da luminosidade do contínuo do AGN, aumenta (diminui) a quantidade de fótons disponíveis para excitar o gás na Região de Linhas Largas (*BLR*), ou o desaparecimento da estrutura da *BEL* em si ocorre quando a baixa taxa de acreção não é capaz de suportar a taxa de fluxo de nuvens necessária de acordo com modelos de vento-disco (*disk-wind*) para a *BLR*.

Considerações Finais

Esse trabalho mostra a importância e o papel das galáxias do universo local no estudo do fenômeno dos *AGNs*, nas quais estruturas na ordem de parsecs podem ser espacialmente resolvidas, e para as quais vários dados em diversos comprimentos de onda e diversas épocas estão publicamente disponíveis. Nele adicionamos evidencias mostrando a influência do AGN em sua galáxia hospedeira e adicionamos mais um objeto na lista de CL-AGNs, em particular, um dos poucos em que a dependência entre as transições de classificação e a taxa de acreção é mostrada explicitamente. Por fim, mencionamos possíveis trabalhos que podem ser realizados baseados nesse sistema de galáxias em interação ou utilizando-se de métodos similares aos empregados aqui.

Palavras-chave: Astrofísica. Galáxias. Nucleos Galácticos Ativos.

LIST OF FIGURES

LIST OF TABLES

LIST OF ABBREVIATIONS

AGB	Asymptotic Giant Branch
AGN	Active Galactic Nuclei
BEL	Broad Emission Line
BLR	Broad Line Region
CL-AGN	'Changing Look' Active Galactic Nuclei
FC	Featureless Continuum
FWHM	Full Width at Half Maximum
FoV	Field of View
GMOS	Gemini Multi-Object Spectrograph
HBLR	Hidden Broad Line Region
HST	Hubble Space Telescope
IFU	Integral Field Unit
IGM	intergalactic Medium
IR	Infrared
ISM	Interstellar Medium
LINER	Low-Ionization nuclear Emission-line Region
LLAGN	Low Luminosity Active Galactic Nuclei
MUSE	Multi-Unit Spectroscopic Explorer
MaNGA	Mapping Nearby Galaxies at APO
NIR	Near Infrared
NLR	Narrow Line Region
PAH	Polycyclic Aromatic Hydrocarbon
RIAF	Radiatively Inefficient Accretion Flow
RL	Radio Loud
RQ	Radio Quiet
SDSS	Sloan Digital Sky Survey
SFH	Star Formation History
SFR	Star Formation Rate
SMBH	Supermassive Black Hole
SSP	Simple Stellar Population
S/N	Signal to Noise Ratio
TDE	Tidal Disruptive Event
UV	Ultraviolet
VLT	Very Large Telescope

CONTENTS

1 ACTIVE GALACTIC NUCLEI

1.1 An Historical Overview

The history of Active Galactic Nuclei (AGNs) started at the beginning of the last century. Fath (1909) undertook a series of observations aimed at understanding the nature of "spiral nebulae", some of the most enigmatic sources at the time. In fact, astronomers were trying to understand whether these objects were nearby gaseous objects similar to the Orion nebula or very distant collections of unresolved stars. Fath found continuous spectra with stellar absorption lines for most objects, which indicated emission from unresolved solar-type stars. However, for one object, NGC 1068, he found a peculiar spectrum, showing both bright emission and absorption lines, similar to what had been observed in gaseous nebulae. This result was later confirmed by Slipher (1917) and by Hubble (1926), who found evidence of this behavior also in the spectra of NGC 4051 and NGC 4151. The first systematic study of galaxies showing nuclear emission lines was performed by Seyfert (1943), who studied the spectra of NGC 1068, NGC 1275, NGC 3516, NGC 4051, NGC 4151, and NGC 7469. He found that while objects like NGC 1068 had forbidden and permitted lines with roughly similar profiles and widths of $\sim$ 1000 $km\,s^{-1}$, objects like NGC 4151 showed narrow forbidden lines and very broad ($\sim$ 7000 $km\,s^{-1}$) hydrogen lines. In the following years, the AGN study developed mostly on the radio, an energy band that had started to be explored by astronomers. Later, it led to the discovery of emission from a discrete source in Cygnus, which was then called Cygnus A (HEY et al., 1946), and later from several other sources (BOLTON; STANLEY, 1948). In the following years, many more radio sources were discovered and their positions accurately estimated, thanks to surveys like the Third Cambridge survey (3C, EDGE et al., 1959). A few years later, the breakthrough came from observations of the very bright quasar 3C 273 by Hazard et al. (1963). In the same year, based on optical observations Schmidt (1963) discovered the presence of redshifted emission lines in 3C 273, which were attributed as being due to Hubble expansion (GREENSTEIN; SCHMIDT, 1964). The luminosity obtained and the cosmological distance excluded the possibility that these objects were highly variable stars. Later, Sandage et al. (1965) reported the discovery of a large number of radio-quiet objects that resembled quasars. These objects had been found as a characteristic population examining color-color ($U-B$, $B-V$) diagrams of stars. They showed a strong "ultraviolet excess", which is now well known to be one of the most important characteristics of AGN. Since then, a large number of AGN were discovered and classified according to their main properties. Today we know that many galaxies harbor AGNs, radio-quiet objects, as the galaxies discovered by Carl Seyfert (and today called Seyfert galaxies) can usually be found in spiral galaxies, while radio-loud objects (as 3C 273) are usually hosted by elliptical galaxies (VÉRON-CETTY; VÉRON, 2001).

The presence of supermassive black holes (SMBHs) in the center of AGNs was first proposed by Lynden-Bell (1969), and later largely confirmed by several observational evidences. From the short time scales variations ($\sim$ 1 hour) observed in AGNs, it is possible to obtain an upper limit on the size of the central source, which, together with mass estimates, points towards very high densities the order of magnitude of those expected in black holes. A rapidly rotating disk of ionized gas has been detected by Hubble Space Telescope (HST) observations of M87,

in agreement with a disk being Keplerian rotating around a black hole Ford et al. (1994), the existence of the supermassive object in M87 was recently undoubtedly confirmed by the Event Horizon Telescope Collaboration et al. (2019). Moreover, the luminosities observed in AGN can be easily explained by accretion onto a supermassive black hole (see section 1.2.2), and no serious alternative explanation to this mechanism exists, although theories involving starburst have long been debated (e.g., TERLEVICH et al., 1992).

In the following, I will first illustrate the several components that constitute an AGN (section 1.2), then I will introduce the classification and the unified model (section 1.3), while in section 1.4 I will discuss the role of the AGNs in the evolution of the galaxies. The main object (NGC 2992, section 1.5) and the overview of this work are further presented (section 1.6).

1.2 Anatomy of an AGN

AGN are thought to be constituted by several components, all of them very likely intrinsically related to the supermassive black hole lying at their nucleus, and driving their growth and evolution. In the following, I will discuss the most important components usually found in AGN. The supermassive black hole is discussed in section 1.2.1. The Ultraviolet(UV)-Optical emitting regions: the accretion disk, the broad line region and the narrow line region are discussed from section 1.2.2 to 1.2.4, while the X-ray emission by the corona and the radio jets are discussed, respectively, in sections 1.2.5 and 1.2.6.

1.2.1 The Supermassive Black Hole

The existence of black holes was predicted by Penrose (1965) as an interpretation to the Schwarzschild (1916) solution to Einstein (1916) formulation of General Relativity. However, it was not until 1972 that evidence for the existence of black holes was found through observations of Cyg X-1 (WEBSTER; MURDIN, 1972; BOLTON, 1972).

The role of the surface for a black hole of mass M is played by the sphere with a radius corresponding to the Schwarzschild radius ($r_g = 2GM/c^2$). The Schwarzschild radius is the distance from the singularity at which a body cannot escape anymore from the gravitational attraction and is bound to fall inside the black hole. The metric of space-time around a non-rotating black hole is given by the Schwarzschild (1916) solution to Einstein's general relativity. From the metric one can deduce the last stable circular orbit around a non-rotating black hole is $r = 3r_g$. So for $r < 3r_g$ no stable orbit exist, and for $r < r_g$ particles rapidly fall in the singularity. The more general solution for a rotating black hole was discovered by Kerr (1963), for a Kerr balck hole the table circular orbit is 0.5 R_g.

SMBH's masses range from 10^6 $M_\odot$– most found in dwarf galaxies – with the massive ones – usually found in massive elliptical galaxies – as massive as 10^{10} $M_\odot$. Although over the past few decades, observational work indicates that most, if not all, massive galaxies with a spheroidal component have a SMBH at their center (e.g., KORMENDY; RICHSTONE, 1995; MAGORRIAN et al., 1998), the origin of these SMBHs is still unknown. Several scenarios have been proposed, among it the collapse of supermassive population III stars or the collapse of massive primordial clouds (DOKUCHAEV et al., 2007; VALIANTE et al., 2017).

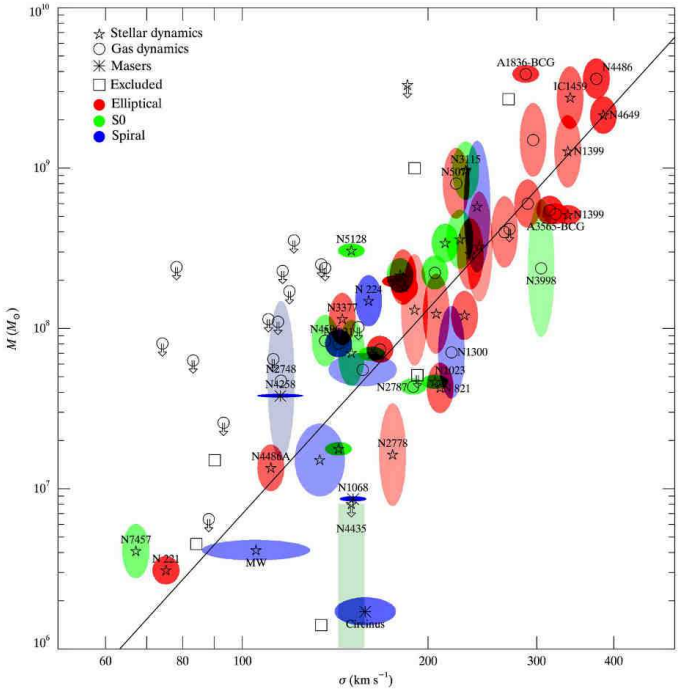

Figure 1 – The M_{BH} - σ_* relation for galaxies with dynamical measurements. The symbol indicates the method of M_{BH} mass measurement: stellar dynamics (pentagrams), gas dynamics (circles), masers (asterisks). The color of the error ellipse indicates the Hubble type of the host galaxy: elliptical (red), S0 (green), and spiral (blue). The line is the best fit relation to the full sample: $M_{BH} = 10^{8.12}\ (\sigma_*/200\ \ km\,s^{-1})^{4.24}$. Figure taken from Gültekin et al. (2009).

Measuring SMBH masses

The high angular resolution of HST and ground-based adaptive optics supported telescopes has enabled the determination of the masses of nuclear black holes; for the first time, the dynamics of stars and gas in the nuclei of nearby galaxies could be studied on scales smaller than the black hole radius of influence, $R_{BH} = GM_{BH}/\sigma_*^2$, where M_{BH} is the SMBH mass, σ_* is the velocity dispersion of the stars in the host galaxy bulge.

There are direct and indirect methods of measuring M_{BH}. Direct measurements are those where the mass is derived from the dynamics of stars or gas accelerated by the black hole itself. These methods include stellar and gas dynamical modeling (e.g., GHEZ et al., 1998; GENZEL et al., 2003) and reverberation mapping (e.g., PETERSON; HORNE, 2004). Indirect methods are those where the black hole mass is inferred from observables that are correlated with the black hole mass. These includes masses based on correlations between black hole masses and host-galaxy properties, such as the velocity dispersion of bulge stars, i.e., the M_{BH} - σ_* relationship (Figure 1, FERRARESE; MERRITT, 2000; GEBHARDT et al., 2000; GÜLTEKIN et al., 2009; WOO et al., 2013), the bulge luminosity, i.e., the he M_{BH} - L_{bulge} relationship (KORMENDY; RICHSTONE, 1995; MAGORRIAN et al., 1998), or even the X-ray variability time scales, given by the M_{BH} - σ^{rms}_{x-ray} relation (GIERLI NSKI et al., 2008; PONTI et al., 2012) .

One of the most common ways to measure the mass of M_{BH} is through the width of their broad emission lines (see section 1.2.3), more specific by reverberation mapping. This technique

exploits the fact that emission lines variations are lagged with respect to the continuum (see section 1.2.2), from which one can calculate r_{BLR}, the distance of the broad emission line region to the central black hole, by taking into account the light travel time. Using the following equation one can estimate the SMBH mass (PETERSON et al., 1995):

$$M_{BH} = \frac{f\, r_{BLR}\, (\Delta V)^2}{G} \tag{1}$$

where ΔV is the velocity of the gas in the broad line region (as measured by the width of the emission lines). It is also common to distinguish among 'primary','secondary' and even 'tertiary' methods for the the mass determination, based on the number of assumptions and model dependence. Reverberation mapping is an interesting example: it is a direct method as it is based on observations of gas that is accelerated by the gravitational potential of the central black hole, but, as generally practiced, it is also a secondary method because absolute calibration of the mass scale depends on another method (the f scale parameter in equation 1, PETERSON; HORNE, 2004).

1.2.2 The Accretion Disk

Before the 1970s, the importance of accretion in astrophysics was poorly understood. With the discovery of the first X-ray binaries, it was soon realized that the only mechanism that could produce the luminosities observed in many of these sources was accretion onto compact objects.

To have a qualitative idea of the amount of energy produced by accretion processes, one can consider the gravitational potential energy released by the free fall of a mass m on a body of mass M and radius R:

$$\Delta E_{acc} = \frac{M\, m\, G}{R} \tag{2}$$

where G is the gravitational constant. To compare it with nuclear processes, the maximum amount of energy per gram released by nuclear fusion of hydrogen into helium is:

$$\Delta E_{nuc} = 0.007\, m\, c^2 \tag{3}$$

where c is the speed of light. Considering, for example, the values typical for a neutron star (radius of $R \sim 10$ km and $M \sim M_{\odot}$), the quantity of energy released by accretion would be larger than that of nuclear fusion. The energy released ΔE_{acc} depends on how compact the accreting object is ($E_{acc} \propto M/R$), thus one can expect that black holes are the sources that exploit best this source of energy. The luminosity of an accreting black hole can be expressed as (FRANK et al., 2002):

$$L_{acc} \propto \eta\, \dot{m}\, c^2 \tag{4}$$

η is the efficiency of the conversion of rest energy of the accreting matter into radiation, and $\dot{m}$ is the accretion rate. In the case of a non-rotating spherically symmetric black hole, the last stable orbit is $r_l = 3r_g = 6GM/c^2$, which results in a binding energy that is $\sim 6\%$ of the mass of

the particle. In the case of rotating black holes, where $r_l = 0.5 r_g = GM/c^2$, up to 42.3% of the rest energy of the material can be released as it spirals into the black hole.

Eddigton luminosity

Accretion is limited by the radiation pressure. At high accretion rates the luminosity increases and so does the outward force exerted by the radiation (F_{rad}). On a free electron this force is:

$$F_{rad} = \frac{L_{acc}\,\sigma_T}{4\,\pi\,r^2\,c} \tag{5}$$

where $\sigma_T = 6.65 \times 10^{25}$ cm^2 is the Thomson cross-section. The radiation pressure balances the gravitational force ($F_G = GMm_p/r^2$, where m_p is the mass of the proton) at the so called Eddington luminosity. For a fully ionized medium in a spherically symmetric geometry such a luminosity is:

$$L_{Edd} = \frac{4\pi\,G\,M\,m_p\,c}{\sigma_T} \backsimeq 1.3 \times 10^{38} \left(\frac{M}{M_\odot}\right) erg\ s^{-1}. \tag{6}$$

An accretion disk's power output across all wavelengths is called its bolometric luminosity. The ratio between the bolometric luminosity of an object and its Eddington luminosity is called the Eddington ratio:

$$\lambda_{Edd} = \frac{L_{Bol}}{L_{Edd}}. \tag{7}$$

Although this derivation of the Eddington luminosity is limited by the spherical symmetry approximation, which does not represent the physical situation of an accreting disk, it still provides a useful approximation of the limit luminosity for an accreting system.

The Shakura-Sunyaev accretion disks

Matter falling onto a compact object from infinity acquires kinetic energy as its gravitational potential energy decreases. To conserve the angular momentum, the matter cannot fall directly into the compact object, but it is commonly believed to form an accretion disk. The simplest case of accretion disks is the thin accretion disks described by Shakura and Sunyaev (1973). In this picture, the matter is supposed to form a geometrically thin and optically thick disk and follows Keplerian orbits at any radius. Angular momentum is transported outwards due to viscosity produced by turbulent effects and magnetic instabilities (FRANK et al., 2002). The heat energy produced in the disk is then radiated in the form of multi-temperature blackbodies, each of them having a temperature

$$T(R) = \left(T_* \frac{R}{R_*}\right)^{-3/4} \tag{8}$$

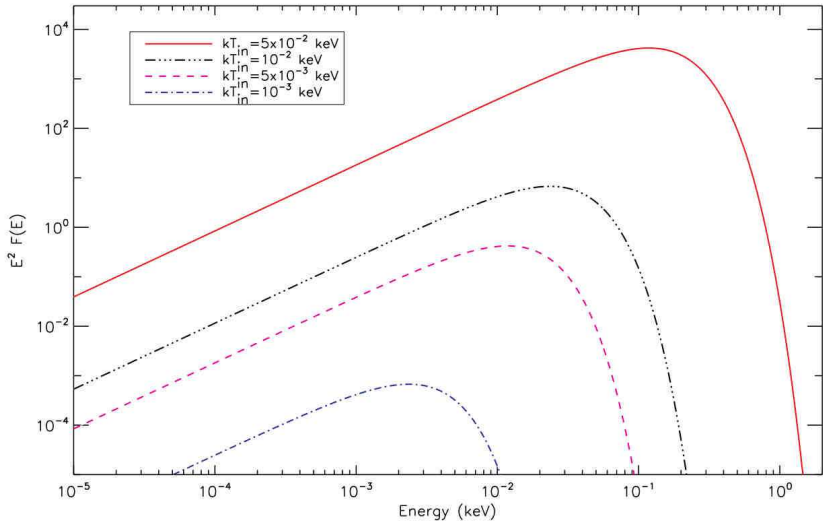

Figure 2 – Multicolor blackbody emission from geometrically thin optically thick Shakura and Sunyaev (1973) accretion disks with different values of the temperature of the inner layer T_{in}. Figure taken from Ricci (2011).

where R is the radius at which it is emitted, R_* is the radius of a body of mass M_* accreting at a rate $\dot{M}$, and T_* is given by:

$$T_* \propto \left(\frac{M_* \dot{M}}{R_*^3} \right)^{1/4} . \tag{9}$$

Between frequencies corresponding to the minimum (r_I) and maximum (r_{max}) distance from the accreting object, the spectrum of the accretion disk is given by:

$$I(\nu) \propto \nu^{1/3} \tag{10}$$

at frequencies less than that corresponding to the temperature of the disc at r_{max}, the spectrum tends towards a Rayleigh-Jeans spectrum, $I(\nu) \propto \nu^2$, while it shows a cutoff in the inner parts, $I(\nu) \propto exp(-h\nu/kT_{in})$, where T_{in} is the temperature of the innermost layers of the thin accretion disc. An example of the spectrum expected from an accretion disk (for different values of T_{in}, SHAKURA; SUNYAEV, 1973) is shown in Figure 2. Observationally this is seems as is show in Figure 3, and the optical portion is well fitted by a power-law, $Flux(\lambda) \propto \lambda^{-\alpha}$, with α usually ranging from 0.5 to 2.5.

The maximum temperature of a thin accretion disk around a Schwarzschild black hole occurs at r = 49/36 r_g (SHAKURA; SUNYAEV, 1973), and is:

$$T_{max} = 1.4 \times 10^5 \left(\frac{\dot{M}}{0.1 \dot{M}_{Edd}} \right)^{1/4} \left(\frac{\eta}{0.08} \right)^{-1/4} \left(\frac{M}{10^7 M_\odot} \right)^{-1/4} K \tag{11}$$

where $\dot{M}_{Edd} = L_{Edd}/\eta c^2$. For parameters typical of a Seyfert galaxy, one obtains an energy of kT_{max} = 12 eV, where k is Boltzmann's constant. From this value one can already see that the disk alone cannot account for the X-ray emission observed in AGN, we will discuss X-ray emission in section 1.2.5.

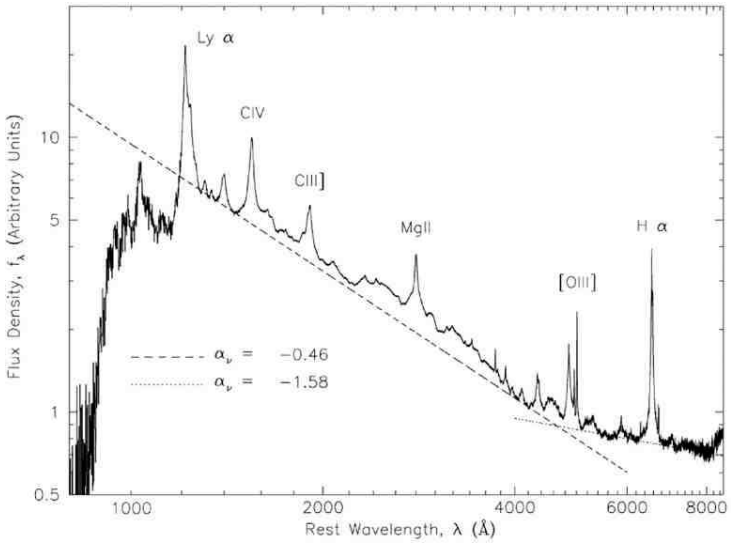

Figure 3 – Composite optical/UV spectra of an AGN. Taken from Vanden Berk et al. (2001).

Alternative accretion scenarios

The Shakura and Sunyaev (1973) model is today believed to be a precise model for the accretion disks in X-ray Binaries (stellar-mass black holes). However, the predictions by a simple scaled-up version of the model to SMBHs do not seem to fit well AGN observations. Given that for AGN scales (where the model still predicts the existence of a geometrically thin disk), the viscous time scale of the disk is in the order of 10^4 to 10^5 years, significantly exceeding the timescales over which AGN varies. Even more to the transitions of so-called "Changing Look" AGN's (CL-AGNS, see section 3.1) where abrupt variations are know to occur in few years time scales. This incompatibility was noticed long ago (e.g., KORATKAR; BLAES, 1999; ANTONUCCI, 2013), however, just recently, some modification or alternatives to the application of Shakura and Sunyaev (1973) model to AGNs have been proposed in order to explain the increasing number of the discovery of these highly variable sources.

For example, Dexter and Begelman (2018) propose that alternatively AGN accretion discs are vertically supported by magnetic pressure, which makes it geometrically thick (height/radius between 0.1 and 1.0) at all luminosities. Using three dimensional radiation magneto-hydrodynamic simulations, Jiang and Blaes (2020) show that, for a 5×10^8 $M_\odot$ mass black hole, the Rosseland mean opacity is expected to be larger than the electron scattering value, and the iron opacity bump then causes the disk to be convectively unstable. This results in strong fluctuations in surface density and heating of the disk, the opacity drops with increasing temperature, and convection is suppressed, the disk then cools down, and the whole process repeats. This causes strong oscillations of the disk scale height and luminosity variations by more than a factor of $\sim 3 - 6$ over a few years' timescales. They argue that since the iron opacity bump will move to different locations of the disk for black holes with different masses and accretion rates, this is a physical mechanism that can explain the accretion rate variability of AGN with a wide range of amplitudes over a time scale of years to decades.

The above-described scenario of an accretion disk seems not to apply for very Low Luminosity AGNs (LLAGNs). At very low ($\lambda_{Edd} \ll 0.01$) accretion rates, the low-density, tenuous

material is optically thin and cannot cool efficiently. Rather than settling into a classical radiatively efficient disk – the normal configuration for luminous AGNs – the accretion flow puffs up into a hot, quasi-spherical, radiatively inefficient distribution, whose dynamics may be dominated by advection, convection, or outflows. The existence of radiatively inefficient accretion flows (RIAFs, XIE; YUAN, 2012; YUAN; NARAYAN, 2014), or conversely, the absence of a standard disk extending to small radii (a few r_s), is suggested by the weak luminosities of LLAGNs, by their low Eddington ratios, and especially by their low inferred radiative efficiencies. The great disparity between the available fuel supply and the observed accretion luminosity demands that the accretion flow's radiative efficiency be much less than $\eta = 0.1$. The predictions for RIAF's spectral energy distribution seems to fit well the broad-band spectrum of a number of LLAGNs, including NGC 4258 (LASOTA et al., 1996), M81 and NGC 4579 (QUATAERT; NARAYAN, 1999), NGC 3998 (PTAK et al., 2004), and NGC 1097 (NEMMEN et al., 2006).

1.2.3 The Broad Line Region

Broad emission lines are one of the dominant characteristics of AGN spectra. These lines are assumed to be Doppler-broadened and are thought to be produced in a region close to the black hole, generally referred to as the Broad Line Region (BLR). The broad emission lines of AGN are a useful probe of the central engine. In fact, the bulk motions in the BLR are regulated both by gravity (due to the black hole) and by the radiation pressure (from the accretion disk). The widths of AGN broad lines span over two orders of magnitudes, and range from a minimum Full Width at Half Maximum (FWHM) of 800 $km\,s^{-1}$ to FWHM up to 10^4 $km\,s^{-1}$, with typical values of FWHM $\sim$ 5000 $km\,s^{-1}$. The strongest lines observed in the typical spectrum of an AGN are the hydrogen Balmer-series lines (Hα, Hβ, and Hγ), the hydrogen Lyα, and lines from abundant ions (Mg II, C III], and C IV), for an example see Figure 4.

The absence of forbidden lines such as [O III] λ5007 gives a lower limit to the ion density of $\sim 10^8$ cm^{-3} (NETZER; BLANDFORD, 1990). The BLR mass can be calculated from the luminosity of C IV and is negligible compared to that of the SMBH. Even for the most luminous AGN, it is estimated at $M_{BLR} \sim 10\ M_\odot$. The distance of the BLR from the central black hole can be inferred by studying the delay of the broad emission lines with respect to the continuum (reverberation mapping, see section 1.2.1), and it is found to vary with the luminosity, $R_{BLR} \propto L^{0.7}$ (KASPI et al., 2000). The average values found are 0.01-0.1 pc for local AGN and up to $\sim$ 1 pc for bright quasars.

1.2.4 The Narrow Line Region

The narrow-line region (NLR) is the most extensive AGN component and the only one which can be resolved by optical and infrared observations. Unlike the BLR, the electron density in the NLR is low enough that many forbidden transitions are not collisionally suppressed. Some of the most prominent narrow lines are Lyα λ1216, C IV λ1549, [O III] λ4959, [O III] λ5007, [N II] λ6584, [S II] λ6717 and [S II] λ6731. The FWHM for narrow emission lines lies in the range 200 $km\,s^{-1}$ to 900 $km\,s^{-1}$, with most of the lines having values of 350-500 $km\,s^{-1}$. Analogous to the BLR, the distance of the NLR to the central engine also scales with luminosity ($R_{NLR} \propto L^{0.5}$), and in Seyfert galaxies has sizes of $\sim$ 100-300 pc, while it might reach diameters of up to few

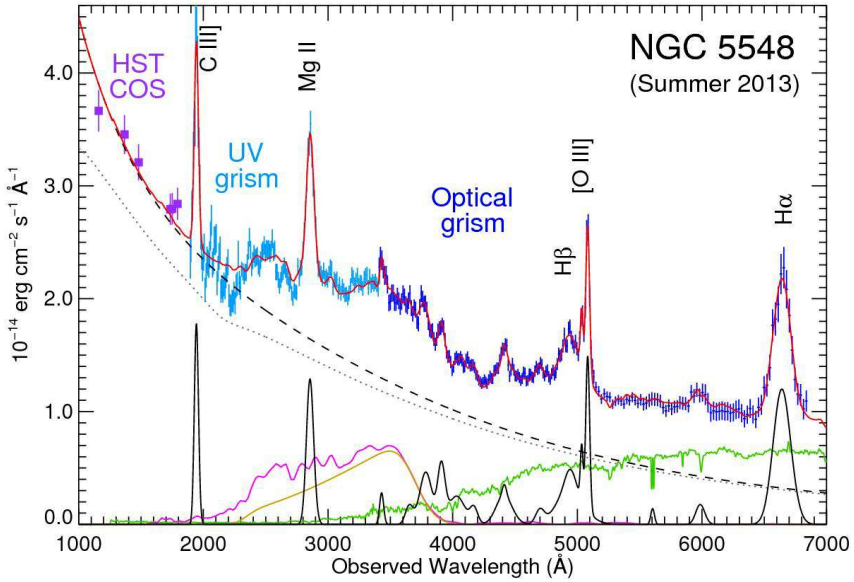

Figure 4 – UV/Optical spectrum of the Seyfert 1 galaxy NGC 5548. The spectrum highlights some of the most important features produced in the BLR. Figure from Mehdipour et al. (2015).

kpc for bright quasars. The NLR mass is several orders of magnitude larger than that of the BLR, although the amount of line emission produced is often comparable for the two regions. This is because recombination lines' emissivity is proportional to the ion density, which makes the BLR more efficient than the NLR.

The NLR is typically found to be axisymmetric rather than spherically symmetric. One of the most interesting features of AGN are the "ionization cones" which are clearly detected in maps of high-excitation lines as [O III] λ5007. These cones have a [O III]/Hα flux ratio higher than one, which is characteristic of low-density gas ionized by the AGN continuum (see section 1.3). Outside the cone, the ratio is instead lower than unity, which implies that the gas is mostly ionized by starlight. Figure 5 panel b shows clearly this distinction between the ionization cone, ionized by the AGN, and the galaxy bar, ionized by the stars.

1.2.5 The Corona

X-ray variability time scales indicate that the X-rays in AGN are produced in a small region located close to the black hole. The possibility that the disk is responsible for the X-ray emission can be discarded on the basis that even very warm disks are not supposed to exceed a few hundred eV (see section 1.2.2 and Figure 2). It is now widely accepted that the X-ray emission of AGN is produced by Comptonization of optical-UV photons produced in the accretion disk by a corona of hot electrons. Inverse Compton upscatters to higher energies photons when their mean energy ($\langle E \rangle$) is smaller than the thermal energy of the electrons (of temperature T_e): $\frac{\langle E \rangle}{mc^2} < \frac{4kT_e}{mc^2}$. For $h\nu \ll m_e c^2$ the gain rate of the photon field is:

$$\frac{dE}{dt} = \frac{4}{3}\,\sigma_T c\, U_{rad}\,(v^2/c^2)\,\gamma^2 \tag{12}$$

where σ_T is the Thomson cross-section, U_{rad} the energy density of the photon field, and $\gamma = \sqrt{1 - v^2/c^2}$. The spectrum created by this process depends on the Compton parameter y, given

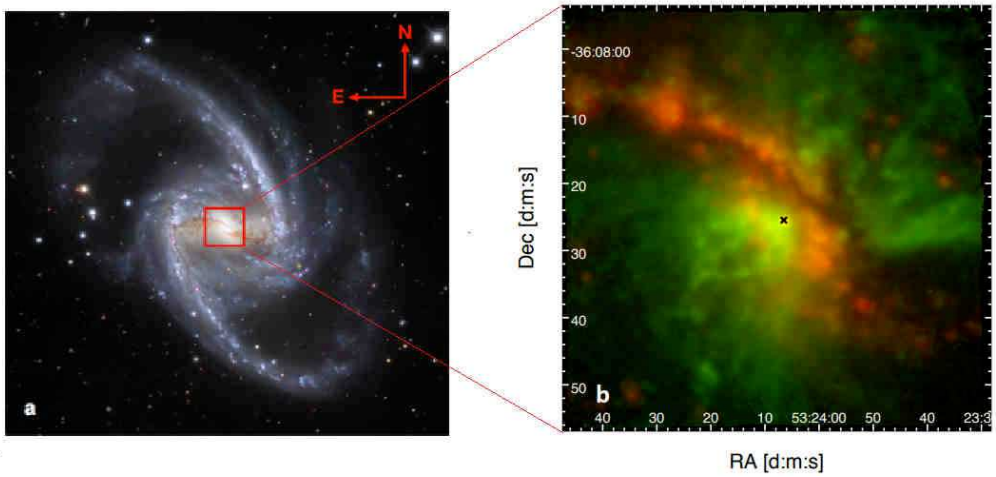

Figure 5 – (a) Three-color optical image of NGC 1365 combining observations performed through three different filters (B, V, R). (b) Two-color image of [O III] (green) and Hα (red) stellar subtracted integrated emission, showing the distinction between the AGN ionization cone (green) and the stellar ionized bar-like structure (red). Figure adapted from Venturi et al. (2018).

by:

$$y = \frac{k\, T_e\, \tau_e}{m_e\, c^2} \tag{13}$$

where τ_e is the optical depth of the corona. If the electron gas is optically thin, it can be shown (see Shapiro et al. (1976) for deduction) that the spectrum is a power-law with a photon index given by:

$$\Gamma = -\frac{1}{2} + \sqrt{\frac{9}{4} + \frac{4}{y}} \tag{14}$$

As the photons' energy becomes comparable to the electrons' thermal energy, the power-law emission declines in a cutoff at $E_C \approx 3kT_e$. The origin and geometry of the hot corona are still debated. A popular explanation for the heating of the electrons in the corona, is related to the presence of flares above the accretion disc, similarly to what is observed in the solar corona. Although the physical details are somewhat unclear, magnetic flares are a reasonably working hypothesis to model X-ray spectra and variability of AGN (e.g., HAARDT et al., 1994; GOOSMANN et al., 2006). In this scenario, the magnetic flares heat the electrons, which then Comptonize the UV photons from the disk, upscattering them into the X-rays.

The X-rays spectrum of AGNs

Comptonization of low energy seed photons in the hot corona plasma produces a power-law continuum. Such a power-law continuum that extends from the lowest observable X-ray energies to a cutoff energy somewhere after $\sim$ 100 keV is consistent with X-ray observations of Seyfert galaxies. The flux as a function of the energy of the power-law continuum is given by:

$$F(E) = A\, E^{-\Gamma}\ photons\ cm^{-2} s^{-1}\ keV^{-1} \tag{15}$$

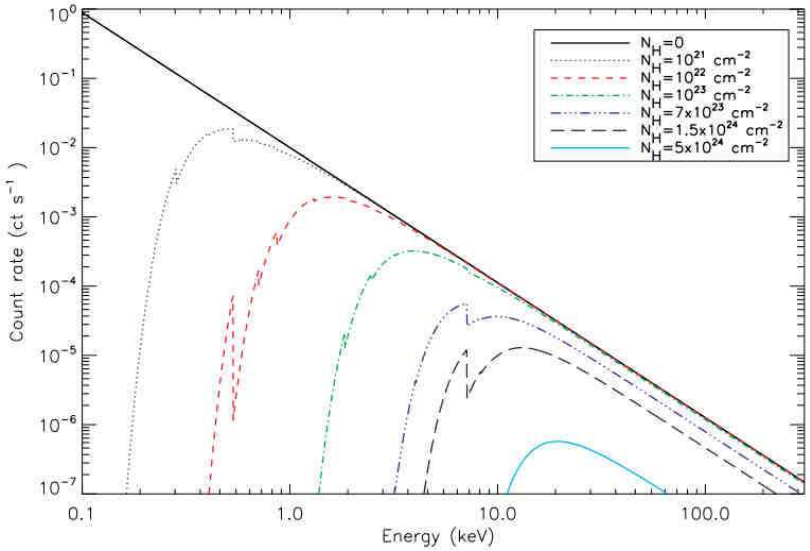

Figure 6 – Effect of photoelectric absorption and Compton scattering on a power law with a photon index of $\Gamma = 1.95$ in the X-rays for different values of the column density N_H. Figure taken from Ricci (2011).

where A is the normalization of the power-law at 1 keV, Γ is the photon index (equation 14).

Another important component of AGN X-ray spectra is absorption. Absorption manifests itself through two processes in the X-rays: photoelectric absorption (boundbound and bound-free transitions), and Compton scattering (free-free transitions). To model the effect of absorption one has to take into account both effects. The photoelectric cross section σ_{ph} has a strong dependence on the energy, and can be approximated according to the analytic formulae of Morrison and McCammon (1983):

$$\sigma_{ph}(E) = (C_0 + C_1 E + C_2 E^2)\, E^{-3} \times 10^{-24}\ cm^{-2}, \tag{16}$$

where C_0, C_1 and C_2 are constants. Compton scattering depends on the Thomson cross section (σ_T), and does not vary with the energy, it becomes significant only for column densities higher than σ_T^{-1} ($1 \times 10^{24}\ cm^{-2}$), and sources with the column density (N_H) higher than σ_T^{-1} are called Compton-thick. The Effect of photoelectric absorption and Compton scattering on a power law with a photon index of $\Gamma = 1.95$ is shown is Figure 6 for different values of N_H.

An important feature observed in the X-ray spectra of AGN is the reflection component, produced by Compton scattering of the primary emission in some Compton thick material close to the X-ray source. Reprocessed emission from neutral material is commonly observed in AGN through the iron (Fe) Kα emission line. The Fe Kα line is now known to be often constituted by two components, a narrow and a broad one. The widths of the narrow line core component usually are of the order of a few thousand $km\,s^{-1}$, values which are consistent with the line originating in the BLR (e.g., YAQOOB et al., 2001; KASPI et al., 2002). However, the lack of a correlation between the width of the narrow Fe Kα line and the Hβ width or the black hole mass (NANDRA, 2006) suggests that a significant fraction of the narrow Fe Kα line is produced in some other region, possibly in the outer part of the accretion disk. This would explain the rapid (tens of ks) variability observed in some objects (e.g., PETRUCCI et al., 2002). Most of

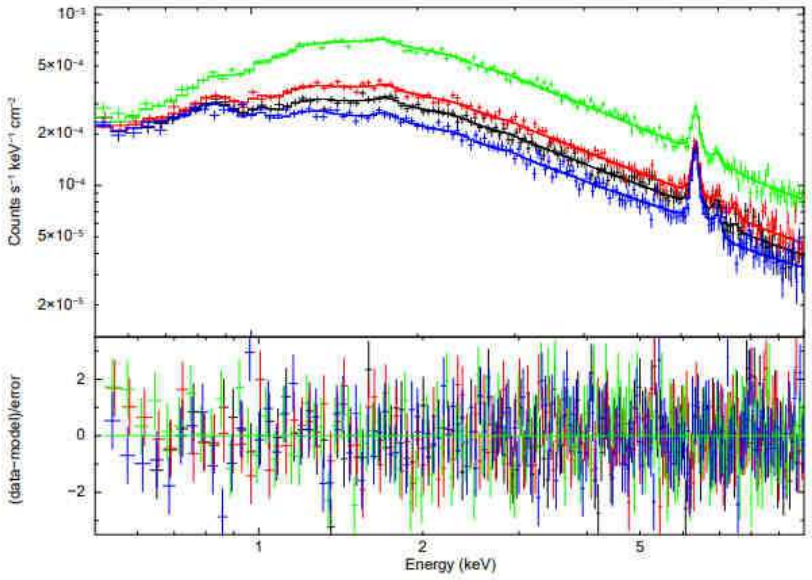

Figure 7 – Top: Four 0.2-10 keV X-ray spectra of NGC 2992, showing the power law corona emission and the 6.4 keV Kα lines. Bottom: Residual between equation 17 model and data. Figure taken from Marinucci et al. (2018).

the reflected emission is, in fact, nowadays believed to originate in the accretion disk, where the broad relativistic component is also thought to arise (e.g., NANDRA et al., 2007), while the narrow portion arises in the outer disk and the broader arrises near r_I.

In the simplest case, the X-ray spectra for a Compton-thin AGN (where reflection by Compton scattering is negligible) can be written as:

$$F(E) = e^{-\sigma_{ph}(E)N_H^G} \times \left[e^{-\sigma_{ph}(E)N_H} \times A\,E^{-\Gamma} + G(E)\right] \tag{17}$$

where the term $e^{-\sigma_{ph}(E)N_H^G}$ represents the Galactic photoelectric absorption, by a N_H^G Galactic column density in the line-of-sight, $e^{-\sigma_{ph}(E)N_H}$ the photoelectric absorption by a N_H column density in the AGN. $AE^{-\Gamma}$ is the primary power-law corona emission and $G(E)$ a Gaussian profile to fit the 6.4 keV Fe kα (if both narrow and broad components are present, other Gaussian profiles can be added). Several other physical components can also be found in AGN X-ray spectra, e.g., the soft excess and the reflection hump; however, they will not be taken into account here, because they are not present in NGC 2992 spectra. In Figure 7 four X-ray spectra, taken in different dates, of NGC 2992 are shown as an example.

1.2.6 The Jets

AGNs can be divided in two classes related to their radio emission, Radio-Loud (RL) and Radio-Quiet (RQ) AGNs. For the RL the radio emission is typically 10^3 times brighter than that in RQ ones. However, a sharp separation between RL and RQ is hard to set, as AGN show a large variety of radio properties and morphologies, with sources exhibiting compact cores, jets, knots, and extended diffuse emission in a wide range of strengths and sizes ranging from sub-pc up to kpc and even Mpc scales.

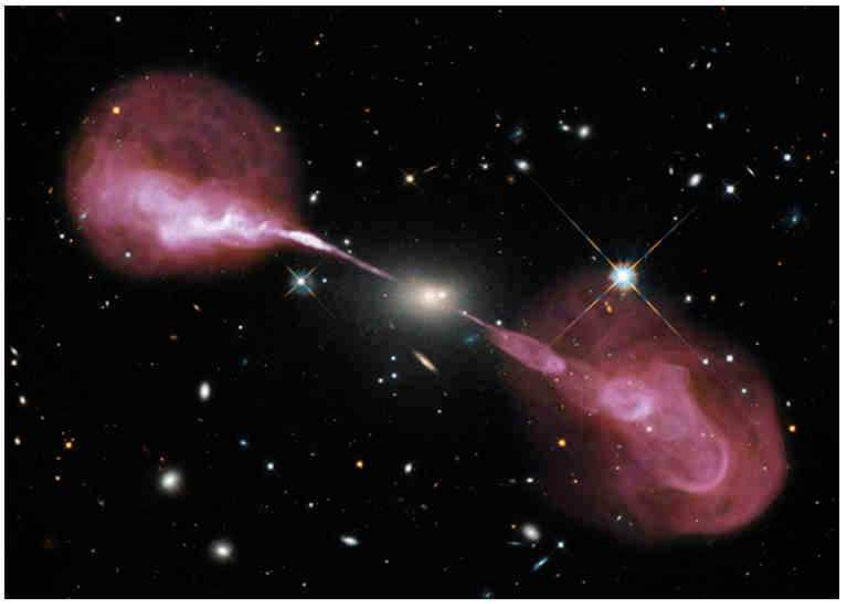

Figure 8 – Combination of images using data from the VLA (radio) and HST (optical) from the Radio Hercules A galaxy, showing the radio jet extending greater distances from the nucleus than the galaxy itself. Figure taken from O'Dea et al. (2013).

For the RL the radio emission is due to the synchrotron radiation generated in the relativistic jets, as well as the Radio lobes resulting from the interaction of the jets with intergalactic medium, sometimes present in these objects (see Hercules A, in Figure 8, for a example of the radio emission). The production, acceleration and collimation of jets is still poorly understood. Some of the most popular models are based on magneto-hydrodynamics (BLANDFORD, 2001), and involve the presence of strong electromagnetic fields that convert the rotational kinetic energy of a rotating black hole into an outflow through coupling with differential rotation. The Radio emission in RQ AGNs is thought to have distinct origins, e.g., star formation, accretion disc winds, expanding plasma bubbles, low-power short jets[1] or a combination of them.

1.3 AGN Selection, Classifications and Models

1.3.1 The BPT Diagram

AGN can be distinguished from normal non-active galaxies in several different ways. Apart from its ubiquitous X-ray emission, one of the most commonly used diagnostics are the so-called BPT diagrams (BALDWIN et al., 1981), which show the ratios of several lines (e.g., [O III]/Hβ vs [N II]/Hα, [O III]/Hβ vs [S II]/Hα, and [O III]/Hβ vs [O I]/Hα, see Figure 9).

Limiting regions based on empirical or theoretical models are used as a division between distinct ionization sources in the BPT diagram. The Kewley et al. (2001) curve, red in Figure 9, traces the theoretical upper limit of regions ionized by pure star formation, and therefore all spectra lying above the Kewley et al. (2001) line must include ionization mechanism more energetic than star formation. The dashed blue curve on the [N II]/Hα vs. [O III]/Hβ diagnostic diagram

[1] Here we use the 'jet' term to indicate an outflow that becomes collimated, whereas a 'wind' is an uncollimated outflow. Both transport outwards mass, energy and angular momentum.

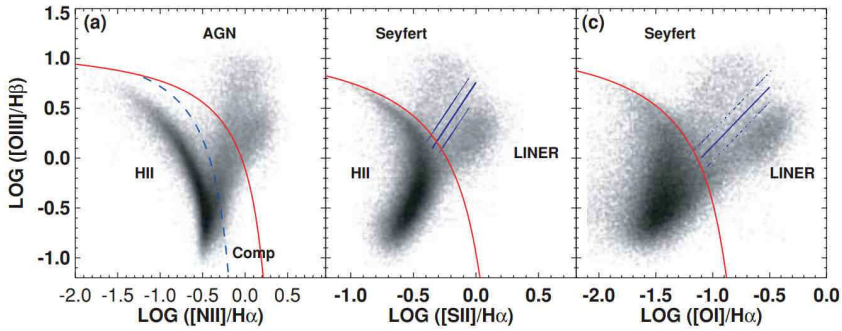

Figure 9 – Three BPT diagrams showing the classification of galaxies using emission-line ratios. The Kewley et al. (2001) extreme starburst classification line (red solid), the Kauffmann et al. (2003) pure star-formation line (blue dashed), and the Seyfert and "LINER" line (blue solid) by Kewley et al. (2006) are used to separate galaxies into H II region-like (star formation), AGN and LINERs (but not only, also shocks and retired galaxies) ionization and composite types. Figure taken from Kewley et al. (2006).

shows the Kauffmann et al. (2003) empirical classification line, which traces the upper boundary of the Sloan Digital Sky Survey (SDSS, STRAUSS et al., 2002) star formation sequence.

The full blue curve on the [S II]/Hα vs. [O III]/Hβ and [O III]/Hβ vs [O I]/Hα diagnostic diagrams traces the Kewley et al. (2006) empirical classification line, which separates high ionization spectra associated with Seyfert (AGN) and intermediate ionization mechanisms. This region is often referred to as being the Low-ionization nuclear emission-line region (LINER)'s region – a class of LLAGNS – however, besides AGNs and LINERs, several excitation mechanisms can also increase the collisional excitation rate, enhancing the ratios of the forbidden to recombination lines, among them shock excitation and evolved stellar populations (pos-AGB). Particularly, Cid Fernandes et al. (2011) proposed another classification diagram that uses the Equivalent Width of Hα ($W_{H\alpha}$) versus [N II]/Hα (WHAN diagram), to distinguish from LINERs and Retired Galaxies with Diffuse Gas (DIG) Ionized by pos-AGB stars, the later having $W_{H\alpha} < 3$ Å (STASINSKA et al., 2008; CID FERNANDES et al., 2011).

Starburst-AGN mixing

The original BPT and its application to SDSS data (previous section and Figure 4) were based on spectra taken using a single large aperture, and therefore accounting for the emission lines in the entire or most of the central portion of the galaxies. However, using spatially resolved spectroscopy (Longslits or Integral Field Unit), it is possible to resolve the internal structures in the ionization mechanism of galaxies. In particular, the spatially resolved BPT of some AGNs show an interesting feature – known as Starburst-AGN mixing (e.g., DAVIES et al., 2014b, 2014a; D'AGOSTINO et al., 2018) – in these galaxies the nuclear spectra are located above Kewley et al. (2001) line, but they cross the line continuously, as the radius increases, towards Kauffmann et al. (2003) line, and end up, at the outer radius, below the line, at the pure-starburst region. Figure 10 illustrates this feature in NGC 5728 as an example.

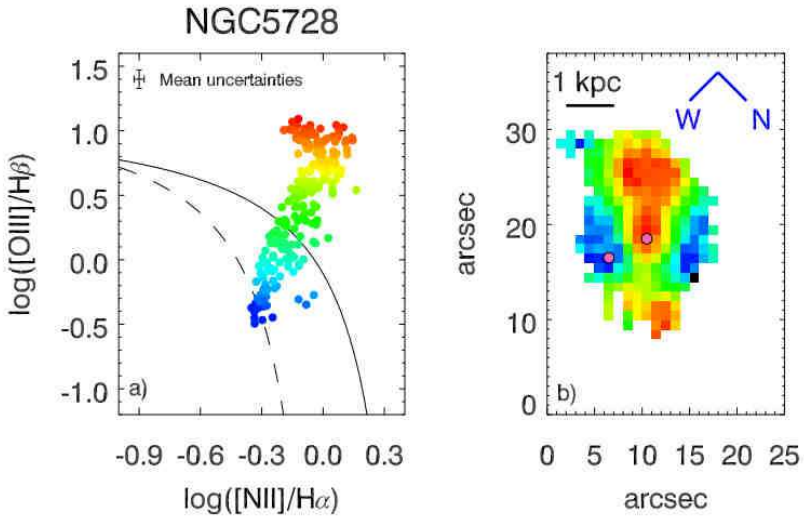

Figure 10 – Resolved BPT diagram showing the Starburst-AGN mixing for NGC 5728. Figure taken from Davies et al. (2016).

1.3.2 AGN Classes and the Unified Model

Radio-quiet AGNs are divided into low luminosity Seyfert galaxies (the most common AGN in the local universe) and high luminosity quasars. The division between the two classes is usually set to $M_B = -23$ *mag*, where M_B is the absolute magnitude in the *B* band. Historically, Type 1 AGNs are those showing both broad (section 1.2.3) permitted emission lines and narrow (section 1.2.4) forbidden lines in their optical spectra; while Type 2 AGNs lack Broad Emission Lines (BEL). Intermediate AGN types were added by Osterbrock (1981), including types 1.8 and 1.9, classified according to the presence of a weak (type 1.8), or absent (type 1.9), Hβ BEL, while retaining an Hα BEL. Type 1 AGN spectra usually present a power-law like featureless continuum (FC) emission from the accretion disk (section 1.2.2), while Type 2 usually lack this feature.

The presence of intermediate objects between Seyfert 1s and Seyfert 2s was firstly explained by differences due to varying amounts of absorbing material along the line of sight. This led to introducing a dust shell with any possible geometry, from a 4π shell with varying thickness to an angle-dependent axisymmetric structure or a patchy distribution of dust. The discovery of polarized BELs in the spectrum of the Seyfert 2 galaxy NGC 1068 by Antonucci and Miller (1985, see original plot in Figure 11) led to the idea that a torus-like distribution of matter surrounds AGNs. In this scheme the broad lines observed in the polarized spectrum of NGC 1068 are produced by the reflection of the radiation emitted in the BLR. According to the unified model of AGN, all the objects have a dusty torus extending from 1 to 100 pc from the center, and in this frame, Seyfert 1s are observed pole on (see Figure 12) so that the observer can look at both the BLR and the NLR at the same time, whereas Seyfert 2s are observed edge-on so that the BLR is obscured and one can see only the NLR (ANTONUCCI, 1993; URRY; PADOVANI, 1995).

The Unified Model has been conceived to explain the large zoo of different AGN with a

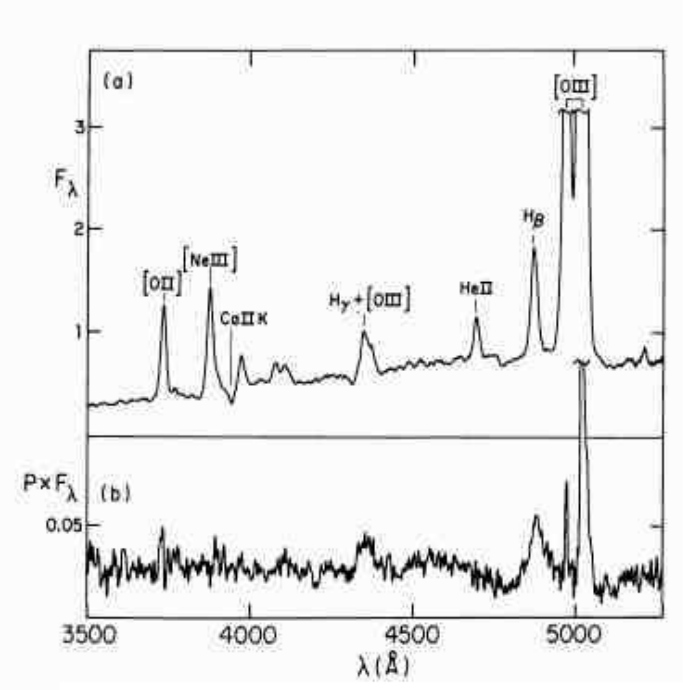

Figure 11 – The original spectro-polarimetric observation of NGC 1068 by Antonucci and Miller (1985).

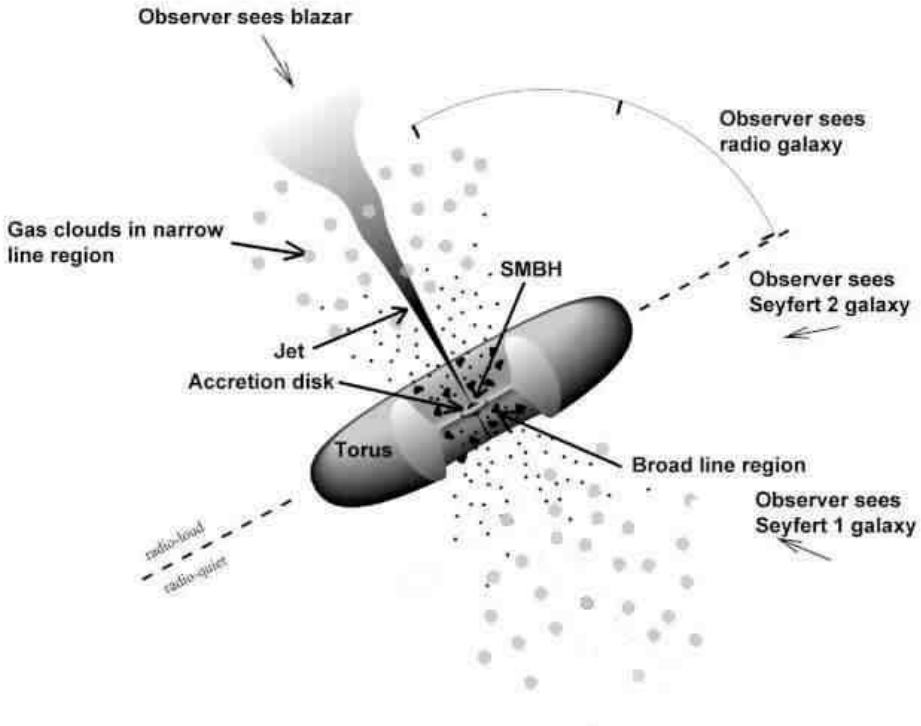

Figure 12 – Illustrative diagram of the unified model for AGNs. Adapted from Urry and Padovani (1995).

single physical object. However, while it is well recognized that it works for unifying the so-called "Hidden Broad Line Region Galaxies"(HBLR), i.e., those galaxies for which either polarization or near-IR spectra show BELs, with the AGN type 1, it cannot be generalized to all AGN types. At least three main observational evidence goes against the Unified Model in some way (SPINOGLIO; FERN ANDEZ-ONTIVEROS, 2019):

- It seems so far that no strong observational evidence of tori with the needed characteristics to block BLR, collimate radiation, and let AGN feeding has yet been found, on the other hand, there seems to have more evidence for models where the tori has a more patch-like structure (e.g., NENKOVA et al., 2008; ELITZUR, 2012).
- The recently discovery of several CL-AGNs (more on this in section 3).
- The existence of galaxies which does not have BELs even in polarized spectrum, the so-called 'True' type 2 Seyfert galaxies, or even non-HBLR (e.g., TRAN, 1995, 2003; LUMSDEN; ALEXANDER, 2001; MARINUCCI et al., 2012).

1.3.3 The 'True' Type 2 and the Disk-Wind BLR Models

The existence of these AGNs that do not have a BLR, in particular the fact that these AGN are all accreting at very low Eddington Ratio ($\lambda_{Edd} \ll 0.01$, MARINUCCI et al., 2012) and that a simple orientation-based unification model can not explain this effect, has led to the development of complementary, or even alternative, models in order to explain these phenomena.

Several authors have proposed models that posit different accretion rates as a cause of the differences between observed AGNs. Elitzur and Ho (2009) suggests that the BLR and the "torus" are inner (ionized) and outer (clumpy and dusty) parts of the same disk-driven wind and that this wind is no longer supported at low accretion rates (NICASTRO, 2000; ELITZUR; SHLOSMAN, 2006; ELITZUR; HO, 2009; ELITZUR et al., 2014). Based on this disk-wind BLR model, Elitzur et al. (2014) proposed that the intrinsic spectral sequence Seyfert 1$\rightarrow$ Seyfert 1.8/Seyfert 1.9$\rightarrow$ Seyfert 2[2] is a true evolutionary sequence, reflecting the evolution of the BLR structure with decreasing accretion rate onto the central black hole and that this evolution is regulated by the $L_{bol}/M_{BH}^{2/3}$ variable (which behaves similarly to λ_{Edd}). These models have been successfully used to explain the existence of 'True' Type 2 Seyferts as shown by Marinucci et al. (2012) as well as have been used, recently, as possible scenario for the transitions in CL-AGNS.

1.4 The Role the AGNs in the Evolution of Galaxies

The strong relation between the SMBH masses and their host galaxies' properties (e.g., $M_{BH} - \sigma_*$, see Figure 1, section 1.2.1 and references therein) has generated intense interest in connecting the growth of SMBHs with the formation of galaxies, thus creating a research subfield, which tries to understand and quantify such a connection.

The presence of these correlations suggests a causal link between the formation of the spheroid and the central black hole, or that a common cause regulates the evolution of both. Another piece of evidence also suggests such a link, the evolution, and growth of both SMBH

[2] Referring here only to the "True" Type 2 Seyferts, therefore excluding those which have hidden Type 1 nucleus.

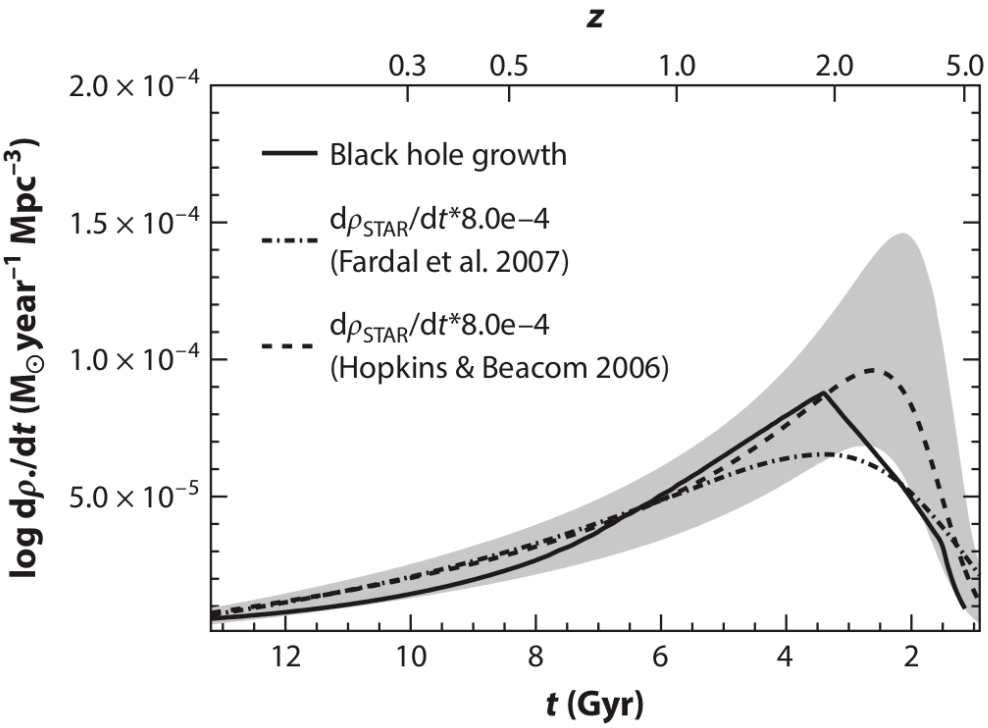

Figure 13 – The cosmological growth of SMBH and stellar mass in the universe. Figure taken from Shankar et al. (2009).

(as traced by AGN accretion rate) and galaxies (as traced by star formation rate) is surprisingly similar during the history of the universe. There seems to have a sharp increase in the density star formation rate (SFR) and the SMBH growth rate at about a factor of 10, at $0 < z < 1$, a broad maximum at both rates at $z \sim$ 2-3 and then a relatively sharp decline in higher redshifts (see Figure 13). At least for the last $\sim$ 11 billion years (Gyr) the ratio between the growth of both SMBHs mass and stellar mass has remained approximately constant, in the order of 10^{-3}. Somehow the growth of both has been kept in synchronized (HOPKINS; BEACOM, 2006; FARDAL et al., 2007; SHANKAR et al., 2009).

Although such relationships exist, AGNs' exact role in the evolution of galaxies is not yet fully understood. It is known that the energy released by AGN feedback in the form of radiation, winds, or radio-plasma jets has a significant impact on the interstellar medium of the host galaxy. However, the exact role of feedback is still a matter of debate (feeding and feedback mechanism will be further discussed in section 2.1). However, hydrodynamic simulations of galaxy formation are not able to reproduce the observed galaxy mass function if no AGNs feedback mechanism is inserted in the simulations (SPRINGEL et al., 2005; SILK; MAMON, 2012; BULLOCK; BOYLAN-KOLCHIN, 2017), where these processes are responsible for suppressing the growth of more massive galaxies heating up and/or expelling the gas that would form more stars, thus limiting the growth of very massive galaxies. Figure 14, as an example, shows the mass function for dark matter, expected by numerical simulations, and the observed mass function of galaxies, it is clear that there is a significant discrepancy between the two functions for galaxies more massive than $10^{11.5}$ $M_\odot$, indicating the need for some kind of AGN feedback effect. There is also a discrepancy in the number of dwarf galaxies, which can be explained only by stellar winds

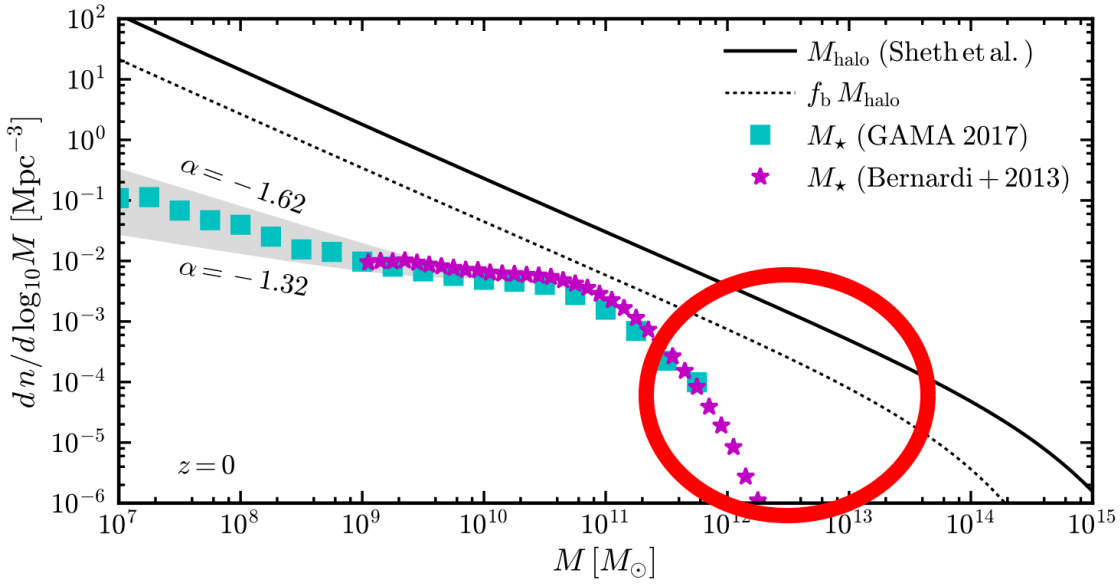

Figure 14 – The filled black curve shows the global mass function for dark matter. The dotted curve shows the same function shifted to the left, representing the fraction of baryons for each dark matter halo. This is compared to stars' observed mass function in galaxies (blue dots and purple stars). The red circle shows the absence of very massive galaxies as expected by the simulations, showing the need for mechanisms that prevent the formation of galaxies with these masses. Figure adapted from Bullock and Boylan-Kolchin (2017).

and supernovae feedback.

1.5 NGC 2992

NGC 2992 is an interacting Seyfert galaxy which is part of the merger system Arp 245. The system is composed of two spiral galaxies, NGC 2992 and NGC 2993 and is in an initial stage of interaction but already has strong morphological disorders. In addition to the two main galaxies, the prominent tidal tale north of NGC 2992 hosts a candidate Tidal Dwarf Galaxy (TDG), called Arp 245 North (A245N), see Figure 15 and Duc et al. (2000).

The system as a whole was studied in detail by Duc et al. (2000), where the main goal was to understand the interaction process and the formation of TDGs, the authors used observations – i.e., optical and infrared photometry, optical spectroscopy and neutral hydrogen mapping using the 21 cm line – as well as numerical simulations of the interaction. H I maps show long tidal ranges, see Figure 16, which are even more extensive than in optical images, a gas bridge between the two galaxies, and also clearly shows a gas reservoir in the north tail at the same location as A245N. The simulations suggests that the system is in an initial phase of the interaction, $\sim$ 100 million years (Myr) after the first perigalactic passage and 700 Myr before final coalescence. The Figure 17 shows the snapshots of simulation whose initial parameters better reproduce the system; more details of the simulations and choice of parameters can be seen in section 3 of Duc et al. (2000).

NGC 2992 is seen almost edge-on ($i \approx 70°$, MARQUEZ et al., 1998) at a distance, as measured using the Tully-Fisher relation and corrected for proper motions, of 38 M*pc*

Figure 15 – LRGB image composition of Arp 245 from Block (2011). North is up and east is left, NGC 2992 is the reddish galaxy.

(THEUREAU et al., 2007), which translates into a projected angular scale of $\sim$ 150 pc per arcsec. The galaxy nuclear activity has been the subject of several studies, partly due to its variability as seen both in X-rays (GILLI et al., 2000; MARINUCCI et al., 2018) and in the optical (TRIPPE et al., 2008b), even leading to changes in spectral classification (these will be fully explored in chapter 3).

In the radio, the galaxy is a RQ AGN, however its 6 cm radio observations show a double lobe 8-shaped structure of about 8 arcsec ($\sim$ 1 kpc) extension to the northwest and Southeast of the galaxy, along position angle (PA) of –26° (ULVESTAD; WILSON, 1984). From IR observations, Chapman et al. (2000) suggest the best interpretation is that this structure is related to expanding plasma bubbles, possibly carried by internal jets from the AGN. More recently, using radio polarimetry, Irwin et al. (2017) found another double-lobed radio morphology within its spiral disc, which was revealed in linearly polarized emission but not in total intensity emission. This second structure by Irwin et al. (2017) is much more extended than the one found by Ulvestad and Wilson (1984) reaching several kpcs from the nucleus, being interpreted by the authors as a relic of an earlier episode of AGN activity. The X-ray properties of the galaxy will be fully explored in chapter 3.

NGC 2992 gas kinematics is complex as found by several long slit spectroscopy studies (e.g., MARQUEZ et al., 1998; VEILLEUX et al., 2001) as well as by several IFU data (GARCA-LORENZO et al., 2001; FRIEDRICH et al., 2010; MULLER-SANCHEZ et al., 2011). These

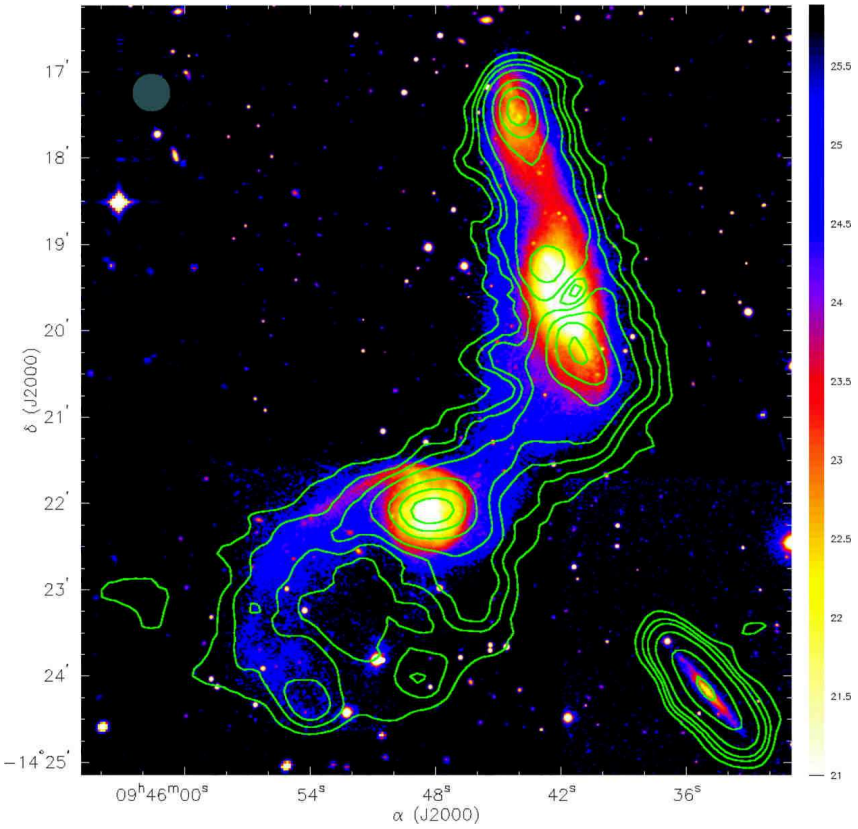

Figure 16 – H I distribution in Arp 245. H I lines contours are superimposed on an image in the V band, taken from Duc et al. (2000). The contours are 1, 2, 3, 5, 10, 15 and 20 $\times$ 10^{20} cm^{-2}.

observations show, at most slit positions, the presence of a double component line profile. While one component follows the galaxy rotation curve, the other is interpreted as outflowing gas by the authors. Using The Multi Unit Spectroscopic Explorer (MUSE, BACON et al., 2010) at the Very Large Telescope (VLT) Mingozzi et al. (2019) show the presence of a kpc-scale, bipolar outflow with a large opening angle.

1.6 This Work

The peak of star formation and SMBH growth in the universe was between redshift 3 and 2 (Figure 13), and therefore the effects of both AGN feedback and mergers were more critical to galaxy evolution at that time than they are in the local universe. However, the high redshift universe is only now becoming accessible, and the observational facilities can not yet reach the pc scales resolution need to resolve the internal structures of these galaxies. Therefore, nearby galaxies, such as NGC 2992, are still essential laboratories to study these processes, not only due to the high physical spatial resolution that can be reached but also because this sources have been followed-up since the early '50s by distinct instruments in several wavelengths.

The following sections are the result of two independent works in which we apply distinct methods and techniques to probe distinct physical regions of the AGN in NGC 2992:

- In chapter 2, we explore the feeding and feedback process that may operate in the circumnuclear region of this galaxy as it is both an interacting galaxy and an AGN, therefore,

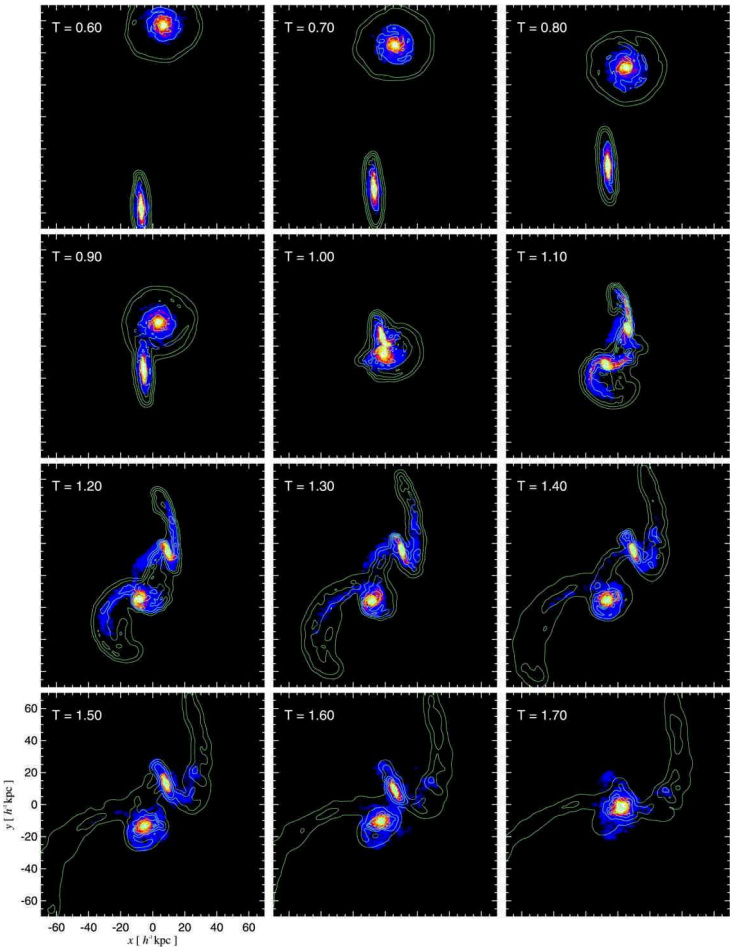

Figure 17 – Time evolution of the numerical model of the system Arp 245 by Duc et al. (2000). In each panel, it is shown the projected distribution of the stars (color scale) and that of the gas (green contours). Each panel is 140 h^{-1} kpc on a side, and the labels give the elapsed time after the start of the simulation in units of 0.1 Hubble times (or 0.98 h^{-1} Gyr). The model is shown in the plane of the sky and the orientation is the same as in Figure 15.

being one of the nearest probes of the so-called AGN-Merger connection. We do so by using optical Integral Field Unit (IFU) spectroscopic observations, using the GMOS instrument at the Gemini South Telescope, of the galaxy's inner kpc to spatially resolve both the stellar populations and the properties of the ionized gas as well as the effect of the radio-emitting structure in the interstellar medium.

- In chapter 3, we use time-domain astronomy to probe the central engine of the AGN, since it can not be spatially resolved. We analyze all historical (1978 to 2019) optical and X-ray spectra of the source in order to investigate its long-term variability and the singular physics of this source, which is an example of a rare 'Changing Look' AGN.

2 THE CIRCUMNUCLEAR REGION OF NGC 2992

This chapter is fully based on the following paper, of which I am the lead author, and therefore is not intended as an original work:

"Exploring the AGN-Merger Connection in Arp 245 I: Nuclear Star Formation and Gas Outflow in NGC 2992", **Guolo-Pereira, M.**, Ruschel-Dutra, D., Storchi-Bergmann, T., Schnorr-Müller, A., Cid Fernandes, R., Couto, G., Dametto, N, Hernandez-Jimenez, J. A., 2021, MNRAS, 502, 3618.

2.1 Introduction: Feeding and Feedback

As discussed in section 1.4 AGNs may have had an important role in the evolution of galaxies. The energy released by the AGN in the form of radiation, winds, or radio plasma jets is known to impact the interstellar medium of the host galaxy. However, it is still the subject of an ongoing debate about such AGN feedback's exact role. Some studies indicate that the shocks resulting from the interaction between the jets and interstellar medium may trigger star formation (e.g., OOSTERLOO; MORGANTI, 2005; ISHIBASHI; FABIAN, 2012; ZINN et al., 2013; SILK, 2013). On the other hand, as exemplified by Figure 14, feedback may be an important factor in the quenching of star formation, mainly at late stages of galaxy evolution (e.g., DI MATTEO et al., 2005; CROTON et al., 2006), in which these processes are responsible for suppressing the growth of most massive galaxies, by heating and expelling that gas that would form stars. Observationally, feedback in the form of large scales gas outflows are observed in very energetic forms (e.g., RUPKE; VEILLEUX, 2011; GREENE et al., 2012) reaching up to 1000 $km\,s^{-1}$, those being usually produced by the interaction between the ionized gas and strong magnetic fields (BISNOVATYI-KOGAN; LOVELACE, 2001), but also in the less energetic forms, in nearby galaxies, with velocities as low as $\sim 100 - 200$ $km\,s^{-1}$, with mass outflow rates averaging at a few solar masses per year (e.g., RIFFEL; STORCHI-BERGMANN, 2011; CRENSHAW et al., 2015; REVALSKI et al., 2018, see Figure 31 for more examples).

In order for a passive SMBH to be activated, the interstellar medium (ISM) or even intergalactic medium (IGM) material has to lose angular momentum and by some dynamical mechanism be transported from regions in galactic scales (kpc) to nuclear regions (sub-pc) in order to feed the central object. Two types of feeding process are proposed: environmental mechanism and secular mechanism (STORCHI-BERGMANN; SCHNORR-MÜLLER, 2019, for a revision in the feeding mechanisms). Secular mechanisms are those internal to the host galaxy, which can lead its gas to lose angular momentum. Theoretical studies and simulations show that non-asymmetric potential wells may efficiently promote gas inflow towards the nuclear regions of the galaxy (e.g., SHLOSMAN et al., 1990; ENGLMAIER; SHLOSMAN, 2004; KNAPEN, 2005). Using IFU observations, several authors were able to detect gas inflows in nuclear bars as well as in small-scale nuclear spiral arms, in both ionized and molecular gas (e.g., STORCHI-BERGMANN et al., 2007; RIFFEL et al., 2008; SCHNORR MÜLLER et al., 2011; COMBES et al., 2014).

Environmental mechanisms are those in which external factors to the host galaxy are responsible for driving the inflows; between them, mergers may be the most efficient ones.

Theoretical studies suggest large scale events like major mergers are the dominant processes leading to SMBH growth at high masses (MENCI et al., 2014). At high redshifts (z > 2), major mergers have also been proposed as fuelling mechanisms of the fastest-growing SMBHs (TREISTER et al., 2012). A major merger can destabilize large quantities of gas due to tidal forces, driving, therefore, massive inflows towards the nuclear region of galaxies and triggering bursts of star formation and nuclear activity (HOPKINS; ELVIS, 2010; BLUMENTHAL; BARNES, 2018). Many studies have found that the most luminous AGN are preferentially hosted by galaxy mergers (e.g., SCHAWINSKI et al., 2010; GLIKMAN et al., 2015; FAN et al., 2016). At lower luminosities, several studies have found a higher incidence of galaxies with signatures of interactions in AGN hosts as compared to control samples (KOSS et al., 2010) and particularly in close galaxy pairs (ELLISON et al., 2011; SATYAPAL et al., 2014) suggesting kinematic pairs are conducive environments for SMBH growth.

The inflow of gas, by either secular or environmental mechanism, drives the simultaneous growth of the stellar mass (by triggering star formation) in the nuclear region and of the SMBH, this may be a possible explanation to the existence of the relations between bulge's and SMBH's properties (as described in 1.2.1 and Figure 1). Observationally, Seyfert galaxies have younger nuclear stellar populations than those present in normal (non-active) galaxies. In fact, young stars seem to commonly coexist with AGNs in nuclear regions of active galaxies, as shown by several stellar populations analyses (e.g., STORCHI BERGMANN et al., 1990; STORCHI-BERGMANN et al., 2000, 2002; DELGADO et al., 2001; CID FERNANDES et al., 2004; RIFFEL et al., 2007). Kauffmann et al. (2003), for example, have studied a sample of more than twenty-two thousand AGN host galaxies from the SDSS and concluded that luminous AGNs are commonly found in bulges with younger stellar populations. Recently, Mallmann et al. (2018) explored the spatially resolved stellar populations of 62 AGNs with the Mapping Nearby Galaxies at APO (MaNGA, BUNDY et al., 2015) Survey and found a higher fraction of young stars ($t < 4 \times 10^7$ years) in the central regions ($R \leq 0.5 R_e$) of luminous AGNs ($L[O\,III] \geq 10^{41.25}$ ergs/s) when compared with the control sample.

To explore these multiple scenarios and possibilities, in this section, we use spatially resolved optical spectroscopy data to probe both the stellar populations and the ionized gas properties of NGC 2992's circumnuclear region.

2.2 Observations and Data Reduction

This chapter's work is mostly based on data obtained with the Integral Field Unit (IFU) of the Gemini Multi Object Spectrograph (GMOS) at the Gemini South telescope on the night of February 15, 2018 (Gemini project GS-2018A-Q-208, P.I. Ruschel-Dutra). The observations consisted of two adjacent IFU fields (covering $5'' \times 3\farcs5$ each). The fields are slightly offset, both in Right Ascension (RA) and Declination (Dec), in order to increase the field of view (FoV) and cover a larger portion of the galaxy plane. For each IFU field, there are six exposures, with an integration time of 560 seconds each. Each science observation is accompanied by a $5'' \times 1\farcs75$ sky observation for atmospheric lines removal.

The reduction procedures were performed using the Gmos Ifu REDuction Suite (`GIREDS`)[1].

[1] `GIREDS` is a set of python scripts to automate the reduction of GMOS IFU data, available at GitHub.

The process for each of the 12 observations comprised the usual following steps:

- Bias subtraction: Essentially, all detectors have non-zero counts on 0-second exposure; these counts are called bias. In order to remove this signature from the instrument, the bias counts are subtracted from the science files.
- Flat-field correction: A flat field is the response of the telescope/camera system to a source of uniform illumination. A flat field frame is basically an image of a uniformly illuminated field. Since the image of the flat field contains differences in illumination due to variations within the optical system, dividing the science image by the normalized flat field frame corrects the scientific image for these instrumental variations.
- Removal of cosmic rays: cosmic rays are highly energetic particles that generate a high number of counts when reaching the CCD, which can be identified as the black dots randomly scattered in the images. Their removal is done using the routine L.A.Cosmic (VAN DOKKUM, 2001)
- Wavelength calibration: a spectrum obtained from observation does not have associated wavelength values. One needs to use a calibration based on a spectrum with known lines, which is obtained by inserting a calibration lamp in the optical path of the spectrograph, in this case, a Copper-Argon (CuAr) lamp.
- Flux calibration: consists of associating flux values to each wavelength of the observed spectrum. This is done by comparing the instrumental counts per unit of time from a known source, a standard star, with the science spectral counts.

Finally the registering and combination of the 12 individual exposures was done. The final cube was built with a spatial sampling of $0\farcs1 \times 0\farcs1$, resulting in a FoV with $\approx$ 2800 spaxels. After cropping the borders and superimposing the FoVs, it results in a total useful combined FoV, with total angular coverage of 29 arcsec^2 around the nucleus. The spatial resolution was limited by the seeing, which was at $0\farcs8$ during the observations (as measured from the field stars in the acquisition image), corresponding to 120 pc at the galaxy. The observed spectra covered a range from 4075 to 7285 Å with an instrumental dispersion $\sigma_{instr} \approx 40$ k$m\,s^{-1}$, obtained from the CuAr arc lamp lines.

Many Gemini data cubes show certain "instrumental fingerprints", in the form of vertical stripes in the reconstructed data cube. Such features also have specific spectral signatures. In order to identify and remove these instrumental features, we use a technique based on Principal Component Analysis (PCA, MENEZES et al., 2014). The fingerprint removal is fundamental for the stellar population synthesis because its effect is more apparent for lower instrumental counts. The data cube spectra were corrected for Galactic extinction using the Cardelli et al. (1989) extinction curve (CCM), and a R_V =3.1, for an A_V = 0.166 (SCHLAFLY; FINKBEINER, 2011) and by Doppler effect using the radial velocity of 2345 k$m\,s^{-1}$(see section 2.4).

We show in the upper panel of the Figure 18 an LRGB image of the Arp 245 system (Left) and the acquisition image taken with a r' filter (Right). In the middle panel we show a zoomed version of the acquisition image superimposed with the the (ULVESTAD; WILSON, 1984) figure

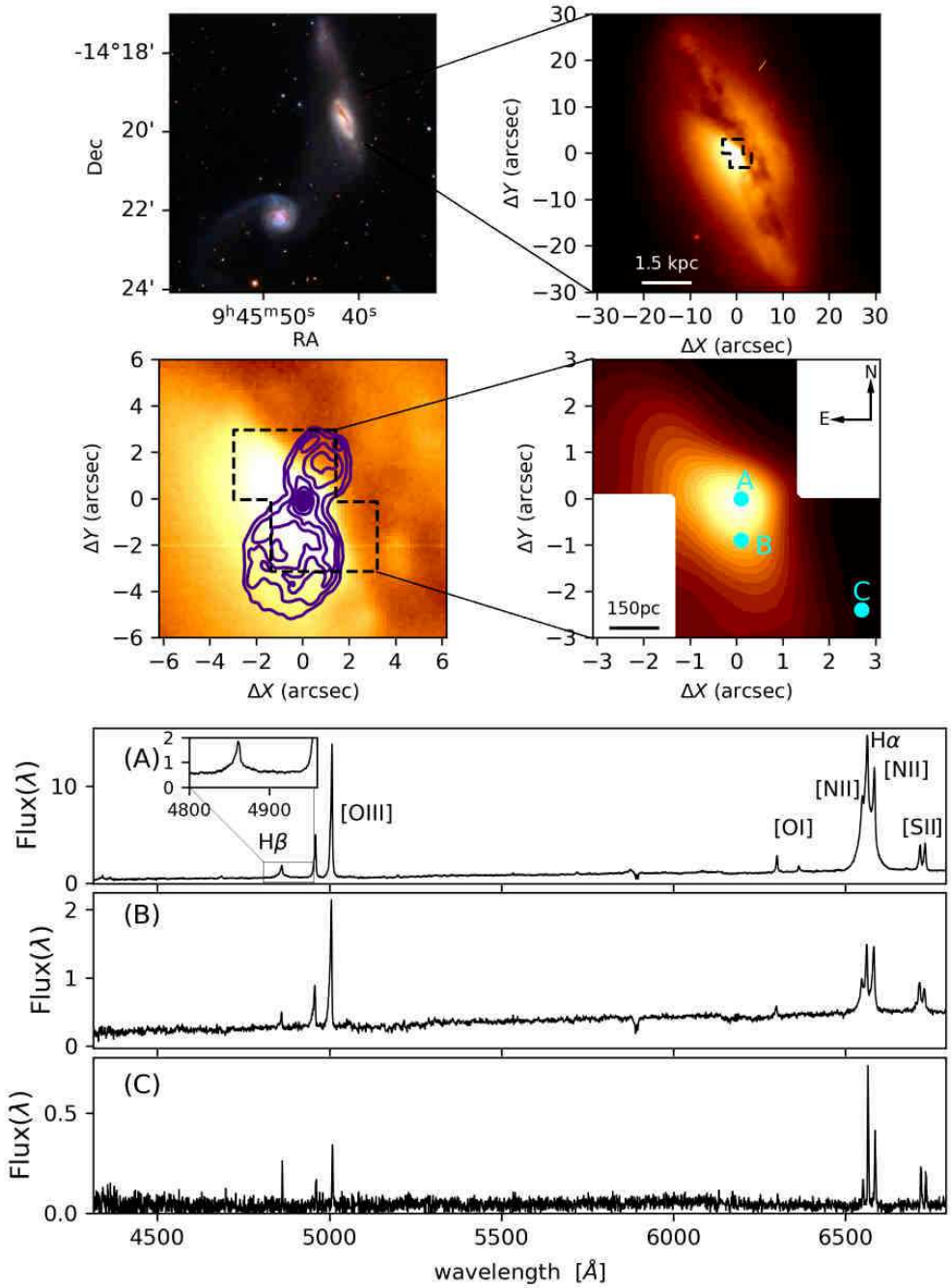

Figure 18 – Top Left: LRGB image composition of Arp 245 from Block (2011). Top Right: GMOS r' band acquisition image of NGC 2992. Middle Left: Zoomed acquisition image, and the Ulvestad and Wilson (1984) radio emission in purple (contours : 3, 6, 9, 15, 30, 50, 70, 90 percent of the peak of 7.2 mJy). The dashed rectangles show the two IFU FoV's. Middle Right: IFU continuum mean flux in the combined FoV. Bottom, from top to bottom: Spectra corresponding to the regions marked as A, B, and C, with spectral flux density in units of 10^{-15} $erg\,s^{-1}\,cm^{-2}$ $Å^{-1}$. North is up and East to the left in this and all figures of this chapter. The black cross represents the continuum nuclear position in all figures of this chapter. All maps of this section were smoothed using a Gaussian kernel with FHWM with half of the spatial resolution, see section 2.2.

of 8-shaped radio emission of the galaxy (Left) and the mean continuum flux in the IFU's FoV (Right), while in the bottom panels we show three sample spectra from representative regions marked, respectively from top to bottom, A, B and C. The prominent dust lane seen in the acquisition image, and in the stellar continuum image from the IFU, has a reported A_V greater than 3 (COLINA et al., 1987; SCHNORR-MULLER et al., 2016a). Spectra from this region of high extinction have no measurable stellar component above the noise level, as exemplified by the spectrum extracted from C. The nuclear spectrum shows a broad Hα component, and a faint broad Hβ is also present.

2.3 Stellar Populations

In order to obtain the spatially resolved star formation history (SFH), and to fit the gas emission features, free from the stellar population contamination, we performed stellar population synthesis on the data cube by employing the `starlight` full spectra fitting code (CID FERNANDES et al., 2005a). Briefly, `starlight` fits an observed stellar spectrum O_λ with a model M_λ built from a linear combination of N spectral components. Dust attenuation is treated as if due to a foreground screen and parametrised by the V-band extinction A_V. Stellar kinematics is modelled with a Gaussian line-of-sight velocity distribution centred at velocity v_*, and with a dispersion σ_*.

Besides the model spectrum M_λ, the code outputs the corresponding values of A_V, v_*, σ_*, and a population vector $\vec{x}$ containing the percentage contribution of each base population to the flux at a chosen normalisation wavelength λ_0, which in our fits was chosen as λ_0 = 5500 Å. The code minimises the χ^2 of the fit, though a more convenient and intuitive figure of merit to assess the quality of the fit is through *adev* parameter, defined as the mean value of $\left|O_\lambda - M_\lambda\right| / O_\lambda$ over the fitted wavelengths.

We note that, while there are many different spectral fitting codes and techniques available, cross-comparison of these various techniques have shown to yield rather consistent results (e.g. KOLEVA et al., 2008; FERR E-MATEU et al., 2012; MAKSYM et al., 2014; MENTZ et al., 2016; CID FERNANDES, 2018). Therefore, rather than trying different fitting codes, we chose to maintain `starlight` and investigate the differences introduced by the choice of models and stellar libraries, which are known to produce variations in the recovered properties (e.g. MARASTON; STROMBACK, 2011; CHEN et al., 2010; WILKINSON et al., 2017; BALDWIN et al., 2018; DAMETTO et al., 2019).

2.3.1 Evolutionary Models, Stellar Libraries and Featureless Continuum

This section discusses the stellar population models and stellar libraries used in this work, and how we can account for the contribution of a featureless continuum due to the AGN in NGC 2992.

The key ingredients in the stellar population synthesis method are the spectral base elements, i.e. those spectra available to the fitting code to combine in order to recover the galaxy properties. The base elements are, usually, Simple Stellar Population (SSP), i.e. a collection of stars with same age and metallicity, taken from an evolutionary model which are constructed using a stellar spectra library and an Initial Mass Function (IMF).

Table 1 – SSPs used in the stellar population synthesis.

Model	BC03			M11		
Spectral Library	STELIB			MILES		
Metallicity	0.2	1.0	2.5	0.5	1.0	2.0
Ages(Gyr)	0.001, 0.003, 0.005, 0.01, 0.025, 0.04, 0.1, 0.3, 0.6, 0.9, 1.5, 3.0, 5.0, 11.0, 13.0			0.055, 0.065, 0.075, 0.085, 0.1, 0.15, 0.3, 0.6, 0.9	0.007, 0.008, 0.009, 0.01, 0.015, 0.025, 0.04, 0.055, 0.065, 0.075, 0.085, 0.1, 0.15, 0.3, 0.9, 1.5, 3.0, 5.0 11.0, 13.0	0.1, 0.15, 0.3, 0.6, 0.9, 1.5, 3.0, 5.0, 11.0, 13.0

In this work we have used SSPs from two models: Bruzual and Charlot (2003, here after BC03), which uses the STELIB (LE BORGNE et al., 2003) spectral library, and Maraston and Stromback (2011, hereafter M11), which employs the MILES (S ANCHEZ-BL AZQUEZ et al., 2006) spectral library. For both models/libraries we use the same Chabrier (2003) IMF and instantaneous star formation bursts. We found varying the IMF produces only minor variations in the recovered SFH when compared to the changes introduced by using distinct models. The former is outside the scope of this work, and we refer the reader interested in this particular effect to Chen et al. (2010), Ge et al. (2019) and references therein. From the SSPs provided by BC03 we choose a set of 45 representative elements divided into three metallicities (0.2, 1.0, 2.5 $Z_{\odot}$) and an age range covering from t(Gyr) = 0.001 to t(Gyr) = 13. From those available by M11 with the MILES library we chose a set of 40 SSPs with age and metallicity coverage as similar as possible to the BC03 ones: three metallicities (0.5, 1.0, 2.0 $Z_{\odot}$) and ages ranging from t(Gyr) = 0.007 to t(Gyr) = 13. The complete list of SSPs used from each model is shown in Table 1. It is important to mention that the MILES Library does not provide metal-poor stars (Z = 0.5 $Z_{\odot}$) younger than 55 Myr (0.055 Gyr), and neither metal-rich stars (Z = 2.0 $Z_{\odot}$) younger than 100 Myr (0.1 Gyr), while BC03/STELIB provide the same age range for the three metallicities (see Table 1).

We define a reduced population vector with three age ranges: $t < 100$ Myr; 100 Myr $\leq t \leq 1.4$ Gyr; and $t > 1.4$ Gyr, to obtain a more robust description of the SFH than that obtained with the full population vector (see, e.g. CID FERNANDES et al., 2005a), as well as to facilitate the visualisation of the spatially resolved fit results. The population vector components are denoted by x_Y, x_I and x_O, where Y, I and O stands for young, intermediate and old respectively. The division in a reduced population vector has been used in several works in stellar population synthesis (e.g. CID FERNANDES et al., 2005a; RIFFEL et al., 2010a; CID FERNANDES et al., 2013; GONZALEZ DELGADO et al., 2015; MALLMANN et al., 2018), while the range values may be slightly distinct from one another, the ones adopted here are the most common. Also, for the young population the cutting value of 100 Myr is the estimated age of the pericentre passage between NGC2992 and its companion (section 1.5).

When dealing with stellar populations in Seyfert galaxies, a power law ($F_{\lambda} \propto \lambda^{-\alpha}$) featureless continuum (FC) should be added to the spectral base (KOSKI, 1978) to account for the AGN emission. Values for α are between 0.5 – 2.0 (OSTERBROCK; FERLAND, 2006), with many authors working with large samples of galaxies assuming a general value of α = 1.5 (e.g.,

RAIMANN et al., 2003; KAUFFMANN et al., 2003; CID FERNANDES et al., 2004; MALLMANN et al., 2018). Since this work is focused on a single object, we propose a method to specifically fit the α index for the optical spectrum of NGC 2992. We extracted two integrated spectra: an inner one, hereafter $S(\lambda)$, defined as the sum of spectra within a circular region with radius of 0.″4, and an external one, $E(\lambda)$, in an annulus with inner radius of 1″and outer radius of 1.″4, both centred at the peak of continuum emission. We model the $S(\lambda)$ spectrum as a combination of $E(\lambda)$ and a power law FC , both reddened by the same factor and normalized in the same wavelength, λ_0 = 5500 Å, as follows:

$$\left(\frac{S_m(\lambda)}{S_m(\lambda_0)}\right) = \left[(1-\boldsymbol{p})\left(\frac{E(\lambda)}{E(\lambda_0)}\right) + \boldsymbol{p}\left(\frac{\lambda}{\lambda_0}\right)^{-\alpha}\right] \times 10^{-0.4\,\delta\boldsymbol{A_V}\,q_\lambda} \tag{18}$$

where $S_m(\lambda)$ is the model spectrum, p is the fraction contribution of the FC, δA_V is the difference in extinction between the $S(\lambda)$ and $E(\lambda)$ regions. The values which minimise the residuals between $S(\lambda)$ and $S_m(\lambda)$ are p = 0.23, δA_V = 2.2 and α =1.7.

It should be noted we are over-simplifying by assuming that $S(\lambda)$ is the combination of $E(\lambda)$ and an FC, i.e. the stellar spectrum of both are the same. However, we argue this is just a method to get a data-based value for α, instead of just assuming a fixed value which is even less physically justified. Also, no further interpretation will be given in this regard besides the adoption of this α value to produce the FC base element.

2.3.2 Spatially Resolved Stellar Populations Synthesis

In order to perform the spatially resolved stellar synthesis with enough signal to noise ratio (S/N) we employed the Voronoi tessellation technique (CAPPELLARI; COPIN, 2003) in our data cube, with a S/N target set to 20. Results from Cid Fernandes et al. (2005a) show at this level `starlight` is able to reliably recover input parameters. Some spectra, however, failed to reach the desired S/N, even when combining several tens of spaxels, specifically those obscured by the galaxy's dust lane. Henceforward we will just analyse and show the results for those voronoi zones which the combined-spectra has $S/N \geq 10$, relying again on Cid Fernandes et al. (2005a) tests that show it to be the minimum value to the reliability of the code.

In order to be able to explore both the effects of the FC component and the change of model/library, we run the `starlight` code in the spaxels of the binned cube using three distinct spectral bases:

- *BC03*: Only stellar SSP components from the BC03/STELIB models, see Table 1 for ages and metallicities.
- *BC03+FC*: Same as BC03 stellar SSPs, with the addition of an FC component ($F_\lambda \propto \lambda^{-1.7}$) to the spectral base.
- *M11+FC*: Stellar SSP components from M11/MILES, see Table 1 for ages and metallicities, in addition to the FC component.

Since the effects of the presence/absence of FC component can be tested comparing *BC03* with *BC03+FC*, and the change of model/library is explored comparing *BC03+FC* with *M11+FC*,

we did not find necessary to test the synthesis using *M11* without FC, therefore we kept our analyze within these three configurations.

The FC component is available for `starlight` only in the spaxels of the inner 1.1 arcsec[2], which equals 3σ of the Gaussian point spread function. The reason for not allowing the FC to be used throughout the field is that there is a high level of degeneracy between the FC and a young reddened population (further discussion in Cid Fernandes and Gonzlez Delgado (2010) and the next section), and also because there is no physical reason to have an FC emission outside the nucleus since it is emitted by the spatially unresolved accretion disk. We will call the percentage contribution of the FC to total light of a spaxel as x_{agn}. During the synthesis all the emission lines were masked (see Figure 19), the mask is the same in all spaxels with exception to the central ones ($r < 1.1''$) where Hβ and [N II] +Hα masks are broader. The sum of x_Y, x_I, x_O, x_{agn} values is always 100% for all spaxels.

The maps of the recovered properties from the three distinct bases are shown in Figure 39, Figure 40 and Figure 41 at the Appendix A.1. These figures show the maps for x_Y, x_I, x_O, x_{agn}, A_V, the light-weighted stellar mean age $\langle log\ t_* \rangle$ defined as:

$$\langle log\ t_* \rangle = \frac{\sum_{j=1}^{N_*} x_j\ log(t_j)}{\sum_{j=1}^{N_*} x_j} \tag{19}$$

where x_j are the elements of the population vector $\vec{x}$, i.e. the fraction contribution of each component to the total light, t_j is the ages of j-th component, and N_* is the number of stellar spectra in the base (SSPs). The figures in Appendix A.1 also shows the light-weighted stellar mean metallicity $\langle Z \rangle$ for each reduced population vector component x_Y, x_I and x_O, respectively $\langle Z \rangle_Y$, $\langle Z \rangle_I$ and $\langle Z \rangle_O$, defined as:

$$\langle Z \rangle = \frac{\sum_{j=t_0}^{t_f} x_j\ z_j}{\sum_{j=t_0}^{t_f} x_j} \tag{20}$$

where t_0 and t_f are respectively the lower and upper age limit of the reduced population vector components as defined in the previous section.

The upper panel of Figure 19 shows an example fit for a spaxel at $r = 0\farcs6$, the residuals between the observed and the fitted spectra and the emission line mask. At the bottom panels the age/metallicity/FC decomposition for the three syntheses are shown as an example of the small differences resulting from the change of spectral base (see sections 2.3.3 and 2.3.4).

In Figure 20 we show the radial profiles of x_Y, x_I, x_O, x_{agn} and $\langle log\ t_* \rangle$, in bins of $0\farcs45$ ($\approx$ 70 pc), with points representing the median, and the colored region represents the 25 and 75 percentiles of the azimuthal distribution for the given radial bin. In Figure 21 we show the values of $\langle Z \rangle$ for each one of the bases integrated over the entire FoV.

In general terms the presence of a large contribution of old metal-rich SSPs and a smaller, but significant, contribution of young metal-poor stars seems to be independent of the presence of an FC component, or the change of model/library. The detailed analyses of the

[2] The radius(r)= 0.0 is set as the peak of the continuum emission.

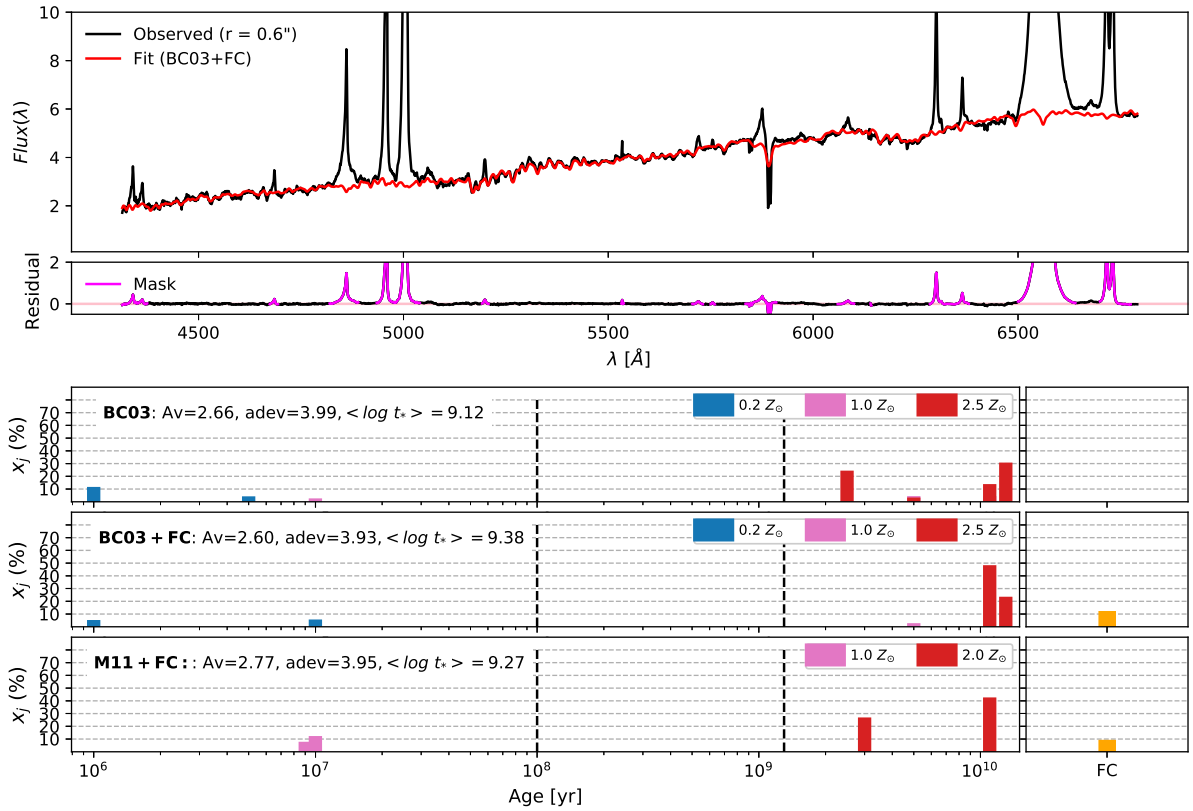

Figure 19 – Example of stellar population synthesis fit. Top: Observed (black) and synthetic (red) spectra both in units of 10^{-15} $erg\,s^{-1}\,cm^{-2}\,\text{Å}^{-1}$ in a spaxel at radius equal to 0.″6. Middle: Residual between the observed and synthetic spectra, masked emission lines are shown in purple. Bottom: Age/metallicity and FC decomposition for the three synthesis, *BC03*, *BC03+FC* and *M11+FC*. The dashed lines show the division between x_Y, x_I and x_O SSPs.

differences caused by the distinct spectral bases available to the code will be better explored in the sections below.

2.3.3 The FC Component Usage: Comparing *BC03* and *BC03+FC*

As shown by Figure 20, the differences in the *BC03* and *BC03+FC* synthesis are seen only at the inner spaxels and are linked to the presence of the FC component in the spectral base. For the external spaxels ($r > 1.''1$), where only BC03 stellar components are used in both synthesis, the recovered properties are identical, as one would expect. In the external spaxels, the x_O values range between 75% and 85%, with all spaxels having super-solar mean metallicity, $\langle Z \rangle_O > 1.5\ Z_\odot$, and the majority of them being close to the upper limit of the models, $\langle Z \rangle_O \approx 2.5\ Z_\odot$. The x_Y values are between 15% and 25%, with most spaxels having a sub-solar mean metallicity, $\langle Z \rangle_Y \leq 1.0\ Z_\odot$, with a considerable portion of them at the lower limit of the model, i.e. $\langle Z \rangle_Y = 0.2\ Z_\odot$. Some properties are identical in all runs even at the inner spaxels, A_V is very high in the innermost spaxels ($A_V > 3$ mag) declining rapidly to $A_V \approx 2.5$ mag and reaching 1.5 mag at the border spaxels (A_V map shown at Appendix A.1). Similarly, the contribution from intermediate SSPs, x_I, is null at most spaxels and reaches a maximum value between 10 and 20% in very few regions.

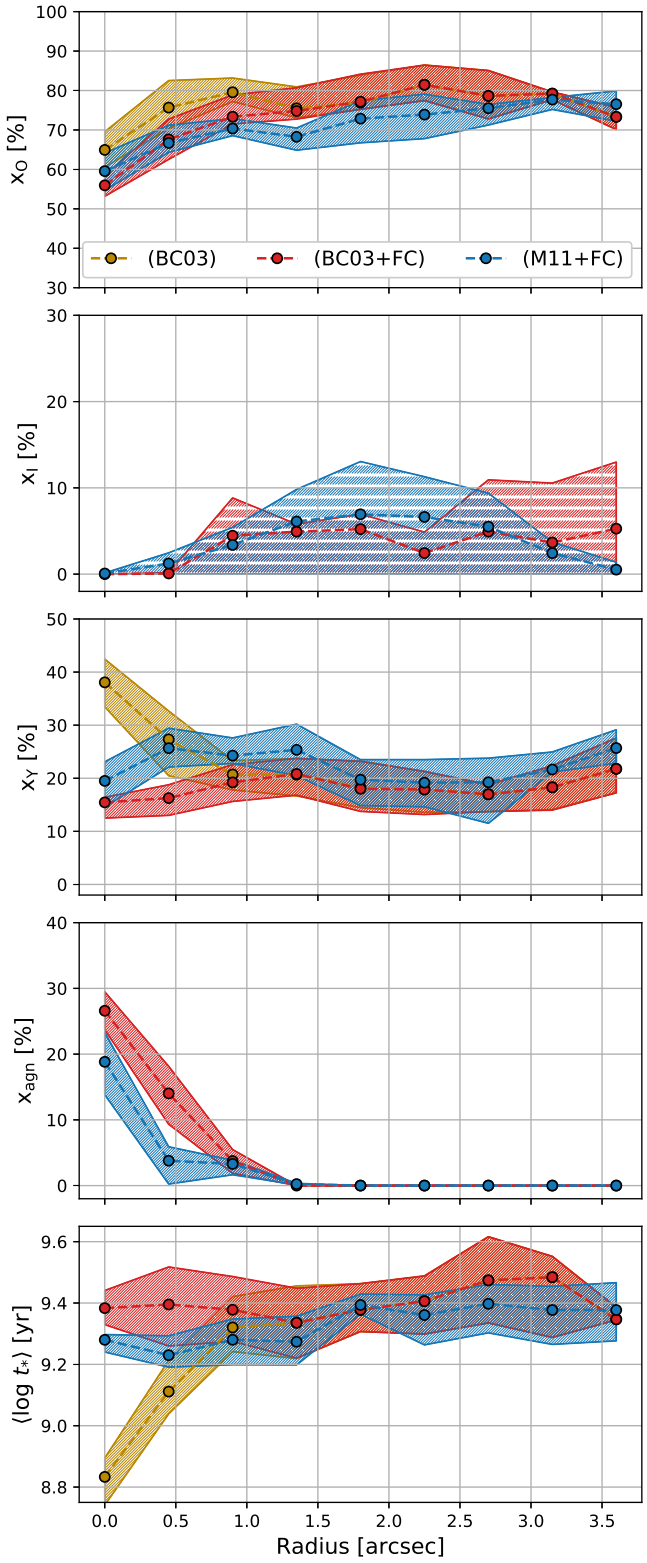

Figure 20 – Radial profiles of the recovered properties for *BC03* (gold), *BC03+FC* (red) and *M11+FC* (blue) in bins of 0.″45 ($\sim$ 70 pc). From top to bottom:% contribution to the total light from young (x_O), intermediate (x_I) and old (x_Y) SSPs, from the FC (x_{agn}) and the light-weighed mean stellar age ($\langle log\ t_* \rangle$). x_{agn} is null for *BC03* by definition. The x_I values for *BC03* are not shown, however they are exactly the same as *BC03+FC*.

Comparing the inner spaxels of *BC03* and *BC03+FC*, we see that the presence of an FC component in the base causes a decrease in x_O by just a few%. Larger differences, however, are seen in the contribution from young stars, especially where an FC component is not available (*BC03*).

In this case, there is a sharp increase in x_Y from a steady 20% at $r > 1''$to more than 40% at the centre. On the other hand, the (*BC03+FC*) base produces a roughly constant x_Y at $r < 1.0''$, while x_{agn} increases from $\sim$0% at 1.0″to $\sim$20% in the innermost spaxels. This effect is caused by the above-mentioned degeneracy between an FC spectrum and a young-reddened SSP (CID FERNANDES et al., 2004; CID FERNANDES; GONZLEZ DELGADO, 2010). As shown by Cardoso et al. (2017), fitting a spectrum that contains an AGN power law-like continuum with only stellar components causes the solution to have an excess of young populations, which leads to a drop in the $\langle log\ t_* \rangle$ (see the bottom panel of Figure 20). Although such degeneracy can cast some doubts in the exact values of the x_Y and x_{agn} decomposition in *BC03+FC*, the fact that the solution at the center has x_Y values compatible with the ones of the external regions of the FoV, and that the FC component contribution follows a radial profile compatible with an unresolved source (i.e increasing from $x_{agn} \approx 0\%$ to $x_{agn} \approx 20\%$ at the continuum peak) is strong evidence in favour of the existence of an FC emission in NGC 2992.

2.3.4 Decomposition Stability: Comparing BC03/STELIB and M11/MILES

In this section we discuss differences in the recovered properties between *BC03+FC* and *M11+FC* bases and their derivations. We do not intend to make a detailed analysis of the models and its derivations, nor to suggest one is a better choice than the other for use with this type of data. Such discussions can be found in other studies, e.g. Riffel et al. (2015), Baldwin et al. (2018) and Ge et al. (2019). Instead, we merely want to test the stability of the inferred stellar properties with changes in models.

Besides the distinct stellar libraries used in these model libraries, they also employ different evolutionary prescriptions (see CONROY, 2013, for a review on stellar evolutionary models). BC03 is constructed using the isochrone synthesis approach, while M11 uses the fuel consumption theory. The treatment of the thermally pulsing asymptotic giant branch (TP-AGB) phase is also a major topic of disagreement between different models. For example, Dametto et al. (2019) found a relative excess of young populations and lack of intermediate-age components when Near-Infrared (NIR) stellar populations synthesis are performed with BC03 SSPs, favoring results achieved with the M11 models. Nevertheless, these effects are much more important when modelling stellar populations in the NIR, being significantly less relevant in the optical.

Both x_{agn} and A_V are very similar to those obtained with *BC03+FC*, but the population vectors have notable differences. For instance, x_O values for *M11+FC* are systematically lower by $\sim$5 to 10% than those recovered with *BC03+FC*, while at the same time both x_Y and x_I are conversely higher for *M11+FC*. Given the increase of both x_Y and x_I and the decrease in x_O, the light-weighted mean stellar age $\langle log\ t_* \rangle$ for *M11+FC* is systematically lower than for *BC03+FC* by $\sim$ 0.05 to 0.1 dex, as show in the bottom panel of Figure 20.

Although there are small differences in age decomposition, the metallicity general pattern

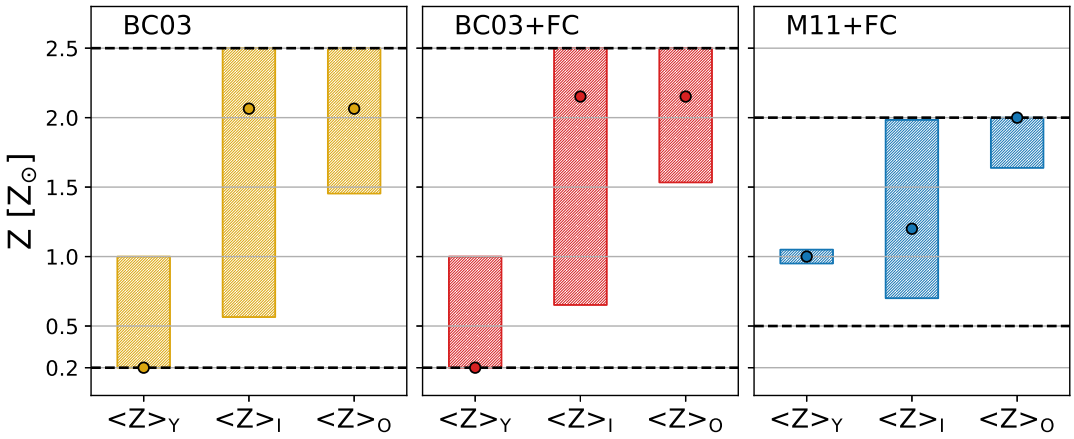

Figure 21 – Values of $\langle Z \rangle_Y$, $\langle Z \rangle_I$ and $\langle Z \rangle_O$ integrated over the entire FoV for each base, from left to right, respectively, *BC03*, *BC03+FC* and *M11+FC*. Points are the median values, and the coloureds bars are the 25 and 75 percentiles. The dashed black lines show the metallicity limit for each of the models.

seems to be maintained. As can be seen in Figure 21, the old populations have a super-solar mean metallicity, close to the upper limit of the model (1.5 $Z_\odot$ < $\langle Z \rangle_O$ $\leq$ 2.0 $Z_\odot$) and the young populations have a solar to sub-solar mean metallicity ($\langle Z \rangle_Y$ $\leq$ 1.0 $Z_\odot$), as shown in the middle panels of Figure 21. However, while the values of $\langle Z \rangle_Y$ in *BC03+FC* are mostly sub-solar ($\langle Z \rangle_Y$ < 1.0 $Z_\odot$) the values in *M11+FC* are all solar ($\langle Z \rangle_Y$ = 1.0 $Z_\odot$). This discrepancy is probably caused by the fact that the MILES library does not contain SSPs with a sub-solar metallicity younger than 55 Myr (see Table 1). For instance, in the example of Figure 19, while *BC03* and *BC03+FC* recover its young populations as a combination of three SSPs with ages of 1 Myr, 5 Myr and 10 Myr, the two first with sub-solar metallicity (Z = 0.2 $Z_\odot$) and the later with solar metallicity (Z = 1.0 $Z_\odot$), the *M11+FC* recovers it as both 9 Myr and 10 yr solar metallicity SSPs, and the fitting code would not be able to fit such a young component with lower metallicity precisely because MILES library does not provide an SSPs with Z = 0.5 $Z_\odot$ younger than 55 Myr. Therefore, we can see these $\langle Z \rangle_Y$ = 1.0 $Z_\odot$ values in the synthesis using *M11+FC* base as an upper limit for the young population metallicity.

As mentioned, above, we do not claim any of the three syntheses to be the one that better describes the data. In fact, there are no significant differences in the *adev* parameters among the bases: *adev* values range from 3% at the inner spaxels up to 8% at larger radius. Recovered properties produced with the distinct models present the same general trend (see section 2.3.2). However, we argue the bases which include an FC component are more physically justified. Both the large decrease in $\langle log\ t_* \rangle$ in the inner spaxels, when this component is ignored, and the fact that the FC components fluxes have a spatial profile characteristic of a point-like source (FWHM $\approx$ 0.″8, see Figure 24) are strong evidence of the existence of an FC like emission in NGC 2992. It is worth mentioning even though we are not discussing results for the stellar kinematics, we have made sure all the three decompositions were kinematically consistent with each other, and no non-physical value was fitted to v_*, σ_* parameters, which would cause an incorrect subtraction of the continuum used in emission line fitting procedures of the next sections.

2.4 Gas kinematics

2.4.1 Emission Lines Fitting

In order to fit the emission lines in NGC 2992 we use the `IFSCube` package. `IFSCube` is a python based software package designed to perform analysis tasks in IFU data, mainly focused on the fitting of spectral features, such as atomic lines. It allows for multiple combinations of Gaussian and Gauss-Hermite functions, with or without constraints to its parameters. Stellar continuum subtraction, as well as pseudo continuum fitting if necessary, are performed internally. In this case, we used the residual spectra from the stellar population synthesis performed with `starlight`. Initial guesses for the parameters are set for the first spaxel, usually, the one with the highest S/N, and all subsequent spectra use the output of neighboring successful fits as the initial guess.

When dealing with complex emission, the standard approach is to model the line profile with a combination of Gaussian functions. Visual inspection of our IFU shows distinct velocity components, evidenced by large asymmetries in the line profiles, in over one-third of the spectra in the FoV. As a result, we decided to model these components separately and to investigate whether they possessed any meaningful physical information, following previous works (e.g. VILLAR-MARTIN et al., 2011; MCELROY et al., 2015; FISCHER et al., 2018).

For every fitted emission line, we determined if the multi-component model was statistically justified, and not a better fit purely by virtue of the extra model parameters, by performing a series of f-tests. The f-test is a standard statistical test to gauge whether a higher order model is preferable to a simpler model when fitting a particular data set. We set the false rejection probability for the lower order model to 10^{-5}. The higher this threshold is set, the harder it is to justify a more complex model and the more likely it is to be over-fitting noise. The reader interested in more detailed analyses and a step-by-step deduction of the application of f-test in astrophysics emission line fitting is referred to Freund (1992) and statistical references therein.

As an Intermediate-type Seyfert nucleus, NGC 2992 presents both BLR (section 1.2.3) and NLR (section 1.2.4) emission. The BLR emission lines (Hα and Hβ) are blended with some NLR emission lines (Hα, [N II] λ6548, [N II] λ6583 and Hβ), leading to degeneracies if both NLR and BLR emission lines are fitted, spaxel by spaxel, at the same time with all parameters free. Fortunately, the fact that the BLR is not spatially resolved, i.e. its kinematics and its Balmer decrement (Hα/Hβ) can not vary spatially, can be used to decrease this degeneracy. Our chosen methodology consists on first fitting an integrated spectrum to fix the BLR emission line profile (kinematics and Balmer decrement), and later using this BLR spectrum as a fixed component, except for the flux, on the spatially resolved NLR fits.

We extracted a spectrum centered at the continuum peak, using a virtual aperture of $3\sigma = 1\farcs1$ (σ refers to the Gaussian point spread function). In this spectrum we fitted [N II] λ6548, [N II] λ6583, Hα (both BLR and NLR) and Hβ (both BLR and NLR), adding Gaussian components to the emission lines until the addition of a new component does not increase the fitting quality, as measured by the f-test described above. The final fit has shown that two Gaussians are necessary to fit each one of the BLR Balmer emission lines. This resulting profile, meaning the superposition of two Gaussian functions, hereafter called as BLR Component, can

be seen in panel (1) of Figure 22.

In order to resolve the kinematics of the NLR and obtain maps of emission line ratios, we fitted the following eight strongest emission lines present in the data cube: Hβ, [O III] λ4959,λ5007, Hα, [N II] λ6548,λ6583 and [S II] λ6716,λ6731. Each emission line was modeled with a set of Gaussian functions. The central wavelength of the Gaussian functions was allowed to vary by up to $\pm$400 kms^{-1} and the velocity dispersion up to 400 kms^{-1} (FWHM $\approx$ 1000 kms^{-1}). We added one more set of Gaussians to the fit, meaning that each emission line is modeled by up to two Gaussian components[3]. To reduce the number of free parameters, each set of Gaussians was required to have the same velocity and velocity dispersion (meaning their relative wavelengths were fixed), while their fluxes were allowed to vary. The reason for this is each component represents a kinematically distinct part of the gas, meaning that they may have different ionization states determined by their relative fluxes. This means that, for example, the single-component set of Gaussians fit to the eight emission lines instead of having twenty four (eight lines $\times$ three parameters) free parameters, only had nine (a single velocity, v, and velocity dispersion, σ, amplitudes of Hα, Hβ, the two [S II] and the stronger [N II] and [O III], while the amplitudes of the weaker [N II] and [O III] were set fixed as 1/3 of the stronger ones, as given by their Quantum Mechanics' probabilities (hereafter we call [O III] λ5007 as [O III], [N II] λ6583 as [N II], and the [S II] λ6716,λ6731 as [S II]). As described in the previous paragraph, the BLR Component was also included in the fit with only the amplitude as free parameter.

To estimate the uncertainties in the parameters, we performed Monte Carlo simulations, in which Gaussian noise was added to the observed spectrum. One hundred iterations were performed and the estimated uncertainty in each parameter was derived from the standard deviation in all the iterations. The uncertainty maps are presented in Appendix A.2.

We then applied the f-test to each one of the NLR emission lines, spaxel by spaxel, in order to assess if the simple model (single-Gaussian) is enough to fit the data or the more complex model (two Gaussians) is required. The f-test results in spatially contiguous regions of the required number of components for each emission line. The maps for [N II] and [O III] emission lines are shown in Figure 22 and Figure 23. The figures also show spectral and emission line fits in selected regions of the FoV.

The maps are not exactly equal for all emission lines. The size of the region in which two components are needed depends on the line S/N[4]. Therefore the size is maximum for [O III] (Figure 23) and Hα (Figure 28), a little bit smaller for [N II] (Figure 22) and the [S II] doublets (not shown) and much smaller for the low S/N line, Hβ (not shown). However, the general pattern is the same for all emission lines: the data are well fitted by a single-Gaussian in most of the FoV, but in a region, from the nucleus to the end of the FoV in the northwest (NW) direction two Gaussians are needed.

As can be seen in both figures, for those spaxels in which the emission lines are well behaved and symmetric, a single-Gaussian function, which we will call Component 1, is enough to fit the data. However, in the spaxels where two components were statistically significant, the

[3] Given that usually the NLR emission lines are some times not well fitted by a simple Gaussian profile, due to the presence of multiple kinematical components in the line of sight, e.g. gaseous disk rotation, gas outflows and inflows (e.g. ZAKAMSKA et al., 2016; SCHNORR-MULLER et al., 2017).

[4] Because the f-test detection is sensible to how much the second component, the more complex model, stands out from the noise. Therefore in low S/N lines, it is less likely the f-test will require a complex model.

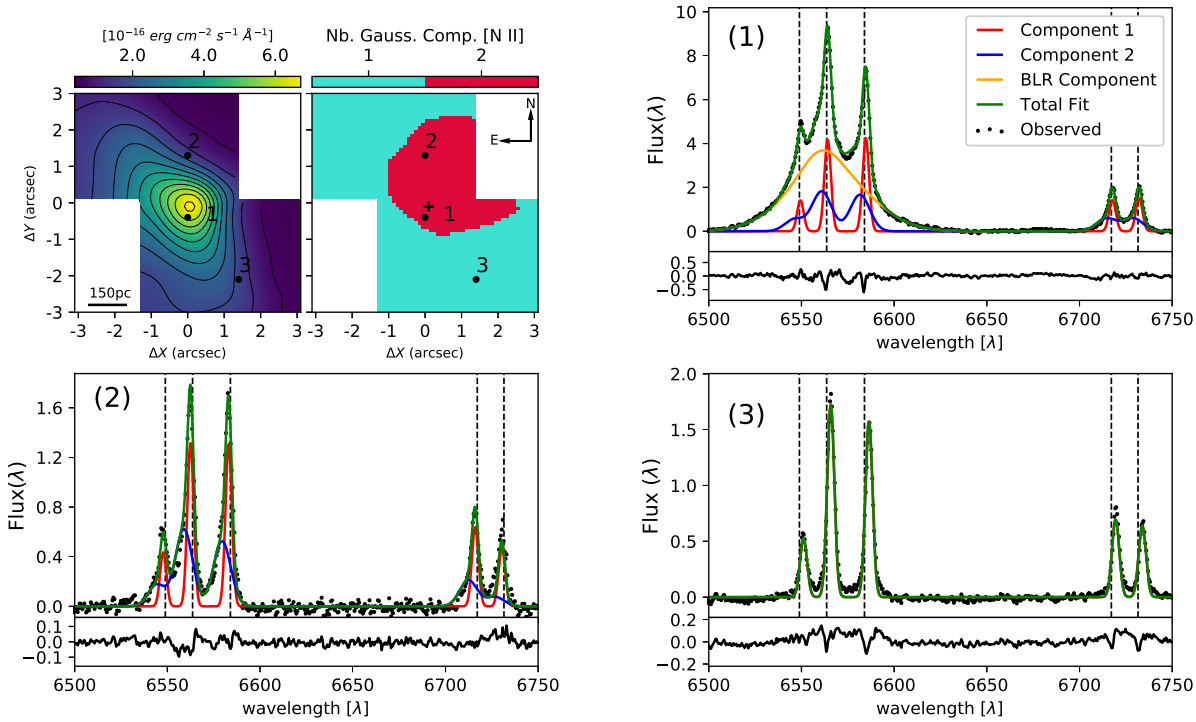

Figure 22 – Top left: Map of the continuum emission at λ = 5500 Å and map of the preferred number of Gaussian components to the [N II] emission-lines. Top right and bottom: Examples of the Hα, [N II] λ6548,λ6583 and [S II] λ6716,λ6730 emission lines fitting and their residual in distinctly regions of the FoV marked in the maps. The vertical axis units in the panels showing the emission-line profiles are 10^{-15} $erg\,s^{-1}\,cm^{-2}$ $Å^{-1}$ and the dashed vertical lines show rest-frame wavelength of the lines.

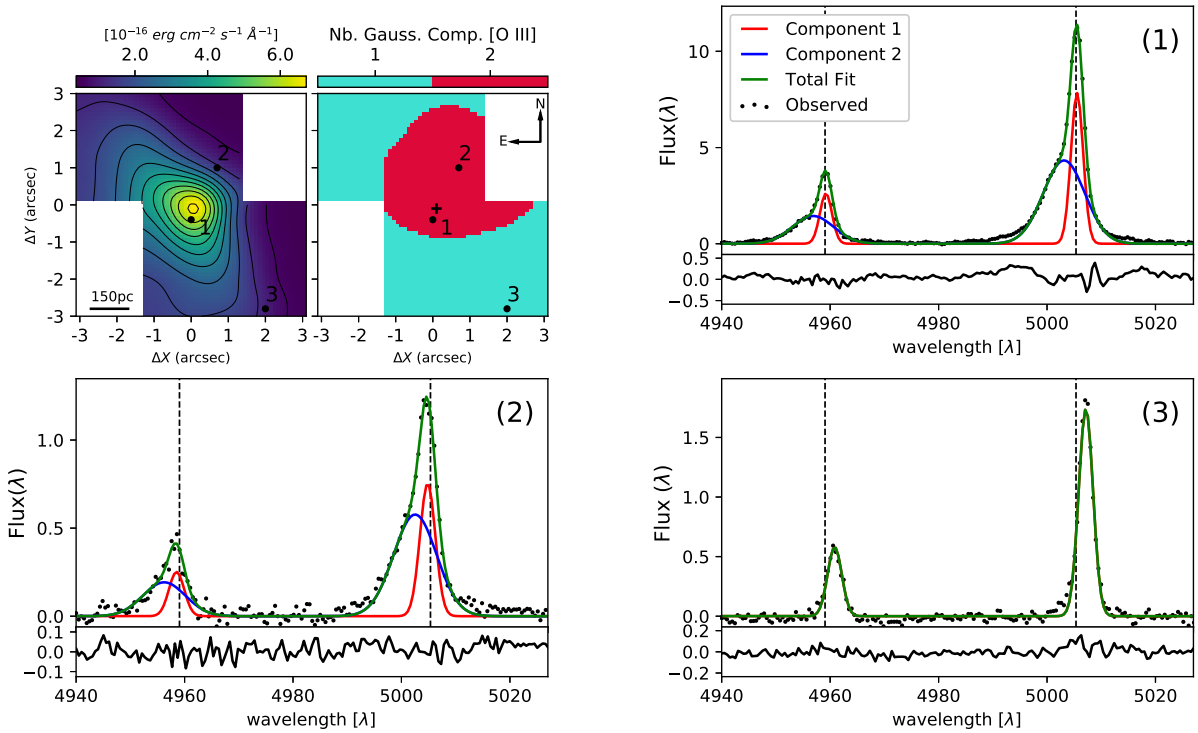

Figure 23 – Same as Figure 22 but for [O III] emission lines.

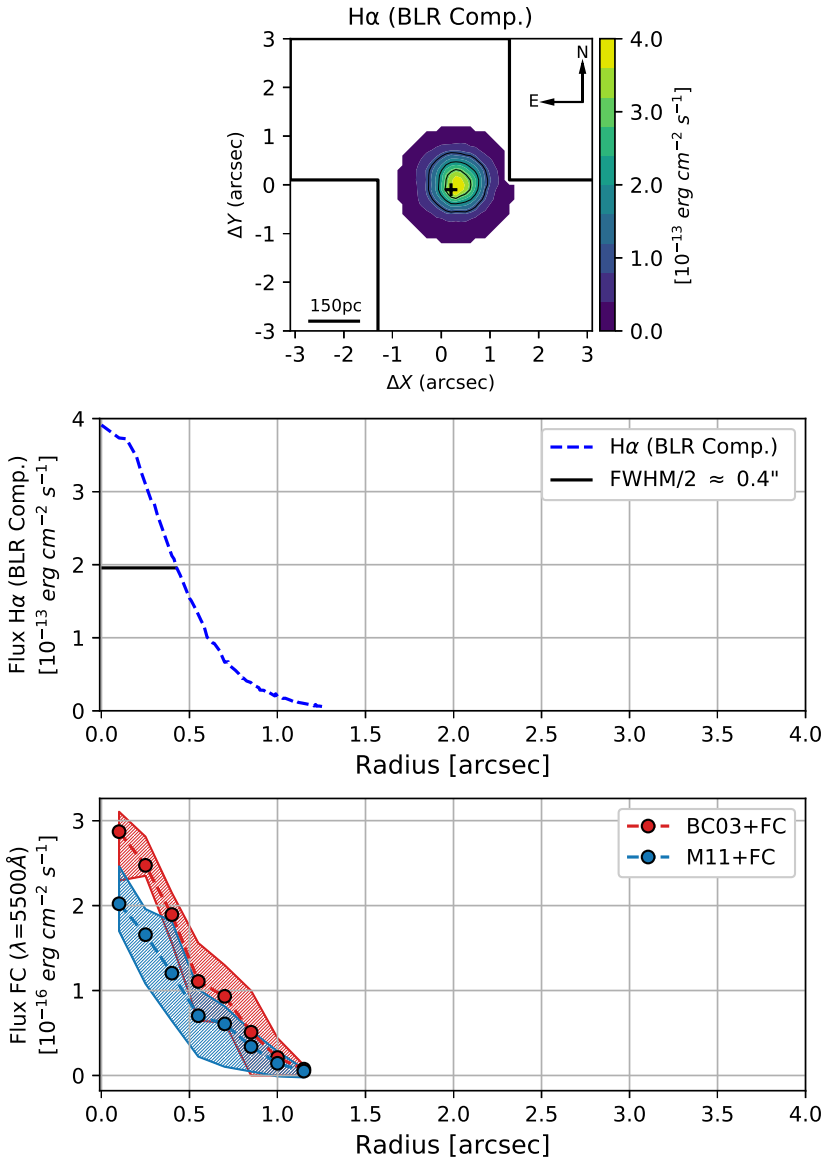

Figure 24 – Top: Spatial distribution of the BLR Component. Middle: Radial projection of the BLR Component profile, vertical axis units of 10^{-13} $erg\,s^{-1}\,cm^{-2}$. Both show the point-like source emission of the BLR, with a FWHM $\approx$ 0.″8 given by the spatial resolution of the observation. Bottom: Radial projection of the FC components fluxes (see section 2.3), also presenting a point-like source emission.

profiles show an asymmetry in the form of a blueshifted wing (see panels (1) and (2) in Figure 22 and Figure 23) requiring the addition of a second Gaussian, which we will call Component 2.

In Figure 24 we show the spatial and radial profile of the BLR Component. As expected for an unresolved structure, this component is detected just in the innermost spaxels, with a spatial distribution of a point-like source, equal to that of the stars in the acquisition image (FWHM $\approx$ 0.″8, see section 2.2); at radii larger than 3σ (1.1 arcsec) it is almost undetectable.

Table 2 – Best Fitting Parameters Bertola et al. (1991) Model.

Parameters	Values
v_{sys}	2345 ± 5 [$km\,s^{-1}$]
A	132 ± 4 [$km\,s^{-1}$]
p	1^a
c_0	3.5 ± 0.1 [arcsec]
ψ_0	$32^\circ \pm 1^\circ$
i	$70^\circ \pm 1^\circ$

[a] In the model the parameters p is allowed to vary between 1 and 1.5, the fitted value was equals to 1 in all the Monte Carlo iterations.

2.4.2 Rotational and Non-Rotational Components in the NLR

Let us now discuss the spatially resolved properties of the NLR Components 1 and 2 and their possible physical interpretation. Component 1 is present in the entire FoV. In the top panels of Figure 25 we show, from left to right, [O III] flux, velocity dispersion (σ), already corrected by instrumental dispersion. In the middle left panel, we present the radial velocity (v). We show the [O III] flux as an example of the morphology of this component, which is similar to the continuum morphology, with the peak of the emission shifted by only $\sim 0\farcs2$ to southwest (SW), with a steep decrease (up to 2 *dex*) towards the dust lane region. The σ values range from 50-100 $km\,s^{-1}$and show a very disturbed pattern. The radial velocity map shows values from -130 to 120 $km\,s^{-1}$and although it presents some disturbance, a rotation pattern is clearly discernible, with the SW portion receding and the northeastern (NE) approaching. We have considered the west side of the galaxy is the near one, following the literature (e.g. MARQUEZ et al., 1998; VEILLEUX et al., 2001); this explains why the emission is seen mainly to the east and less to the west where it is attenuated by the dust lane in the line-of-sight.

In order to quantify how much the velocity field deviates from a pure rotation and to derive both the major axis PA and the inclination of disk we fit the (BERTOLA et al., 1991) model. The model assumes a spherical potential with pure circular orbits, in which the observed radial velocity at a position (R, ψ) in the plane of the sky is given by the relation:

$$v(R,\psi) = v_{sys} + \frac{A\,R\,\cos(\psi-\psi_0)\,\sin\theta\,\cos^p i}{\left\{R^2\left[\sin^2(\psi-\psi_0)+\cos^2(\psi-\psi_0)\right]+c_0^2\,cos^2 i\right\}^{p/2}} \quad (21)$$

where v_{sys} is the systemic velocity, i the inclination of the disk (with i = 0 for a face-on disk), A is the amplitude of the curve, c_0 is the concentration parameter and ψ_0 the line of nodes PA. The parameter p defines the form of the rotation curve, varying in the range between 1 (logarithm potential) and 1.5 (Keplerian potential). To avoid the degeneracy between the parameters, we restricted the disk inclination to have values of $i = 70 \pm 10$ (based on DUC et al., 2000, photometric analyses) and we assumed the kinematical center to be co-spatial with the peak of the continuum emission. A Levenberg-Marquardt least-squares minimization was performed to determine the best fitting parameters and the uncertainties were obtained by making one hundred Monte Carlo iterations. We show the best parameters and their uncertainties in Table 2.

The PA of the line of nodes was measured as $32\pm1^\circ$, in agreement with previous values from the literature: PA = 32° (VEILLEUX et al., 2001, hereafter V01), PA= 30° (MARQUEZ et al.,

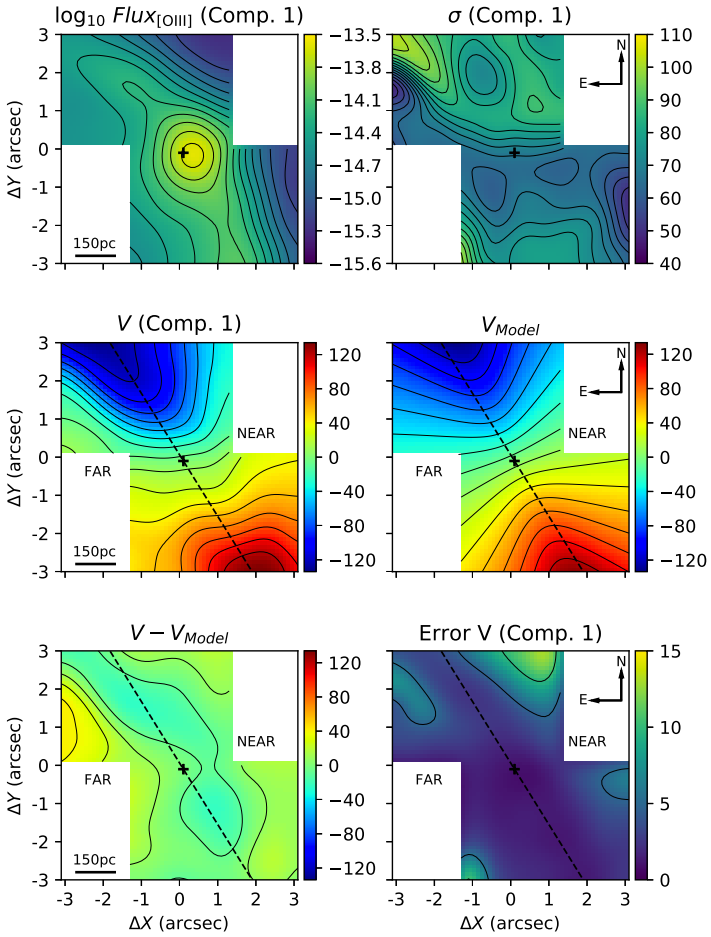

Figure 25 – Component 1 properties. Top left: Log_{10} Flux [O III] λ5007 ($erg\,s^{-1}\,cm^{-2}$). Top right: Velocity dispersion σ ($km\,s^{-1}$). Middle left: Radial velocity v ($km\,s^{-1}$). Middle right: Modelled radial velocity ($km\,s^{-1}$), from the Bertola et al. (1991) rotation model fitting. Bottom left: Residual between the measured and the modeled velocity field. Bottom right: Uncertainties in the radial velocity v ($km\,s^{-1}$). Black cross is the continuum peak and the dashed black line is the fitted major axis PA.

1998, hereafter M98). V_{sys} and i are also in reasonable agreement with other studies of the galaxy: V01 found, respectively, 2335 $\pm$ 20 $km\,s^{-1}$and 68°, while M98 found 2330 $km\,s^{-1}$and 70°. The velocity field amplitude (A = 132$\pm$4 $km\,s^{-1}$), though, is much lower than the ones found by both V01 and M98 (225$\pm$20 $km\,s^{-1}$and 250 $km\,s^{-1}$). This discrepancy is probably due to the fact that both have used long-slit data in their studies, therefore being able to map the velocity field up to several kpc. Thus having a better constraint in the behavior of the field at a larger radius, while our data can only recover the internal portion of the velocity field.

The modeled velocity field is shown in the middle right panel of Figure 25, and the residuals between the observed field and model are shown in the bottom left panel of the same figure. The uncertainty map for the Comp. 1 v field, as measured by the Monte Carlo simulations described in the section 2.4.1, is shown in the bottom right of Figure 25. While most of the field is well represented by the disk rotation model ($\left|v - v_{Model}\right| < 20\ km\,s^{-1}$), there is only one region at the eastern border with residuals up to 40 $km\,s^{-1}$.

The fainter component of the NLR (Component 2) is detected in a smaller region, orig-

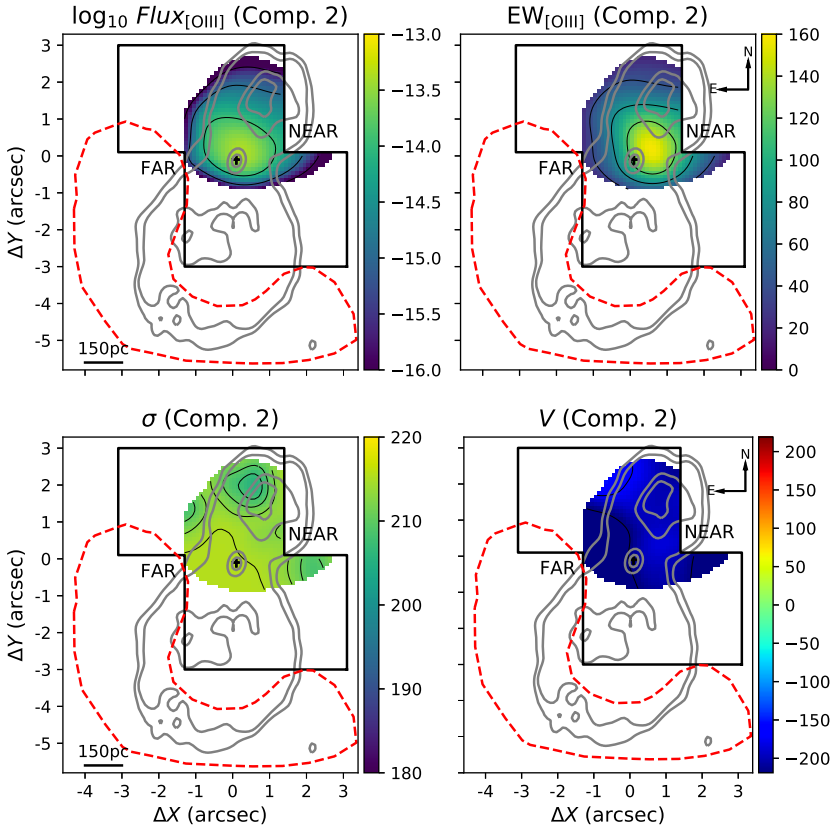

Figure 26 – Component 2 properties. Top left: $\mathrm{Log_{10}}$ Flux [O III] λ5007 ($erg\,s^{-1}\,cm^{-2}$). Top right: Equivalent Width of [O III] λ5007 (Å). Bottom left: Velocity dispersion, σ ($km\,s^{-1}$). Bottom right: Radial velocity, v ($km\,s^{-1}$). Solid black lines represent our FoV. Black cross is the continuum peak. Grey contours are the 6cm radio emission (ULVESTAD; WILSON, 1984). Red dashed line is the contour of the redshifted structure found by Garca-Lorenzo et al. (2001), at the farthest part of the radio emission major loop, taken from Fig. 9 of their paper.

inating near the continuum peak and extending towards the NW. For the brightest line, [O III] λ5007, the emission extends up to $\sim 3''$, as shown by both the flux map, top left panel of Figure 26 and the P-V plot in Figure 27. In Figure 26, we show the maps of equivalent width (EW) of [O III], σ and v for the Component 2. The v map shows only blueshifted velocities, with values ranging from -250 to -200 $km\,s^{-1}$. The velocity dispersion is higher than that of Comp. 1, ranging from 200 to 215 $km\,s^{-1}$. We also show in all the panels, the contours of the 8-shaped region detected in the 6 cm radio emission (in grey) in which the smaller loop seems to be co-spatial with Component 2.

The position-velocity plot along the major kinematical axis (PA = 32°) and the major axis of the Radio emission (PA = -26°) of NGC 2992 are shown in Figure 27. It is clear that while Comp. 1 has a rotational pattern, Comp. 2 deviates considerably from this pattern. Considering:

- Component 2 is not following the galaxy's rotation;
- It is co-spatial with the radio emission;
- It has higher velocity dispersion values than those of Comp. 1, σ > 200 $km\,s^{-1}$;

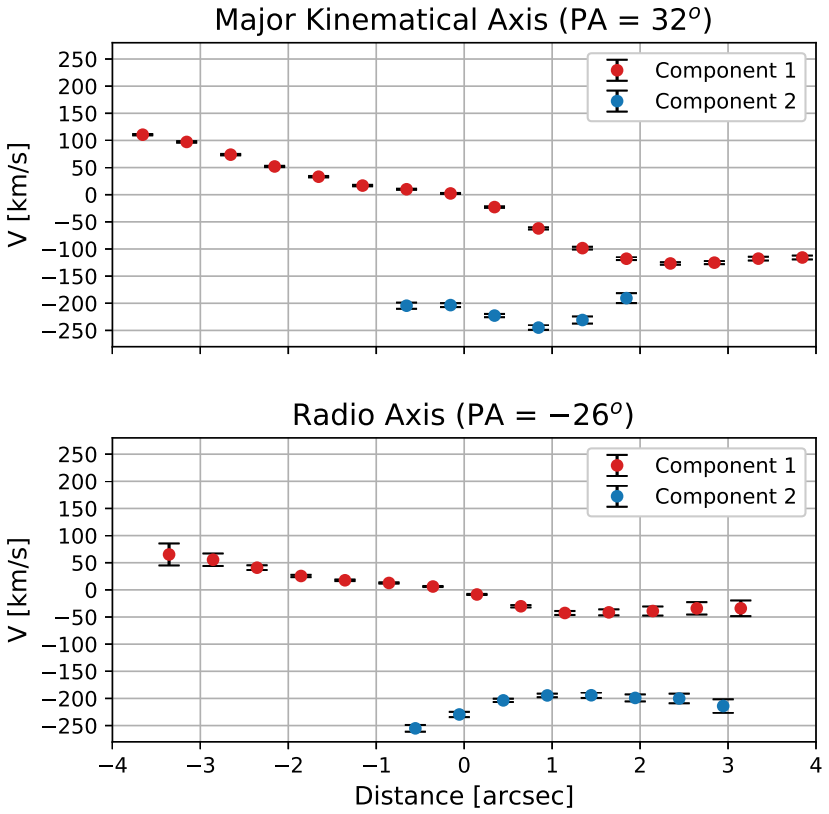

Figure 27 – Position-Velocity plot in virtual slits with 0.″4 width. In the top panel the slit is at the PA of the major kinematical axis, in the bottom the slit is at the PA of 8-shaped radio emission major axis. Points are the measured velocity values, and the error bars are the uncertainties in the velocities. Red points are the velocities of Component 1 and blue points the Component 2 ones.

- It has blueshifted velocities in the near side of the galaxy;

we are led to the conclusion that it is tracing a radio-jet driven gas outflow since all these are well-known characteristics of this type of phenomena. In fact, this ionized gas outflow was already reported by other IFU studies, e.g. Garca-Lorenzo et al. (2001), Friedrich et al. (2010) and Mingozzi et al. (2019). Particularly, Garca-Lorenzo et al. (2001) interpreted this blueshifted structure as the interaction of the minor loop of the radio-jet with the ISM. Garca-Lorenzo et al. (2001) also found a similar, however redshifted, structure in the far side of the galaxy, co-spatial with the farthest part of the radio emission major loop, which is mostly not visible in our FoV. We have extracted the contours of this structure from Figure 9 of their paper and show it as the red dashed line in Figure 26. This finding supports the scenario in which a bipolar over-pressure relativistic plasma is expanding, accelerating and compressing the ISM gas in its path (CHAPMAN et al., 2000). Interestingly, the only portion of this structure which falls within our FoV is co-spatial with the largest velocity residuals seen in figure Figure 25. Although our statistical analysis does not indicate the necessity of a separate component, the large residuals clearly indicate a perturbation in the velocity field.

A very similar geometry was found by Riffel and Storchi-Bergmann (2011) in the galaxy

Mrk 1157, in which non-rotational blueshifted and redshifted structures are present and co-spatial to the two loops of a very similar nuclear 8-shaped radio emission. The authors also interpreted these structures as the effect of the expanding radio-emitting plasma into the ionized ISM.

2.4.3 Outflow Properties

If we consider Component 2 as ionised outflowing gas, we can measure its properties such as mass, mass outflow rate and kinetic power. We followed the prescriptions described in Lena et al. (2015), in which a biconical outflow geometry is assumed, even though in our case we can see only one of the cones.

The mass outflow rate can be estimated as the ratio between the mass of the outflowing gas and the dynamical time (time for the gas to reach the present distance from the nucleus), M_g/t_d. The mass of the gas in outflow (Component 2) is estimated as:

$$M_g = n_e \, m_p \, V \, f \tag{22}$$

where m_p is the proton mass, n_e and V are the electron density and the volume of the region where the component is detected, f is the filling factor. The filling factor and volume are eliminated by combining equation 22 with the following expression for the Hα luminosity:

$$L(H\alpha) \approx f \, n_e^2 \, j_{H\alpha} \, V \tag{23}$$

with $j_{H\alpha} = 3.534 \times 10^{-25}$ $erg\,cm^3\,s^{-1}$ at $T = 10000$K (OSTERBROCK; FERLAND, 2006). Therefore, the gas mass can be written as:

$$M_g = \frac{m_p \, L(H\alpha)}{n_e \, j_{H\alpha}} \tag{24}$$

Our estimates for n_e are based on the flux ratio between [S II] lines, as will be described in next section. Note that the $L(H\alpha)$ used here is based on the flux of Comp. 2 Hα emission only, corrected by extinction as described in next section. The spatially resolved $L(H\alpha)$ and M_g (i.e. gas mass surface density, Σ_g) are shown in Figure 28.

The integrated gas mass is $M_g = 3.6 \pm 0.6 \times 10^6$ $M_\odot$. The t_d was estimated as the ratio between the maximum extension of the outflow $\sim 3'' \approx 450$ pc (see Figure 27) to its mean velocity, $\langle v_{out} \rangle \approx 210$ $km\,s^{-1}$, which gives $t_d \approx 2.2 \times 10^6$ yr. Combining these values we estimated an outflow mass rate of $\dot{M}_{out} \approx 1.6 \pm 0.6$ $M_\odot$.

We also estimated the outflow kinetic power as:

$$\dot{E}_{out} = \frac{\dot{M}_{out} \, v_{out}^2}{2} \tag{25}$$

where v_{out} is the radial velocity of Component 2 (Figure 26). Integrating the entire outflow we obtained a total outflow kinetic power $\dot{E}_{out} \approx 2.2 \pm 0.3 \times 10^{40}$ $erg\,s^{-1}$. In section 2.6.3, we

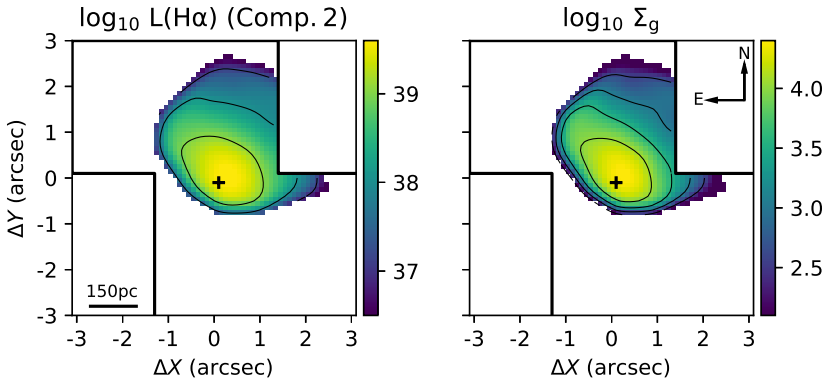

Figure 28 – Left: Logarithm of Component 2 dereddened Hα luminosity in erg s^{-1}. Right: Logarithm of Component 2 surface mass density in units of $M_\odot$ (0.″1)$^{-2}$. Black cross is the peak of the continuum emission.

compare these values with the ones found in the literature and those expected by outflow-AGN relations.

2.5 Ionization Mechanism and ISM properties

2.5.1 Nebular Extinction and Electron Density

In order to measure the extinction in the NLR, we adopt the Calzetti et al. (2000) attenuation law, and assume the case B recombination and the intrinsic Hα/Hβ value for the NLR (OSTERBROCK; FERLAND, 2006), which combined leads to the following expression to the V-band extinction:

$$A_V = 7.95 \times \log_{10}\left(\frac{H\alpha/H\beta}{3.1}\right) \tag{26}$$

In order to improve the S/N and given the fact that Hβ Component 2 is detected in a very small region, we used the integrated flux (Component 1 + Component 2) of the NLR Hα and Hβ lines. The A_V map is presented in the top left panel of Figure 29, and its uncertainty in the bottom left panel. The A_V peak at $\sim$ 4.5 mag at the peak of the gas emission lines, and has values > 3.5 mag in the dust lane portion of the FoV. However, this value may be even higher as the uncertainties are up to 2 mag in this region, caused by high impression on the Hβ flux measurement, as seen in Figure 42. Although the A_V are not the same in the continuum Appendix A.1 and in the NLR, the spatial patterns are similar: the higher values are found the central spaxels and towards the dust lane, and the lower towards the SE direction.

The electron density (n_e) of the ionized gas in the NLR can be obtained from the ratio between the [S II] lines, [S II] λ6716/λ6731 (OSTERBROCK; FERLAND, 2006). We applied the solution of the collisional equilibrium equations given by Proxauf et al. (2014) to obtain the n_e values, as follows:

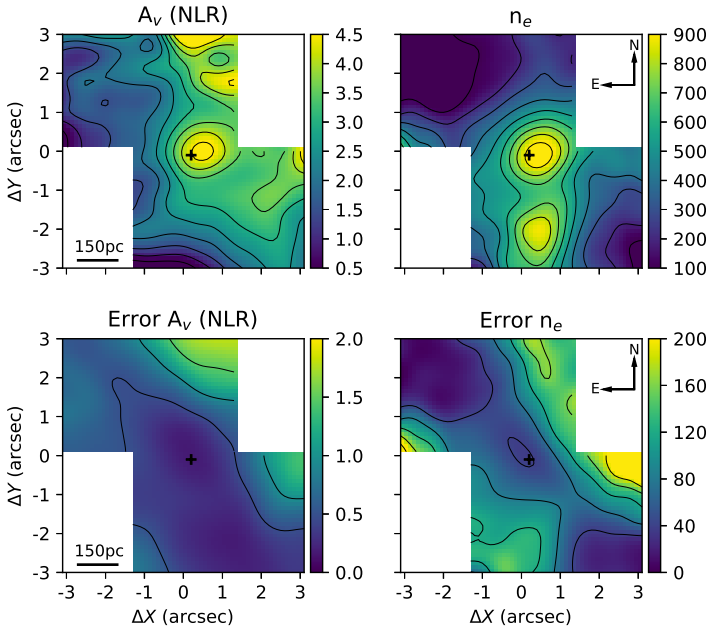

Figure 29 – Top left and bottom left panels, shows, respectively the V-band extinction A_V map and its uncertainties, both in units of magnitudes. Top right and bottom right panel show, respectively, the electron density (n_e) and its uncertainties both in cm^{-3} units. The black cross shows the peak of the continuum emission.

$$\log_{10}(n_e\,[cm^3]) = 0.0543\tan(-3.0553R + 2.8506) + 6.98 - 10.6905R + 9.9186R^2 - 3.5442R^3 \quad (27)$$

with R = F_{6716}/F_{6731}, the ratio between the [S II] lines. The n_e map in its uncertainties are presented, respectively, in the top right and bottom right panel of Figure 29. The maximum value of n_e is 950 cm^{-3} reached at the peak of the emission lines, decreasing radially down to 100 cm^{-3}, another high ($\sim$ 800 cm^{-3}) density knot is present at the south of the nucleus. Both the values as well as the spatial profiles of both A_V and n_e measured here are in agreement with the recent published analyses by Mingozzi et al. (2019) using MUSE instrument, see their Figures A1 and B1.

2.5.2 Ionization Mechanisms

Given the presence of young stars discussed in section 2.3, NLR and BLR emission (section 2.4) which indicate AGN excitation, and the presence of radio emission that can drive shocks (DOPITA, 2002; ALLEN et al., 2008), we used the [N II]/Hα vs. [O III]/Hβ and [S II]/Hα vs. [O III]/Hβ BPT diagnostic diagrams (section 1.3.1) to investigate which of these excitation mechanisms are dominant in the innermost region of the galaxy.

In the bottom panels of Figure 30, we show the maps of [O III]/Hβ, [N II]/Hα and [S II]/Hα line ratios for the entire line profile (by summing the kinematical components; we do that to increase the precision in the flux measurement and to avoid regions where a second component

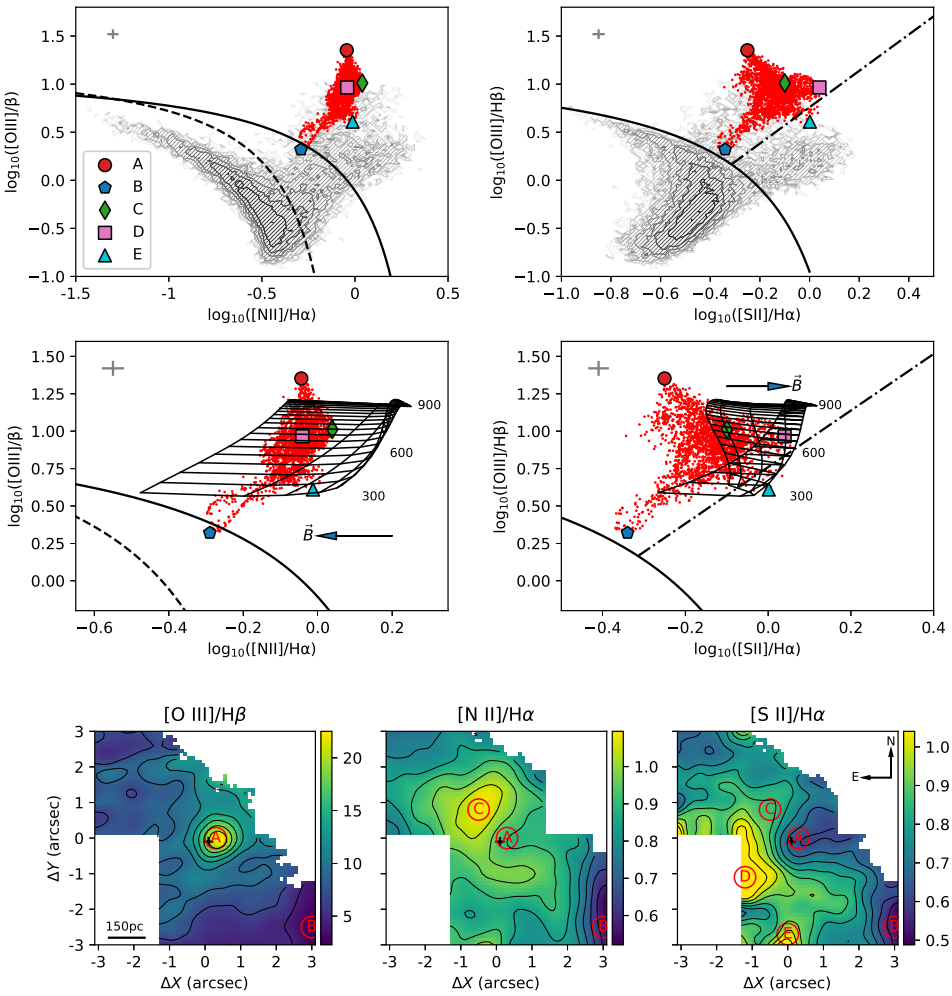

Figure 30 – Top: [N II]/Hα vs. [O III]/Hβ and [S II]/Hα vs. [O III]/Hβ BPT diagrams; grey contours are galaxies from the SDSS main galaxy sample measured by Kewley et al. (2006). Red points are the spaxels of NGC 2992. Colored markers are the selected regions of NGC 2992, as shown in the bottom panels, representing: red (Region A), blue (B), green (C), pink (D) and cyan (E). Middle: Zoomed BPT diagrams with shock+precursor grid models as measured with MAPPINGS V code (SUTHERLAND et al., 2018); the $\vec{B}$ indicates increasing magnetic field of the model (from 0.01 to 4 μG); the black numbers indicates the velocities of the shocks, ranging from 300 to 900 k$m\,s^{-1}$. Bottom: Respectively, from left to right, [O III]/Hβ, [N II]/Hα, and [S II]/Hα emission lines ratio maps; red circles show the selected regions shown in the upper panels. In BPT diagrams the grey crosses are the typical errors in the emission line ratios; the solid black lines are the Kewley et al. (2001) theoretical upper limits for pure star forming galaxies. In the [N II]/Hα vs. [O III]/Hβ diagram the dashed black line represents the Kauffmann et al. (2003) line which traces the upper boundary of the SDSS star formation sequence. In the [S II]/Hα vs. [O III]/Hβ diagram the dashed-dotted black line represents the empirical division between AGN like and low-ionization nuclear emission-line region (LINER) by Kewley et al. (2006).

is detected in high S/N lines, like [O III], but not detected in lower S/N ones, like Hβ.) We excluded the regions where uncertainties in the total flux, as shown in Appendix A.2, are higher than 30%. The [O III]/Hβ shows a clear AGN signature, with its peak, up to [O III]/H$\beta \approx 25$, at the center of the FoV and decreasing radially down to [O III]/H$\beta \approx 2$ at SW corner of the FoV. The [N II]/Hα and [S II]/Hα, however, do not show the same pattern: their maximum values are off-nuclear, and they do not present a radial decrease as in the [O III]/Hβ one. This indicates a lower energy mechanism (lower than an AGN, but higher than H II regions) can be ionizing the gas too. In fact, shock ionized regions are characterized by having smaller [O III]/Hβ ratios and larger [S II] (or [N II])/Hα than those ionized by AGN (VEILLEUX; OSTERBROCK, 1987; KEWLEY et al., 2006; ALLEN et al., 2008).

We selected limiting regions in the line ratio maps and shown it in the respectively BPT diagrams in the top panels of Figure 30. We also show some division lines: the solid black curves on both diagnostic diagrams trace the Kewley et al. (2001) theoretical upper limit of regions ionized by pure star formation. Several excitation mechanisms can increase the collisional excitation rate, enhancing the ratios of the forbidden to recombination lines, among them energetic photons from a power law-like emission (AGN); shock excitation and evolved stellar populations can also produce line ratios along this branch of the diagram. The latter case does not apply to the nuclear region of NGC 2992 given that it requires EW(Hα) < 3 Å (see section 1.3.1) and our entire FoV has EW(Hα) > 10 Å. We also show the dashed black curve on the [N II]/Hα vs. [O III]/Hβ diagnostic diagram: the Kauffmann et al. (2003) empirical classification line. The dashed-dotted black curve on the [S II]/Hα vs. [O III]/Hβ diagnostic diagram traces the Kewley et al. (2006) empirical classification line. We also show as grey points in the top BPT diagrams a collection of single-fiber emission line measurement from SDSS main galaxy sample by Kewley et al. (2006).

Region A is the peak of the [O III]/Hβ map, it shows clear AGN-like ratios, with an upper [O III]/Hβ value higher than any SDSS AGN, which corresponds to a 3″diameter aperture, and therefore have a diluted AGN/host-galaxy emission line ratio. Region B has the lowest value in all the maps, it lies bellow Kewley et al. (2001) showing the radial decrease in the AGN contribution to the emission lines, and significant contributions from both star formation and AGN excitation. Regions C, D and E display the highest values in the [S II]/Hα and [N II]/Hα maps; however, they have lower [O III]/Hβ values than region A. Region E, in fact, crosses the Kewley et al. (2006) line in the [S II]/Hα diagram, which again indicates the presence of another ionization mechanism.

In order to search for an explanation to the increase in this intermediary ionization energy lines ([N II] and [S II]) we used the `MAPPINGS V` shock models by Sutherland et al. (2018). We explored the parameter space in the pure shock and shock+precursor grids of the models. None of the pure shock models could explain these line ratios, given the high [O III]/Hβ values. However shock+precursor (Shock ionization in a medium already ionized by power-law like emission) with shock velocities between 300 k$m\,s^{-1}$and 900 k$m\,s^{-1}$and magnetic field ($\vec{B}$) between 0.01μG and 4μG, with a two-solar metallicity and a pre-shock density of 1 cm^{-3}, successfully reproduce the line ratios of regions C, D and E. In the middle panels of Figure 30 we show the grid models in these shock velocity and magnetic field ranges superimposed with the emission line ratios of the regions. The shocks in NGC 2992 have been extensively studied by Allen et al.

(1999a), who conclude that shocks are the predominant ionization mechanism in the extended NLR cones at a distance of several kpc from the nucleus.

We can conclude that a more simple Starburst-AGN mixture (section 1.3.1) in which the maximum values of all [O III]/Hβ, [N II]/Hα and [S II]/Hα are located in the innermost spaxel (location of the AGN), and all decrease radially towards the H II ionization region of the BPT in a straight line (Figure 10), cannot describe the ionization at the circumnuclear region of NGC 2992. Instead, a more complex Starburst-AGN-Shocks mixture is responsible for its ionization. However, the very high values of [O III]/Hβ indicate the most important among these three mechanisms is AGN ionization, at least in the innermost portion (see further discussion in section 2.6.4).

2.6 Discussion

2.6.1 Interaction-Driven Circumnuclear Star formation

In general terms, the stellar population synthesis discussed in section 2.3 shows that stellar content in the inner 1.1 kpc of NGC 2992 is mainly composed by an old metal-rich population, with a smaller but considerable contribution from young metal-poor stars. The presence of the latter is supported by other studies, for instance, using the Bica and Alloin (1986) base of star clusters for stellar population synthesis, Storchi Bergmann et al. (1990) found a predominance of old stellar populations (10^{10} yr) and a small contribution of at least 5% by recent star formation in the inner 5″. Moreover, Friedrich et al. (2010) find that 10-20% of the IR flux is attributable to a starburst, based on the emission from polycyclic aromatic hydrocarbon (PAH) molecules. Additionally, these authors estimate the starburst to have occurred between 40-50 Myr, based on the equivalent width of the Brγ line.

Major merger processes are known to be responsible for gas inflow towards the central regions of galaxies enhancing circumnuclear star formation and possibly triggering nuclear activity. Merger galaxies have an increase in the SFR, mainly at the nuclear regions (ELLISON et al., 2013; PAN et al., 2019). Thus, these sources have younger nuclear populations than those found in isolated galaxies, in which most of their recent formed stars are concentrated at the spiral arms. Moreover, major mergers are also able to modify the metallicity gradients of galaxies (BARRERA-BALLESTEROS et al., 2015). Galaxy simulations show that the gas, originally located at external portions of the isolated galaxy (metal-poor regions), moves towards internal regions (metal-rich regions) of the companion galaxy during the encounter and is capable of cooling and forming stars.. Such processes are able to explain both the increase in the SFR and the modifications in the metallicity gradient (DALCANTON, 2007; TORREY et al., 2012; SILLERO et al., 2017). In fact, the pericentre passage between NGC 2992 and its companion NGC 2993 is estimated to have occurred $\sim$ 100 Myr ago (DUC et al., 2000). Thus, a possible scenario is that metal-poor gas inflow has led to interaction-driven circumnuclear star formation which can explain the presence of such young metal-poor stellar population in the nucleus.

2.6.2 Feeding vs Feedback

We can compare the mass outflow rate, estimated in section 2.4.3, with the accretion rate necessary to power the AGN at the nucleus of NGC 2992, calculated as follows:

$$\dot{M}_{BH} = \frac{L_{bol}}{c^2 \eta} \tag{28}$$

where η is the mass-energy conversion efficiency, which for Seyfert galaxies is usually assumed to be $\eta = 0.1$ (FRANK et al., 2002), L_{bol} is the bolometric luminosity of the AGN, and c is the speed of light. To measure L_{bol} we applied the bolometric correction by Marconi et al. (2004) on the most recent X-ray luminosity measurement of NGC 2992 made by Marinucci et al. (2018). The author used a 2015 *NuSTAR* observation and obtained an absorption corrected 2-10 Kev Luminosity of $7.6 \pm 0.1 \times 10^{42}$ $ergs^{-1}$ that translates to $L_{bol} = 9.1 \pm 0.2 \times 10^{43}$ $ergs^{-1}$. We use these values to derive an accretion rate of $\dot{M}_{BH} \approx 0.02$ $M_{\odot} yr^{-1}$.

The nuclear accretion rate is two orders of magnitude smaller than the mass outflow rate ($\dot{M}_{out} \approx 1.6 \pm 0.6$ $M_{\odot}$ yr^{-1}, see section 2.4.3). This implies that most of the outflowing gas does not originate in the AGN, but in the surrounding ISM, and this result supports the scenario in which the plasma bubbles (radio loops) are expanding, pushing gas away from the nuclear region. However, the ratio between the kinetic power of this blueshifted outflow loop and the bolometric luminosity is ~ 0.002, which means only 0.2% of the AGN radiative power is in this outflow. Many authors argue that such a low value is not enough to have the feedback effects expected by cosmological simulations (SPRINGEL et al., 2005; SILK; MAMON, 2012; BULLOCK; BOYLAN-KOLCHIN, 2017), stating that $\dot{E}_{out}/L_{bol}$ should be closer to 5% or above in order to effectively suppress growth in the most massive galaxies. However, some models show that coupling efficiencies of $\dot{E}_{out}/L_{bol} \approx 0.5\%$ (HOPKINS; ELVIS, 2010), and even 0.1% (COSTA et al., 2018) could successfully prevent star formation.

2.6.3 AGN-Wind Scaling Relations

Comparing our outflow measurements with those from the literature we noted ours results disagree with those presented in Muller-Sanchez et al. (2011), who reported $\dot{M}_{out} = 120$ M$_{\odot}$ yr^{-1} and $\dot{E}_{out} = 2.5 \times 10^{42}$ erg s^{-1}, both almost one hundred times greater than ours. We attribute this difference to two factors: **i)** they assumed the filling factor f to be constant equal to 0.001, while we have measured the filling factor from L(Hα) and n_e (see equation 23). This assumption makes their M$_g$ proportional to n_e, and not inversely proportional (as in equation 24); **ii)** they assume an electronic density of $n_e = 5000$ cm^{-3}, a value more than 5 times larger than the maximum value we measured in the nuclear region of the galaxy. These two factors combined explain their overestimation of both $\dot{M}_{out}$ and $\dot{E}_{out}$. We also argue these differences cannot be due to a larger coverage of the outflow by a larger field of view, in the sense of seeing the farthest part of the radio emission major loop and its redshifted outflow structure, given the authors have used the OSIRIS/VLT instrument, which has an even smaller FoV than GMOS.

We can compare our values to the properties of outflows found in other previous papers across the literature. In Figure 28, we show the Fiore et al. (2017) compilation of a set of outflow energetics from various studies over the years spanning a large range of AGN luminosity

($L_{bol} \geq 10^{44}$), which they use to establish AGN wind scaling relations, mass outflow rate and outflow power as a function of bolometric luminosity, together with several measurements of nearby galaxies from individual studies compiled by us from the literature or obtained by our collaborators: NGC 1068, NGC 3783, NGC 6814, NGC 7469 (MULLER-SANCHEZ et al., 2011), NGC 4151 (CRENSHAW et al., 2015), Mrk 573 (REVALSKI et al., 2018), Mrk 34 (REVALSKI et al., 2018), NGC 7582 (RIFFEL et al., 2009), Mrk 1066 (RIFFEL et al., 2010b), Mrk 1157 (RIFFEL; STORCHI-BERGMANN, 2011), Mrk 79 (RIFFEL; STORCHI-BERGMANN, 2013), NGC 5728 (SHIMIZU et al., 2019), and NGC 3081 (SCHNORR-MULLER et al., 2014), ESO 362-G18 (HUMIRE et al., 2018), NGC 1386 (LENA et al., 2015), ESO 153-G20 (SOTO-PINTO et al., 2019), 3C 33 (COUTO et al., 2017), including NGC 2992 measurement by Muller-Sanchez et al. (2011). Although these estimates are made using different recipes, leading to differences between methods, they are generally similar to the one adopted here. Therefore, this comparison with the literature may be useful at least as an order of magnitude approximation.

As we can see, the overestimated previous measurement of NGC 2992's outflow made this source to be an outlier in the Fiore et al. (2017) relations, while our values make the galaxy more likely to be explained by these relations. However, the other measurements in nearby Seyfert galaxies support the existence of a larger scatter of these relations, both in $\dot{E}_{out}$ and $\dot{M}_{out}$, at lower luminosities. To confirm whether this extension is valid or not, more detailed studies like this, mainly using IFU, are needed so that outflow properties can be properly and systematically measured, without assuming fixed values of n_e and f.

2.6.4 Multiple Ionization Mechanisms

In section **??** we showed that despite being dominated by AGN excitation, star formation and shocks cannot be excluded as ionization mechanisms in the nuclear region of the galaxy. The existence of star formation ionization in the nucleus is confirmed by Friedrich et al. (2010) IR emission line analyses, as mentioned in section 2.6.1. The presence of shocks is also supported by Allen et al. (1999a) using long-slit spectroscopy. The authors also argue the dominance of shocks increases, compared to ionization by the central source, at larger radius.

Galaxies undergoing rapid phases of evolution (through processes such as galaxy-galaxy interactions, gas outflows and radio jets) often have multiple ionization mechanisms contributing to their optical line emission (e.g. RICH et al., 2011; LANZ et al., 2015; RICH et al., 2015; DAVIES et al., 2017). These multiple ionization mechanisms are also in agreement with evolutionary scenarios in which gas inflows (driven either by secular mechanisms, like nuclear bars or nuclear spiral arms, or environmental ones, like minor and major mergers) triggers nuclear star formation and nuclear activity (feeding process) and then the active nucleus can drive both ionizing photons from the accretion disk and radio jets (feedback process) that impacts the ISM physical conditions (HOPKINS et al., 2008; HOPKINS; ELVIS, 2010).

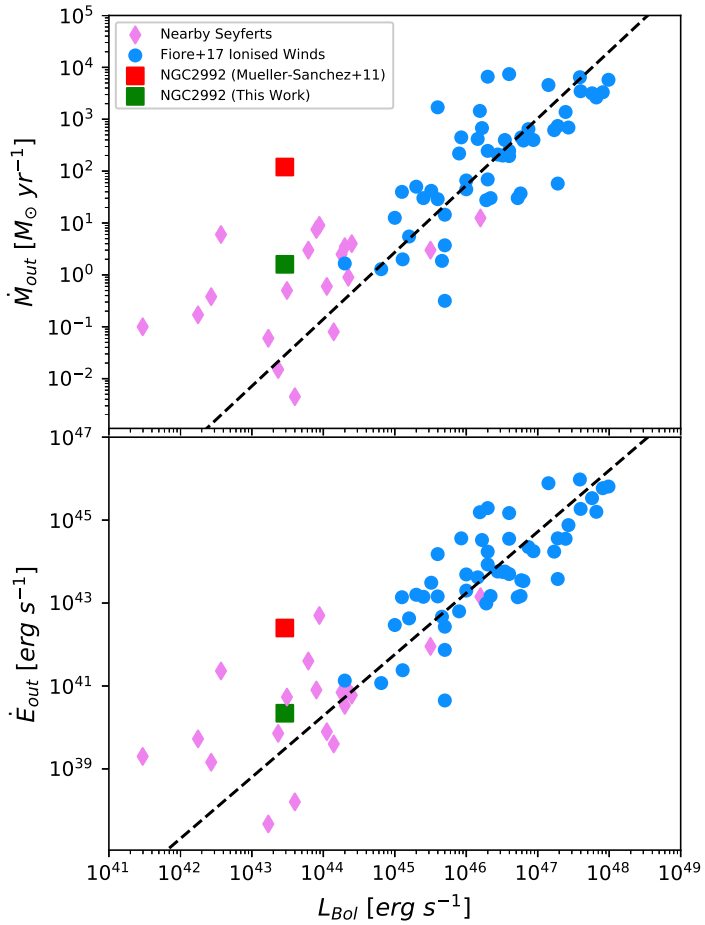

Figure 31 – Correlations between the mass outflow rate ($\dot{M}_{out}$, Top Panel) and kinetic outflow power ($\dot{E}_{out}$, Bottom Panel). Blue points are the data compiled by Fiore et al. (2017) and the black dashed lines show the best fit correlations for these points. Red Squares are the previous measurement of NGC 2992 by Muller-Sanchez et al. (2011), and green ones are the results of this work. Violet diamonds are compiled from various literature sources for more modest AGN luminosities.

3 THE LONG-TERM VARIABILITY OF NGC 2992

This chapter is fully based on the following paper, of which I am the lead author, and therefore is not intended as an original work:

"The Eddington ratio-dependent multiple 'changing look' events in NGC 2992", **Guolo-Pereira, M.**, Ruschel-Dutra, D., Schimoia, J., Grupe, D., Peterson, B., Nemmen, R., Storchi-Bergmann, T., Robinson, A., under review in the MNRAS.

3.1 Introduction: 'Changing Look' AGNs

The AGN Unified Model (section 1.3) attribute differences in AGN type to the viewing angle toward an axisymmetric, parsec scale obscuring structure, which can block our direct view of the AGN central engine (ANTONUCCI, 1993; URRY; PADOVANI, 1995) and is responsible for the lack of Broad Emission Line (BEL) in the Type 2 ones. However, a relatively small number of AGN show transitions from one type to another in a few years (e.g., Type 1 to Type 2 or Type 1 to Type 1.9); these objects are known as 'changing look' (CL) AGNs. CL-AGNs challenge the widely accepted AGN paradigm, not only in the orientation-based unified model but also standard accretion disk models (section 1.2.2). Their extreme and fast variability has motivated alternatives and/or modifications for both the AGN Unified Model (e.g., NICASTRO, 2000; ELITZUR; SHLOSMAN, 2006; ELITZUR et al., 2014, see also section 1.3.3) and for the standard Shakura and Sunyaev (1973) accretion disk model (e.g., SNIEGOWSKA et al., 2020; JIANG; BLAES, 2020)

Until recently there were only a handful of CL events reported, including NGC 3516 (ANDRILLAT; SOUFFRIN, 1971), NGC 1566 (PASTORIZA; GEROLA, 1970; OKNYANSKY et al., 2019), Mrk 590 (DENNEY et al., 2014), NGC 2617 (SHAPPEE et al., 2014), NGC 7603 (TOHLINE; OSTERBROCK, 1976), Mrk 1018 (COHEN et al., 1986), NGC 1097 (STORCHI-BERGMANN et al., 1993), NGC 3065 (ERACLEOUS; HALPERN, 2001) and NGC 7582 (ARETXAGA et al., 1999). In 2015 (LAMASSA et al.) discovered the first CL Quasar and since then the number of known CL-AGNs has increased rapidly (e.g., MACLEOD et al., 2016; MCELROY et al., 2016; RUNNOE et al., 2016; YANG et al., 2018; RUAN et al., 2016; SHENG et al., 2017; KOLLATSCHNY et al., 2018; GUO et al., 2019; WANG et al., 2019; GRAHAM et al., 2019; KOLLATSCHNY et al., 2020); however, the number is still less than a hundred.

Some of these CL might be successfully explained via variable obscuration (e.g.„ MATT et al., 2003; PUCCETTI et al., 2007; RISALITI et al., 2010; MARINUCCI et al., 2013; MARCHESE et al., 2012): in models where the obscuring material has a patchy distribution (e.g., NENKOVA et al., 2008; ELITZUR, 2012), the dynamical movement of the dust clouds could result in a change of classification. Transient events such as tidal disruption events (TDE) of a star by the SMBH were also claimed as possible drivers of CL events (ERACLEOUS et al., 1995); however, this scenario does not apply to sources presenting multiple (and quasi-periodic) CL events.

In a third scenario, it has been argued that changes in type are expected with variations in accretion rate. In this scenario either the BELs disappear (reappear) due to the reduction (increase) of ionising photons available to excite the gas in the vicinity of the black hole (e.g.,

STORCHI-BERGMANN et al., 2003; LAMASSA et al., 2015) or the BLR itself disappears, given that in disk-wind BLR models (e.g., NICASTRO, 2000; ELITZUR; SHLOSMAN, 2006; ELITZUR; HO, 2009, section 1.3.3) the broad line emission region follows an evolutionary sequence that is directly related to the accretion rate of the compact source. In such disk-wind BLR models, a low accretion efficiency is not able to sustain the required cloud flow rate responsible for the formation of the BLR clouds which gives origin to the distinct (intrinsic) AGN types, as proposed by Elitzur et al. (2014).

NGC 2992 was the subject of several studies and target of all major X-ray missions due to its variability. In the hard X-rays band (2-10 keV), it steadily declined in observed flux from 1978, when it was observed by *HEAO1* (MUSHOTZKY, 1982) at a flux level of about 8×10^{-11} *erg cm*^{3} *s*$^{-1}$ until 1994 when it was observed by *ASCA* (WEAVER et al., 1996) at a flux level by about a factor 20 fainter. Then it underwent a rapid recovery: in 1997 it was observed by *BeppoSAX* at a flux level somewhat higher than in 1994, while in 1998 the source fully recovered its *HEAO1* brightness (GILLI et al., 2000). In 2003, when observed by *XMM-Newton*, the flux was even higher, about 10^{-10} *erg cm*^{3} *s*$^{-1}$ (SHU et al., 2010). The source was then observed by *Suzaku* on November/December 2005, and found in a much fainter state, almost an order of magnitude fainter than in the *XMM-Newton* observation.

The Rossi X-ray Timing Explorer (RXTE, SWANK, 2006) monitoring campaign between early March 2005 and late January 2006 found large amplitude (almost an order of magnitude) variability, indicating that apart from the long-term variability of the source, it also presents short-term outbursts with variations in the order of days, while no significant variation of the primary power-law index was found (MURPHY et al., 2007); at the end of the campaign the source was again at a low flux state, confirmed by *Suzaku*, at a flux level of $\sim 1 \times 10^{-11}$ *erg cm*^{3} *s*$^{-1}$ (PTAK et al., 2007; YAQOOB et al., 2007) and *Chandra*, at flux level of $\sim 0.3 \times 10^{-11}$ *erg cm*^{3} *s*$^{-1}$ (its historical minimum flux, MURPHY et al., 2017). In 2010, NGC 2992 was observed eight times for $\sim$ 40 ks by *XMM-Newton* with a flux ranging from 0.3×10^{-11} *erg cm*^{3} *s*$^{-1}$ to 1.3×10^{-11} *erg cm*^{3} *s*$^{-1}$. A further 2013 *XMM-Newton* observation caught the source in a higher but still low flux state (1.6×10^{-11} *erg cm*^{3} *s*$^{-1}$). In 2015, observations performed simultaneously with *Swift* and *NuSTAR* found a flux of 6×10^{-11} *erg cm*^{3} *s*$^{-1}$ (MARINUCCI et al., 2018). The most recent observations was performed again with *XMM-Newton* in May 2019, when the flux was again at the highest levels seen, ranging from 6.8 to 10×10^{-11} *erg cm*^{3} *s*$^{-1}$ (MARINUCCI et al., 2020).

The optical variability of the source was first explored by Gilli et al. (2000) who noticed that in 1999 the Hα BEL was present again, as it was in early observations of the galaxy by (VERON et al., 1980) at the end of the '70s (what led to its first classification as a Seyfert 1.9), in contrast to the Type 2 spectra seen in 1994 by Allen et al. (1999b). Later, Trippe et al. (2008a) showed that from the beginning of 2006 to the middle of 2007 the source had lost its BEL. Recently Schnorr-Muller et al. (2016b) and Guolo-Pereira et al. (2021, chapter 2) not only showed that the Hα BEL was detectable again but also, for the first time, a very faint Hβ BEL was claimed to be present.

Besides being a very well studied galaxy, to the best of our knowledge no study has yet explored the entire X-ray and optical historical emission of NGC 2992, nor attempted to link the behavior in the two wavelength bands. These are our goals in this chapter, which is organized as follow: In section 3.2 we describe the data collection. The analysis of the data is described

in section 3.3, while the results are discussed in section 3.4.

3.2 Data Collection

This work results from a careful re-examination of the entire literature on NGC 2992, both X-rays and optical spectra, from its discovery as an X-ray source (COOKE et al., 1978; WARD et al., 1980) and classification as a Seyfert galaxy (OSMER et al., 1974) to the most recent optical and X-ray spectra published to date (MARINUCCI et al., 2020; GUOLO-PEREIRA et al., 2021, chapter 2).

3.2.1 X-ray Spectra

The X-ray spectrum of NGC 2992 is very well fitted by an absorbed power-law which accounts for most of the X-ray emission (spectra examples are show in Figure 7). However, the spectrum also presents a narrow iron Kα component, which becomes more intense at high flux levels (YAQOOB et al., 2007; MARINUCCI et al., 2018; MARINUCCI et al., 2020). We collected the fluxes in the 2-10 keV X-ray band (F_{2-10}) and the best-fitting parameters for the absorbed continuum model, namely the power-law continuum photon indexes (Γ) and the absorbed material column densities (N_H), as reported by the authors throughout the literature on the source (equation 17). For the more recent spectra, where the narrow Fe Kα is detected we also collected their measured fluxes, F(Fe Kα). In the top panel of Figure 32, we show the historical 2-10 keV light curve. In Table 3, we show the best-fitting continuum model parameters, the Fe Kα fluxes, the observation dates, and references. The N_H are only accounting for the absorption at the redshift of the source therefore not including Galactic absorption, $N_H^G \approx 5.5\times10^{20}$ cm^{-2} (KALBERLA et al., 2005). Errors in the X-rays parameters correspond to the 90% confidence level for the parameter of interest ($\Delta\chi^2 = 2.7$), as reported by the authors. For the papers in which the authors reported their uncertainties in another scale, e.g., $\Delta\chi^2 = 4.6$, the errors were re-scaled using a Python package (`asymmetric_uncertainties`) for treatment of asymmetric statistical errors derived from confidence levels, which employs a combination of the methods proposed by Barlow (2004) and Possolo et al. (2019). The method and a brief discussion on uncertainties can be found in Appendix B.1. The propagation of the uncertainties for the X-ray derived quantities (see section 3.1 and Table 3) is also performed with this same method, see appendix B.1.

3.2.2 Historical Optical Spectra

To access the historical presence or absence of Hα BEL and the galaxy optical classification, we reviewed all papers that report optical spectra of the galaxy. As most of these spectra are not available to allow inter-calibration and measurement of the BELs flux variability, we restrict ourselves to a binary classification of the Hα BEL, i.e., whether the component was undoubtedly detected (D) or not-detected (N-D) by the authors. We do so by searching for a detection/non-detection claim in the original text and by visually inspecting the published spectra. In the middle panel of Figure 32, we show the Hα BEL detection history. In Table 4 we show the observation dates, the references and the Seyfert Type at the time.

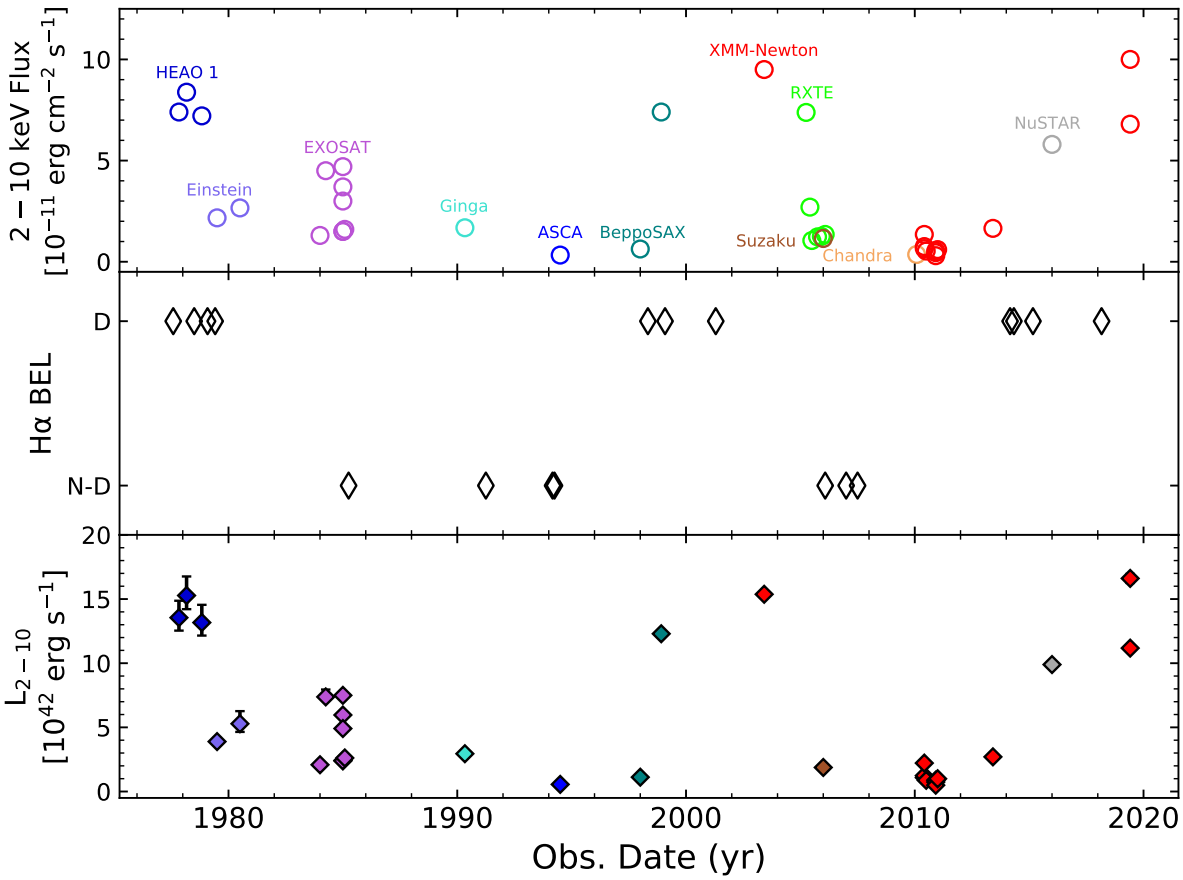

Figure 32 – Top: Historical 2-10 keV light curve of the source. Middle: Historical detections (D) and non-detections (N-D) of the broad Hα emission line. Bottom: Intrinsic (absorption corrected) 2-10 keV Luminosity (L_{2-10}) light curve. Each color represents a distinct X-ray mission, and will be maintained throughout the entire paper. In the L_{2-10} panel, the points without error bars have errors smaller then 3×10^{41} erg s^{-1}, see Table 3 for the exact values.

In summary: the first spectra of the galaxy in the '70s (WARD et al., 1980; VERON et al., 1980; SHUDER, 1980; DURRET; BERGERON, 1988) detected only Hα broad components, with no counterpart in Hβ, resulting in its original classification as a Seyfert 1.9 galaxy. Throughout mid '80s to the mid '90s several authors have reported that the BEL Hα was not detectable anymore (BUSKO; STEINER, 1990; ALLEN et al., 1999b; MARQUEZ et al., 1998; VEILLEUX et al., 2001), changing its classification to Seyfert 2 Type. However the broad component was detected again from the end of the '90s to the beginning of the 2000s (GILLI et al., 2000; GARCIA-LORENZO et al., 2001; STOKLASOVÁ et al., 2009). Later, Trippe et al. (2008a) performed an 18 months long monitoring campaign from the beginning of 2006 to mid 2007 that revealed the Hα BEL component was missing again, throughout the entire campaign. More recent observations have shown that the galaxy has regained the broad Hα component (DOPITA et al., 2015; SCHNORR-MULLER et al., 2016b; MINGOZZI et al., 2019), and for the first time, an Hβ BEL was unambiguously detected, in late 2018, by Guolo-Pereira et al. (2021, chapter 2), therefore changing its classification to a 1.8 Type Seyfert galaxy.

It is important to note the great number of data points collected: 40 in the X-rays (33 with

Table 3 – Historical X-ray data for NGC 2992.

Obs. Date[a]	Satellite	$F_{2-10}^{(b)}$	$N_H^{(c)}$	Γ	F(Fe Kα)[d]	Reference	$L_{2-10}^{(e)}$
10/1977	*HEAO 1*	7.40	$16.0^{+8.0}_{-6.0}$	$1.79^{+0.09}_{-0.07}$	–	Mushotzky (1982)	$13.48^{+1.40}_{-0.99}$
02/1978		8.38			–		$15.30^{+1.52}_{-1.13}$
10/1978		7.21			–		$13.09^{+1.34}_{-0.85}$
06/1979	*Einstein*	2.17	$14.3^{+6.0}_{-4.0}$	$1.82^{+0.14}_{-0.14}$	–	Maccacaro et al. (1982)	$3.89^{+0.30}_{-0.20}$
06/1980		2.66	$22.3^{+15.2}_{-10.7}$	$1.92^{+0.47}_{-0.47}$	–		$5.25^{+1.01}_{-0.64}$
12/1983	*EXOSAT*	1.30	$7.0^{+3.5}_{-1.2}$	$1.46^{+0.23}_{-0.16}$	–	Turner and Pounds (1989)	$2.09^{+0.10}_{-0.03}$
03/1984		4.50	$7.8^{+6.2}_{-1.6}$	$1.68^{+0.31}_{-0.22}$	–		$7.37^{+0.59}_{-0.17}$
12/1984		4.70	$6.0^{+1.7}_{-0.6}$	$1.64^{+0.07}_{-0.09}$	–		$7.50^{+0.18}_{-0.07}$
12/1984		3.70	$7.0^{+1.2}_{-0.3}$	$1.56^{+0.10}_{-0.06}$	–		$5.96^{+0.12}_{-0.03}$
12/1984		3.00	$8.6^{+2.6}_{-0.3}$	$1.48^{+0.15}_{-0.11}$	–		$4.91^{+0.27}_{-0.03}$
12/1984		1.50	$6.9^{+7.1}_{-1.8}$	$1.49^{+0.46}_{-0.27}$	–		$2.42^{+0.23}_{-0.07}$
12/1984		1.50	$5.6^{+5.2}_{-1.2}$	$1.58^{+0.39}_{-0.20}$	–		$2.39^{+0.19}_{-0.05}$
01/1985		1.60	$7.4^{+4.7}_{-1.2}$	$1.67^{+0.31}_{-0.17}$	–		$2.61^{+0.18}_{-0.05}$
04/1990	*GINGA*	1.68	$13.6^{+3.3}_{-3.3}$	$1.64^{+0.08}_{-0.08}$	–	Nandra and Pounds (1994)	$2.94^{+0.12}_{-0.12}$
06/1994	*ASCA*	0.33	$10.1^{+2.7}_{-2.3}$	1.70[f]	–	Weaver et al. (1996)	$0.56^{+0.02}_{-0.02}$
12/1997	*BeppoSAX*	0.63	$14.0^{+5.0}_{-4.0}$	$1.72^{+0.13}_{-0.12}$	–	Gilli et al. (2000)	$1.12^{+0.07}_{-0.06}$
11/1998		7.40	$9.0^{+0.3}_{-0.3}$	$1.70^{+0.02}_{-0.02}$	–		$12.29^{+0.05}_{-0.05}$
05/2003	*XMM-Newton*	9.50	$6.5^{+0.3}_{-0.2}$	$1.83^{+0.06}_{-0.04}$	–	Shu et al. (2010)	$15.37^{+0.07}_{-0.05}$
03/2005	*RXTE*	7.38	–(g)	$1.71^{+0.03}_{-0.03}$	–	Murphy et al. (2007)	–
05/2005		2.70	–	$1.72^{+0.04}_{-0.04}$	–		–
06/2005		1.05	–	$1.75^{+0.10}_{-0.10}$	–		–
09/2005		1.23	–	$1.85^{+0.13}_{-0.12}$	–		–
11/2005		1.25	–	$1.96^{+0.12}_{-0.11}$	–		–
01/2006		1.35	–	$1.76^{+0.08}_{-0.08}$	–		–
12/2005	*SUZAKU*	1.15	$8.0^{+0.6}_{-0.4}$	$1.57^{+0.05}_{-0.03}$	$3.99^{+0.80}_{-0.80}$	Yaqoob et al. (2007)	$1.88^{+0.01}_{-0.01}$
01/2010	*CHANDRA*	0.36	–	–	–	Murphy et al. (2017)	–
05/2010	*XMM-Newton*	0.65	$9.2^{+1.0}_{-1.0}$	$1.67^{+0.05}_{-0.05}$	$3.51^{+0.35}_{-0.35}$	Marinucci et al. (2018)	$1.08^{+0.01}_{-0.01}$
05/2010		0.75	$8.6^{+1.0}_{-1.0}$	$1.64^{+0.04}_{-0.04}$	$2.96^{+0.42}_{-0.42}$		$1.24^{+0.02}_{-0.01}$
05/2010		1.35	$8.4^{+1.0}_{-1.0}$	$1.61^{+0.04}_{-0.04}$	$4.49^{+0.48}_{-0.48}$		$2.22^{+0.03}_{-0.03}$
06/2010		0.53	$8.5^{+1.0}_{-1.0}$	$1.67^{+0.05}_{-0.05}$	$3.69^{+0.32}_{-0.32}$		$0.87^{+0.01}_{-0.01}$
11/2010		0.54	$8.0^{+1.0}_{-1.0}$	$1.67^{+0.05}_{-0.05}$	$3.64^{+0.34}_{-0.34}$		$0.88^{+0.01}_{-0.01}$
11/2010		0.45	$8.0^{+1.0}_{-1.0}$	$1.70^{+0.06}_{-0.06}$	$3.70^{+0.35}_{-0.35}$		$0.74^{+0.01}_{-0.01}$
11/2010		0.30	$8.1^{+1.0}_{-1.0}$	$1.71^{+0.09}_{-0.09}$	$3.19^{+0.32}_{-0.32}$		$0.49^{+0.01}_{-0.01}$
12/2010		0.60	$9.0^{+1.0}_{-1.0}$	$1.68^{+0.04}_{-0.04}$	$3.00^{+0.37}_{-0.37}$		$1.00^{+0.01}_{-0.01}$
05/2013		1.65	$8.1^{+1.0}_{-1.0}$	$1.63^{+0.06}_{-0.06}$	$5.66^{+1.12}_{-1.12}$		$2.70^{+0.03}_{-0.03}$
12/2015	*NuSTAR*	5.80	$11.0^{+2.0}_{-2.0}$	$1.72^{+0.03}_{-0.03}$	$8.68^{+1.92}_{-1.92}$		$9.89^{+0.26}_{-0.24}$
05/2019	*XMM-Newton*	10.00	$9.0^{+1.6}_{-1.6}$	$1.68^{+0.10}_{-0.10}$	$12.96^{+1.60}_{-1.60}$	Marinucci et al. (2020)	$16.59^{+0.34}_{-0.34}$
05/2019		6.80	$8.5^{+1.6}_{-1.6}$	$1.63^{+0.06}_{-0.06}$	$12.96^{+1.60}_{-1.60}$		$11.18^{+0.23}_{-0.22}$

(a) mm/yyyy. (b) in units of 10^{-11} *erg cm*$^{-2}$ *s*$^{-1}$. (c) in units of 10^{21} *cm*$^{-2}$. (d) in units of 10^{-14} erg cm^{-2} s^{-1} (e) Absorption corrected, in units of 10^{42} *erg s*$^{-1}$. (f) The value was frozen in the model fitting, therefore it was excluded in the analyses of the Γ parameter variability of section 3.3.1. (g) Values not provided by the authors.

reported N_H and Γ values) and 18 in the optical; allow us to have a quasi-contemporaneous X-ray measurement for each optical spectrum, within less than one year for most, and less than two years for all of them, see Figure 32.

3.2.3 Modern Optical Spectra

For four of the six recent spectra of NGC 2992, we were able to apply methods of flux intercalibration that have been developed for reverberation mapping studies (PETERSON, 1993; VAN GRONINGE; WANDERS, 1992; PETERSON et al., 1995; FAUSNAUGH, 2017) and measure the intrinsic flux variability of the BELs. The spectra are from:

- Trippe et al. (2008a) and taken in December of 2006 in the Cerro Tololo Inter-American Observatory; the spectrum was obtained by private communication with one of the authors;
- Dopita et al. (2015) as part of the Siding Spring Southern Seyfert Spectroscopic Snapshot Survey (S7), taken in April of 2014 and publicly available at the S7 survey website;

Table 4 – Historical broad Hα line and Seyfert type classification for NGC 2992.

Obs. Date[(a)]	Hα BEL[(b)]	Reference	Seyfert Type
07/1977	D	Ward et al. (1980)	1.9
< 1978	D	Veron et al. (1980)	1.9
01/1979	D	Shuder (1980)	1.9
05/1979	D	Durret and Bergeron (1988)	1.9
03/1985	N-D	Busko and Steiner (1990)	2
03/1991	N-D	Marquez et al. (1998)	2
02/1994	N-D	Veilleux et al. (2001)	2
03/1994	N-D	Allen et al. (1999b)	2
04/1998	D	Garcia-Lorenzo et al. (2001)	1.9
01/1999	D	Gilli et al. (2000)	1.9
03/2001	D	Stoklasová et al. (2009)	1.9
01/2006	N-D		2
12/2006	N-D	Trippe et al. (2008a)	2
06/2007	N-D		2
02/2014	D	Schnorr-Muller et al. (2016b)	1.8/1.9
04/2014	D	Dopita et al. (2015)	1.9
02/2015	D	Mingozzi et al. (2019)	1.8/1.9
02/2018	D	Guolo-Pereira et al. (2021, chapter 2)	1.8

(a) mm/yyyy. (b) Whether the Hα BEL was Detected (D) or Non-Detected (N-D).

- Mingozzi et al. (2019) as part of the Measuring Active Galactic Nuclei Under MUSE Microscope (MAGNUM) survey using the MUSE instrument at the Very Large Telescope (VLT) and taken in February of 2015; the spectral data cube is public available at the VLT archive;
- Data cube from chapter 2 (GUOLO-PEREIRA et al., 2021).

The inter-calibration, aperture/seeing corrections, and the process for emission line fitting of these spectra will be presented in section 3.3.2.

3.2.4 Estimates of the Black Hole Mass

Precise black hole mass measurements are essential for the energetic calibrations and scaling to come. Using stellar velocity dispersion measurements of $\sigma_* = 158$ km s^{-1}, Woo and Urry (2002) estimated the black hole mass of NGC 2992 to be 5.2×10^7 $M_\odot$ by applying the Tremaine et al. (2002) M_{BH}- σ_* relation. The value obtained from Gultekin et al. (2009) M_{BH}- σ_* relation is $M_{BH} = 4.8^{+3.9}_{-2.4} \times 10^7$ $M_\odot$, using a bulge stellar velocity dispersion $\sigma_* = 158 \pm 13$ km s^{-1} (NELSON; WHITTLE, 1995). From the normalized excess variance σ^2_{rms} in the 2-10 keV band and assuming the σ^2_{rms}- M_{BH} correlation from Ponti et al. (2012), Marinucci et al. (2020) reported a $M_{BH} = 3.0^{+5.5}_{-1.5} \times 10^7$ $M_\odot$. Furthermore, we also estimate the SMBH mass using the emission line measurements, to be described in section 3.3.2, by using single-epoch (SE M_{BH} estimates. We applied Dalla Bonta et al. (2020) $M_{\rm SE}(\sigma_{H\beta}, L_{H\beta})$ relation in all the four modern spectra. We corrected extinction effects using the measured Balmer decrements and assuming Calzetti et al. (2000) extinction law. We obtained the following values for M_{BH}: $1.3^{+2.8}_{-0.9} \times 10^7$ $M_\odot$, $3.5^{+7.4}_{-2.4} \times 10^7$ $M_\odot$ and $2.4^{+5.1}_{-1.4} \times 10^7$ $M_\odot$, respectively for 2014, 2015 and 2018 spectra. For 2006 spectrum, as the the Hβ BEL was not detected we use the Hα BEL, assuming a Balmer decrement of 9 (see section 3.3.2), we obtained $M_{BH} = 0.5^{+1.5}_{-0.4} \times 10^7$ $M_\odot$. In summary, although

the distinct methods results in distinct M_{BH} values, they are all within the $0.5-5.5 \times 10^7\ M_\odot$ range.

3.3 Data Analyses

3.3.1 X-ray Variability

In the scenario where the CL events are caused by variable absorption, two natural consequences are an anti-correlation between the N_H and F_{2-10} and a constant intrinsic (absorption corrected) luminosity. In the top panel of Figure 33 we show log N_H as function of F_{2-10}: no clear anti-correlation can be seen. The Spearman rank correlation coefficient (r_s) for the two variables and its corespondent p_{value} are $r_s = 0.19^{+0.15}_{-0.14}$ and $p_{value} = 0.22^{+0.45}_{-0.17}$, while the best-fitting constant value is $N_H = 22.01^{+0.03}_{-0.03}$, where the errors correspond to 90% confidence level measured by performing a thousand Monte Carlo iterations (see details in appendix B.1).

We can therefore conclude that although there were some variations in the column density it is not anti-correlated with the X-ray flux as seen in variable absorption CL-AGNs (e.g., PUCCETTI et al., 2007; BIANCHI et al., 2009).A further confirmation that the absorption is not the main factor responsible for the behavior of the source can be seen by the intrinsic (i.e., absorption corrected) rest-frame luminosity (L_{2-10}). The measured L_{2-10} values, for each observation in which a N_H value is provided, are presented in Table 3. The values range from $4.9 \times 10^{41}\ erg\,s^{-1}$to $\sim 1.7 \times 10^{43}\ erg\,s^{-1}$. The L_{2-10} light curve is shown in the bottom panel of Figure 32, and it has the same behavior as the F_{2-10} and this indicates/confirms that the variations are intrinsic and not due to changes in absorption.

The Sperman rank correlation test shows that there is no monotonic correlation between the photon index Γ and the X-rays flux (or luminosity) for NGC 2992 (bottom panel of Figure 33). The values found were $r_s = 0.15^{+0.12}_{-0.12}$ and $p_{value} = 0.27^{+0.55}_{-0.23}$. The existence of a correlation between luminosity and photon index is in fact debatable, and several contradictory results have been presented in the last years. While Dai et al. (2004) reported the existence of a positive correlation, other works found none (e.g., WINTER et al., 2009) or a negative correlation (e.g., CORRAL et al., 2011). A 'V' shape for the Γ versus L_{Edd} relation for NGC 2992 was claimed by Liu et al. (2019); the authors interpreted this as a change in accretion mode, similar to the ones that occur in stellar-mass X-ray binaries (e.g., QIAO; LIU, 2013), in the AGN. We argue here that their finding is due to selection effects, as the authors only used data from 2003 to 2013. When the entire historical data of the source is shown (Figure 33), this effect is not seen. However, there is a positive correlation between F_{2-10} and the flux of the Fe Kα, with $r_s = 0.69^{+0.07}_{-0.11}$ and $p_{value} = 0.01^{+0.03}_{-0.01}$. Fitting the data by assuming a relation of the type:

$$log\ F(Fe\ K\alpha) = \alpha + \beta\ log\ F_{2-10} \tag{29}$$

we obtained a slope of $\beta = 0.39 \pm 0.04$. As the iron Kα line is created by reprocessing of the primary X-ray continuum, a tight correlation between the flux of the line and that of the continuum is expected. For large samples of galaxies Ricci et al. (2014), found $\beta = 0.89 \pm 0.04$, while Shu et al. (2010) found $\beta = 0.86 \pm 0.01$. However, NGC 2992 seems to be one of a few

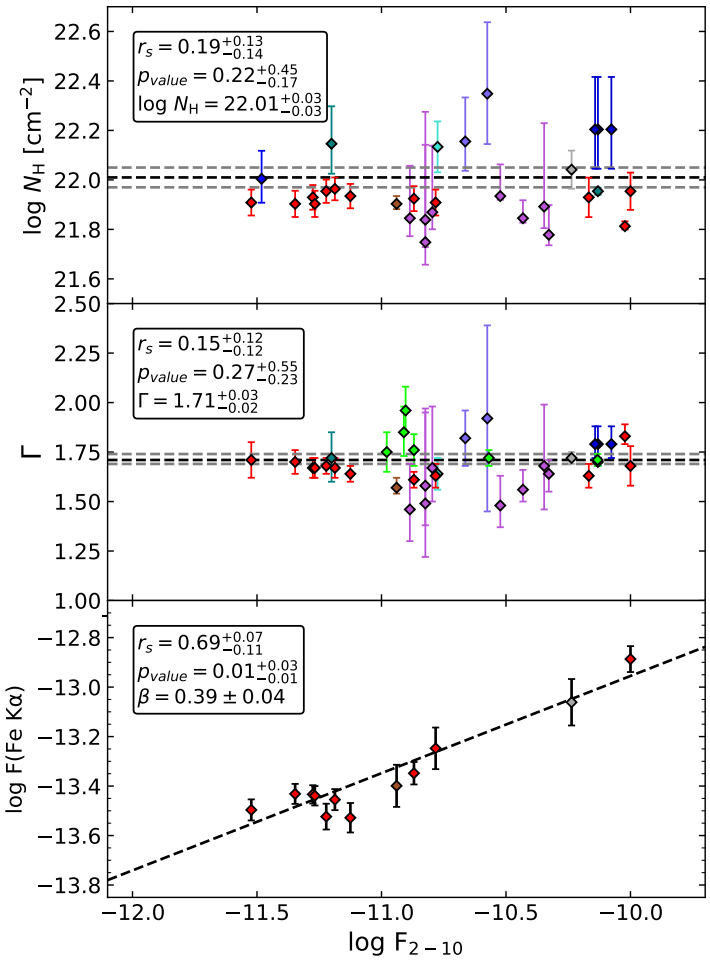

Figure 33 – Best-fitting parameters N_H (top panel) and Γ (middle panel) for an absorbed power-law continuum model as function of the 2-10 keV Flux. The left top boxes show the Spearman rank correlation coefficient (r_s) for the two variables and its corresponding p_{value}, as well as the best-fitting constant values. Fe Kα flux as function as function of the 2-10 keV flux. The left top box show the Spearman rank correlation coefficient (r_s) for the two variables and its corresponding p_{value}, β is the slope of the best fitting line (see equation 29).

objects where this correlation is found in a single object, though with a lower slope than the ones found in the general AGN population.

3.3.2 Modern Optical Spectra Analyses

In this section, we explore the flux variability of the BELs using four of the six most recent spectra, namely from 12/2006, 04/2014, 02/2015 and 02/2018 (see Table 4).

Absolute calibration of the spectra

Even under the best conditions, which are not often realized, flux calibration of ground-based spectrophotometry is no better than ∼5%, which is insufficient for detailed comparisons of variable spectra. Thus the standard technique of flux calibration, through comparison with stars of known spectral energy distribution, is not good enough for the study of AGN variability.

Table 5 – Emission line measurements of the modern optical spectra. Point-Source Scale Factor (φ) is measured using Peterson et al. (1995) algorithm (described in section B.2), the errors in φ represents the uncertainty in the centering of the virtual apertures.

Obs. Date (mm/yyyy)	Aperture	Point-Source Scale Factor φ	F(Hα) (10^{-13} *erg cm^{-2} s^{-1}*)	FWHM(Hα) (*km s^{-1}*)	F(Hβ) (10^{-13} *erg cm^{-2} s^{-1}*)
12/2006	Slit (width = 2.0″)	0.734 ± 0.063	≤ 4.4	2733 ± 55	–
04/2014	Circular (radius = 2.8″)	0.972 ± 0.025	27.5 ± 1.4	2002 ± 28	3.6 ± 2.6
02/2015	Circular (radius = 3.0″)	1.000 ± 0.011	33.8 ± 1.5	2313 ± 17	3.3 ± 2.2
02/2018	Circular (radius = 3.0″)	0.973 ± 0.013	43.8 ± 2.2	2016 ± 13	4.9 ± 1.4

Instead, we use the fluxes of the narrow emission lines known to be non-variable on time scales of tens of years in most AGN. Consequently, the bright narrow emission lines can be adopted as internal calibrators for scaling AGN spectra (PETERSON, 1993). We assume that the flux of the [O III] λ5007 line remains constant during the interval covered by these spectra.

We extracted the spectra using virtual apertures from the original data, making them as similar as possible to each other in the data cubes, as shown in Table 5. The scaling of the extracted spectra was carried out using a refinement of the method of van Groningen and Wanders (1992), employed as a Python package (`mapspec`) by Fausnaugh (2017). This method allows us to obtain a homogeneous set of spectra with the same wavelength solution, same spectral resolution (at $\sim$ 6300Å), and the same [O III] λ5007 flux value.

Stellar component subtraction and emission-line fitting

We subtracted the host galaxy stellar continuum fitted using the `starlight` (CID FERNANDES et al., 2005b) full spectra fitting code, using a base of 45 Simple Stellar Population (SSP) spectra, with 15 ages (from 1 Myr to 13 Gyr) and 3 metallicities (0.2, 1.0 and 2.5 $Z_{\odot}$). The emission line fitting was performed using the `IFSCube` package[1] (RUSCHEL-DUTRA, 2020). The code employs Sequential Least Square Programming and allows multiple components with physically motivated constraints. In order to measure the BEL fluxes, the narrow emission components must be separated from the broad components. This process is not straightforward due to the fact the BELs are blended with the narrow lines, for both Hα and Hβ.

The narrow line subtraction was performed in two steps. First we fitted the narrow and broad Hα and Hβ simultaneously. For the narrow lines, we created a template comprised of two Gaussian components that were based on the [S II] λ6716 profile. This template was used to fit the [N II] and narrow Hα and Hβ lines by adjusting its flux scaling factor only. The fits to the broad lines were subtracted from the spectra, isolating the narrow emission; we then re-fitted the narrow lines assuming the H I and [N II] lines have the same velocity dispersion and redshift and we set the flux of [N II] λ6583 line as 2.96 times that of the [N II] λ6548 line, in accordance with the ratio of their transition probabilities (OSTERBROCK; FERLAND, 2006), while the Hα and [N II] λ6583 fluxes were free parameters in the fit. Finally, we subtracted the resulting narrow lines from the original spectrum and re-fit only broad lines using three Gaussian components, in order to account for the known non-Gaussian profiles of the BEL. The errors were taken as the standard deviations of one hundred Monte Carlo iterations. The resulting fits for the four spectra are shown in Figure 34.

[1] http://github.com/danielrd6/ifscube

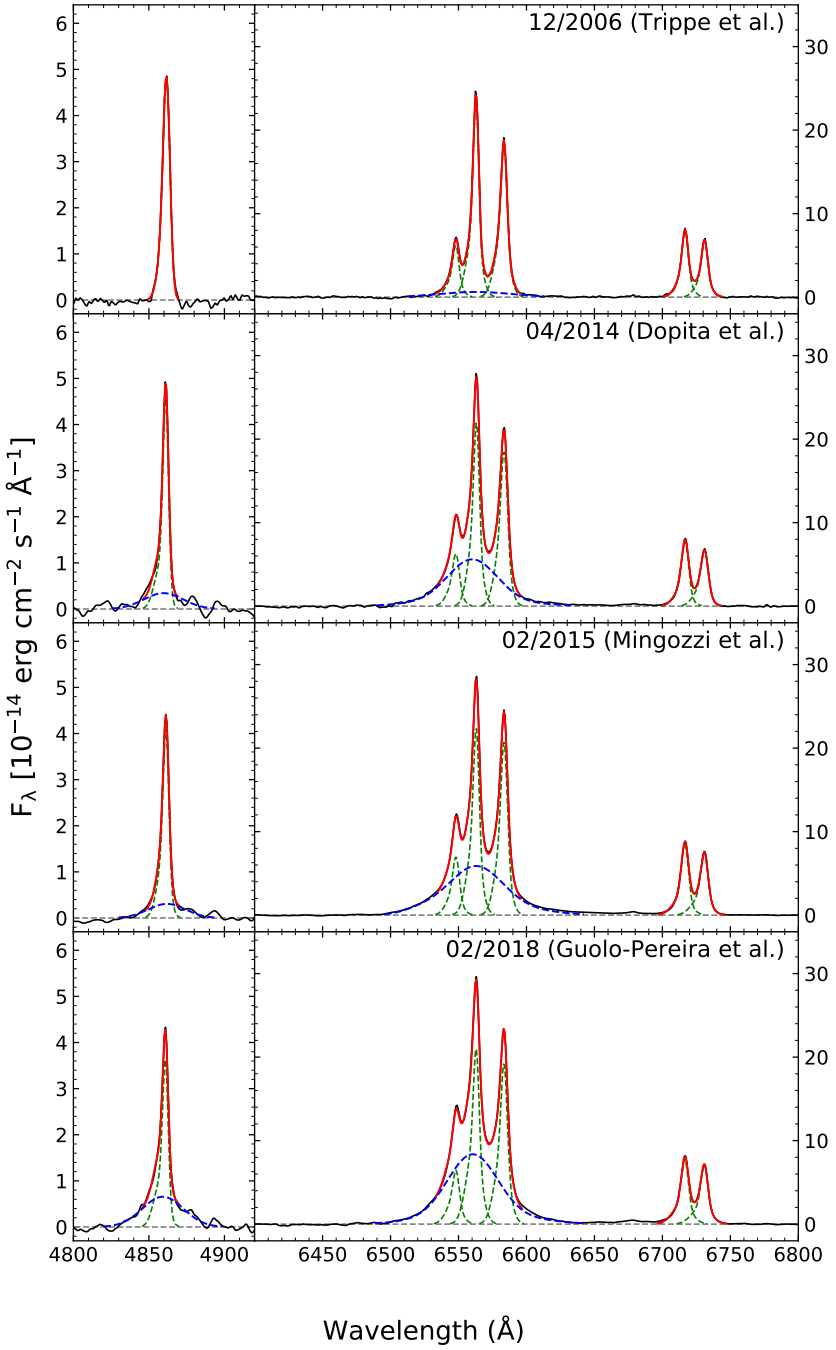

Figure 34 – Fit of the emission lines for the modern optical spectra. From top to bottom: 12/2006 (TRIPPE et al., 2008a), 04/2014 (DOPITA et al., 2015), 02/2015 (MINGOZZI et al., 2019) and 02/2018 (GUOLO-PEREIRA et al., 2021). Scaled observed spectra (black), narrow components (green), broad components (blue) and total model (red) are shown. Left panels show the Hβ lines while right ones show the Hα, [N II] and [S II] lines.

Inter-calibration of the spectral data

The fluxes measured in the scaled spectrum described in the previous sections were corrected for aperture and distinct seeing effects, because while the BLR is effectively a point-like source, the NLR is an extended one. Consequently, the measured NLR flux depends on the size of the spectrograph's entrance aperture and the observations seeing (see PETERSON et al., 1995, and section B.2 for more detailed discussion). In order to correct our fluxes for these effects, we determined a point-source correction factor (φ), which was measured using the procedure described in section B.2. The φ value represents the differences in the amount of light from the NLR with respect to the amount of light from the BLR for each observation, it is normalized using the largest aperture (φ = 1.0, for 04/2015 spectrum). Then the scaled inter-calibrated and aperture/seeing corrected BEL fluxes were measured as follows:

$$F(H\alpha) = \varphi \cdot F_{\lambda 5007} \left[\frac{F(H\alpha)}{F([\mathrm{O\,III}]\lambda 5007)} \right]_{obs} \tag{30}$$

where $F_{\lambda 5007}$ is the scaling absolute flux in the [O III] λ5007 line, described in section 3.3.2, and the value in brackets is the broad Hα to [O III] λ5007 measured flux ratio for each spectrum as described in section 3.3.2. The same procedure was applied to Hβ BEL.

The BEL Hα and Hβ fluxes and the Balmer decrements (Hα/Hβ) are shown in Table 5 and in the right panels of Figure 35. In the 12/2006 spectrum, the Hα BEL is not unambiguously detected (which leads to its classification as a Seyfert 2), and if it is indeed present, it is very faint, with a maximum flux of 4.4×10^{-13} *erg cm*^{3} *s*$^{-1}$. From 2014 to 2018 the broad Hα flux increases from $\sim 28 \times 10^{-13}$ *erg cm*^{3} *s*$^{-1}$ to $\sim 44 \times 10^{-13}$ *erg cm*^{3} *s*$^{-1}$. The Hβ BEL flux, however, does not increase monotonically: in the 04/2014 spectrum it had a flux of 3.6×10^{-13} *erg cm*^{3} *s*$^{-1}$, and a lower flux, 3.3×10^{-13} *erg cm*^{3} *s*$^{-1}$, in 02/2015, while in 02/2018 it was measured as 4.9×10^{-13} *erg cm*^{3} *s*$^{-1}$. In the middle right panel of Figure 35 we also show an estimate of the detection limit for each spectrum. The broad Hβ is only well above this limit in the 02/2018 spectrum and possibly in 02/2015. Therefore, based on these spectra, the galaxy can be classified as a Seyfert 1.8. Within the uncertainties the Balmer decrements seems to be constant at a value of ~ 9.

3.3.3 The Link Between the X-ray Luminosity and the BELs

Comparing the middle and bottom panels of Figure 32, one can directly see a correlation between the intrinsic X-ray luminosity and the detection of the broad Hα component. The periods in which the broad component is detectable are the ones where L_{2-10} shows the highest values; the epochs when the galaxy is classified as a Seyfert 2 are those when closest available X-ray spectra show lower L_{2-10} values. Given that the X-ray and optical observations are not simultaneous, in order to quantify the correlation between the BELs and the X-ray luminosity we linearly interpolate the L_{2-10} curve (bottom panel of Figure 32) and attribute a L_{2-10} value for each historical optical spectrum. In Figure 36 we show the interpolated L_{2-10} value for each spectrum as function of the bi-modal Hα BEL detection.

From Figure 36, the link between the BEL and the X-ray luminosity is clear: at all epochs when an Hα BEL is detected, $L_{2-10} > 4 \times 10^{42}$ erg s^{-1}; conversely, when a Seyfert 2 spectrum

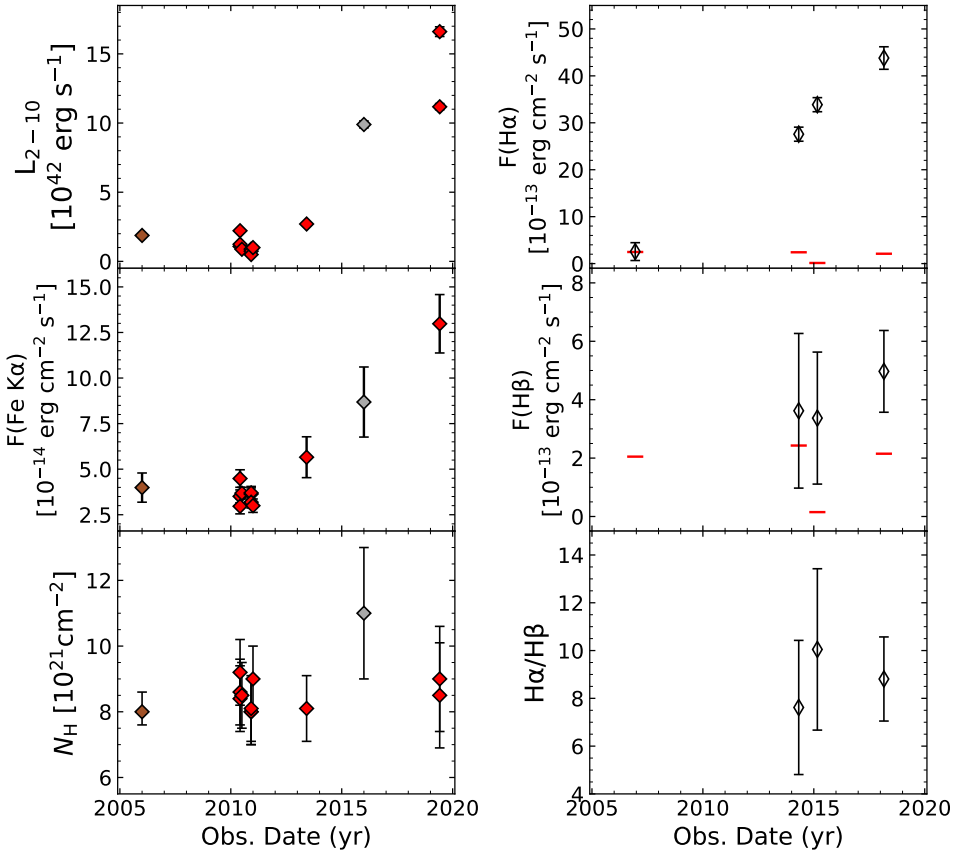

Figure 35 – X-ray (left) and optical (right) properties from 2005 to 2020. From top to bottom in the X-ray panels: Intrinsic 2-10 keV Luminosity (L_{2-10}), narrow Fe Kα line flux, and the column density (N_H). From top to bottom in the optical panels: Flux of the Hα BEL, the flux of the Hβ BEL, and the Balmer decrement (Hα/Hβ). In the optical panels, the red lines represent a lower limit for the detection of the lines, being measured as the flux of a line with a signal to noise ratio equal to 3.

is observed, $L_{2-10} < 4 \times 10^{42}$ erg s^{-1};. Moreover, from Figure 35 (top panels) and Figure 37 (top panel) we can see that for the modern spectra (2006-2018) the Hα BEL flux increases with the increase in the L_{2-10}. From the same figures, we can see that the transitions between Type 1.9 to Type 1.8 (i.e., the clear detection of the Hβ BEL) occurs between 10 - 15 $\times 10^{42}$ erg s^{-1}. It is possible that the oldest high Eddington Ratio optical observations did not detect the broad Hβ due to its faintness or lower signal to noise ratio.

Under some assumptions one can convert the transitional X-ray luminosity (4×10^{42} erg s^{-1}) into a Bolometric luminosity (L_{bol}) and than into Eddington ratio (λ_{Edd}), as follows:

$$\lambda_{Edd} = \frac{L_{bol}}{L_{Edd}} = \frac{[K_X(L_{2-10}) \pm \Delta K_X] \times L_{2-10}}{1.3 \times 10^{38}\ M_{BH}} \tag{31}$$

where K_X is the bolometric correction and ΔK_X is uncertainty in the bolometric correction (the intrinsic spread of the AGN population dominates this uncertainty). We use Duras et al. (2020) correction, which assumes values of $K_X(L_{2-10} = 4 \times 10^{42}$ erg s$^{-1}) = 15.64$ and $\Delta K_X = 0.37$ *dex*,

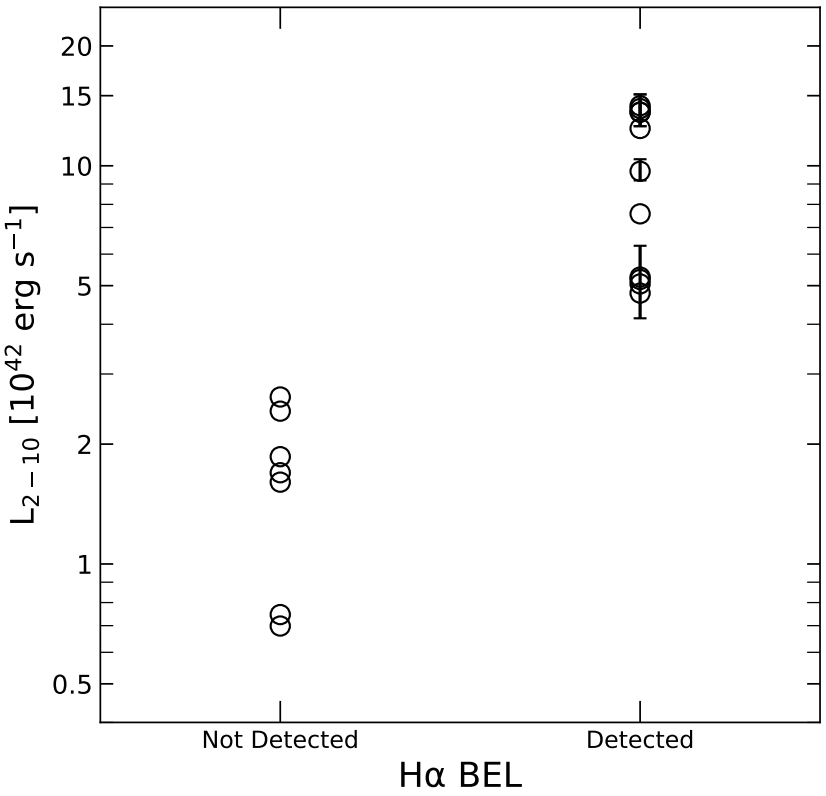

Figure 36 – Interpolated intrinsic 2-10 keV X-ray luminosity ($L_{2–10}$) for each optical spectrum as function of the detection or non-detection of the Hα BEL. Showing a clear lower boundary of $L_{2–10} \approx 4 \times 10^{42}$ erg s^{-1} for the detection of the component.

we can therefore estimate the Eddington ratio in which the transitions occurs as being:

$$\lambda_{Edd} \approx 2.0^{+2.0}_{-1.3} \times \left(\frac{3 \times 10^7\ M_\odot}{M_{BH}}\right)\ \% \tag{32}$$

where $\left(3 \times 10^7\ M_\odot\ /\ M_{BH}\right)$ is written as a systematic scaling factor to take into account the uncertainties in the black hole mass and the distinct values that can be considered (see section 3.2.4), since if we would have propagated it would dominate the λ_{Edd} uncertainty.

In summary, this analysis strongly supports the hypothesis that the CL phenomenon in NGC 2992 is caused by variations in the accretion rate and not due to changes in absorption nor due to TDEs (which we discard due to the several repeated CL events). The idea that the orientation-based Unification Models alone cannot explain the variety of AGNs, and that the specific accretion rate, as given by the Eddington ratio, is as essential as obscuration in the classification of the distinct AGN types, has been explored by several authors recently as we discussed in section 1.3.3.

We have shown that the variability in NGC 2992 is intrinsically driven by changes in accretion rate, and not due to variable obscuration. In this scenario, the CL events (i.e., the disappearing and reappearing of the BELs) can be due to two distinct effects:

- Dimming/brightening of the AGN continuum, which changes the supply of ionizing photons available to excite the gas in the immediate vicinity of the black hole and therefore the BLR. In this case, variations in the BEL fluxes are due to changes in the ionization state

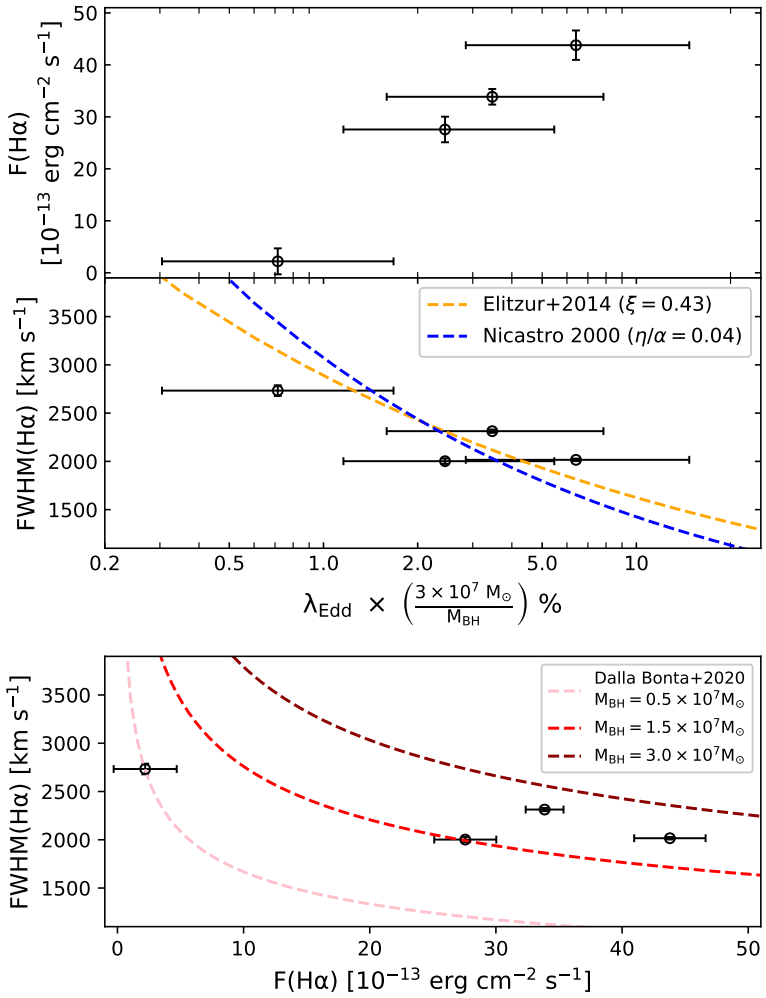

Figure 37 – Top: flux of Hα BEL as function of Eddington Ratio (λ_{Edd}), measured using equations 31 and 32, for each modern optical spectrum. Middle: FHWM of Hα BEL as function of λ_{Edd} for each modern optical spectrum. Blue and orange dashed lines are, respectively, are the best-fitting Nicastro (2000) and Elitzur et al. (2014) disk-wind models (see section 3.3.3 and equations 33 and 34). Bottom: FHWM of Hα broad as function of Hα BEL flux for for each modern optical spectrum. Each dashed line represent the Dalla Bonta et al. (2020) relation between the two parameters, assuming a constant Balmer decrement of 9 and Calzetti et al. (2000) extinction law, for distinct supermassive black hole masses (M_{BH}) in the range discussed in section 3.2.4.

of the BLR clouds and not to change in its geometry or structure (STORCHI-BERGMANN et al., 2003; SCHIMOIA et al., 2012; LAMASSA et al., 2015);

- The fading of the BLR structure itself as proposed by the disk-wind BLR models (see section 1.3.3), in which a low accretion rate is not able to sustain the required cloud flow rate (NICASTRO, 2000; TRUMP et al., 2011; ELITZUR et al., 2014), that makes up the BLR.

The first scenario is supported in the case of the double-peaked LINER/Seyfert 1 nucleus of NGC 1097, for which Storchi-Bergmann et al. (2003) and Schimoia et al. (2012) found an inverse correlation between the width of the Hα broad profile and the flux of the line, as well as for NGC 5548 by Peterson et al. (2002) and for the CL-Quasar SDSS J015957.64+003310.5 by LaMassa et al. (2015). The authors preferred explanation for this is the fact that, when the AGN is brightest, it ionizes farther out in the BLR, reaching lower velocity clouds, and the profile becomes narrower. When the AGN is dimmer, it ionizes only the closest regions, where the velocities are higher and the profile becomes wider, in agreement with a virialized BLR. In our data, there seems to be such a inverse correlation between FWHM(Hα) and F(Hα), in the modern optical spectra, as can be seen in the bottom panel of Figure 37.

However, in the second scenario, where the BLR is described as a disk-driven wind and not as clouds orbiting in Keplerian-like orbits, this inverse correlation is also predicted. Using distinct, prescriptions both Nicastro (2000) and Elitzur et al. (2014) show that with increasing accretion rate (which increases Hα BEL flux) the FWHM in the BLR decreases. In the Nicastro (2000) model, the relation between the two parameters is written as:

$$\log(\lambda_{Edd}) = -3\log(FWHM) + 9.86 + \log(\eta/\alpha) \tag{33}$$

where η/α is the ratio between the disk efficiency (η) and its viscosity (α), while Elitzur et al. (2014) use:

$$\log(\lambda_{Edd}) = -4\log(FWHM) + 3.60 + \log(M_{BH}) + \log(\xi) \tag{34}$$

where ξ is the ratio between the BLR radius (r_{BLR}) and the dust sublimation radius (R_d) with $\xi < 1.0$. The reader is referred to the original papers as well as to Nicastro et al. (2018) for detailed explanation of the models and equations. In the middle panel of Figure 37, we show both models with best-fitting parameters ($\eta/\alpha = 0.04$ and $\xi = 0.42$) for the measured Hα BEL FWHM and λ_{Edd}, measured from the interpolated L_{2-10} (Figure 36) using the above prescription (equations 31 and 32).

While we have successfully shown that the CL events in NGC 2992 are driven by changes in the accretion rate, we could not determine the true nature of the BEL variability, mainly because, as discussed, we still do not have a full understanding of the formation and evolution of the BLRs in AGNs. In the next section we discuss the overall state-of-art modeling of the innermost structure of CL-AGNs as well as a proposed technique to distinguish between the two above proposed scenario.

3.4 Discussion

In both the scenarios discussed on previous section, quick ($\sim$ 10 years between the maximum and the minimum activity) and large (a factor of $\sim$ 35 in L_{2-10}) variations in the accretion rate are necessary. However, the standard Shakura and Sunyaev (1973) accretion disk model does not support such variations as we discussed in section 1.2.2.

The Eddington ratio in which the BEL transitions occurs in NGC 2992 contains the critical value at which there is a state transition between a radiatively inefficient accretion flow (RIAF, see section 1.2.2) and a thin accretion disk $\lambda_{Edd} \sim 0.01$ (e.g., XIE; YUAN, 2012, see also 'Alternative accretion scenarios' in section 1.2.2). The similarity between these values suggests that NGC 2992 is operating at the threshold mass accretion rate between the two accretion modes. Indeed, Sniegowska et al. (2020) proposed an explanation for the sources displaying multiple quasi-periodic CL phenomena according to which they would be operating at a few per cent of the Eddington limit. They argue that the outbursts are caused by the radiation pressure instability operating in the narrow ring between the standard (SHAKURA; SUNYAEV, 1973) thin pressure dominated outer disk and the hot optically thin inner RIAF (YUAN; NARAYAN, 2014). The corresponding limit cycle is responsible for periodic outbursts, and the timescales are therefore much shorter than the standard viscous timescale due to the narrowness of the unstable radial zone.

Even with the possibility of such rapid variability in the accretion rate (given some of these alternatives to the classical accretion disk, e.g., section 1.2.2), the cause of the type transition remains uncertain, dimming of the ionizing source or fading of the BLR structure itself. By using radiative transfer Monte Carlo simulations to test the multiple causes of the CL phenomenon, Marin (2017) argues that the differences between these two scenarios can only be observable in polarized light: in the ionizing source dimming scenario, the polarization properties between the high and low flux state should be the same, while that for the BLR fading a decrease in the degree of polarization and a rotation in the polarization angle are expected in the low flux state. We had access to a spectropolarimetric observation of NGC 2992 obtained in 2006 (Robinson et al., in prep), when the galaxy was at a dim state (see Figure 32). In Figure 38 we show the polarization angle (top panel), the polarimetric spectrum (middle panel), and polarization degree as function of wavelength. The data shows no signs of BEL in the polarimetric spectrum (as well as in normal flux). To test Marin (2017) predictions, we would need recent (with the AGN at its bright state) observations. As this data is not available to us now, the exact intrinsic cause of the CL-AGN events in NGC 2992 is still an open question. We join these authors in advocating for systematic polarimetric observations of CL-AGN to understand their true nature fully.

In this sense, follow up observations of NGC 2992 in the next decades will continue to help constrain the physics of AGNs. Furthermore, this source joins several others in the literature that show that the accretion rate is a fundamental variable for any model that tries to unify the AGN zoology and that viewing angle or obscuration effects alone cannot fully explain differences seen in SMBH activity in galaxies. For now, in this chapter, we mapped the historical emission of this AGN, which after this work, is one of the very few known accretion rate-dependent CL-AGN.

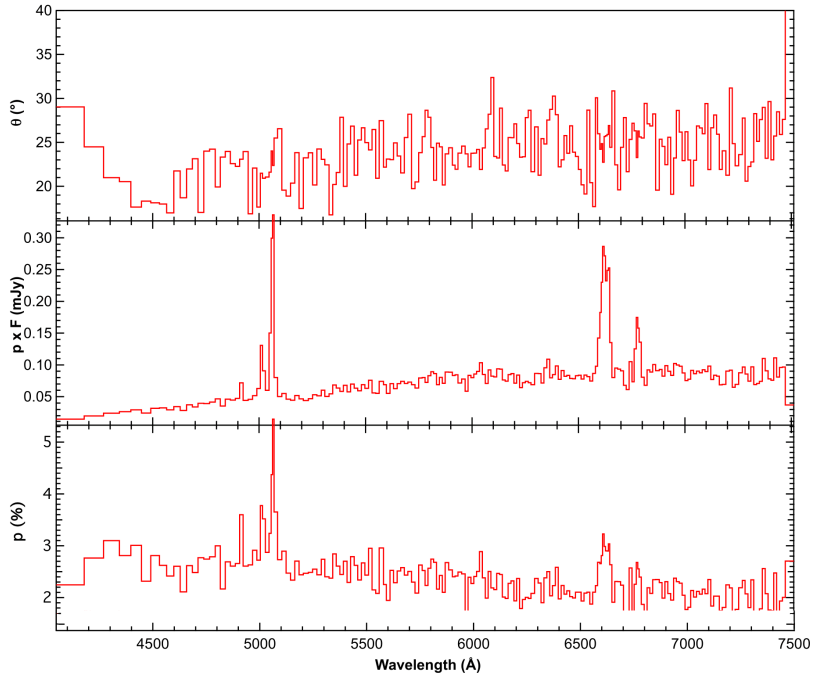

Figure 38 – Top: polarization angle (θ) as function of wavelength. Middle: Polarized spectra. Bottom: Polarization degree (p) in % of the total flux as function of wavelength. Figure kindly provided by Prof. Andrew Robinson in a private communication (Robinson et al, in prep.).

4 CONCLUSIONS AND FUTURE WORK

This dissertation has presented a multi-wavelength spatial and temporal analyses of the AGN in the interacting Seyfert galaxy NGC 2992. To spatially resolve the galaxy's circumnuclear region, we use optical spectra obtained with the GMOS IFU on the Gemini South telescope, with a spatial resolution of $\approx$ 120 pc and spectral resolution $\approx$ 40 k$m\,s^{-1}$. The main results are:

- The stellar population in the nuclear region of the galaxy is mainly composed (60%$\leq$ $x_O \leq$ 80%) by an old (t > 1.4 Gyr) metal-rich ($\langle Z \rangle_O \geq$ 2.0 $Z_\odot$) population with a smaller, but considerable contribution (10% $\leq x_Y \leq$ 30%) of an young (t < 100 Myr) metal-poor ($\langle Z \rangle_Y \leq$ 1.0 $Z_\odot$) population. A possible scenario is that metal-poor gas inflow during the pericentre passage of NGC 2993 has led to interaction-driven circumnuclear star formation, which can explain the presence of such young metal-poor stellar population in the nuclear region;

- The NLR presents two distinctly kinematical components: one that although disturbed is well fitted by a disk model, and therefore can be identified as gas following regular orbits in the galactic disk, with radial velocities ranging from -130 to 130 k$m\,s^{-1}$; another that we interpreted as an outflow associated with the radio emission, with blueshifted velocities of $\sim$ 200 k$m\,s^{-1}$, a mass outflow rate of $\dot{M}_{out} \approx 1.6 \pm 0.6\ M_\odot$ and a kinematic power of $\dot{E}_{out} \approx 2.2 \pm 0.3 \times 10^{40}$ erg s^{-1};

- The BPT diagnostic diagrams show the galaxy posses multiple ionization mechanisms: a mixture of AGN, star-formation and shocks, the former being the dominant one. The [O III]/Hβ ratio peaks at the innermost spaxels, and is located in the upper region of the BPT diagram. The lower values, located at the border of the FoV, decreases down to below the Kewley et al. (2001) line, showing an increase in the star-formation ionization compared to the AGN ionization at larger radius. Off-nuclear peaks in the [N II]/Hα and [S II]/Hα maps indicate the presence of another mechanism and are successfully explained by Sutherland et al. (2018) shock+precursor models.

Regarding the source's variability, we have explored its historical X-ray and optical spectra from 1978 to 2019, focusing mainly on its CL events. The main results are:

- The source presents large intrinsic X-ray luminosity variability, by a factor of $\sim$ 35, ranging from $4.9 \times 10^{41}\ erg\,s^{-1}$up to $1.7 \times 10^{43}\ erg\,s^{-1}$;

- The source presents several transitions between type 2 Seyfert to intermediate-type spectrum, losing and regaining its Hα BEL on timescales of several years;

- We ruled out TDEs or variable obscuration as causes of the type transitions. We show that the presence (and the flux) of the Hα BEL is directly correlated with the 2-10 keV X-ray luminosity: a minimum value of $L_{2-10} \approx 4 \times 10^{42}$ erg s^{-1} is necessary for its appearance. This value translates to a Eddington ratio of $2.0^{+2.0}_{-1.3}$%, if we assume $M_{BH} = 3 \times 10^7\ M_\odot$. Due to its faintness, the unambiguously detection of the Hβ BEL was only possible in the most recent spectrum, at even higher accretion rates of $\lambda_{Edd} \approx$ 5–8%;

- We find a correlation between the narrow Fe Kα flux and λ_{Edd}, and an anti-correlation between full width at half maximum of Hα BEL and λ_{Edd}, as predicted by the disk-wind BLR models.
- Two possible scenarios for type transitions are still open: either the dimming (brightening) of the AGN continuum luminosity, which reduces (increases) the supply of ionizing photons available to excite the gas in the immediate vicinity of the black hole or the disappearance of the BLR structure itself occurs as the low accretion efficiency is not able to sustain the required cloud flow rate in a disk-wind BLR model. Multi-epoch polarimetric observations may distinguish between the two scenarios.
- We added another object to the list of CL-AGNs, in particularly, one of the very few known to be accretion rate-dependent. Furthermore, this study supports the idea that the accretion rate is a fundamental variable in determining the observed AGN type, and therefore should be included in a more complete model to unify the AGN zoology.

This work shows the importance and the role of the local universe targets to the study of the AGN phenomena, in which the parsec scale structures can be resolved and public multi-wavelength (we have used here, radio, optical and X-ray data) and multi-epoch observations are available. Following, I list some ideas of studies that are being developed or can be developed based on this galaxy (system of galaxies) or applying similar approaches:

- Modern simulations of Arp 245 system are being developed/studied by another member of our group, focusing this time on gas inflows and interaction-driven star formation, since those were not the focus of Duc et al. (2000) work.
- IFU data of NGC 2993 would be very useful to probe the interaction's effects in the other object of the system, particularly with a large FoV IFU instrument such as MUSE.
- A spectropolarimetric observation of NGC 2992 at its high state, to compare with the one presented in Figure 38, allowing us to test Marin (2017) model.
- A similar re-examination of the entire literature, as we have done in chapter 3, to others well studied/sampled variable AGNs.

REFERENCES

ALLEN, Mark G.; DOPITA, Michael A.; TSVETANOV, Zlatan I.; SUTHERLAND, Ralph S. Physical Conditions in the Seyfert Galaxy NGC 2992. **The Astrophysical Journal**, v. 511, n. 2, p. 686–708, Feb. 1999a. DOI: 10.1086/306718. arXiv: astro-ph/9809123 [astro-ph].

ALLEN, Mark G.; DOPITA, Michael A.; TSVETANOV, Zlatan I.; SUTHERLAND, Ralph S. Physical Conditions in the Seyfert Galaxy NGC 2992. **The Astrophysical Journal**, v. 511, n. 2, p. 686–708, Feb. 1999b. DOI: 10.1086/306718. arXiv: astro-ph/9809123 [astro-ph].

ALLEN, Mark G.; GROVES, Brent A.; DOPITA, Michael A.; SUTHERLAND, Ralph S.; KEWLEY, Lisa J. The MAPPINGS III Library of Fast Radiative Shock Models. **The Astrophysical Journal Supplement Series**, v. 178, n. 1, p. 20–55, Sept. 2008. DOI: 10.1086/589652. arXiv: 0805.0204 [astro-ph].

ANDRILLAT, Y.; SOUFFRIN, S. Sur les Abondances et le Rougissement dans les Noyaux de Galaxies de Seyfert. **Astronomy and Astrophysics**, v. 11, p. 286, Mar. 1971.

ANTONUCCI; MILLER, J. S. Spectropolarimetry and the nature of NGC 1068. **The Astrophysical Journal**, v. 297, p. 621–632, Oct. 1985. DOI: 10.1086/163559.

ANTONUCCI, Robert. Astrophysics: Quasars still defy explanation. **Nature**, v. 495, n. 7440, p. 165–167, Mar. 2013. DOI: 10.1038/495165a.

ANTONUCCI, Robert. Unified models for active galactic nuclei and quasars. **Annual Review of Astronomy and Astrophysics**, v. 31, p. 473–521, Jan. 1993. DOI: 10.1146/annurev.aa.31.090193.002353.

ARETXAGA, Itziar; JOGUET, B.; KUNTH, D.; MELNICK, J.; TERLEVICH, R. J. Seyfert 1 Mutation of the Classical Seyfert 2 Nucleus NGC 7582. **The Astrophysical Journal**, IOP Publishing, v. 519, n. 2, p. l123–l126, July 1999. ISSN 0004-637X. DOI: 10.1086/312114. Available from: http://dx.doi.org/10.1086/312114.

AVNI, Y. Energy spectra of X-ray clusters of galaxies. **The Astrophysical Journal**, v. 210, p. 642–646, Dec. 1976. DOI: 10.1086/154870.

BACON, R. et al. The MUSE second-generation VLT instrument. In: MCLEAN, Ian S.; RAMSAY, Suzanne K.; TAKAMI, Hideki (Eds.). **Ground-based and Airborne Instrumentation for Astronomy III**. [S.l.: s.n.], July 2010. (Society of Photo-Optical Instrumentation Engineers (SPIE) Conference Series), p. 773508. DOI: 10.1117/12.856027.

BALDWIN, C.M.; MCDERMID, R. M.; KUNTSCHNER, H.; MARASTON, C.; CONROY, C. Comparison of stellar population model predictions using optical and infrared spectroscopy. **Monthly Notices of the Royal Astronomical Society**, v. 473, n. 4, p. 4698–4721, Feb. 2018. DOI: 10.1093/mnras/stx2502. arXiv: 1709.09300 [astro-ph.GA].

BALDWIN, J. A.; PHILLIPS, M. M.; TERLEVICH, R. Classification parameters for the emission-line spectra of extragalactic objects. **Publications of the Astronomical Society of the Pacific**, v. 93, p. 5–19, Feb. 1981. DOI: 10.1086/130766.

BARLOW, Roger. Asymmetric Errors. In: LYONS, L.; MOUNT, R.; REITMEYER, R. (Eds.). **Statistical Problems in Particle Physics, Astrophysics, and Cosmology**. [S.l.: s.n.], Jan. 2003a. P. 250. arXiv: physics/0401042 [physics.data-an].

BARLOW, Roger. **Asymmetric Statistical Errors**. [S.l.: s.n.], 2004. arXiv: physics/0406120 [physics.data-an].

BARLOW, Roger. Asymmetric Systematic Errors. **arXiv e-prints**, physics/0306138, physics/0306138, June 2003b. arXiv: physics/0306138 [physics.data-an].

BARRERA-BALLESTEROS, J. K. et al. Central star formation and metallicity in CALIFA interacting galaxies. **Astronomy and Astrophysics**, v. 579, A45, a45, July 2015. DOI: 10.1051/0004-6361/201425397. arXiv: 1505.03153 [astro-ph.GA].

BERTOLA, F.; BETTONI, D.; DANZIGER, J.; SADLER, E.; SPARKE, L.; DE ZEEUW, T. Testing the gravitational field in elliptical galaxies - NGC 5077. **The Astrophysical Journal**, v. 373, p. 369–390, June 1991. DOI: 10.1086/170058.

BIANCHI, Stefano; PICONCELLI, Enrico; CHIABERGE, Marco; BAIL ON, Elena Jim enez; MATT, Giorgio; FIORE, Fabrizio. How Complex is the Obscuration in Active Galactic Nuclei? New Clues from the Suzaku Monitoring of the X-Ray Absorbers in NGC 7582. **The Astrophysical Journal**, v. 695, n. 1, p. 781–787, Apr. 2009. DOI: 10.1088/0004-637X/695/1/781. arXiv: 0901.1973 [astro-ph.GA].

BICA, E.; ALLOIN, D. A base of star clusters for stellar population synthesis. **Astronomy and Astrophysics**, v. 162, p. 21–31, July 1986.

BISNOVATYI-KOGAN, G. S.; LOVELACE, R. V. E. Advective accretion disks and related problems including magnetic fields. **Nature**, v. 45, n. 11-12, p. 663–742, Dec. 2001. DOI: 10.1016/S1387-6473(01)00146-4. arXiv: astro-ph/0207625 [astro-ph].

BLANDFORD. Black Holes and Relativistic Jets. **Progress of Theoretical Physics Supplement**, v. 143, p. 182–201, Jan. 2001. DOI: 10.1143/PTPS.143.182. arXiv: astro-ph/0110394 [astro-ph].

BLOCK, Adam. **Caelum-Observatory:NGC2992**. [S.l.], 2011. Available from: http://www.caelumobservatory.com/gallery/n2992.shtml.

BLUMENTHAL, K. A.; BARNES, J. E. Go with the Flow: Understanding inflow mechanisms in galaxy collisions. **Monthly Notices of the Royal Astronomical Society**, v. 479, p. 3952–3965, Sept. 2018. DOI: 10.1093/mnras/sty1605. arXiv: 1806.05132.

BOLTON. Identification of Cygnus X-1 with HDE 226868. **Nature**, v. 235, n. 5336, p. 271–273, Feb. 1972. DOI: 10.1038/235271b0.

BOLTON; STANLEY, G. J. Observations on the Variable Source of Cosmic Radio Frequency Radiation in the Constellation of Cygnus. **Australian Journal of Scientific Research A Physical Sciences**, v. 1, p. 58, Mar. 1948. DOI: 10.1071/PH480058.

BRUZUAL, G.; CHARLOT, S. Stellar population synthesis at the resolution of 2003. **Monthly Notices of the Royal Astronomical Society**, v. 344, p. 1000–1028, Oct. 2003. DOI: 10.1046/j.1365-8711.2003.06897.x. eprint: astro-ph/0309134.

BULLOCK, James S.; BOYLAN-KOLCHIN, Michael. Small-Scale Challenges to the ΛCDM Paradigm. **Annual Review of Astronomy and Astrophysics**, v. 55, n. 1, p. 343–387, Aug. 2017. DOI: 10.1146/annurev-astro-091916-055313. arXiv: 1707.04256 [astro-ph.CO].

BUNDY, Kevin et al. Overview of the SDSS-IV MaNGA Survey: Mapping nearby Galaxies at Apache Point Observatory. **The Astrophysical Journal**, v. 798, n. 1, 7, p. 7, Jan. 2015. DOI: 10.1088/0004-637X/798/1/7. arXiv: 1412.1482 [astro-ph.GA].

BUSKO, I. C.; STEINER, J. E. Profiles of emission lines in active galactic nuclei. III. Observations of Hα, [N II] and [S II] profiles. **Monthly Notices of the Royal Astronomical Society**, v. 245, p. 470, Aug. 1990.

CALZETTI, D.; ARMUS, L.; BOHLIN, R. C.; KINNEY, A. L.; KOORNNEEF, J.; STORCHI-BERGMANN, T. The Dust Content and Opacity of Actively Star-forming Galaxies. **The Astrophysical Journal**, v. 533, p. 682–695, Apr. 2000. DOI: 10.1086/308692. eprint: astro-ph/9911459.

CAPPELLARI, M.; COPIN, Y. Adaptive spatial binning of integral-field spectroscopic data using Voronoi tessellations. **Monthly Notices of the Royal Astronomical Society**, v. 342, p. 345–354, June 2003. DOI: 10.1046/j.1365-8711.2003.06541.x. eprint: astro-ph/0302262.

CARDELLI, J. A.; CLAYTON, G. C.; MATHIS, J. S. The relationship between infrared, optical, and ultraviolet extinction. **The Astrophysical Journal**, v. 345, p. 245–256, Oct. 1989. DOI: 10.1086/167900.

CARDOSO, Leandro S. M.; GOMES, Jean Michel; PAPADEROS, Polychronis. Impact of an AGN featureless continuum on estimation of stellar population properties. **Astronomy and Astrophysics**, v. 604, A99, a99, Aug. 2017. DOI: 10.1051/0004-6361/201630378. arXiv: 1705.04224 [astro-ph.GA].

CHABRIER, G. Galactic Stellar and Substellar Initial Mass Function. **Publications of the Astronomical Society of the Pacific**, v. 115, p. 763–795, July 2003. DOI: 10.1086/376392. eprint: astro-ph/0304382.

CHAPMAN, S. C.; MORRIS, S. L.; ALONSO-HERRERO, A.; FALCKE, H. Adaptive optics near-infrared imaging of NGC 2992 - unveiling core structures related to radio figure-of-8 loops. **Monthly Notices of the Royal Astronomical Society**, v. 314, p. 263–272, May 2000. DOI: 10.1046/j.1365-8711.2000.03303.x. eprint: astro-ph/9908222.

CHEN, X. Y.; LIANG, Y. C.; HAMMER, F.; PRUGNIEL, Ph.; ZHONG, G. H.; RODRIGUES, M.; ZHAO, Y. H.; FLORES, H. Comparing six evolutionary population synthesis models by performing spectral synthesis for galaxies. **Astronomy and Astrophysics**, EDP Sciences, v. 515, a101, June 2010. ISSN 1432-0746. DOI: 10.1051/0004-6361/200913894. Available from: http://dx.doi.org/10.1051/0004-6361/200913894.

CID FERNANDES; GONZLEZ DELGADO, Rosa M. Testing spectral models for stellar populations with star clusters - I. Methodology. **Monthly Notices of the Royal Astronomical Society**, v. 403, n. 2, p. 780–796, Apr. 2010. DOI: 10.1111/j.1365-2966.2009.16153.x. arXiv: 0912.0410 [astro-ph.CO].

CID FERNANDES; GU, Q.; MELNICK, J.; TERLEVICH, E.; TERLEVICH, R.; KUNTH, D.; RODRIGUES LACERDA, R.; JOGUET, B. The star formation history of Seyfert 2 nuclei. **Monthly Notices of the Royal Astronomical Society**, v. 355, n. 1, p. 273–296, Nov. 2004. DOI: 10.1111/j.1365-2966.2004.08321.x. arXiv: astro-ph/0408483 [astro-ph].

CID FERNANDES; MATEUS, A.; SODR E, L.; STASI NSKA, G.; GOMES, J. M. Semi-empirical analysis of Sloan Digital Sky Survey galaxies - I. Spectral synthesis method. **Monthly Notices of the Royal Astronomical Society**, v. 358, p. 363–378, Apr. 2005a. DOI: 10.1111/j.1365-2966.2005.08752.x. eprint: astro-ph/0412481.

CID FERNANDES; MATEUS, A.; SODR E, L.; STASI NSKA, G.; GOMES, J. M. Semi-empirical analysis of Sloan Digital Sky Survey galaxies - I. Spectral synthesis method. **Monthly Notices of the Royal Astronomical Society**, v. 358, p. 363–378, Apr. 2005b. DOI: 10.1111/j.1365-2966.2005.08752.x. eprint: astro-ph/0412481.

CID FERNANDES, R. On tests of full spectral fitting algorithms. **Monthly Notices of the Royal Astronomical Society**, v. 480, n. 4, p. 4480–4488, Nov. 2018. DOI: 10.1093/mnras/sty2012.

CID FERNANDES, R.; STASINSKA, G.; MATEUS, A.; VALE ASARI, N. A comprehensive classification of galaxies in the Sloan Digital Sky Survey: how to tell true from fake AGN? **Monthly Notices of the Royal Astronomical Society**, v. 413, n. 3, p. 1687–1699, May 2011. DOI: 10.1111/j.1365-2966.2011.18244.x. arXiv: 1012.4426 [astro-ph.CO].

CID FERNANDES, R. et al. Resolving galaxies in time and space. I. Applying STARLIGHT to CALIFA datacubes. **Astronomy and Astrophysics**, v. 557, A86, a86, Sept. 2013. DOI: 10.1051/0004-6361/201220616. arXiv: 1304.5788 [astro-ph.CO].

COHEN, Ross D.; RUDY, Richard J.; PUETTER, R. C.; AKE, T. B.; FOLTZ, Craig B. Variability of Markarian 1018: Seyfert 1.9 to Seyfert 1. **The Astrophysical Journal**, v. 311, p. 135, Dec. 1986. DOI: 10.1086/164758.

COLINA, L.; FRICKE, K. J.; KOLLATSCHNY, W.; PERRYMAN, M. A. C. Extended emission line regions in nearby Seyfert galaxies. I. NGC 2992. **Astronomy and Astrophysics**, v. 178, p. 51–61, May 1987.

COMBES, F. et al. ALMA reveals the feeding of the Seyfert 1 nucleus in NGC 1566. **Astronomy and Astrophysics**, EDP Sciences, v. 565, a97, May 2014. ISSN 1432-0746. DOI: 10.1051/0004-6361/201423433. Available from: http://dx.doi.org/10.1051/0004-6361/201423433.

CONROY, Charlie. Modeling the Panchromatic Spectral Energy Distributions of Galaxies. **Annual Review of Astronomy and Astrophysics**, Annual Reviews, v. 51, n. 1, p. 393–455, July 2013. ISSN 1545-4282. DOI: 10.1146/annurev-astro-082812-141017. Available from: http://dx.doi.org/10.1146/annurev-astro-082812-141017.

COOKE, B. A. et al. The Ariel V (SSI) catalogue of high galactic latitude (. **Monthly Notices of the Royal Astronomical Society**, v. 182, p. 489–515, Feb. 1978. DOI: 10.1093/mnras/182.3.489.

CORRAL, A.; DELLA CECA, R.; CACCIANIGA, A.; SEVERGNINI, P.; BRUNNER, H.; CARRERA, F. J.; PAGE, M. J.; SCHWOPE, A. D. The X-ray spectral properties of the AGN population in the XMM-Newton bright serendipitous survey. **Astronomy and Astrophysics**, v. 530, A42, a42, June 2011. DOI: 10.1051/0004-6361/201015227. arXiv: 1104.2173 [astro-ph.CO].

COSTA, Tiago; ROSDAHL, Joakim; SIJACKI, Debora; HAEHNELT, Martin G. Quenching star formation with quasar outflows launched by trapped IR radiation. **Monthly Notices of the Royal Astronomical Society**, v. 479, n. 2, p. 2079–2111, Sept. 2018. DOI: 10.1093/mnras/sty1514. arXiv: 1709.08638 [astro-ph.GA].

COUTO, Guilherme S.; STORCHI-BERGMANN, Thaisa; SCHNORR-MULLER, Allan. Gas rotation, shocks and outflow within the inner 3 kpc of the radio galaxy 3C 33. **Monthly Notices of the Royal Astronomical Society**, v. 469, n. 2, p. 1573–1586, Aug. 2017. DOI: 10.1093/mnras/stx962. arXiv: 1704.06343 [astro-ph.GA].

CRENSHAW, D. Michael; FISCHER, Travis C.; KRAEMER, Steven B.; SCHMITT, Henrique R. Feedback from Mass Outflows in Nearby Active Galactic Nuclei. II. Outflows in the Narrow-line Region of NGC 4151. **The Astrophysical Journal**, v. 799, n. 1, 83, p. 83, Jan. 2015. DOI: 10.1088/0004-637X/799/1/83. arXiv: 1411.4507 [astro-ph.GA].

CROTON, D. J. et al. The many lives of active galactic nuclei: cooling flows, black holes and the luminosities and colours of galaxies. **Monthly Notices of the Royal Astronomical Society**, v. 365, p. 11–28, Jan. 2006. DOI: 10.1111/j.1365-2966.2005.09675.x. eprint: astro-ph/0508046.

D'AGOSTINO, Joshua J; POETRODJOJO, Henry; HO, I-Ting; GROVES, Brent; KEWLEY, Lisa; MADORE, Barry F; RICH, Jeff; SEIBERT, Mark. Starburst–AGN mixing: TYPHOON observations of NGC 1365, NGC 1068, and the effect of spatial resolution on the AGN fraction. **Monthly Notices of the Royal Astronomical Society**, Oxford University Press (OUP), v. 479, n. 4, p. 4907–4935, June 2018. ISSN 1365-2966. DOI: 10.1093/mnras/sty1676. Available from: http://dx.doi.org/10.1093/mnras/sty1676.

DAI, Xinyu; CHARTAS, George; ERACLEOUS, Michael; GARMIRE, Gordon P. A Study of Quasar Evolution in the X-Ray Band with the Aid of Gravitational Lensing. **The Astrophysical Journal**, IOP Publishing, v. 605, n. 1, p. 45–57, Apr. 2004. ISSN 1538-4357. DOI: 10.1086/382205. Available from: http://dx.doi.org/10.1086/382205.

DALCANTON, Julianne J. The Metallicity of Galaxy Disks: Infall versus Outflow. **The Astrophysical Journal**, IOP Publishing, v. 658, n. 2, p. 941–959, Apr. 2007. DOI: 10.1086/508913. Available from: https://doi.org/10.10862F508913.

DALLA BONTA et al. **The Sloan Digital Sky Survey Reverberation Mapping Project: Estimating Masses of Black Holes in Quasars with Single-Epoch Spectroscopy**. [S.l.: s.n.], 2020. arXiv: 2007.02963 [astro-ph.GA].

DAMETTO, Natacha Z. et al. A SINFONI view of the nuclear activity and circumnuclear star formation in NGC 4303 - II. Spatially resolved stellar populations. **Monthly Notices of the Royal Astronomical Society**, v. 482, n. 4, p. 4437–4453, Feb. 2019. DOI: 10.1093/mnras/sty2996. arXiv: 1811.01875 [astro-ph.GA].

DAVIES, Rebecca L.; KEWLEY, Lisa J.; HO, I. -Ting; DOPITA, Michael A. Starburst-AGN mixing - II. Optically selected active galaxies. **Monthly Notices of the Royal Astronomical Society**, v. 444, n. 4, p. 3961–3974, Nov. 2014a. DOI: 10.1093/mnras/stu1740. arXiv: 1408.5888 [astro-ph.GA].

DAVIES, Rebecca L.; RICH, Jeffrey A.; KEWLEY, Lisa J.; DOPITA, Michael A. Starburst-AGN mixing - I. NGC 7130. **Monthly Notices of the Royal Astronomical Society**, v. 439, n. 4, p. 3835–3846, Apr. 2014b. DOI: 10.1093/mnras/stu234. arXiv: 1402.0493 [astro-ph.GA].

DAVIES, Rebecca L. et al. Dissecting galaxies: separating star formation, shock excitation and AGN activity in the central region of NGC 613. **Monthly Notices of the Royal Astronomical Society**, Oxford University Press (OUP), v. 470, n. 4, p. 4974–4988, June 2017. ISSN 1365-2966. DOI: 10.1093/mnras/stx1559. Available from: http://dx.doi.org/10.1093/mnras/stx1559.

DAVIES, Rebecca L. et al. Dissecting galaxies: spatial and spectral separation of emission excited by star formation and AGN activity. **Monthly Notices of the Royal Astronomical Society**, Oxford University Press (OUP), v. 462, n. 2, p. 1616–1629, July 2016. ISSN 1365-2966. DOI: 10.1093/mnras/stw1754. Available from: http://dx.doi.org/10.1093/mnras/stw1754.

DELGADO, Rosa M. Gonzalez; HECKMAN, Timothy; LEITHERER, Claus. The Nuclear and Circumnuclear Stellar Population in Seyfert 2 Galaxies: Implications for the Starburst–Active Galactic Nucleus Connection. **The Astrophysical Journal**, IOP Publishing, v. 546, n. 2, p. 845–865, Jan. 2001. DOI: 10.1086/318295. Available from: https://doi.org/10.10862F318295.

DENNEY, K. D. et al. THE TYPECASTING OF ACTIVE GALACTIC NUCLEI: Mrk 590 NO LONGER FITS THE ROLE. **The Astrophysical Journal**, IOP Publishing, v. 796, n. 2, p. 134, Nov. 2014. ISSN 1538-4357. DOI: 10.1088/0004-637x/796/2/134. Available from: http://dx.doi.org/10.1088/0004-637X/796/2/134.

DEXTER, Jason; BEGELMAN, Mitchell C. Extreme AGN variability: evidence of magnetically elevated accretion? **Monthly Notices of the Royal Astronomical Society: Letters**, Oxford University Press (OUP), v. 483, n. 1, p. l17–l21, Nov. 2018. ISSN 1745-3933. DOI: 10.1093/mnrasl/sly213. Available from: http://dx.doi.org/10.1093/mnrasl/sly213.

DI MATTEO, T.; SPRINGEL, V.; HERNQUIST, L. Energy input from quasars regulates the growth and activity of black holes and their host galaxies. **Nature**, v. 433, p. 604–607, Feb. 2005. DOI: 10.1038/nature03335. eprint: astro-ph/0502199.

DOKUCHAEV, V. I.; EROSHENKO, Yu. N.; RUBIN, S. G. Origin of supermassive black holes. **arXiv e-prints**, arXiv:0709.0070, arxiv:0709.0070, Sept. 2007. arXiv: 0709.0070 [astro-ph].

DOPITA, M. A. Spectral Signatures of Jet-Driven Shocks in Active Galactic Nuclei. In: HENNEY, William J.; STEFFEN, Wolfgang; BINETTE, Luc; RAGA, Alejandro (Eds.). **Revista Mexicana de Astronomia y Astrofisica Conference Series**. [S.l.: s.n.], June 2002. (Revista Mexicana de Astronomia y Astrofisica Conference Series), p. 177–182.

DOPITA, Michael A. et al. Probing the Physics of Narrow Line Regions in Active Galaxies. II. The Siding Spring Southern Seyfert Spectroscopic Snapshot Survey (S7). **The Astrophysical Journal Supplement Series**, v. 217, n. 1, 12, p. 12, Mar. 2015. DOI: 10.1088/0067-0049/217/1/12. arXiv: 1501.02022 [astro-ph.GA].

DUC, P.-A.; BRINKS, E.; SPRINGEL, V.; PICHARDO, B.; WEILBACHER, P.; MIRABEL, I. F. Formation of a Tidal Dwarf Galaxy in the Interacting System Arp 245 (NGC 2992/93). **The Astronomical Journal**, IOP Publishing, v. 120, n. 3, p. 1238–1264, Sept. 2000. DOI: 10.1086/301516. Available from: https://doi.org/10.10862F301516.

DURAS, F. et al. Universal bolometric corrections for active galactic nuclei over seven luminosity decades. **Astronomy and Astrophysics**, EDP Sciences, v. 636, a73, Apr. 2020. ISSN 1432-0746. DOI: 10.1051/0004-6361/201936817. Available from: http://dx.doi.org/10.1051/0004-6361/201936817.

DURRET, F.; BERGERON, J. Long slit spectroscopy of emission line galaxies. I. The sample. **Astronomy and Astrophysics Supplement Series**, v. 75, p. 273–297, Oct. 1988.

EDGE, D. O.; SHAKESHAFT, J. R.; MCADAM, W. B.; BALDWIN, J. E.; ARCHER, S. A survey of radio sources at a frequency of 159 Mc/s. **Monthly Notices of the Royal Astronomical Society**, v. 68, p. 37–60, Jan. 1959.

EINSTEIN, A. Die Grundlage der allgemeinen Relativitatstheorie. **Annalen der Physik**, v. 354, n. 7, p. 769–822, Jan. 1916. DOI: 10.1002/andp.19163540702.

ELITZUR, Moshe. ON THE UNIFICATION OF ACTIVE GALACTIC NUCLEI. **The Astrophysical Journal**, IOP Publishing, v. 747, n. 2, p. l33, Feb. 2012. ISSN 2041-8213. DOI: 10.1088/2041-8205/747/2/l33. Available from: http://dx.doi.org/10.1088/2041-8205/747/2/L33.

ELITZUR, Moshe; HO, Luis C. ON THE DISAPPEARANCE OF THE BROAD-LINE REGION IN LOW-LUMINOSITY ACTIVE GALACTIC NUCLEI. **The Astrophysical Journal**, IOP Publishing, v. 701, n. 2, p. l91–l94, July 2009. ISSN 1538-4357. DOI: 10.1088/0004-637x/701/2/191. Available from: http://dx.doi.org/10.1088/0004-637X/701/2/L91.

ELITZUR, Moshe; HO, Luis C.; TRUMP, Jonathan R. Evolution of broad-line emission from active galactic nuclei. **Monthly Notices of the Royal Astronomical Society**, v. 438, n. 4, p. 3340–3351, Mar. 2014. DOI: 10.1093/mnras/stt2445. arXiv: 1312.4922 [astro-ph.GA].

ELITZUR, Moshe; SHLOSMAN, Isaac. The AGN-obscuring Torus: The End of the "Doughnut" Paradigm? **The Astrophysical Journal Letters**, v. 648, n. 2, p. l101–l104, Sept. 2006. DOI: 10.1086/508158. arXiv: astro-ph/0605686 [astro-ph].

ELLISON, S. L.; PATTON, D. R.; MENDEL, J. T.; SCUDDER, J. M. Galaxy pairs in the Sloan Digital Sky Survey - IV. Interactions trigger active galactic nuclei. **Monthly Notices of the Royal Astronomical Society**, v. 418, p. 2043–2053, Dec. 2011. DOI: 10.1111/j.1365-2966.2011.19624.x. arXiv: 1108.2711.

ELLISON, Sara; MENDEL, J. Trevor; PATTON, David R.; SCUDDER, Jillian M. Galaxy pairs in the Sloan Digital Sky Survey - VIII. The observational properties of post-merger galaxies. **Monthly Notices of the Royal Astronomical Society**, v. 435, n. 4, p. 3627–3638, Nov. 2013. DOI: 10.1093/mnras/stt1562. arXiv: 1308.3707 [astro-ph.CO].

ENGLMAIER, Peter; SHLOSMAN, Isaac. Dynamical oupling of Nested Bars: Self-gravitating Gaseous Nuclear Bars. **The Astrophysical Journal**, IOP Publishing, v. 617, n. 2, p. l115–l118, Nov. 2004. DOI: 10.1086/427280. Available from: https://doi.org/10.10862F427280.

ERACLEOUS, Michael; HALPERN, Jules P. NGC 3065: A Certified LINER with Broad, Variable Balmer Lines. **The Astrophysical Journal**, IOP Publishing, v. 554, n. 1, p. 240–244, June 2001. DOI: 10.1086/321331. Available from: https://doi.org/10.10862F321331.

ERACLEOUS, Michael; LIVIO, Mario; HALPERN, Jules P.; STORCHI-BERGMANN, Thaisa. Elliptical Accretion Disks in Active Galactic Nuclei. **The Astrophysical Journal**, v. 438, p. 610, Jan. 1995. DOI: 10.1086/175104.

EVENT HORIZON TELESCOPE COLLABORATION et al. First M87 Event Horizon Telescope Results. I. The Shadow of the Supermassive Black Hole. **The Astrophysical Journal Letters**, v. 875, n. 1, L1, p. l1, Apr. 2019. DOI: 10.3847/2041-8213/ab0ec7. arXiv: 1906.11238 [astro-ph.GA].

FAN, Lulu; HAN, Yunkun; FANG, Guanwen; GAO, Ying; ZHANG, Dandan; JIANG, Xiaoming; WU, Qiaoqian; YANG, Jun; LI, Zhao. The Most Luminous Heavily Obscured Quasars Have a High Merger Fraction: Morphological Study of WISE-selected Hot Dust-obscured Galaxies. **The Astrophysical Journal Letters**, v. 822, n. 2, L32, p. l32, May 2016. DOI: 10.3847/2041-8205/822/2/L32. arXiv: 1605.00661 [astro-ph.GA].

FARDAL, M. A.; KATZ, N.; WEINBERG, D. H.; DAVE, R. On the evolutionary history of stars and their fossil mass and light. **Monthly Notices of the Royal Astronomical Society**, Oxford University Press (OUP), v. 379, n. 3, p. 985–1002, July 2007. ISSN 1365-2966. DOI: 10.1111/j.1365-2966.2007.11522.x. Available from: http://dx.doi.org/10.1111/j.1365-2966.2007.11522.x.

FATH, Edward Arthur. The spectra of some spiral nebulae and globular star clusters. **Lick Observatory Bulletin**, v. 149, p. 71–77, Jan. 1909. DOI: 10.5479/ADS/bib/1909LicOB.5.71F.

FAUSNAUGH, M. M. A New Approach to the Internal Calibration of Reverberation-Mapping Spectra. **Publications of the Astronomical Society of the Pacific**, IOP Publishing, v. 129, n. 972, p. 024007, Jan. 2017. ISSN 1538-3873. DOI: 10.1088/1538-3873/129/972/024007. Available from: http://dx.doi.org/10.1088/1538-3873/129/972/024007.

FERR E-MATEU, A.; VAZDEKIS, A.; TRUJILLO, I.; S ANCHEZ-BL AZQUEZ, P.; RICCIARDELLI, E.; DE LA ROSA, I. G. Young ages and other intriguing properties of massive compact galaxies in the local Universe. **Monthly Notices of the Royal Astronomical Society**, v. 423, n. 1, p. 632–646, June 2012. DOI: 10.1111/j.1365-2966.2012.20897.x. arXiv: 1203.2623 [astro-ph.CO].

FERRARESE, Laura; MERRITT, David. A Fundamental Relation between Supermassive Black Holes and Their Host Galaxies. **The Astrophysical Journal Letters**, v. 539, n. 1, p. l9–l12, Aug. 2000. DOI: 10.1086/312838. arXiv: astro-ph/0006053 [astro-ph].

FIORE, F. et al. AGN wind scaling relations and the co-evolution of black holes and galaxies. **Astronomy and Astrophysics**, v. 601, A143, a143, May 2017. DOI: 10.1051/0004-6361/201629478. arXiv: 1702.04507 [astro-ph.GA].

FISCHER, Travis C. et al. Hubble Space Telescope Observations of Extended [O III]λ 5007 Emission in Nearby QSO2s: New Constraints on AGN Host Galaxy Interaction. **The Astrophysical Journal**, v. 856, n. 2, 102, p. 102, Apr. 2018. DOI: 10.3847/1538-4357/aab03e. arXiv: 1802.06184 [astro-ph.GA].

FORD, Holland C. et al. Narrowband HST Images of M87: Evidence for a Disk of Ionized Gas around a Massive Black Hole. **The Astrophysical Journal Letters**, v. 435, p. l27, Nov. 1994. DOI: 10.1086/187586.

FRANK, J.; KING, A.; RAINE, D. J. **Accretion Power in Astrophysics: Third Edition**. [S.l.: s.n.], Jan. 2002. P. 398.

FREUND, J. How many spectral lines are statistically significant? **Annalen Der Physik - ANN PHYS-BERLIN**, v. 504, p. 380–385, Jan. 1992. DOI: 10.1002/andp.19925040508.

FRIEDRICH, S.; DAVIES, R. I.; HICKS, E. K. S.; ENGEL, H.; MÜLLER-SÁNCHEZ, F.; GENZEL, R.; TACCONI, L. J. Adaptive optics near infrared integral field spectroscopy of NGC 2992. **Astronomy and Astrophysics**, EDP Sciences, v. 519, a79, Sept. 2010. ISSN 1432-0746. DOI: 10.1051/0004-6361/200913924. Available from: http://dx.doi.org/10.1051/0004-6361/200913924.

GARCA-LORENZO, B.; ARRIBAS, S.; MEDIAVILLA, E. Stellar and ionized gas kinematics of the interacting Seyfert 1.9 galaxy <ASTROBJ>NGC 2992</ASTROBJ>. **Astronomy and Astrophysics**, v. 378, p. 787–799, Nov. 2001. DOI: 10.1051/0004-6361:20011243.

GARCIA-LORENZO, B.; ARRIBAS, F.; MEDIAVILLA, E. Stellar and ionized gas kinematics of the interacting Seyfert 1.9 galaxy <ASTROBJ>NGC 2992</ASTROBJ>. **Astronomy and Astrophysics**, v. 378, p. 787–799, Nov. 2001. DOI: 10.1051/0004-6361:20011243.

GE, Junqiang; MAO, Shude; LU, Youjun; CAPPELLARI, Michele; YAN, Renbin. Recovering stellar population parameters via different population models and stellar libraries. **Monthly Notices of the Royal Astronomical Society**, Oxford University Press (OUP), v. 485, n. 2, p. 1675–1693, Feb. 2019. ISSN 1365-2966. DOI: 10.1093/mnras/stz418. Available from: http://dx.doi.org/10.1093/mnras/stz418.

GEBHARDT, Karl et al. A Relationship between Nuclear Black Hole Mass and Galaxy Velocity Dispersion. **The Astrophysical Journal Letters**, v. 539, n. 1, p. l13–l16, Aug. 2000. DOI: 10.1086/312840. arXiv: astro-ph/0006289 [astro-ph].

GENZEL, R.; SCHODEL, R.; OTT, T.; ECKART, A.; ALEXANDER, T.; LACOMBE, F.; ROUAN, D.; ASCHENBACH, B. Near-infrared flares from accreting gas around the supermassive black hole at the Galactic Centre. **Nature**, v. 425, n. 6961, p. 934–937, Oct. 2003. DOI: 10.1038/nature02065. arXiv: astro-ph/0310821 [astro-ph].

GHEZ, A. M.; KLEIN, B. L.; MORRIS, M.; BECKLIN, E. E. High Proper-Motion Stars in the Vicinity of Sagittarius A*: Evidence for a Supermassive Black Hole at the Center of Our Galaxy. **The Astrophysical Journal**, v. 509, n. 2, p. 678–686, Dec. 1998. DOI: 10.1086/306528. arXiv: astro-ph/9807210 [astro-ph].

GIERLI NSKI, Marek; NIKOŁAJUK, Marek; CZERNY, Bożena. High-frequency X-ray variability as a mass estimator of stellar and supermassive black holes. **Monthly Notices of the Royal Astronomical Society**, v. 383, n. 2, p. 741–749, Jan. 2008. DOI: 10.1111/j.1365-2966.2007.12584.x. arXiv: 0710.1566 [astro-ph].

GILLI, R.; MAIOLINO, R.; MARCONI, A.; RISALITI, G.; DADINA, M.; WEAVER, K. A.; COLBERT, E. J. M. The variability of the Seyfert galaxy NGC 2992: the case for a revived AGN. **Astronomy and Astrophysics**, v. 355, p. 485–498, Mar. 2000. eprint: astro-ph/0001107.

GLIKMAN, Eilat; SIMMONS, Brooke; MAILLY, Madeline; SCHAWINSKI, Kevin; URRY, C. M.; LACY, M. **Major Mergers Host the Most Luminous Red Quasars at z 2: A Hubble Space Telescope WFC3/IR Study**. [S.l.: s.n.], 2015. arXiv: 1504.02111 [astro-ph.GA].

GONZALEZ DELGADO, R. M. et al. The CALIFA survey across the Hubble sequence. Spatially resolved stellar population properties in galaxies. **Astronomy and Astrophysics**, v. 581, A103, a103, Sept. 2015. DOI: 10.1051/0004-6361/201525938. arXiv: 1506.04157 [astro-ph.GA].

GOOSMANN, R. W.; CZERNY, B.; MOUCHET, M.; KARAS, V.; DOVČIAK, M.; PONTI, G.; R OŻA NSKA, A. Magnetic flares in Active Galactic Nuclei: modeling the iron Kα line. **Astronomische Nachrichten**, v. 327, n. 10, p. 977–980, Dec. 2006. DOI: 10.1002/asna.200610674. arXiv: astro-ph/0611020 [astro-ph].

GRAHAM, Matthew J et al. Understanding extreme quasar optical variability with CRTS: II. Changing-state quasars. **Monthly Notices of the Royal Astronomical Society**, Oxford University Press (OUP), Nov. 2019. ISSN 1365-2966. DOI: 10.1093/mnras/stz3244. Available from: http://dx.doi.org/10.1093/mnras/stz3244.

GREENE, J. E.; ZAKAMSKA, N. L.; SMITH, P. S. A Spectacular Outflow in an Obscured Quasar. **The Astrophysical Journal**, v. 746, 86, p. 86, Feb. 2012. DOI: 10.1088/0004-637X/746/1/86. arXiv: 1112.3358.

GREENSTEIN, Jesse L.; SCHMIDT. The Quasi-Stellar Radio Sources 3C 48 and 3C 273. **The Astrophysical Journal**, v. 140, p. 1, July 1964. DOI: 10.1086/147889.

GULTEKIN, Kayhan et al. The M-σ and M-L Relations in Galactic Bulges, and Determinations of Their Intrinsic Scatter. **The Astrophysical Journal**, v. 698, n. 1, p. 198–221, June 2009. DOI: 10.1088/0004-637X/698/1/198. arXiv: 0903.4897 [astro-ph.GA].

GÜLTEKIN, Kayhan et al. THEM- ANDM-LRELATIONS IN GALACTIC BULGES, AND DETERMINATIONS OF THEIR INTRINSIC SCATTER. **The Astrophysical Journal**, IOP Publishing, v. 698, n. 1, p. 198–221, May 2009. ISSN 1538-4357. DOI: 10.1088/0004-637x/698/1/198. Available from: http://dx.doi.org/10.1088/0004-637X/698/1/198.

GUO, Hengxiao; SUN, Mouyuan; LIU, Xin; WANG, Tinggui; KONG, Minzhi; WANG, Shu; SHENG, Zhenfeng; HE, Zhicheng. Discovery of an Mg II Changing-look Active Galactic Nucleus and Its Implications for a Unification Sequence of Changing-look Active Galactic Nuclei. **The Astrophysical Journal Letters**, v. 883, n. 2, L44, p. l44, Oct. 2019. DOI: 10.3847/2041-8213/ab4138. arXiv: 1908.00072 [astro-ph.GA].

GUOLO-PEREIRA, Muryel; RUSCHEL-DUTRA, Daniel; STORCHI-BERGMANN, Thaisa; SCHNORR-MÜLLER, Allan; CID FERNANDES, Roberto; COUTO, Guilherme; DAMETTO, Natacha; HERNANDEZ-JIMENEZ, Jose A. Exploring the AGN-merger connection in Arp 245 I: Nuclear star formation and gas outflow in NGC 2992. **Monthly Notices of the Royal Astronomical Society**, v. 502, n. 3, p. 3618–3637, Apr. 2021. DOI: 10.1093/mnras/stab245. arXiv: 2101.10875 [astro-ph.GA].

HAARDT, Francesco; MARASCHI, Laura; GHISELLINI, Gabriele. A Model for the X-Ray and Ultraviolet Emission from Seyfert Galaxies and Galactic Black Holes. **The Astrophysical Journal Letters**, v. 432, p. l95, Sept. 1994. DOI: 10.1086/187520. arXiv: astro-ph/9405059 [astro-ph].

HAZARD, C.; MACKEY, M. B.; SHIMMINS, A. J. Investigation of the Radio Source 3C 273 By The Method of Lunar Occultations. **Nature**, v. 197, n. 4872, p. 1037–1039, Mar. 1963. DOI: 10.1038/1971037a0.

HEY, J. S.; PARSONS, S. J.; PHILLIPS, J. W. Fluctuations in Cosmic Radiation at Radio-Frequencies. **Nature**, v. 158, n. 4007, p. 234, Aug. 1946. DOI: 10.1038/158234a0.

HOPKINS, Andrew M.; BEACOM, John F. On the Normalization of the Cosmic Star Formation History. **The Astrophysical Journal**, IOP Publishing, v. 651, n. 1, p. 142–154, Nov. 2006. DOI: 10.1086/506610. Available from: https://doi.org/10.10862F506610.

HOPKINS, P.; HERNQUIST, L.; COX; KERES, Duvsan. A Cosmological Framework for the Co-Evolution of Quasars, Supermassive Black Holes, and Elliptical Galaxies. I. Galaxy Mergers and Quasar Activity. **The Astrophysical Journal Supplement Series**, v. 175, n. 2, p. 356–389, Apr. 2008. DOI: 10.1086/524362. arXiv: 0706.1243 [astro-ph].

HOPKINS, Philip F.; ELVIS, Martin. Quasar feedback: more bang for your buck. **Monthly Notices of the Royal Astronomical Society**, v. 401, n. 1, p. 7–14, Jan. 2010. DOI: 10.1111/j.1365-2966.2009.15643.x. arXiv: 0904.0649 [astro-ph.CO].

HUBBLE, E. P. Extragalactic nebulae. **The Astrophysical Journal**, v. 64, p. 321–369, Dec. 1926. DOI: 10.1086/143018.

HUMIRE, Pedro K. et al. An outflow in the Seyfert ESO 362-G18 revealed by Gemini-GMOS/IFU observations. **Astronomy and Astrophysics**, v. 614, A94, a94, June 2018. DOI: 10.1051/0004-6361/201731671. arXiv: 1802.07853 [astro-ph.GA].

IRWIN, Judith A. et al. CHANG-ES - VIII. Uncovering hidden AGN activity in radio polarization. **Monthly Notices of the Royal Astronomical Society**, v. 464, n. 2, p. 1333–1346, Jan. 2017. DOI: 10.1093/mnras/stw2414. arXiv: 1609.07609 [astro-ph.GA].

ISHIBASHI, W.; FABIAN, A. C. Active galactic nucleus feedback and triggering of star formation in galaxies. **Monthly Notices of the Royal Astronomical Society**, v. 427, n. 4, p. 2998–3005, Dec. 2012. DOI: 10.1111/j.1365-2966.2012.22074.x. arXiv: 1209.1480 [astro-ph.GA].

JIANG, Yan-Fei; BLAES, Omer. Opacity-driven Convection and Variability in Accretion Disks around Supermassive Black Holes. **The Astrophysical Journal**, American Astronomical Society, v. 900, n. 1, p. 25, July 2020. ISSN 1538-4357. DOI: 10.3847/1538-4357/aba4b7. Available from: http://dx.doi.org/10.3847/1538-4357/aba4b7.

KALBERLA, P. M. W.; BURTON, W. B.; HARTMANN, Dap; ARNAL, E. M.; BAJAJA, E.; MORRAS, R.; POPPEL, W. G. L. The Leiden/Argentine/Bonn (LAB) Survey of Galactic HI. Final data release of the combined LDS and IAR surveys with improved stray-radiation

corrections. **Astronomy and Astrophysics**, v. 440, n. 2, p. 775–782, Sept. 2005. DOI: 10.1051/0004-6361:20041864. arXiv: astro-ph/0504140 [astro-ph].

KASPI, Shai; SMITH, Paul S.; NETZER, Hagai; MAOZ, Dan; JANNUZI, Buell T.; GIVEON, Uriel. Reverberation Measurements for 17 Quasars and the Size-Mass-Luminosity Relations in Active Galactic Nuclei. **The Astrophysical Journal**, v. 533, n. 2, p. 631–649, Apr. 2000. DOI: 10.1086/308704. arXiv: astro-ph/9911476 [astro-ph].

KASPI, Shai et al. The Ionized Gas and Nuclear Environment in NGC 3783. I. Time-averaged 900 KilosecondChandraGrating Spectroscopy. **The Astrophysical Journal**, American Astronomical Society, v. 574, n. 2, p. 643–662, July 2002. ISSN 1538-4357. DOI: 10.1086/341113. Available from: http://dx.doi.org/10.1086/341113.

KAUFFMANN, G. et al. The host galaxies of active galactic nuclei. **Monthly Notices of the Royal Astronomical Society**, v. 346, n. 4, p. 1055–1077, Dec. 2003. DOI: 10.1111/j.1365-2966.2003.07154.x. arXiv: astro-ph/0304239 [astro-ph].

KERR, Roy P. Gravitational Field of a Spinning Mass as an Example of Algebraically Special Metrics. **Physical Review Letters**, v. 11, n. 5, p. 237–238, Sept. 1963. DOI: 10.1103/PhysRevLett.11.237.

KEWLEY, L.; DOPITA, M. A.; SUTHERLAND, R. S.; HEISLER, C. A.; TREVENA, J. Theoretical Modeling of Starburst Galaxies. **The Astrophysical Journal**, v. 556, p. 121–140, July 2001. DOI: 10.1086/321545. eprint: astro-ph/0106324.

KEWLEY, L.; GROVES, Brent; KAUFFMANN, Guinevere; HECKMAN, Tim. The host galaxies and classification of active galactic nuclei. **Monthly Notices of the Royal Astronomical Society**, v. 372, n. 3, p. 961–976, Nov. 2006. DOI: 10.1111/j.1365-2966.2006.10859.x. arXiv: astro-ph/0605681 [astro-ph].

KNAPEN, J. H. Gravitationally Induced Inflow in Starbursts and Agn. **Astrophysics and Space Science**, v. 295, n. 1-2, p. 85–94, Jan. 2005. DOI: 10.1007/s10509-005-3664-3.

KOLEVA, M.; PRUGNIEL, Ph.; OCVIRK, P.; LE BORGNE, D.; SOUBIRAN, C. Spectroscopic ages and metallicities of stellar populations: validation of full spectrum fitting. **Monthly Notices of the Royal Astronomical Society**, v. 385, n. 4, p. 1998–2010, Apr. 2008. DOI: 10.1111/j.1365-2966.2008.12908.x. arXiv: 0801.0871 [astro-ph].

KOLLATSCHNY, W.; GRUPE, D.; PARKER, M. L.; OCHMANN, M. W.; SCHARTEL, N.; HERWIG, E.; KOMOSSA, S.; ROMERO-COLMENERO, E.; SANTOS-LLEO, M. Optical and X-ray discovery of the changing-look AGN IRAS 23226-3843 showing extremely broad and double-peaked Balmer profiles. **Astronomy and Astrophysics**, EDP Sciences, v. 638, a91, June 2020. ISSN 1432-0746. DOI: 10.1051/0004-6361/202037897. Available from: http://dx.doi.org/10.1051/0004-6361/202037897.

KOLLATSCHNY, W.; OCHMANN, M. W.; ZETZL, M.; HAAS, M.; CHELOUCHE, D.; KASPI, S.; POZO NUÑEZ, F.; GRUPE, D. Broad-line region structure and line profile variations in the changing look AGN HE 1136-2304. **Astronomy and Astrophysics**, EDP Sciences, v. 619, a168, Nov. 2018. ISSN 1432-0746. DOI: 10.1051/0004-6361/201833727. Available from: http://dx.doi.org/10.1051/0004-6361/201833727.

KORATKAR, Anuradha; BLAES, Omer. Invited Review: The Ultraviolet and Optical Continuum Emission in Active Galactic Nuclei: The Status of Accretion Disks. **Publications of the Astronomical Society of the Pacific**, IOP Publishing, v. 111, n. 755, p. 1–30, Jan. 1999. DOI: 10.1086/316294. Available from: https://doi.org/10.10862F316294.

KORMENDY, John; RICHSTONE, Douglas. Inward Bound—The Search For Supermassive Black Holes In Galactic Nuclei. **Annual Review of Astronomy and Astrophysics**, v. 33, p. 581, Jan. 1995. DOI: 10.1146/annurev.aa.33.090195.003053.

KOSKI, A. T. Spectrophotometry of Seyfert 2 galaxies and narrow-line radio galaxies. **The Astrophysical Journal**, v. 223, p. 56–73, July 1978. DOI: 10.1086/156235.

KOSS, Michael; MUSHOTZKY, Richard; VEILLEUX, Sylvain; WINTER, Lisa. Merging and Clustering of the Swift BAT AGN Sample. **The Astrophysical Journal Letters**, v. 716, n. 2, p. l125–l130, June 2010. DOI: 10.1088/2041-8205/716/2/L125. arXiv: 1006.0228 [astro-ph.CO].

LAMASSA, Stephanie M.; CALES, Sabrina; MORAN, Edward C.; MYERS, Adam D.; RICHARDS, Gordon T.; ERACLEOUS, Michael; HECKMAN, Timothy M.; GALLO, Luigi; URRY, C. Megan. The discovery of the first "changing look" Quasar: New insights into the physics and phenomenology of active galactic nuclei. **Astrophysical Journal**, IOP Publishing, v. 800, n. 2, p. 144, 2015. ISSN 15384357. DOI: 10.1088/0004-637X/800/2/144. Available from: http://dx.doi.org/10.1088/0004-637X/800/2/144.

LAMPTON, M.; MARGON, B.; BOWYER, S. Parameter estimation in X-ray astronomy. **The Astrophysical Journal**, v. 208, p. 177–190, Aug. 1976. DOI: 10.1086/154592.

LANZ, L.; OGLE, P. M.; EVANS, D.; APPLETON, P. N.; GUILLARD, P.; EMONTS, B. JET-ISM INTERACTION IN THE RADIO GALAXY 3C 293: JET-DRIVEN SHOCKS HEAT ISM TO POWER X-RAY AND MOLECULAR H2EMISSION. **The Astrophysical Journal**, IOP Publishing, v. 801, n. 1, p. 17, Feb. 2015. ISSN 1538-4357. DOI: 10.1088/0004-637x/801/1/17. Available from: http://dx.doi.org/10.1088/0004-637X/801/1/17.

LASOTA, J. -P.; ABRAMOWICZ, M. A.; CHEN, X.; KROLIK, J.; NARAYAN, R.; YI, I. Is the Accretion Flow in NGC 4258 Advection Dominated? **The Astrophysical Journal**, v. 462, p. 142, May 1996. DOI: 10.1086/177137. arXiv: astro-ph/9510083 [astro-ph].

LE BORGNE, J.-F.; BRUZUAL, G.; PELL O, R.; LANÇON, A.; ROCCA-VOLMERANGE, B.; SANAHUJA, B.; SCHAERER, D.; SOUBIRAN, C.; V ILCHEZ-G OMEZ, R. STELIB: A library of stellar spectra at R ˜ 2000. **Astronomy and Astrophysics**, v. 402, p. 433–442, May 2003. DOI: 10.1051/0004-6361:20030243. eprint: astro-ph/0302334.

LENA, D.; ROBINSON, A.; STORCHI-BERGMAN, T.; SCHNORR-MULLER, A.; SEELIG, T.; RIFFEL, R. A.; NAGAR, N. M.; COUTO, G. S.; SHADLER, L. The Complex Gas Kinematics in the Nucleus of the Seyfert 2 Galaxy NGC 1386: Rotation, Outflows, and Inflows. **The Astrophysical Journal**, v. 806, n. 1, 84, p. 84, June 2015. DOI: 10.1088/0004-637X/806/1/84. arXiv: 1504.05089 [astro-ph.GA].

LIU, Hao; WU, Qingwen; LYU, Bing; YAN, Zhen. **Evidence for changing-look AGNs is caused by change of accretion mode**. [S.l.: s.n.], 2019. arXiv: 1912.03972 [astro-ph.GA].

LUMSDEN, S. L.; ALEXANDER, D. M. The infrared luminosity of the torus and the visibility of scattered broad line emission in Seyfert 2 galaxies. **Monthly Notices of the Royal Astronomical Society**, v. 328, n. 3, p. l32–l36, Dec. 2001. DOI: 10.1046/j.1365-8711.2001.05074.x. arXiv: astro-ph/0110174 [astro-ph].

LYNDEN-BELL, D. Galactic Nuclei as Collapsed Old Quasars. **Nature**, v. 223, n. 5207, p. 690–694, Aug. 1969. DOI: 10.1038/223690a0.

MACCACARO, T.; PEROLA, G. C.; ELVIS, M. X-ray observations with the EINSTEIN OBSERVATORY of emission-line galaxies. **The Astrophysical Journal**, v. 257, p. 47–55, June 1982. DOI: 10.1086/159961.

MACLEOD, Chelsea L. et al. A systematic search for changing-look quasars in SDSS. **Monthly Notices of the Royal Astronomical Society**, v. 457, n. 1, p. 389–404, Mar. 2016. DOI: 10.1093/mnras/stv2997. arXiv: 1509.08393 [astro-ph.GA].

MAGORRIAN, John et al. The Demography of Massive Dark Objects in Galaxy Centers. **The Astronomical Journal**, v. 115, n. 6, p. 2285–2305, June 1998. DOI: 10.1086/300353. arXiv: astro-ph/9708072 [astro-ph].

MAKSYM, W. P.; ULMER, M. P.; ROTH, K. C.; IRWIN, J. A.; DUPKE, R.; HO, L. C.; KEEL, W. C.; ADAMI, C. Deep spectroscopy of the $M_V \sim$ -14.8 host galaxy of a tidal disruption flare in A1795. **Monthly Notices of the Royal Astronomical Society**, v. 444, n. 1, p. 866–873, Oct. 2014. DOI: 10.1093/mnras/stu1485. arXiv: 1407.6737 [astro-ph.HE].

MALLMANN, Nícolas Dullius et al. The first 62 AGN observed with SDSS-IV MaNGA – II. Resolvedstellar populations. **Monthly Notices of the Royal Astronomical Society**, Oxford University Press (OUP), v. 478, n. 4, p. 5491–5504, May 2018. ISSN 1365-2966. DOI: 10.1093/mnras/sty1364. Available from: http://dx.doi.org/10.1093/mnras/sty1364.

MARASTON, C.; STROMBACK, G. Stellar population models at high spectral resolution. **Monthly Notices of the Royal Astronomical Society**, v. 418, n. 4, p. 2785–2811, Dec. 2011. DOI: 10.1111/j.1365-2966.2011.19738.x. arXiv: 1109.0543 [astro-ph.CO].

MARCHESE, E.; BRAITO, V.; DELLA CECA, R.; CACCIANIGA, A.; SEVERGNINI, P. NGC 454: unveiling a new 'changing look' active galactic nucleus. **Monthly Notices of the Royal Astronomical Society**, v. 421, n. 2, p. 1803–1812, Apr. 2012. DOI: 10.1111/j.1365-2966.2012.20445.x. arXiv: 1201.2169 [astro-ph.CO].

MARCONI, A.; RISALITI, G.; GILLI, R.; HUNT, L. K.; MAIOLINO, R.; SALVATI, M. Local supermassive black holes, relics of active galactic nuclei and the X-ray background. **Monthly Notices of the Royal Astronomical Society**, v. 351, n. 1, p. 169–185, June 2004. DOI: 10.1111/j.1365-2966.2004.07765.x. arXiv: astro-ph/0311619 [astro-ph].

MARIN, F. Unveiling the physics behind the spectral variations of changing-look quasars with optical polarimetry. **Astronomy and Astrophysics**, EDP Sciences, v. 607, a40, Nov. 2017. ISSN 1432-0746. DOI: 10.1051/0004-6361/201731726. Available from: http://dx.doi.org/10.1051/0004-6361/201731726.

MARINUCCI, A.; BIANCHI, S.; BRAITO, V.; MATT, G.; NARDINI, E.; REEVES, J. Tracking the iron K α line and the ultra fast outflow in NGC 2992 at different accretion states. **Monthly Notices of the Royal Astronomical Society**, v. 478, n. 4, p. 5638–5649, Aug. 2018. DOI: 10.1093/mnras/sty1436. arXiv: 1805.12149 [astro-ph.HE].

MARINUCCI, A.; BIANCHI, Stefano; NICASTRO, Fabrizio; MATT, Giorgio; GOULDING, Andy D. The Link between the Hidden Broad Line Region and the Accretion Rate in Seyfert 2 Galaxies. **The Astrophysical Journal**, v. 748, n. 2, 130, p. 130, Apr. 2012. DOI: 10.1088/0004-637X/748/2/130. arXiv: 1201.5397 [astro-ph.CO].

MARINUCCI, Andrea; RISALITI, Guido; WANG, Junfeng; BIANCHI, Stefano; ELVIS, Martin; MATT, Giorgio; NARDINI, Emanuele; BRAITO, Valentina. X-ray absorption variability in NGC 4507. **Monthly Notices of the Royal Astronomical Society**, Oxford University Press (OUP), v. 429, n. 3, p. 2581–2586, Jan. 2013. ISSN 0035-8711. DOI: 10.1093/mnras/sts534. Available from: http://dx.doi.org/10.1093/mnras/sts534.

MARINUCCI; BIANCHI, S.; BRAITO, V.; DE MARCO, B.; MATT, G.; MIDDEI, R.; NARDINI, E.; REEVES, J. N. The lively accretion disk in NGC 2992. I. Transient iron K emission lines in the high flux state. **Monthly Notices of the Royal Astronomical Society**, staa1683, June 2020. arXiv: 2006.05280. ISSN 0035-8711, 1365-2966. DOI: 10.1093/mnras/staa1683. Available from: http://arxiv.org/abs/2006.05280. Visited on: 15 July 2020.

MARQUEZ, I.; BOISSON, C.; DURRET, F.; PETITJEAN, P. A kinematical analysis of NGC 2992. **Astronomy and Astrophysics**, v. 333, p. 459–465, May 1998. arXiv: astro-ph/9802029 [astro-ph].

MATT, G.; GUAINAZZI, M.; MAIOLINO, R. Changing look: from Compton-thick to Compton-thin, or the rebirth of fossil active galactic nuclei. **Monthly Notices of the Royal Astronomical Society**, Oxford University Press (OUP), v. 342, n. 2, p. 422–426, June 2003. ISSN 1365-2966. DOI: 10.1046/j.1365-8711.2003.06539.x. Available from: http://dx.doi.org/10.1046/j.1365-8711.2003.06539.x.

MCELROY, R. E. et al. The Close AGN Reference Survey (CARS). Mrk 1018 returns to the shadows after 30 years as a Seyfert 1. **Astronomy and Astrophysics**, v. 593, L8, p. l8, Sept. 2016. DOI: 10.1051/0004-6361/201629102. arXiv: 1609.04423 [astro-ph.GA].

MCELROY, Rebecca; CROOM, Scott M.; PRACY, Michael; SHARP, Rob; HO, I. -Ting; MEDLING, Anne M. IFU observations of luminous type II AGN - I. Evidence for ubiquitous winds. **Monthly Notices of the Royal Astronomical Society**, v. 446, n. 2, p. 2186–2204, Jan. 2015. DOI: 10.1093/mnras/stu2224. arXiv: 1410.6552 [astro-ph.GA].

MEHDIPOUR, M. et al. Anatomy of the AGN in NGC 5548. **Astronomy & Astrophysics**, EDP Sciences, v. 575, a22, Feb. 2015. ISSN 1432-0746. DOI: 10.1051/0004-6361/201425373. Available from: http://dx.doi.org/10.1051/0004-6361/201425373.

MENCI, N.; GATTI, M.; FIORE, F.; LAMASTRA, A. Triggering active galactic nuclei in hierarchical galaxy formation: disk instability vs. interactions. **Astronomy and Astrophysics**, v. 569, A37, a37, Sept. 2014. DOI: 10.1051/0004-6361/201424217. arXiv: 1406.7740 [astro-ph.GA].

MENEZES, R. B.; STEINER, J. E.; RICCI, T. V. A treatment procedure for Gemini North/NIFS data cubes: application to NGC 4151. **Monthly Notices of the Royal Astronomical Society**, v. 438, p. 2597–2620, Mar. 2014. DOI: 10.1093/mnras/stt2381. arXiv: 1401.7078 [astro-ph.IM].

MENTZ, J. J. et al. Abundance ratios and IMF slopes in the dwarf elliptical galaxy NGC 1396 with MUSE. **Monthly Notices of the Royal Astronomical Society**, v. 463, n. 3, p. 2819–2838, Dec. 2016. DOI: 10.1093/mnras/stw2129. arXiv: 1608.07042 [astro-ph.GA].

MINGOZZI, M. et al. The MAGNUM survey: different gas properties in the outflowing and disc components in nearby active galaxies with MUSE. **Astronomy and Astrophysics**, v. 622, A146, a146, Feb. 2019. DOI: 10.1051/0004-6361/201834372. arXiv: 1811.07935 [astro-ph.GA].

MORRISON, R.; MCCAMMON, D. Interstellar photoelectric absorption cross sections, 0.03-10 keV. **The Astrophysical Journal**, v. 270, p. 119–122, July 1983. DOI: 10.1086/161102.

MULLER-SANCHEZ, F.; PRIETO, M. A.; HICKS, E. K. S.; VIVES-ARIAS, H.; DAVIES, R. I.; MALKAN, M.; TACCONI, L. J.; GENZEL, R. Outflows from Active Galactic Nuclei: Kinematics of the Narrow-line and Coronal-line Regions in Seyfert Galaxies. **The Astrophysical Journal**, v. 739, 69, p. 69, Oct. 2011. DOI: 10.1088/0004-637X/739/2/69. arXiv: 1107.3140.

MURPHY, K. D.; NOWAK, M. A.; MARSHALL, H. L. The Nuclear X-Ray Emission-line Structure in NGC 2992 Revealed by Chandra-HETGS. **The Astrophysical Journal**, v. 840, n. 2, 120, p. 120, May 2017. DOI: 10.3847/1538-4357/aa6d6a.

MURPHY, K. D.; YAQOOB, Tahir; TERASHIMA, Yuichi. Monitoring the Violent Activity from the Inner Accretion Disk of the Seyfert 1.9 Galaxy NGC 2992 withRXTE. **The Astrophysical Journal**, IOP Publishing, v. 666, n. 1, p. 96–108, Sept. 2007. ISSN 1538-4357. DOI: 10.1086/520039. Available from: http://dx.doi.org/10.1086/520039.

MUSHOTZKY, R. F. The X-ray spectrum and time variability of narrow emission line galaxies. **The Astrophysical Journal**, v. 256, p. 92–102, May 1982. DOI: 10.1086/159886.

NANDRA, K. On the origin of the iron K line cores in active galactic nuclei. **Monthly Notices of the Royal Astronomical Society: Letters**, Oxford University Press (OUP), v. 368, n. 1, p. l62–l66, May 2006. ISSN 1745-3933. DOI: 10.1111/j.1745-3933.2006.00158.x. Available from: http://dx.doi.org/10.1111/j.1745-3933.2006.00158.x.

NANDRA, K.; O'NEILL, P. M.; GEORGE, I. M.; REEVES, J. N. An XMM-Newton survey of broad iron lines in Seyfert galaxies. **Monthly Notices of the Royal Astronomical Society**, v. 382, n. 1, p. 194–228, Nov. 2007. DOI: 10.1111/j.1365-2966.2007.12331.x. arXiv: 0708.1305 [astro-ph].

NANDRA, K.; POUNDS, K. A. GINGA observations of the X-ray spectra of Seyfert galaxies. **Monthly Notices of the Royal Astronomical Society**, v. 268, p. 405–429, May 1994. DOI: 10.1093/mnras/268.2.405.

NELSON, Charles H.; WHITTLE, Mark. Stellar and Gaseous Kinematics of Seyfert Galaxies. I. Spectroscopic Data. **The Astrophysical Journal Supplement Series**, v. 99, p. 67, July 1995. DOI: 10.1086/192179.

NEMMEN, Rodrigo S.; STORCHI-BERGMANN, Thaisa; YUAN, Feng; ERACLEOUS, Michael; TERASHIMA, Yuichi; WILSON, Andrew S. Radiatively Inefficient Accretion Flow in the Nucleus of NGC 1097. **The Astrophysical Journal**, v. 643, n. 2, p. 652–659, June 2006. DOI: 10.1086/500571. arXiv: astro-ph/0512540 [astro-ph].

NENKOVA, Maia; SIROCKY, Matthew M.; NIKUTTA, Robert; IVEZI C, Željko; ELITZUR, Moshe. AGN Dusty Tori. II. Observational Implications of Clumpiness. **The Astrophysical Journal**, v. 685, n. 1, p. 160–180, Sept. 2008. DOI: 10.1086/590483. arXiv: 0806.0512 [astro-ph].

[S.l.]. **Active Galactic Nuclei**. [S.l.: s.n.], Jan. 1990.

NICASTRO, Fabrizio. Broad Emission Line Regions in Active Galactic Nuclei: The Link with the Accretion Power. **The Astrophysical Journal**, IOP Publishing, v. 530, n. 2, p. l65–l68, Feb. 2000. ISSN 0004-637X. DOI: 10.1086/312491. Available from: http://dx.doi.org/10.1086/312491.

NICASTRO, Fabrizio; MATHUR, S.; KRONGOLD, Y. **When a Seyfert. . . ...has a Crash on a Model**. [S.l.]: Zenodo, Oct. 2018. DOI: 10.5281/zenodo.1473677. Available from: https://doi.org/10.5281/zenodo.1473677.

O'DEA, C. P.; BAUM, S. A.; TREMBLAY, G. R.; KHARB, P.; COTTON, W.; PERLEY, R. Hubble Space Telescope Observations of Dusty Filaments in Hercules A: Evidence for Entrainment. **The Astrophysical Journal**, v. 771, n. 1, 38, p. 38, July 2013. DOI: 10.1088/0004-637X/771/1/38. arXiv: 1305.4935 [astro-ph.CO].

OKNYANSKY, V. L.; WINKLER, H.; TSYGANKOV, S. S.; LIPUNOV, V. M.; GORBOVSKOY, E. S.; VAN WYK, F.; BUCKLEY, D. A. H.; TYURINA, N. V. New changing look case in NGC 1566. **Monthly Notices of the Royal Astronomical Society**, v. 483, n. 1, p. 558–564, Feb. 2019. DOI: 10.1093/mnras/sty3133. arXiv: 1811.06926 [astro-ph.GA].

OOSTERLOO, T. A.; MORGANTI, R. Anomalous HI kinematics in Centaurus A: Evidence for jet-induced star formation. **Astronomy and Astrophysics**, v. 429, p. 469–475, Jan. 2005. DOI: 10.1051/0004-6361:20041379. arXiv: astro-ph/0409500 [astro-ph].

OSMER, P. S.; SMITH, M. G.; WEEDMAN, D. W. The nuclei of peculiar emission-line galaxies. **The Astrophysical Journal**, v. 192, p. 279–291, Sept. 1974. DOI: 10.1086/153058.

OSTERBROCK, D.; FERLAND, G. **Astrophysics of gaseous nebulae and active galactic nuclei**. [S.l.: s.n.], 2006.

OSTERBROCK, D. E. Seyfert galaxies with weak broad H alpha emission lines. **The Astrophysical Journal**, v. 249, p. 462–470, Oct. 1981. DOI: 10.1086/159306.

PAN, Hsi-An et al. SDSS-IV MaNGA: Spatial Evolution of Star Formation Triggered by Galaxy Interactions. **The Astrophysical Journal**, v. 881, n. 2, 119, p. 119, Aug. 2019. DOI: 10.3847/1538-4357/ab311c. arXiv: 1907.04491 [astro-ph.GA].

PASTORIZA, M.; GEROLA, H. Spectral Variation in the Seyfert Galaxy NGC 1566. **The Astrophysical Journal Letters**, v. 6, p. 155, July 1970.

PENROSE, Roger. Gravitational Collapse and Space-Time Singularities. **Physics Review Letters**, v. 14, n. 3, p. 57–59, Jan. 1965. DOI: 10.1103/PhysRevLett.14.57.

PETERSON, B. M.; HORNE, K. Echo mapping of active galactic nuclei. **Astronomische Nachrichten**, Wiley, v. 325, n. 3, p. 248–251, Mar. 2004. ISSN 1521-3994. DOI: 10.1002/asna.200310207. Available from: http://dx.doi.org/10.1002/asna.200310207.

PETERSON, B. M. et al. Steps toward Determination of the Size and Structure of the Broad-Line Region in Active Galactic Nuclei. XVI. A 13 Year Study of Spectral Variability in NGC 5548. **The Astrophysical Journal**, American Astronomical Society, v. 581, n. 1, 2002. ISSN 1538-4357. DOI: 10.1086/344197. Available from: http://dx.doi.org/10.1086/344197.

PETERSON, Bradley M. Reverberation Mapping of Active Galactic Nuclei. **Publications of the Astronomical Society of the Pacific**, v. 105, p. 247, Mar. 1993. DOI: 10.1086/133140.

PETERSON, Bradley M.; POGGE, Richard W.; WANDERS, Ignaz; SMITH, Sean M.; ROMANISHIN, W. Aperture Effects and Limitations on the Accuracy of Ground-Based Spectrophotometry of Active Galactic Nuclei. **Publications of the Astronomical Society of the Pacific**, IOP Publishing, v. 107, p. 579, June 1995. DOI: 10.1086/133595. Available from: https://doi.org/10.10862F133595.

PETRUCCI, P. O. et al. A rapidly variable narrow X-ray iron line in Mkn 841. **Astronomy and Astrophysics**, v. 388, p. l5–l8, June 2002. DOI: 10.1051/0004-6361:20020534. arXiv: astro-ph/0204095 [astro-ph].

PONTI, G.; PAPADAKIS, I.; BIANCHI, S.; GUAINAZZI, M.; MATT, G.; UTTLEY, P.; BONILLA, N. F. CAIXA: a catalogue of AGN in the XMM-Newton archive. III. Excess variance analysis. **Astronomy and Astrophysics**, v. 542, A83, a83, June 2012. DOI: 10.1051/0004-6361/201118326. arXiv: 1112.2744 [astro-ph.HE].

POSSOLO, Antonio; MERKATAS, Christos; BODNAR, Olha. Asymmetrical uncertainties. **Metrologia**, IOP Publishing, v. 56, n. 4, p. 045009, July 2019. DOI: 10.1088/1681-7575/ab2a8d. Available from: https://doi.org/10.10882F1681-75752Fab2a8d.

PROXAUF, B.; OTTL, S.; KIMESWENGER, S. Upgrading electron temperature and electron density diagnostic diagrams of forbidden line emission. **Astronomy and Astrophysics**, v. 561, A10, a10, Jan. 2014. DOI: 10.1051/0004-6361/201322581. arXiv: 1311.5041 [astro-ph.IM].

PTAK, A.; TERASHIMA, Y.; HO, L. C.; QUATAERT, E. Testing Radiatively Inefficient Accretion Flow Theory: An XMM-Newton Observation of NGC 3998. **The Astrophysical Journal**, v. 606, n. 1, p. 173–184, May 2004. DOI: 10.1086/382940. arXiv: astro-ph/0401524 [astro-ph].

PTAK, A.; YAQOOB, T.; MURPHY, K.; SUZAKU NGC 2992 TEAM. Precision Fe Kalpha and Fe Kbeta Line Spectroscopy of the Seyfert 1.9 Galaxy NGC 2992 with Suzaku. **Progress of Theoretical Physics Supplement**, v. 169, p. 252–255, Jan. 2007. DOI: 10.1143/PTPS.169.252. arXiv: astro-ph/0609581 [astro-ph].

PUCCETTI, S.; FIORE, F.; RISALITI, G.; CAPALBI, M.; ELVIS, M.; NICASTRO, F. Rapid N_H changes in NGC 4151. **Monthly Notices of the Royal Astronomical Society**, v. 377, n. 2, p. 607–616, May 2007. DOI: 10.1111/j.1365-2966.2007.11634.x. arXiv: astro-ph/0612021 [astro-ph].

QIAO, Erlin; LIU, B. F. A MODEL FOR THE CORRELATION OF HARD X-RAY INDEX WITH EDDINGTON RATIO IN BLACK HOLE X-RAY BINARIES. **The Astrophysical Journal**, IOP Publishing, v. 764, n. 1, p. 2, Jan. 2013. ISSN 1538-4357. DOI: 10.1088/0004-637x/764/1/2. Available from: http://dx.doi.org/10.1088/0004-637X/764/1/2.

QUATAERT, Eliot; NARAYAN, Ramesh. Spectral Models of Advection-dominated Accretion Flows with Winds. **The Astrophysical Journal**, v. 520, n. 1, p. 298–315, July 1999. DOI: 10.1086/307439. arXiv: astro-ph/9810136 [astro-ph].

RAIMANN, D.; STORCHI-BERGMANN, T.; GONZ ALEZ DELGADO, R. M.; CID FERNANDES, R.; HECKMAN, T.; LEITHERER, C.; SCHMITT, H. Stellar population gradients in Seyfert 2 galaxies: northern sample. **Monthly Notices of the Royal Astronomical Society**, v. 339, p. 772–792, Mar. 2003. DOI: 10.1046/j.1365-8711.2003.06222.x. eprint: astro-ph/0210635.

REVALSKI, M. et al. Quantifying Feedback from Narrow Line Region Outflows in Nearby Active Galaxies. II. Spatially Resolved Mass Outflow Rates for the QSO2 Markarian 34. **The Astrophysical Journal**, American Astronomical Society, v. 867, n. 2, p. 88, Nov. 2018. ISSN 1538-4357. DOI: 10.3847/1538-4357/aae3e6. Available from: http://dx.doi.org/10.3847/1538-4357/aae3e6.

RICCI, C.; UEDA, Y.; PALTANI, S.; ICHIKAWA, K.; GAND HI, P.; AWAKI, H. Iron Kα emission in type-I and type-II active galactic nuclei. **Monthly Notices of the Royal Astronomical Society**, v. 441, n. 4, p. 3622–3633, July 2014. DOI: 10.1093/mnras/stu735. arXiv: 1405.7575 [astro-ph.GA].

RICCI, Claudio. **Active Galactic Nuclei at hard X-ray energies: absorption, reflection and the unified model**. Dec. 2011. PhD thesis. ID: unige:19474. Available from: https://nbn-resolving.org/urn:nbn:ch:unige-194749.

RICH, J. A.; KEWLEY, L. J.; DOPITA, M. A. GALAXY MERGERS DRIVE SHOCKS: AN INTEGRAL FIELD STUDY OF GOALS GALAXIES. **The Astrophysical Journal Supplement Series**, IOP Publishing, v. 221, n. 2, p. 28, Dec. 2015. ISSN 1538-4365. DOI: 10.1088/0067-0049/221/2/28. Available from: http://dx.doi.org/10.1088/0067-0049/221/2/28.

RICH, J. A.; KEWLEY, L. J.; DOPITA, M. A. Galaxy-wide Shocks in Late-merger Stage Luminous Infrared Galaxies. **The Astrophysical Journal**, v. 734, n. 2, 87, p. 87, June 2011. DOI: 10.1088/0004-637X/734/2/87. arXiv: 1104.1177 [astro-ph.CO].

RIFFEL; PASTORIZA; RODRIGUEZ-ARDILA; MARASTON. The First Detection of Near-Infrared CN Bands in Active Galactic Nuclei: Signature of Star Formation. **The Astrophysical Journal**, IOP Publishing, v. 659, n. 2, p. l103–l106, Mar. 2007. DOI: 10.1086/517999. Available from: https://doi.org/10.10862F517999.

RIFFEL, R.; PASTORIZA, M.; RODRIGUEZ-ARDILA, Alberto; BONATTO, Charles. Probing the stellar population of seyfert galaxies: a near infrared perspective. In: BRUZUAL, Gustavo R.; CHARLOT, Stephane (Eds.). **Stellar Populations - Planning for the Next ade**. [S.l.: s.n.], Apr. 2010a. P. 164–167. DOI: 10.1017/S1743921310002711. arXiv: 0909.4312 [astro-ph.CO].

RIFFEL, Rogemar A.; STORCHI-BERGMANN, Thaisa; NAGAR, Neil M. Near-infrared dust and line emission from the central region of Mrk1066: constraints from Gemini NIFS. **Monthly Notices of the Royal Astronomical Society**, v. 404, n. 1, p. 166–179, May 2010b. DOI: 10.1111/j.1365-2966.2010.16308.x. arXiv: 1001.0130 [astro-ph.CO].

RIFFEL, Rogério et al. The stellar spectral features of nearby galaxies in the near infrared: tracers of thermally pulsing asymptotic giant branch stars? **Monthly Notices of the Royal Astronomical Society**, Oxford University Press (OUP), v. 450, n. 3, p. 3069–3079, May 2015. ISSN 1365-2966. DOI: 10.1093/mnras/stv866. Available from: http://dx.doi.org/10.1093/mnras/stv866.

RIFFEL; STORCHI-BERGMANN. Feeding and feedback in the active nucleus of Mrk 1157 probed with the Gemini Near-Infrared Integral-Field Spectrograph. **Monthly Notices of the Royal Astronomical Society**, Oxford University Press (OUP), v. 417, n. 4, p. 2752–2769, July 2011. ISSN 0035-8711. DOI: 10.1111/j.1365-2966.2011.19441.x. Available from: http://dx.doi.org/10.1111/j.1365-2966.2011.19441.x.

RIFFEL; STORCHI-BERGMANN, and Winge. Feeding versus feedback in AGNs from near-infrared IFU observations: the case of Mrk 79. **Monthly Notices of the Royal Astronomical Society**, v. 430, n. 3, p. 2249–2261, Apr. 2013. DOI: 10.1093/mnras/stt045. arXiv: 1301.1242 [astro-ph.CO].

RIFFEL; STORCHI-BERGMANN, Thaisa; DORS, Oli L.; WINGE, Cl audia. AGN-starburst connection in NGC7582: Gemini near-infrared spectrograph integral field unit observations. **Monthly Notices of the Royal Astronomical Society**, v. 393, n. 3, p. 783–797, Mar. 2009. DOI: 10.1111/j.1365-2966.2008.14250.x. arXiv: 0811.2327 [astro-ph].

RIFFEL; STORCHI-BERGMANN; WINGE, Cláudia; MCGREGOR, Peter J.; BECK, Tracy; SCHMITT, Henrique. Mapping of molecular gas inflow towards the Seyfert nucleus of NGC 4051 using Gemini NIFS. **Monthly Notices of the Royal Astronomical Society**, Oxford University Press (OUP), v. 385, n. 3, p. 1129–1142, Apr. 2008. ISSN 1365-2966. DOI: 10.1111/j.1365-2966.2008.12936.x. Available from: http://dx.doi.org/10.1111/j.1365-2966.2008.12936.x.

RISALITI, G.; ELVIS, M.; BIANCHI, S.; MATT, G. Chandra monitoring of UGC 4203: the structure of the X-ray absorber. **Monthly Notices of the Royal Astronomical Society: Letters**, Oxford University Press (OUP), no–no, June 2010. ISSN 1745-3933. DOI: 10.1111/j.1745-3933.2010.00873.x. Available from: http://dx.doi.org/10.1111/j.1745-3933.2010.00873.x.

RUAN, John J. et al. TOWARD AN UNDERSTANDING OF CHANGING-LOOK QUASARS: AN ARCHIVAL SPECTROSCOPIC SEARCH IN SDSS. **The Astrophysical Journal**, American Astronomical Society, v. 826, n. 2, p. 188, July 2016. ISSN 1538-4357. DOI: 10.3847/0004-637x/826/2/188. Available from: http://dx.doi.org/10.3847/0004-637X/826/2/188.

RUNNOE, Jessie C. et al. Now you see it, now you don't: the disappearing central engine of the quasar J1011+5442. **Monthly Notices of the Royal Astronomical Society**, v. 455, n. 2, p. 1691–1701, Jan. 2016. DOI: 10.1093/mnras/stv2385. arXiv: 1509.03640 [astro-ph.GA].

RUPKE, David S. N.; VEILLEUX. INTEGRAL FIELD SPECTROSCOPY OF MASSIVE, KILOPARSEC-SCALE OUTFLOWS IN THE INFRARED-LUMINOUS QSO Mrk 231. **The Astrophysical Journal**, IOP Publishing, v. 729, n. 2, p. l27, Feb. 2011. DOI: 10.1088/2041-8205/729/2/l27. Available from: https://doi.org/10.10882F2041-82052F7292F22Fl27.

RUSCHEL-DUTRA, Daniel. **danielrd6/ifscube v1.0**. [S.l.]: Zenodo, July 2020. DOI: 10.5281/zenodo.3945237. Available from: https://doi.org/10.5281/zenodo.3945237.

S ANCHEZ-BL AZQUEZ, P.; PELETIER, R. F.; JIM ENEZ-VICENTE, J.; CARDIEL, N.; CENARRO, A. J.; FALC ON-BARROSO, J.; GORGAS, J.; SELAM, S.; VAZDEKIS, A. Medium-resolution Isaac Newton Telescope library of empirical spectra. **Monthly Notices of the Royal Astronomical Society**, v. 371, n. 2, p. 703–718, Sept. 2006. DOI: 10.1111/j.1365-2966.2006.10699.x. arXiv: astro-ph/0607009 [astro-ph].

SANDAGE, Allan; V ERON, Philippe; WYNDHAM, John D. Optical Identification of New Quasi-Stellar Radio Sources. **The Astrophysical Journal**, v. 142, p. 1307–1311, Oct. 1965. DOI: 10.1086/148415.

SATYAPAL, Shobita; ELLISON, Sara L.; MCALPINE, William; HICKOX, Ryan C.; PATTON, David R.; MENDEL, J. Trevor. Galaxy pairs in the Sloan Digital Sky Survey - IX. Merger-induced AGN activity as traced by the Wide-field Infrared Survey Explorer. **Monthly Notices of the Royal Astronomical Society**, v. 441, n. 2, p. 1297–1304, June 2014. DOI: 10.1093/mnras/stu650. arXiv: 1403.7531 [astro-ph.GA].

SCHAWINSKI, Kevin; DOWLIN, Nathan; THOMAS, Daniel; URRY, C. Megan; EDMONDSON, Edward. THE ROLE OF MERGERS IN EARLY-TYPE GALAXY EVOLUTION AND BLACK HOLE GROWTH. **The Astrophysical Journal**, IOP Publishing, v. 714, n. 1, p. l108–l112, Apr. 2010. DOI: 10.1088/2041-8205/714/1/l108. Available from: https://doi.org/10.10882F2041-82052F7142F12Fl108.

SCHIMOIA, Jaderson S.; STORCHI-BERGMANN, Thaisa; NEMMEN, Rodrigo S.; WINGE, Cl audia; ERACLEOUS, Michael. Short Timescale Variations of the Hα Double-peaked Profile of the Nucleus of NGC 1097. **The Astrophysical Journal**, v. 748, n. 2, 145, p. 145, Apr. 2012. DOI: 10.1088/0004-637X/748/2/145. arXiv: 1203.6101 [astro-ph.CO].

SCHLAFLY, Edward F.; FINKBEINER, Douglas P. Measuring Reddening with Sloan Digital Sky Survey Stellar Spectra and Recalibrating SFD. **The Astrophysical Journal**, v. 737, n. 2, 103, p. 103, Aug. 2011. DOI: 10.1088/0004-637X/737/2/103. arXiv: 1012.4804 [astro-ph.GA].

SCHMIDT. 3C 273 : A Star-Like Object with Large Red-Shift. **Nature**, v. 197, n. 4872, p. 1040, Mar. 1963. DOI: 10.1038/1971040a0.

SCHNORR MÜLLER, Allan; STORCHI-BERGMANN, Thaisa; RIFFEL, Rogemar A.; FERRARI, Fabricio; STEINER, J. E.; AXON, David J.; ROBINSON, Andrew. Gas streaming motions towards the nucleus of M81. **Monthly Notices of the Royal Astronomical Society**, Oxford University Press (OUP), v. 413, n. 1, p. 149–161, Jan. 2011. ISSN 0035-8711. DOI: 10.1111/j.1365-2966.2010.18116.x. Available from: http://dx.doi.org/10.1111/j.1365-2966.2010.18116.x.

SCHNORR-MULLER, Allan; STORCHI-BERGMANN, Thaisa; NAGAR, Neil M.; ROBINSON, Andrew; LENA, Davide. Gas inflows towards the nucleus of NGC 1358. **Monthly Notices of the Royal Astronomical Society**, v. 471, n. 4, p. 3888–3898, Nov. 2017. DOI: 10.1093/mnras/stx1913. arXiv: 1708.03217 [astro-ph.GA].

SCHNORR-MULLER, Allan; STORCHI-BERGMANN, Thaisa; NAGAR, Neil M.; ROBINSON, Andrew; LENA, Davide; RIFFEL, Rogemar A.; COUTO, Guilherme S. Feeding and feedback in the inner kiloparsec of the active galaxy NGC 2110. **Monthly Notices of the Royal Astronomical Society**, v. 437, n. 2, p. 1708–1724, Jan. 2014. DOI: 10.1093/mnras/stt2001. arXiv: 1310.7916 [astro-ph.CO].

SCHNORR-MULLER, Allan et al. Constraints on the broad-line region properties and extinction in local Seyferts. **Monthly Notices of the Royal Astronomical Society**, v. 462, n. 4, p. 3570–3590, Nov. 2016a. DOI: 10.1093/mnras/stw1865. arXiv: 1607.07308 [astro-ph.GA].

SCHNORR-MULLER, Allan et al. Constraints on the broad-line region properties and extinction in local Seyferts. **Monthly Notices of the Royal Astronomical Society**, v. 462, n. 4, p. 3570–3590, Nov. 2016b. DOI: 10.1093/mnras/stw1865. arXiv: 1607.07308 [astro-ph.GA].

SCHWARZSCHILD, K. On the Gravitational Field of a Mass Point According to Einstein's Theory. **Abh. Konigl. Preuss. Akad. Wissenschaften Jahre 1906,92, Berlin,1907**, v. 1916, p. 189–196, Jan. 1916.

SEYFERT, Carl K. Nuclear Emission in Spiral Nebulae. **The Astrophysical Journal**, v. 97, p. 28, Jan. 1943. DOI: 10.1086/144488.

SHAKURA, N. I.; SUNYAEV, R. A. Reprint of 1973A&A....24..337S. Black holes in binary systems. Observational appearance. **Astronomy and Astrophysics**, v. 500, p. 33–51, June 1973.

SHANKAR, Francesco; WEINBERG, David H.; MIRALDA-ESCUD E, Jordi. Self-Consistent Models of the AGN and Black Hole Populations: Duty Cycles, Accretion Rates, and the Mean Radiative Efficiency. **The Astrophysical Journal**, v. 690, n. 1, p. 20–41, Jan. 2009. DOI: 10.1088/0004-637X/690/1/20. arXiv: 0710.4488 [astro-ph].

SHAPIRO, S. L.; LIGHTMAN, A. P.; EARDLEY, D. M. A two-temperature accretion disk model for Cygnus X-1: structure and spectrum. **The Astrophysical Journal**, v. 204, p. 187–199, Feb. 1976. DOI: 10.1086/154162.

SHAPPEE, B. J. et al. The Man behind the Curtain: X-Rays Drive the UV through NIR Variability in the 2013 Active Galactic Nucleus Outburst in NGC 2617. **The Astrophysical Journal**, v. 788, n. 1, 48, p. 48, June 2014. DOI: 10.1088/0004-637X/788/1/48. arXiv: 1310.2241 [astro-ph.HE].

SHENG, Zhenfeng; WANG, Tinggui; JIANG, Ning; YANG, Chenwei; YAN, Lin; DOU, Liming; PENG, Bo. Mid-infrared Variability of Changing-look AGNs. **The Astrophysical Journal**, American Astronomical Society, v. 846, n. 1, p. l7, July 2017. ISSN 2041-8213. DOI: 10.3847/2041-8213/aa85de. Available from: http://dx.doi.org/10.3847/2041-8213/aa85de.

SHIMIZU, T Taro et al. The multiphase gas structure and kinematics in the circumnuclear region of NGC 5728. **Monthly Notices of the Royal Astronomical Society**, Oxford University Press (OUP), Oct. 2019. ISSN 1365-2966. DOI: 10.1093/mnras/stz2802. Available from: http://dx.doi.org/10.1093/mnras/stz2802.

SHLOSMAN, Isaac; BEGELMAN, Mitchell C.; FRANK, Julian. The fuelling of active galactic nuclei. **Nature**, v. 345, n. 6277, p. 679–686, June 1990. DOI: 10.1038/345679a0.

SHU, X. W.; YAQOOB, T.; MURPHY, K. D.; BRAITO, V.; WANG, J. X.; ZHENG, W. NGC 2992 IN AN X-RAY HIGH STATE OBSERVED BYXMM-NEWTON: RESPONSE OF THE RELATIVISTIC Fe LINE TO THE CONTINUUM. **The Astrophysical Journal**, IOP Publishing, v. 713, n. 2, p. 1256–1265, Apr. 2010. ISSN 1538-4357. DOI: 10.1088/0004-637x/713/2/1256. Available from: http://dx.doi.org/10.1088/0004-637X/713/2/1256.

SHUDER, J. M. The optical spectra of narrow-line X-ray galaxies. **The Astrophysical Journal**, v. 240, p. 32–40, Aug. 1980. DOI: 10.1086/158204.

SILK. UNLEASHING POSITIVE FEEDBACK: LINKING THE RATES OF STAR FORMATION, SUPERMASSIVE BLACK HOLE ACCRETION, AND OUTFLOWS IN DISTANT GALAXIES. **The Astrophysical Journal**, IOP Publishing, v. 772, n. 2, p. 112, July 2013. DOI: 10.1088/0004-637x/772/2/112. Available from: https://doi.org/10.10882F0004-637x2F7722F22F112.

SILK, J.; MAMON, G. A. The current status of galaxy formation. **Research in Astronomy and Astrophysics**, v. 12, p. 917–946, Aug. 2012. DOI: 10.1088/1674-4527/12/8/004. arXiv: 1207.3080 [astro-ph.CO].

SILLERO, Emanuel; TISSERA, Patricia B.; LAMBAS, Diego G.; MICHEL-DANSAC, Leo. The evolution of the metallicity gradient and the star formation efficiency in disc galaxies. **Monthly Notices of the Royal Astronomical Society**, Oxford University Press (OUP), v. 472, n. 4, p. 4404–4413, Sept. 2017. ISSN 1365-2966. DOI: 10.1093/mnras/stx2265. Available from: http://dx.doi.org/10.1093/mnras/stx2265.

SLIPHER, V. M. The spectrum and velocity of the nebula N.G.C. 1068 (M 77). **Lowell Observatory Bulletin**, v. 3, p. 59–62, Jan. 1917.

SNIEGOWSKA, M.; CZERNY, B.; BON, E.; BON, N. **A possible mechanism for multiple changing look phenomenon in Active Galactic Nuclei**. [S.l.: s.n.], 2020. arXiv: 2007.06441 [astro-ph.GA].

SOTO-PINTO, Pamela et al. Outflowing gas in a compact ionization cone in the Seyfert 2 galaxy ESO 153-G20. **Monthly Notices of the Royal Astronomical Society**, v. 489, n. 3, p. 4111–4124, Nov. 2019. DOI: 10.1093/mnras/stz2333.

SPINOGLIO, Luigi; FERN ANDEZ-ONTIVEROS, Juan Antonio. AGN types and unification model. **arXiv e-prints**, arXiv:1911.12176, arxiv:1911.12176, Nov. 2019. arXiv: 1911.12176 [astro-ph.GA].

SPRINGEL, V. et al. Simulations of the formation, evolution and clustering of galaxies and quasars. **Nature**, v. 435, p. 629–636, June 2005. DOI: 10.1038/nature03597. eprint: astro-ph/0504097.

STASINSKA, G.; ASARI, N. Vale; FERNANDES, R. Cid; GOMES, J. M.; SCHLICKMANN, M.; MATEUS, A.; SCHOENELL, W.; SODRÉ JR, L. Can retired galaxies mimic active galaxies? Clues from the Sloan Digital Sky Survey. **Monthly Notices of the Royal Astronomical Society: Letters**, Oxford University Press (OUP), Sept. 2008. ISSN 1745-3933. DOI: 10.1111/j.1745-3933.2008.00550.x. Available from: http://dx.doi.org/10.1111/j.1745-3933.2008.00550.x.

STOKLASOVÁ, I.; FERRUIT, P.; EMSELLEM, E.; JUNGWIERT, B.; PÉCONTAL, E.; SÁNCHEZ, S. F. OASIS integral-field spectroscopy of the central kpc in 11 Seyfert 2 galaxies. **Astronomy and Astrophysics**, EDP Sciences, v. 500, n. 3, p. 1287–1325, Apr. 2009. ISSN 1432-0746. DOI: 10.1051/0004-6361/200811225. Available from: http://dx.doi.org/10.1051/0004-6361/200811225.

STORCHI BERGMANN, T.; BICA, E.; PASTORIZA, M. G. The stellar population and emitting gas in the inner 2-5 KPC for a sample of nine Seyfert 2 galaxies. **Monthly Notices of the Royal Astronomical Society**, v. 245, p. 749, Aug. 1990.

STORCHI-BERGMANN, T.; NEMMEN DA SILVA, Rodrigo; ERACLEOUS, Michael; HALPERN, Jules P.; WILSON, Andrew S.; FILIPPENKO, Alexei V.; RUIZ, Maria Teresa; SMITH, R. Chris; NAGAR, Neil M. Evolution of the Nuclear Accretion Disk Emission in NGC 1097: Getting Closer to the Black Hole. **The Astrophysical Journal**, v. 598, n. 2, p. 956–968, Dec. 2003. DOI: 10.1086/378938. arXiv: astro-ph/0308327 [astro-ph].

STORCHI-BERGMANN, Thaisa; BALDWIN, Jack A.; WILSON, Andrew S. Double-peaked Broad Line Emission from the LINER Nucleus of NGC 1097. **The Astrophysical Journal Letters**, v. 410, p. l11, June 1993. DOI: 10.1086/186867.

STORCHI-BERGMANN, Thaisa; RAIMANN, Daniel; BICA, Eduardo L. D.; FRAQUELLI, Henrique A. The Frequency of Nuclear Star Formation in Seyfert 2 Galaxies. **The Astrophysical Journal**, v. 544, n. 2, p. 747–762, Dec. 2000. DOI: 10.1086/317247. arXiv: astro-ph/0007027 [astro-ph].

STORCHI-BERGMANN, Thaisa; RAIMANN, Daniel I.; DELGADO, R. Gonzalez; SCHMITT, H. R.; FERNANDES, R. Cid; HECKMAN, T.; LEITHERER, Claus. **Stellar population gradients in Seyfert 2 galaxies**. [S.l.: s.n.], 2002. arXiv: astro-ph/0211474 [astro-ph].

STORCHI-BERGMANN, Thaisa; SCHNORR-MÜLLER, Allan. Observational constraints on the feeding of supermassive black holes. **Nature Astronomy**, Springer Science and Business Media LLC, v. 3, n. 1, p. 48–61, Jan. 2019. ISSN 2397-3366. DOI: 10.1038/s41550-018-0611-0. Available from: http://dx.doi.org/10.1038/s41550-018-0611-0.

STORCHI-BERGMANN, Thaisa; DORS JR., Oli L.; RIFFEL, Rogemar A.; FATHI, Kambiz; AXON, David J.; ROBINSON, Andrew; MARCONI, Alessandro; OSTLIN, Goran. Nuclear Spirals as Feeding Channels to the Supermassive Black Hole: The Case of the Galaxy NGC 6951. **The Astrophysical Journal**, IOP Publishing, v. 670, n. 2, p. 959–967, Dec. 2007. ISSN 1538-4357. DOI: 10.1086/521918. Available from: http://dx.doi.org/10.1086/521918.

STRAUSS, Michael A. et al. Spectroscopic Target Selection in the Sloan Digital Sky Survey: The Main Galaxy Sample. **The Astronomical Journal**, v. 124, n. 3, p. 1810–1824, Sept. 2002. DOI: 10.1086/342343. arXiv: astro-ph/0206225 [astro-ph].

SUTHERLAND, Ralph; DOPITA, Mike; BINETTE, Luc; GROVES, Brent. **MAPPINGS V: Astrophysical plasma modeling code**. [S.l.: s.n.], July 2018. ascl:1807.005. ascl: 1807.005.

SWANK, J. H. The Rossi X-ray timing explorer: Capabilities, achievements and aims. **Advances in Space Research**, v. 38, n. 12, p. 2959–2963, Jan. 2006. DOI: 10.1016/j.asr.2006.07.009.

TERLEVICH, Roberto; TENORIO-TAGLE, Guillermo; FRANCO, Jose; MELNICK, Jorge. The starburst model for active galactic nuclei - The broad-line region as supernova remnants evolving in a high-density medium. **Monthly Notices of the Royal Astronomical Society**, v. 255, p. 713–728, Apr. 1992. DOI: 10.1093/mnras/255.4.713.

THEUREAU, G.; HANSKI, M. O.; COUDREAU, N.; HALLET, N.; MARTIN, J. -M. Kinematics of the Local Universe. XIII. 21-cm line measurements of 452 galaxies with the Nançay radiotelescope, JHK Tully-Fisher relation, and preliminary maps of the peculiar velocity field. **Astronomy and Astrophysics**, v. 465, n. 1, p. 71–85, Apr. 2007. DOI: 10.1051/0004-6361:20066187. arXiv: astro-ph/0611626 [astro-ph].

TOHLINE, J. E.; OSTERBROCK, D. E. Variation of the spectrum of the Seyfert galaxy NGC 7603. **The Astrophysical Journal Letters**, v. 210, p. l117–l120, Dec. 1976. DOI: 10.1086/182317.

TORREY, Paul; COX, T. J.; KEWLEY, Lisa; HERNQUIST, Lars. THE METALLICITY EVOLUTION OF INTERACTING GALAXIES. **The Astrophysical Journal**, IOP Publishing, v. 746, n. 1, p. 108, Jan. 2012. ISSN 1538-4357. DOI: 10.1088/0004-637x/746/1/108. Available from: http://dx.doi.org/10.1088/0004-637X/746/1/108.

TRAN. The Nature of Seyfert 2 Galaxies with Obscured Broad-Line Regions. I. Observations. **The Astrophysical Journal**, v. 440, p. 565, Feb. 1995. DOI: 10.1086/175296.

TRAN. The Unified Model and Evolution of Active Galaxies: Implications from a Spectropolarimetric Study. **The Astrophysical Journal**, v. 583, n. 2, p. 632–648, Feb. 2003. DOI: 10.1086/345473. arXiv: astro-ph/0210262 [astro-ph].

TREISTER, E.; SCHAWINSKI, K.; URRY, C. M.; SIMMONS, B. D. MAJOR GALAXY MERGERS ONLY TRIGGER THE MOST LUMINOUS ACTIVE GALACTIC NUCLEI. **The Astrophysical Journal**, IOP Publishing, v. 758, n. 2, p. l39, Oct. 2012. DOI: 10.1088/2041-8205/758/2/l39. Available from: https://doi.org/10.10882F2041-82052F7582F22Fl39.

TREMAINE, Scott et al. The Slope of the Black Hole Mass versus Velocity Dispersion Correlation. **The Astrophysical Journal**, v. 574, n. 2, p. 740–753, Aug. 2002. DOI: 10.1086/341002. arXiv: astro-ph/0203468 [astro-ph].

TRIPPE; CRENSHAW, D; R. P., Deo; DIETRICH, Matthias. Long-Term Variability in the Optical Spectrum of the Seyfert Galaxy NGC 2992. **AJ**, v. 135, Apr. 2008a. DOI: 10.1088/0004-6256/135/6/2048.

TRIPPE, M. L.; CRENSHAW, D. M.; DEO, R.; DIETRICH, M. Long-Term Variability in the Optical Spectrum of the Seyfert Galaxy NGC 2992. **The Astronomical Journal**, v. 135, n. 6, p. 2048–2054, June 2008b. DOI: 10.1088/0004-6256/135/6/2048. arXiv: 0804.1381 [astro-ph].

TRUMP, Jonathan R. et al. ACCRETION RATE AND THE PHYSICAL NATURE OF UNOBSCURED ACTIVE GALAXIES. **The Astrophysical Journal**, IOP Publishing, v. 733, n. 1, p. 60, May 2011. ISSN 1538-4357. DOI: 10.1088/0004-637x/733/1/60. Available from: http://dx.doi.org/10.1088/0004-637X/733/1/60.

TURNER, T. J.; POUNDS, K. A. The EXOSAT spectral survey of AGN. **Monthly Notices of the Royal Astronomical Society**, v. 240, p. 833–880, Oct. 1989. DOI: 10.1093/mnras/240.4.833.

ULVESTAD, J. S.; WILSON, A. S. Radio structures of Seyfert galaxies. VI. VLA observations of a nearby sample. **The Astrophysical Journal**, v. 285, p. 439–452, Oct. 1984. DOI: 10.1086/162520.

URRY, C. Megan; PADOVANI, Paolo. Unified Schemes for Radio-Loud Active Galactic Nuclei. **Publications of the Astronomical Society of the Pacific**, v. 107, p. 803, Sept. 1995. DOI: 10.1086/133630. arXiv: astro-ph/9506063 [astro-ph].

VALIANTE, Rosa; AGARWAL, Bhaskar; HABOUZIT, Melanie; PEZZULLI, Edwige. On the Formation of the First Quasars. **Publications of the Astronomical Society of Australia**, v. 34, e031, e031, July 2017. DOI: 10.1017/pasa.2017.25. arXiv: 1703.03808 [astro-ph.GA].

VAN DOKKUM, Pieter G. Cosmic-Ray Rejection by Laplacian Edge Detection. **Publications of the Astronomical Society of the Pacific**, v. 113, p. 1420–1427, Nov. 2001. DOI: 10.1086/323894. arXiv: astro-ph/0108003 [astro-ph].

VAN GRONINGE, Ernst; WANDERS, Ignaz. An Algorithm for the Relative Scaling of Spectra. **Publications of the Astronomical Society of the Pacific**, v. 104, p. 700, Aug. 1992. DOI: 10.1086/133039.

VAN GRONINGEN, Ernst; WANDERS, Ignaz. An Algorithm for the Relative Scaling of Spectra. **Publications of the Astronomical Society of the Pacific**, v. 104, p. 700, Aug. 1992. DOI: 10.1086/133039.

VANDEN BERK, Daniel E. et al. Composite Quasar Spectra from the Sloan Digital Sky Survey. **The Astronomical Journal**, v. 122, n. 2, p. 549–564, Aug. 2001. DOI: 10.1086/321167. arXiv: astro-ph/0105231 [astro-ph].

VEILLEUX; OSTERBROCK. Spectral Classification of Emission-Line Galaxies. **The Astrophysical Journal Supplement Series**, v. 63, p. 295, Feb. 1987. DOI: 10.1086/191166.

VEILLEUX, S.; SHOPBELL, P. L.; MILLER, S. T. The Biconical Outflow in the Seyfert Galaxy NGC 2992. **The Astronomical Journal**, v. 121, n. 1, p. 198–209, Jan. 2001. DOI: 10.1086/318046. arXiv: astro-ph/0010134 [astro-ph].

VENTURI, Giacomo et al. MAGNUM survey: A MUSE-Chandra resolved view on ionized outflows and photoionization in the Seyfert galaxy NGC1365. **Astronomy and Astrophysics**, v. 619, A74, a74, Nov. 2018. DOI: 10.1051/0004-6361/201833668. arXiv: 1809.01206 [astro-ph.GA].

VERON, P.; LINDBLAD, P. O.; ZUIDERWIJK, E. J.; VERON, M. P.; ADAM, G. On the nature of the so-called narrow-line X-ray galaxies. **Astronomy and Astrophysics**, v. 87, n. 1-2, p. 245–249, July 1980.

VÉRON-CETTY, M. P.; VÉRON, P. Are all radio galaxies genuine ellipticals? **Astronomy and Astrophysics**, v. 375, p. 791–796, Sept. 2001. DOI: 10.1051/0004-6361:20010902.

VILLAR-MARTIN, M.; HUMPHREY, A.; DELGADO, R. Gonz alez; COLINA, L.; ARRIBAS, S. Ionized outflows in SDSS type 2 quasars at z $\sim$ 0.3-0.6. **Monthly Notices of the Royal Astronomical Society**, v. 418, n. 3, p. 2032–2042, Dec. 2011. DOI: 10.1111/j.1365-2966.2011.19622.x. arXiv: 1108.2392 [astro-ph.CO].

WANG, J.; XU, D. W.; WANG, Y.; ZHANG, J. B.; ZHENG, J.; WEI, J. Y. Two New "Turn-off" Changing-look Active Galactic Nuclei and Implication on "Partially Obscured" AGNs. **The Astrophysical Journal**, American Astronomical Society, v. 887, n. 1, p. 15, Dec. 2019. ISSN 1538-4357. DOI: 10.3847/1538-4357/ab4d90. Available from: http://dx.doi.org/10.3847/1538-4357/ab4d90.

WARD, M.; PENSTON, M. V.; BLADES, J. C.; TURTLE, A. J. New optical and radio observations of the X-ray galaxies NGC 7582 andNGC 2992. **Monthly Notices of the Royal Astronomical Society**, v. 193, p. 563–582, Nov. 1980. DOI: 10.1093/mnras/193.3.563.

WEAVER, K. A.; NOUSEK, J.; YAQOOB, T.; MUSHOTZKY, R. F.; MAKINO, F.; OTANI, C. X-Ray Reprocessing by a Molecular Torus in the Seyfert 1.9 Galaxy NGC 2992. **The Astrophysical Journal**, v. 458, p. 160, Feb. 1996. DOI: 10.1086/176800.

WEBSTER, B. Louise; MURDIN, Paul. Cygnus X-1-a Spectroscopic Binary with a Heavy Companion ? **Nature**, v. 235, n. 5332, p. 37–38, Jan. 1972. DOI: 10.1038/235037a0.

WILKINSON, David M.; MARASTON, Claudia; GODDARD, Daniel; THOMAS, Daniel; PARIKH, Taniya. FIREFLY (Fitting IteRativEly For Likelihood analYsis): a full spectral fitting code. **Monthly Notices of the Royal Astronomical Society**, v. 472, n. 4, p. 4297–4326, Dec. 2017. DOI: 10.1093/mnras/stx2215. arXiv: 1711.00865 [astro-ph.GA].

WINTER, Lisa M.; MUSHOTZKY, Richard F.; REYNOLDS, Christopher S.; TUELLER, Jack. X-Ray Spectral Properties of the BAT AGN Sample. **The Astrophysical Journal**, v. 690, n. 2, p. 1322–1349, Jan. 2009. DOI: 10.1088/0004-637X/690/2/1322. arXiv: 0808.0461 [astro-ph].

WOO, Jong-Hak; SCHULZE, Andreas; PARK, Daeseong; KANG, Wol-Rang; KIM, Sang Chul; RIECHERS, Dominik A. DO QUIESCENT AND ACTIVE GALAXIES HAVE DIFFERENTMBH-RELATIONS? **The Astrophysical Journal**, IOP Publishing, v. 772, n. 1, p. 49, July 2013. ISSN 1538-4357. DOI: 10.1088/0004-637x/772/1/49. Available from: http://dx.doi.org/10.1088/0004-637X/772/1/49.

WOO, Jong-Hak; URRY, C. Megan. Active Galactic Nucleus Black Hole Masses and Bolometric Luminosities. **The Astrophysical Journal**, v. 579, n. 2, p. 530–544, Nov. 2002. DOI: 10.1086/342878. arXiv: astro-ph/0207249 [astro-ph].

XIE, Fu-Guo; YUAN, Feng. Radiative efficiency of hot accretion flows. **Monthly Notices of the Royal Astronomical Society**, v. 427, n. 2, p. 1580–1586, Dec. 2012. DOI: 10.1111/j.1365-2966.2012.22030.x. arXiv: 1207.3113 [astro-ph.HE].

YANG, Qian et al. Discovery of 21 New Changing-look AGNs in the Northern Sky. **The Astrophysical Journal**, v. 862, n. 2, 109, p. 109, Aug. 2018. DOI: 10.3847/1538-4357/aaca3a. arXiv: 1711.08122 [astro-ph.GA].

YAQOOB; GEORGE, I. M.; NANDRA, K.; TURNER, T. J.; SERLEMITSOS, P. J.; MUSHOTZKY, R. F. Physical Diagnostics from a Narrow Fe Kα Emission Line Detected by Chandra in the Seyfert 1 Galaxy NGC 5548. **The Astrophysical Journal**, v. 546, n. 2, p. 759–768, Jan. 2001. DOI: 10.1086/318315. arXiv: astro-ph/0008471 [astro-ph].

YAQOOB, Tahir. Parameter Estimation in X-Ray Astronomy Revisited. **The Astrophysical Journal**, v. 500, n. 2, p. 893–898, June 1998. DOI: 10.1086/305781. arXiv: astro-ph/9803057 [astro-ph].

YAQOOB et al. Precision Fe Kα and Fe Kβ Line Spectroscopy of the Seyfert 1.9 Galaxy NGC 2992 with Suzaku. **Publications of the Astronomical Society of Japan**, v. 59, p. 283–299, Jan. 2007. DOI: 10.1093/pasj/59.sp1.S283.

YUAN, Feng; NARAYAN, Ramesh. Hot Accretion Flows Around Black Holes. **Annual Review of Astronomy and Astrophysics**, v. 52, p. 529–588, Aug. 2014. DOI: 10.1146/annurev-astro-082812-141003. arXiv: 1401.0586 [astro-ph.HE].

ZAKAMSKA, Nadia L. et al. Discovery of extreme [O III] λ5007 Å outflows in high-redshift red quasars. **Monthly Notices of the Royal Astronomical Society**, v. 459, n. 3, p. 3144–3160, July 2016. DOI: 10.1093/mnras/stw718. arXiv: 1512.02642 [astro-ph.GA].

ZINN, P.-C.; MIDDELBERG, E.; NORRIS, R. P.; DETTMAR, R.-J. ACTIVE GALACTIC NUCLEUS FEEDBACK WORKS BOTH WAYS. **The Astrophysical Journal**, IOP Publishing, v. 774, n. 1, p. 66, July 2013. DOI: 10.1088/0004-637x/774/1/66. Available from: https://doi.org/10.10882F0004-637x2F7742F12F66.

APPENDIX A – APPENDIXES FOR CHAPTER 2

A.1 Stellar Populations Synthesis Maps

We show the maps of the recovered properties from three spatially resolved STARLIGHT synthesis we have performed, namely *BC03*, *BC03+FC* and *M11+FC*. The top panels show, from left to right, the per cent contribution to the total light for young, intermediate and old SSPs (x_Y, x_I and x_O). In the middle panels the light-weighted mean stellar metallicity for the three age groups, from left to right, $\langle Z \rangle_Y$, $\langle Z \rangle_I$ and $\langle Z \rangle_O$. In the bottom panel the V-Band extinction (A_V), the per cent contribution to the total light from the FC component (x_{agn}) and the light-weighted mean stellar age, $\langle log\ t_* \rangle$, are shown, respectively, from left to right.

A.2 Emission Line Fitting Uncertainties

We present here the uncertainties in the parameters of the emission lines fitting described in section 2.4.1. The uncertainties are the standard deviation over the one hundred Monte Carlo iterations. The uncertainties in the radial velocity (V) of Component 1 was already presented in section section 2.4. In Figure 42 we show the uncertainties in the velocity dispersion (σ) of Component 1, the values are mostly smaller than 5 kms^{-1}, reaching a maximum value of 15 kms^{-1}.

In the top panel we also show the uncertainties of v and σ of Component 2, values are less than 10 kms^{-1}in most the region, reaching up to 30 kms^{-1}in a very small region, the σ values are less then 10 kms^{-1}in the peak of component emission and up to 30 kms^{-1}in the borders of the detection region. In the middle and bottom panels the percentile uncertainties in the integrated flux (Component 1 + Component 2) of Hβ, [O III] λ5007, Hα, [N II] λ6583, and [S II] λ6716,6731 are shown.

The Hβ line uncertainties range from 10 per cent at the centre of the FoV, up to 45 per cent in the dust lane region. [O III] and Hα values range from less than 5 per cent up to 25 per cent at the dust lane region. [S II] and [N II] values range from less than 10 per cent up to 35 per cent at the dust lane region.

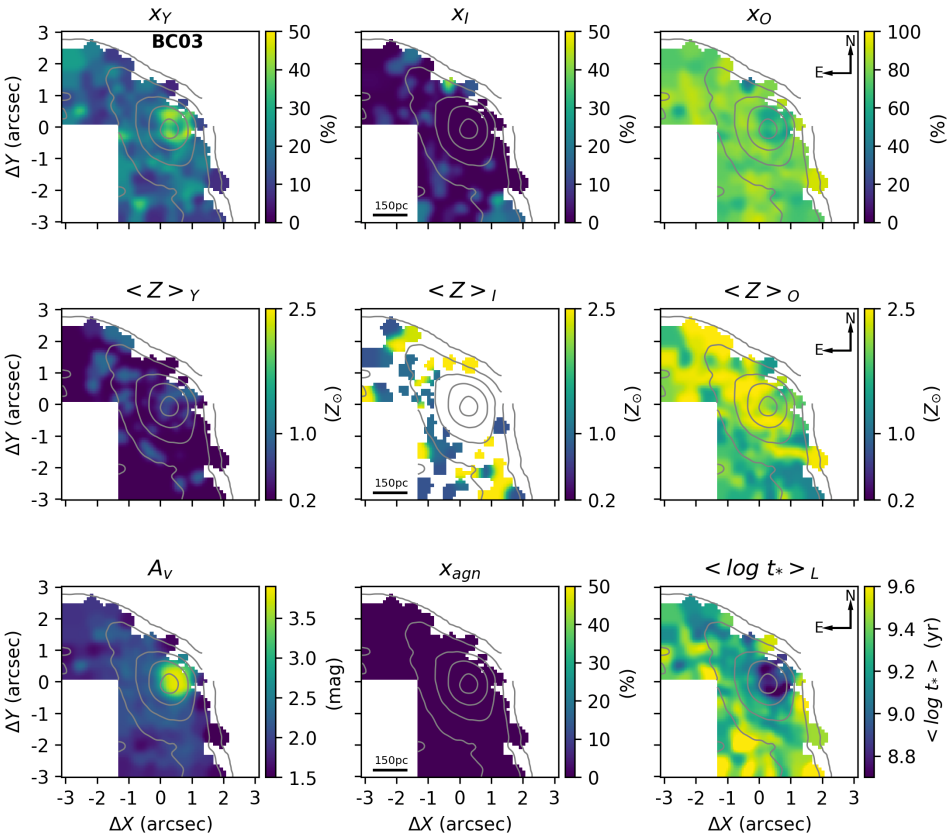

Figure 39 – Maps of the recovered properties from the *BC03* synthesis. Top: from left to right, percentage contribution to the total light from young, intermediate and old SSPs (x_Y, x_I and x_O). Middle: from left to right, light-weighted mean stellar metallicity for the three SSP age groups, $\langle Z \rangle_Y$, $\langle Z \rangle_I$ and $\langle Z \rangle_O$. Bottom left: A_V extinction parameter. Bottom middle: Featureless continuum (FC) component percentage contribution to the total light (x_{agn}). Bottom Right: Light-weighted mean stellar age, $\langle log\ t_* \rangle$. The grey contour in all the maps is the continuum emission, left panel of Figure 18. The x_{agn} is null in all points by definition, because there is no FC component in *BC03* synthesis spectra base.

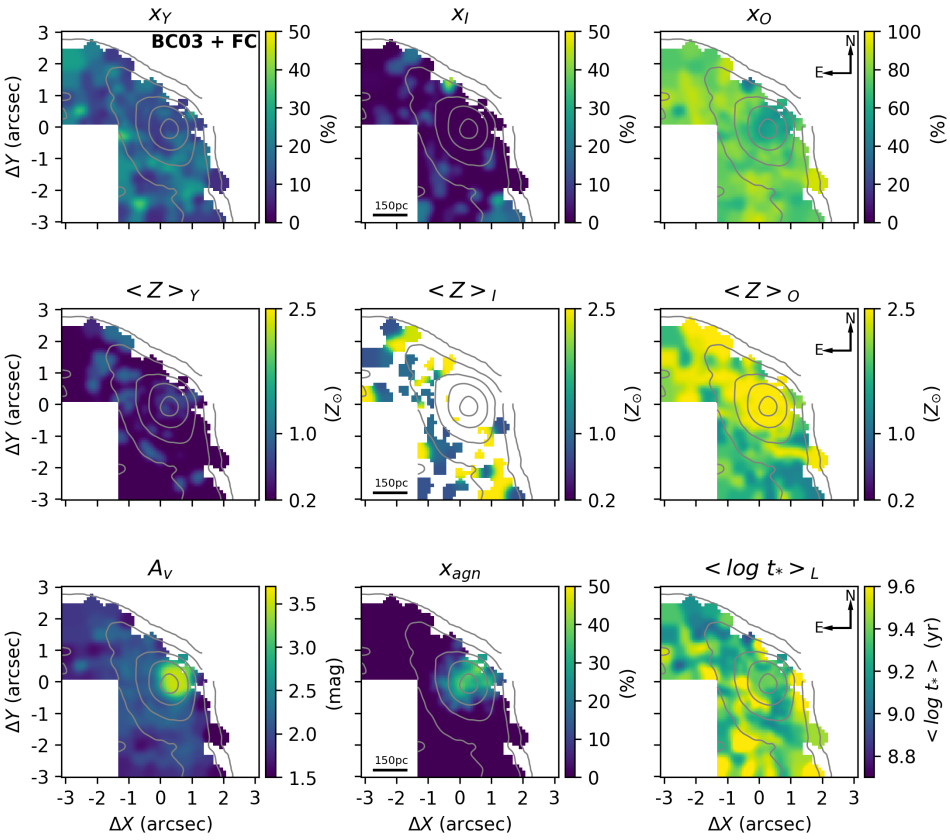

Figure 40 – Same as Figure 39 for *BC03+FC*.

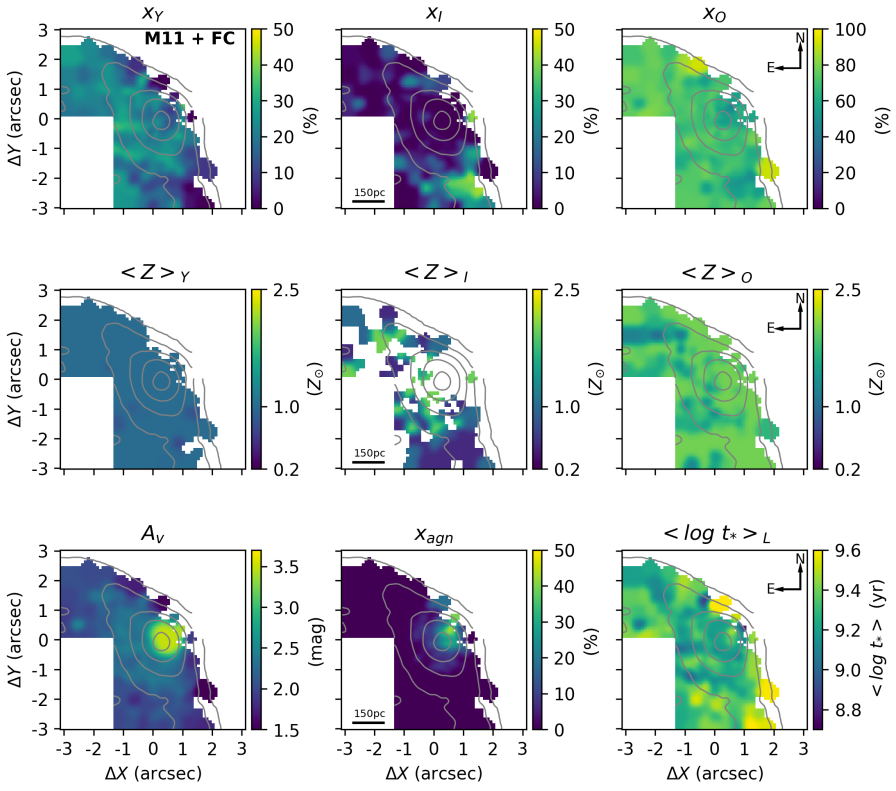

Figure 41 – Same as Figure 39 for *M11+FC*.

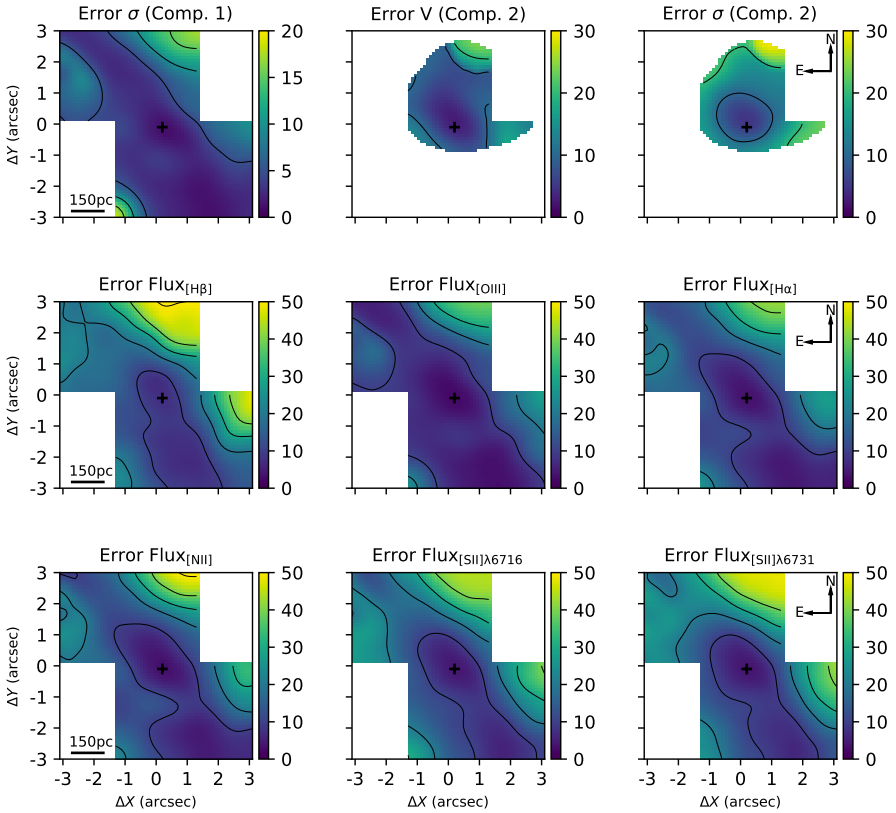

Figure 42 – Emission line fitting uncertainties. Top: from right to left, velocity dispersion of Component 1 (kms^{-1}), radial velocity of Component 2 (kms^{-1}), velocity dispersion of Component 2 (kms^{-1}). Middle and Bottom: percentage uncertainties in the integrated flux (Component 1 + Component) of Hβ, [O III] λ5007, Hα, [N II] λ6583, and [S II] λ6716,6731 (%). The black cross shows the peak of the continuum emission. Each contour in the maps means a 10% variation in the uncertainties.

APPENDIX B – APPENDIXES FOR CHAPTER 3

B.1 Propagation of Asymmetric Uncertainties

When the underlying likelihood function of a parameter is not symmetric, the error distribution will also be asymmetric. Different origins of asymmetry are discussed in detail by Barlow (2003a,b) and Barlow (2004). In high-energy astrophysics it is related to the low photon counting. In this case, the estimated parameters are usually reported in a form like $\hat{x}^{+u_r}_{-u_l}$. Where $\hat{x}$ is the best-fitting parameter (minimum χ^2) and u_l and u_r are draw where the $\Delta\chi^2$ curve reaches some value, for classical 1σ (68%) confidence level $\Delta\chi^2 = 1.0$, however the 90% confidence level ($\Delta\chi^2 = 2.7$) is the most employed in X-ray astronomy (AVNI, 1976; LAMPTON et al., 1976; YAQOOB, 1998).

Usually, one needs to calculate a function of one or more quantities, and propagate its uncertainties. In most circumstances, well known "Error Propagation" formulas are adequate. But there are some assumptions and approximations under the Error Propagation, and if they fail, the method is invalid. These assumptions can be summarised as: the errors are Normally distributed (Gaussian errors) and they are relatively small. For asymmetric errors in astronomy any of these assumptions can be made; if the asymmetry is really small, rounding/averaging the negative and the positive errors into a single value and making the distribution symmetric does not change the result much. But when the values are not appropriate to do that, researchers often tend to put two error values into quadrature separately and combine them in the result. Actually this is not a valid method due to violation of the Central Limit Theorem (BARLOW, 2003b). Eventually more sophisticated methods are needed to use: we present here a Python-based Monte Carlo solution for this problem, based in a combination of Barlow (2004) and Possolo et al. (2019) derivations.

During this research we faced the problem that even with numerous of uncertainties propagation tools publicly-available (e.g. ASTROPY.UNCERTAINTY, UNCERTAINTIES) none of them are able to handle asymmetric uncertainties as we needed, due to the assumptions stated above. We therefore created the ASYMMETRIC_UNCERTAINTIES Python package, the main idea of the code is to generate a random sample from the likelihood function and use this sample in other calculations (POSSOLO et al., 2019). The code assumes a "Variable Width Gaussian" likelihood, which, as shown by Barlow (2004), reproduces very well the underlying likelihood of low counting measurements, and, in contrast to, for example, a "Generalised Poisson" distribution, has a unique and analytical solution for given values of $\hat{x}$, u_l and u_r at a given confidence level ($\Delta\chi^2$). From this likelihood the code generates a random sample of data, that can be passed as parameters for any type of function. Simple operations are deal internally by the code and the more sophisticated ones can be easy performed by the user, for example: L_{2-10} values in Table 3 whose uncertainties were propagated from Γ and N_H uncertainties; as well as the statistical tests (r_s and p_{value}) in Figure 33. The resulting sample is then fitted by the code returning the nominal value and the propagated uncertainties. The code is publicly-available at github[1] where examples in how to use the code are also presented.

[1] https://github.com/muryelgp/asymmetric_uncertainties

B.2 Point-Source Scale Factor Derivation and Measurement

The fluxes of the BELs (from the BLR) measured from spectra taking from different instruments at distinct observational conditions suffers from the effects of distinct apertures and seeing. In this section, based on Peterson et al. (1995), we will derive the expression of the so-called Point-Source Scale Factor (φ), which is used in the correction of these effects in AGN variability studies.

The flux calibration of ground-based optical spectra of variable AGNs is often done by assuming that the narrow line flux is constant with time (as done in section 3.3.2). However, at typical ground-based resolution (generally of order one arcsec), the NLR is often not a point source in nearby AGNs. Thus, the fraction of the total NLR flux that enters the spectrograph aperture is not the same as the fraction recorded from a point source (such as the AGN continuum source or the BLR), and the difference between the recorded NLR flux and point-source flux is a function of the Point Spread Function (PSF), i.e., the seeing, as well as from the size of the aperture.

Consider first the flux recorded from a point source. We characterize the PSF, ρ, by its full width at half-maximum (FWHM), s, measured in arcseconds. In this analysis, the important quantity will be the integral of the PSF, $\Phi(\mathbf{R}, s)$, over the projected aperture, i.e.:

$$\Phi(\mathbf{R}, s) = \int_{\mathbf{R}} \rho(\mathbf{R'}, s) d\mathbf{R'} \tag{35}$$

where the integral is over the projected aperture whose boundaries are specified by **R**. For good quality data, the PSF is azimuthally symmetric, usually assumed to be Gaussian, and the integral over a circular aperture of radius **R** centered on the source simplifies to:

$$\Phi(\mathbf{R}, s) = 2\pi \int_0^R \rho(r, s)\ r\ dr \tag{36}$$

The total narrow line flux measured through the same aperture with the same PSF is given by a similar equation, but using the observed NLR surface-brightness distribution, $\Sigma_{NL}(\mathbf{R}, s)$, the actual surface brightness distribution convoluted with the PSF):

$$F_{\mathrm{NL}}(\mathbf{R}, s) = \int_{\mathbf{R}} \Sigma_{NL}(\mathbf{R'}, s) d\mathbf{R'} \tag{37}$$

Flux calibration of the recorded AGN spectrum is accomplished by assuming that the narrow-line flux is constant and known. However, one can easily see that if the NLR is slightly more extended than the PSF, a small aperture (i.e., one that is slightly larger than the width of the PSF) will admit a larger fraction of light from the point-like source than from the NLR. By assuming that all of the NLR flux was recorded, one makes an error in calibration in the sense that the point-source components appear to be brighter than they actually are, but only because the recorded NLR flux is lower than it should be. To account for this, we define a Point-Source

Scale Factor (φ) by the equation:

$$\varphi(\mathbf{R}, s) = \frac{F_{\mathrm{NL}}(\mathbf{R}, s)}{\Phi(\mathbf{R}, s)} \tag{38}$$

We normalize the correction factor φ to some standard aperture geometry and seeing. The point-source (in this case the BLR) fluxes measured from the calibrated spectrum should be multiplied by this factor to account for the fact that the observed point-source fluxes are too high because of lesser light loss (relative to the narrow lines) at the aperture. Thus, the correct broad-line flux is given by:

$$L = \varphi(\mathbf{R}, s)\ L_{obs} \tag{39}$$

where L_{obs} is the luminosity measured in the calibrated (assuming same narrow line flux) spectrum, and therefore the above expression becomes equation 30.

In our case Σ_{NL} was an [O III] λ5007 image, constructed using the 2015 data cube from the MUSE instrument (see section 3.2.3), ρ a Gaussian function, s the spatial resolution (seeing) of the observations, and **R** the apertures (see Table 5) which were than applied to equation 38 result in the φ values listed in Table 5.

ANNEX A – PAPERS

Attached are the two peer-reviewed papers in which chapters 2 and 3 were based on.

MNRAS 000, 1–20 (2021) Preprint 27 January 2021 Compiled using MNRAS LATEX style file v3.0

Exploring the AGN-Merger Connection in Arp 245 I: Nuclear Star Formation and Gas Outflow in NGC 2992

Muryel Guolo-Pereira[1]★, Daniel Ruschel-Dutra[1], Thaisa Storchi-Bergmann[2], Allan Schnorr-Müller[2], Roberto Cid Fernandes[1], Guilherme Couto[3], Natacha Dametto[3], Jose A Hernandez-Jimenez[4]

[1]*Departamento de Física - CFM - Universidade Federal de Santa Catarina, 476, 88040-900 Florianópolis, SC, Brazil*
[2]*Departamento de Astronomia, Universidade Federal do Rio Grande do Sul. Av. Bento Goncalves 9500, 91501-970 Porto Alegre, RS, Brazil*
[3]*Centro de Astronomía (CITEVA), Universidad de Antofagasta, Avenida Angamos 601, Antofagasta, Chile*
[4] *Departamento de Ciencias Físicas, Universidad Andrés Bello, Fernández Concha 700, Las Condes, Santiago, Chile*

Accepted 2021 January 25. Received 2021 January 25; in original form 2019 November 28.

ABSTRACT

Galaxy mergers are central to our understanding of galaxy formation, especially within the context of hierarchical models. Besides having a large impact on the star formation history, mergers are also able to influence gas motions at the centre of galaxies and trigger an Active Galactic Nucleus (AGN). In this paper, we present a case study of the Seyfert galaxy NGC 2992, which together with NGC 2993 forms the early-stage merger system Arp 245. Using Gemini Multi-Object Spectrograph (GMOS) integral field unit (IFU) data from the inner 1.1 kpc of the galaxy we were able to spatially resolve the stellar populations, the ionisation mechanism and kinematics of ionised gas. From full spectral synthesis, we found that the stellar population is primarily composed by old metal-rich stars ($t \geq 1.4$ Gyr, $Z \geq 2.0\,Z_{\odot}$), with a contribution of at most 30 per cent of the light from a young and metal-poor population ($t \leq 100$ Myr, $Z \leq 1.0\,Z_{\odot}$). We detect Hα and Hβ emission from the Broad Line Region (BLR) with a Full Width at Half Maximum (FWHM) of ~ 2000 km s^{-1}. The Narrow Line Region (NLR) kinematics presents two main components: one from gas orbiting the galaxy disk and a blueshifted (velocity $\approx$ -200 km s^{-1}) outflow, possibly correlated with the radio emission, with mass outflow rate of $\sim 2\,M_{\odot}$ yr^{-1} and a kinematic power of $\sim 2 \times 10^{40}$ erg s^{-1} ($\dot{E}_{out}/L_{bol} \approx 0.2$ per cent). We also show even though the main ionisation mechanism is the AGN radiation, ionisation by young stars and shocks may also contribute to the emission line ratios presented in the innermost region of the galaxy.

Key words: Galaxies: individual (Arp 245, NGC 2992) – Galaxies: Seyfert – Galaxies: interactions – Galaxies: stellar content – Galaxies: kinematics and dynamics

1 INTRODUCTION

The vast majority of galaxies with a spheroid host a supermassive black hole (SMBH) in their centres, with a mass range of $\sim 10^6 - 10^{10}\,M_{\odot}$. In some galaxies, these objects are active and emit intense radiation due to the accretion of matter onto the SMBH through an inner region called accretion disk (Begelman et al. 1984; Peterson et al. 1998; Event Horizon Telescope Collaboration et al. 2019). Active galactic nuclei (AGN) in Seyfert galaxies are classified as type 1 and 2, depending on the presence of broad emission lines of the Balmer series, with intermediate types between these two also possible; these broad lines are produced in a region called Broad Line Region (BLR).

The importance of AGN in the evolution of the host galaxy is not completely understood, but there is evidence pointing to a co-evolution scenario between the two. The $M_{BH}-\sigma_*$ relation (Ferrarese & Merritt 2000; Kormendy & Ho 2013) – which relates the mass of the SMBH with the stellar velocity dispersion in the galactic bulge – and the simultaneous peak between star formation rate (SFR) and SMBH accretion rate in cosmological studies at $z \approx 2$ (Silverman et al. 2008; Madau & Dickinson 2014) are some of the indications towards a causal connection between host galaxy evolution and of its SMBH.

The energy released by the AGN in the form of radiation, winds, or radio plasma jets is known to impact on the interstellar medium of the host galaxy. All these processes are collectively known as feedback. The role of such AGN feedback in the evolution of galaxies, however, is still a subject of ongoing debate. AGN feedback may be a key factor in quenching star formation, mainly in the late stages of the host galaxy's evolution (Di Matteo et al. 2005; Croton et al. 2006). In fact, large scale hydrodynamic simulations of galaxy formation are not able to reproduce observed properties of massive galaxies if AGN feedback models are not included (Springel et al. 2005; Bullock & Boylan-Kolchin 2017) in which these processes are responsible for suppressing the growth of the most massive galaxies by heating and expelling the gas that would form more stars. Powerful AGN

★ E-mail:muryel@astro.ufsc.br

driven winds are a possible mechanism for preventing further growth of the host galaxy. These winds can have outflow velocities as high as 1000 km s^{-1}(Rupke & Veilleux 2011; Greene et al. 2012) and as low as well $\approx 100 - 200$ km s^{-1}, with mass outflow rates in nearby galaxies averaging at a few solar masses per year (e.g. Riffel & Storchi-Bergmann 2011; Crenshaw et al. 2015; Revalski et al. 2018).

Theoretical studies suggest large scale events like major mergers are the dominant processes leading to SMBH growth at high masses (Menci et al. 2014). At high redshifts ($z > 2$), major mergers have also been proposed as fuelling mechanisms of the fastest-growing SMBHs (Treister et al. 2012). A major merger can destabilise large quantities of gas, driving massive inflows towards the nuclear region of galaxies and triggering bursts of star formation and nuclear activity (Hopkins & Quataert 2010; Blumenthal & Barnes 2018). Many studies have found that the most luminous AGN are preferentially hosted by galaxy mergers (Schawinski et al. 2010; Glikman et al. 2015; Fan et al. 2016). At lower luminosities, several studies have found a higher incidence of galaxies with signatures of interactions in AGN hosts as compared to control samples (Koss et al. 2010) and particularly in close galaxy pairs (Ellison et al. 2011; Satyapal et al. 2014) suggesting kinematic pairs are conducive environments for black hole growth.

One possible consequence of gas inflow is the circumnuclear star formation (Hopkins et al. 2008; Hopkins & Quataert 2010). Such merger-driven inflows can both increase the star formation rate (Ellison et al. 2013; Pan et al. 2019) and modify the metallicities gradients of the galaxies (Barrera-Ballesteros et al. 2015). However, classical emission-line SFR probes (e.g. Kennicutt 1998) and metallicity calibrations (e.g. Alloin et al. 1979; Pettini & Pagel 2004) cannot be applied to active galaxies, due to the contamination of the AGN ionisation to the emission lines. In this way, the use of stellar populations synthesis, by performing full spectral fitting, can reveal clues on the star formation history (SFH) and chemical evolution of AGN host galaxies and its content.

In this context, we present high spatial and spectral resolution optical IFU observations of the inner 1.1 kpc of NGC 2992. NGC 2992 is a nearby interacting Seyfert galaxy seen almost edge-on ($i \sim 70°$, Marquez et al. 1998) at a distance, as measured using the Tully-Fisher relation, of 38 Mpc (Theureau et al. 2007), which translates into a projected angular scale of $\sim$ 150 pc per arcsec. Alongside with the starburst galaxy NGC 2993 and the tidal dwarf galaxy A245N it forms the system Arp 245. Using hydrodynamic simulations, Duc et al. (2000) reported the system is currently at an early stage of the interaction, about $\approx$ 100 Myr after pericentre passage. Nevertheless, tidal tails have already developed, which can be seen by optical images (Fig. 1), in CO and HI lines (Duc et al. 2000) and infrared (IR) images (García-Bernete et al. 2015).

The galaxy nuclear activity has been the subject of several studies, partly due to its variability as seen both in X-rays and in the optical (Trippe et al. 2008), even leading to changes in spectral classification. Early spectra published by Shuder (1980), Veron et al. (1980), and Ward et al. (1980) all show the presence of a weak broad Hα component, originated in the BLR, but no detectable corresponding broad Hβ component, leading to its original classification as a Seyfert 1.9. Observations from 1994 (Allen et al. 1999), however, display no broad Hα component, thus having the classification of Seyfert 2. Gilli et al. (2000) reported a broad Hα emission again, just to disappear once again when observed in 2006 by L. Trippe et al. (2008). More recently Schnorr-Müller et al. (2016), after subtracting the narrow component, were able to detect the broad Hβ component for the first time, then classifying the galaxy as a Seyfert 1.8.

In the radio, 6 cm observations show a double lobe 8-shaped structure of about 8 arcsec ($\sim$ 1 kpc) extension to the northwest and Southeast of the galaxy, along position angle (PA) of $-26°$ (Ulvestad & Wilson 1984). From IR observations, Chapman et al. (2000) suggest the best interpretation is that this structure is related to expanding plasma bubbles, possibly carried by internal jets from the AGN. More recently, using radio polarimetry, Irwin et al. (2017) found another double-lobed radio morphology within its spiral disc, which was revealed in linearly polarized emission but not in total intensity emission. This second structure by Irwin et al. (2017) is much more extended than the one found by Ulvestad & Wilson (1984) reaching several kpcs from the nucleus, being interpreted by the authors as a relic of an earlier episode of AGN activity.

NGC 2992 gas kinematics is complex as found by several long slit spectroscopy studies (e.g. Marquez et al. 1998; Veilleux et al. 2001) as well as by several Integral Field Unit observations (García-Lorenzo et al. 2001; Friedrich et al. 2010; Müller-Sánchez et al. 2011). These observations show, at most positions, the presence of a double component line profile. While one component follows the galaxy rotation curve, the other is interpreted as outflowing gas by the authors. Using The Multi Unit Spectroscopic Explorer (MUSE Bacon et al. 2010) at the Very Larga Telescope (VLT) Mingozzi et al. (2019) clearly show the presence of a kpc-scale, bipolar outflow with a large opening angle.

This paper is the first in a series which will explore the possible connection between merger and AGN in Arp 245. In this first paper, we analyse both the stellar populations and the properties of the ionised gas of NGC 2992, in order to better understand the physical conditions of the nuclear region and the mutual role of nuclear activity and the interaction may play. In a second paper (Guolo-Pereira et al., in prep., Paper II) we will observationally explore the effects of the interaction in NGC 2993. While in the third one (Lösch et al., in prep, Paper III) we will present a modern version of the hydrodynamics simulations by Duc et al. (2000) focusing on the possible triggering of the AGN during the merger.

The present paper is organised as follows: in section 2 we describe the observations and data reduction; section 3 we present the stellar populations synthesis and its spatial distribution; the ionised gas kinematics is described in section 4; ionisation mechanisms are discussed in section 5; section 6 presents our discussion of the main results and their significance; and finally section 7 contains our conclusions.

2 OBSERVATIONS AND DATA REDUCTION

This work is mostly based on data obtained with the Integral Field Unit (IFU) of the Gemini Multi Object Spectrograph (GMOS) at the Gemini South telescope on the night of February 15, 2018 (Gemini project GS-2018A-Q-208, P.I. Ruschel-Dutra). The observations consisted of two adjacent IFU fields (covering 5″× 3.″5 each). The fields are slightly offset, both in Right Ascension (RA) and Declination (Dec), in order to increase the field of view (FoV) and cover a larger portion of the galaxy plane. For each IFU field, there are six exposures, with an integration time of 560 seconds each. Each science observation is accompanied by a 5 × 1.″75 sky observation for atmospheric lines removal.

The spatial resolution is limited by seeing, which was at 0.″8 during the observations, corresponding to 120 pc at the galaxy. The observed spectra covered a range from 4075 to 7285 Å with an instrumental dispersion $\sigma_{\rm instr} \approx 40$ km s^{-1}, obtained from the Copper-Argon arc lamp lines.

The reduction procedures were performed using the Gmos Ifu RE-

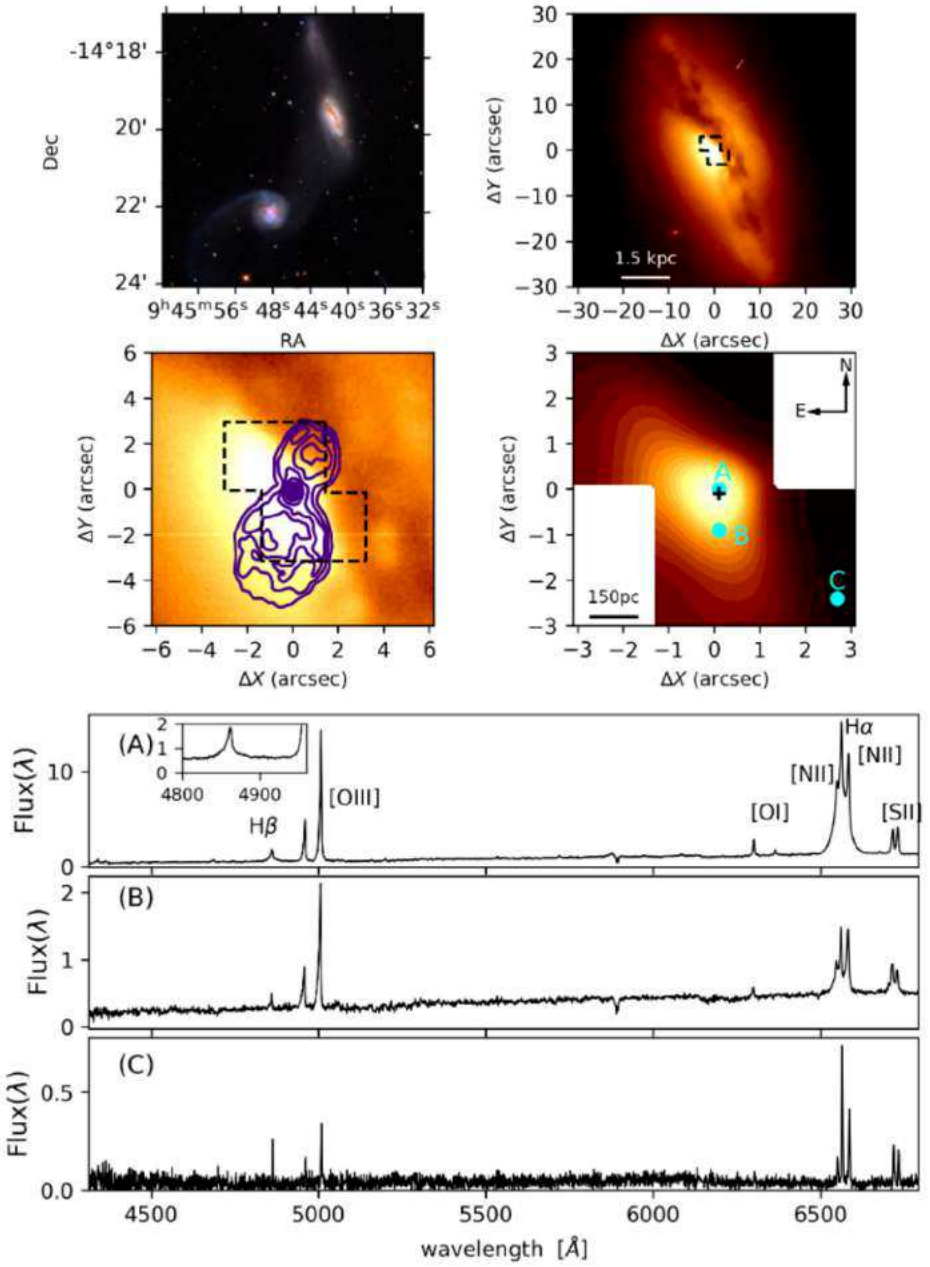

Figure 1. Top Left: LRGB image composition of Arp 245 from Block (2011). Top Right: GMOS r' band acquisition image of NGC 2992. Middle Left: Zoomed acquisition image, and the Ulvestad & Wilson (1984) radio emission in purple (contours : 3, 6, 9, 15, 30, 50, 70, 90 per cent of the peak of 7.2 mJy). The dashed rectangles show the two IFU FoV's. Middle Right: IFU continuum mean flux in the FoV. The black cross represents the continuum nuclear position in all figures of the paper. All maps of the paper were smoothed using a Gaussian kernel with FHWM with half of the spatial resolution, see section 2. Bottom, from top to bottom: Spectra corresponding to the regions marked as A, B and C, with spectral flux density in units of 10^{-15} erg s^{-1} cm^{-2} Å^{-1}. North is up and East to the left in this and all figures of the paper.

Duction Suite (GIREDS)[1]. The process comprised the usual steps: bias subtraction, flatfielding, trimming, wavelength calibration, telluric emission subtraction, relative flux calibration, the building of the data cubes, and finally the registering and combination of the 12 individual exposures. The final cube was built with a spatial sampling of 0.″1 × 0.″1, resulting in a FoV with ≈ 2800 spaxels. After cropping the borders and superimposing the FoVs, it results in a total useful combined FoV, with total angular coverage of 29 arcsec^2 around the nucleus. The combined FoV is centred at RA = 9h45m42s and Dec = -14^{o}9′3″, while the continuum peak is shifted at ΔRA = 0.1″and ΔDec = -0.1″.

Many Gemini data cubes show certain "instrumental fingerprints", in the form of vertical stripes in the reconstructed data cube. Such features also have specific spectral signatures. In order to identify and remove these instrumental features, we use a technique based

[1] GIREDS is a set of python scripts to automate the reduction of GMOS IFU data, available at GitHub.

on Principal Component Analysis (PCA, Menezes et al. 2014). The fingerprint removal is fundamental for the stellar population synthesis because its effect is more apparent for lower instrumental counts. The data cube spectra were corrected for Galactic extinction using the Cardelli et al. (1989) extinction curve (CCM) for an $A_V = 0.166$ (Schlafly & Finkbeiner 2011) and by Doppler effect using the radial velocity of 2345 km s^{-1} (see section 4).

We show in the upper panel of the Fig. 1 an LRGB image of the Arp 245 system (Left) and the acquisition image taken with a r' filter (Right). In the middle panel we show a zoomed version of the acquisition image superimposed with the the Ulvestad & Wilson (1984) figure of 8-shaped radio emission of the galaxy (Left) and the mean continuum flux in the IFU's FoV (Right), while in the bottom panels we show three sample spectra from representative regions marked, respectively from top to bottom, A, B and C. The prominent dust lane seen in the acquisition image, and in the stellar continuum image from the IFU, has a reported A_V greater than 3 (Colina et al. 1987; Schnorr-Müller et al. 2016). Spectra from this region of high extinction have no measurable stellar component above the noise level, as exemplified by the spectrum extracted from C. The nuclear spectrum shows a broad Hα component, and a faint broad Hβ is also present, in contrast with its original Seyfert 1.9 classification but in agreement with its the current state, Seyfert 1.8, proposed by Schnorr-Müller et al. (2016).

3 STELLAR POPULATIONS

In order to obtain the spatially resolved SFH, and to fit the gas emission features, free from the stellar population contamination, we performed stellar population synthesis on the data cube by employing the STARLIGHT full spectra fitting code (Cid Fernandes et al. 2005).

Briefly, STARLIGHT fits an observed stellar spectrum O_λ with a model M_λ built from a linear combination of N spectral components. Dust attenuation is treated as if due to a foreground screen and parametrised by the V-band extinction A_V. Stellar kinematics is modelled with a Gaussian line-of-sight velocity distribution centred at velocity v_*, and with a dispersion σ_*. Besides the model spectrum M_λ, the code outputs the corresponding values of A_V, $v_\star$, $\sigma_\star$, and a population vector $\vec{x}$ containing the percentage contribution of each base population to the flux at a chosen normalisation wavelength λ_0, which in our fits was chosen as $\lambda_0 = 5500$ Å. The code minimises the χ^2 of the fit, though a more convenient and intuitive figure of merit to assess the quality of the fit is through *adev* parameter, defined as the mean value of $|O_\lambda - M_\lambda| / O_\lambda$ over the fitted wavelengths.

We note that, while there are many different spectral fitting codes and techniques available, cross-comparison of these various techniques have shown to yield rather consistent results (e.g. Koleva et al. 2008; Ferré-Mateu et al. 2012; Maksym et al. 2014; Mentz et al. 2016; Cid Fernandes 2018). Therefore, rather than trying different fitting codes, we chose to maintain STARLIGHT and investigate the differences introduced by the choice of models and stellar libraries, which are known to produce variations in the recovered properties (e.g. Maraston & Strömbäck 2011; Chen et al. 2010; Wilkinson et al. 2017; Baldwin et al. 2018; Dametto et al. 2019).

3.1 Evolutionary Models, Stellar Libraries and Featureless Continuum

This section discusses the stellar population models and stellar libraries used in this work, and how we can account for the contribution of a featureless continuum due to the AGN in NGC 2992.

The key ingredients in the stellar population synthesis method are the spectral base elements, i.e. those spectra available to the fitting code to combine in order to recover the galaxy properties. The base elements are, usually, Simple Stellar Population (SSP), i.e. a collection of stars with same age and metallicity, taken from an evolutionary model which are constructed using a stellar spectra library and an Initial Mass Function (IMF).

In this work we have used SSPs from two models: Bruzual & Charlot (2003, BC03), which uses the STELIB (Le Borgne et al. 2003) spectral library, and Maraston & Strömbäck (2011, M11), which employs the MILES (Sánchez-Blázquez et al. 2006) spectral library. For both models/libraries we use the same Chabrier (2003) IMF and instantaneous star formation bursts. We found varying the IMF produces only minor variations in the recovered SFH when compared to the changes introduced by using distinct models. The former is outside the scope of this work, and we refer the reader interested in this particular effect to Chen et al. (2010), Ge et al. (2019) and references therein. From the SSPs provided by BC03 we choose a set of 45 representative elements divided into three metallicities (0.2, 1.0, 2.5 Z$_\odot$) and an age range covering from t(Gyr) = 0.001 to t(Gyr) = 13. From those available by M11 with the MILES library we chose a set of 40 SSPs with age and metallicity coverage as similar as possible to the BC03 ones: three metallicities (0.5, 1.0, 2.0 Z$_\odot$) and ages ranging from t(Gyr) = 0.007 to t(Gyr) = 13. The complete list of SSPs used from each model is shown in Table 1. It is important to mention that the MILES Library does not provide metal-poor stars ($Z = 0.5$ Z$_\odot$) younger than 55 Myr (0.055 Gyr), and neither metal-rich stars ($Z = 2.0$ Z$_\odot$) younger than 100 Myr (0.1 Gyr), while BC03/STELIB provide the same age range for the three metallicities (see Table 1).

We define a reduced population vector with three age ranges: $t <$ 100 Myr; 100 Myr $\leq t \leq$ 1.4 Gyr; and $t >$ 1.4 Gyr, to obtain a more robust description of the SFH than that obtained with the full population vector (see, e.g. Cid Fernandes et al. 2005), as well as to facilitate the visualisation of the spatially resolved fit results. The population vector components are denoted by x_Y, x_I and x_O, where 'Y', 'I' and 'O' stands for young, intermediate and old respectively. The division in a reduced population vector has been used in several works in stellar population synthesis (e.g. Cid Fernandes et al. 2005; Riffel et al. 2010a; Cid Fernandes et al. 2013; González Delgado et al. 2015; Mallmann et al. 2018), while the range values may be slightly distinct from one another, the ones adopted here are the most common. Also, for the young population the cutting value of 100 Myr is the estimated age of the pericentre passage between NGC2992 and its companion (Duc et al. 2000).

When dealing with stellar populations in Seyfert galaxies, a power law ($F_\lambda \propto \lambda^{-\alpha}$) featureless continuum (FC) should be added to the spectral base (Koski 1978) to account for the AGN emission. Values for α are between 0.5 – 2.0 (Osterbrock & Ferland 2006), with many authors working with large samples of galaxies assuming a general value of $\alpha = 1.5$ (Storchi-Bergmann et al. 2003; Raimann et al. 2003; Cid Fernandes et al. 2004; Mallmann et al. 2018). Since this work is focused on a single object, we propose a method to specifically fit the α index for the optical spectrum of NGC 2992. We extracted two integrated spectra: an inner one, hereafter $S(\lambda)$, defined as the sum of spectra within a circular region with radius of 0.″4, and an external one, $E(\lambda)$, in an annulus with inner radius of 1″ and outer radius of 1.″4, both centred at the peak of continuum emission. We model the $S(\lambda)$ spectrum as a combination of $E(\lambda)$ and a power law FC ($F_\lambda \propto \lambda^{-\alpha}$), both reddened by the same factor and normalised in the same wavelength, $\lambda_0 = 5500$ Å, as follows:

Table 1. SSPs used in the stellar population synthesis.

Model	BC03			M11		
Spectral Library	STELIB			MILES		
Metallicity ($Z_\odot$)	0.2	1.0	2.5	0.5	1.0	2.0
Ages (Gyr)	0.001, 0.003, 0.005, 0.01, 0.025, 0.04, 0.1, 0.3, 0.6, 0.9, 1.5, 3.0, 5.0, 11.0, 13.0			0.055, 0.065, 0.075, 0.085, 0.1, 0.15, 0.3, 0.6, 0.9	0.007, 0008, 0.009, 0.01, 0.015, 0.025, 0.04, 0.055, 0.065, 0.075, 0.085, 0.1, 0.15, 0.3, 0.9, 1.5, 3.0, 5.0, 11.0, 13.0	0.1, 0.15, 0.3, 0.6, 0.9, 1.5, 3.0, 5.0, 11.0, 13.0

$$\left(\frac{S_m(\lambda)}{S_m(\lambda_0)}\right) = \left[(1-p)\left(\frac{E(\lambda)}{E(\lambda_0)}\right) + p\left(\frac{\lambda}{\lambda_0}\right)^{-\alpha}\right] \times 10^{-0.4\delta A_V q_\lambda} \quad (1)$$

where $S_m(\lambda)$ is the model spectrum, p is the fraction contribution of the FC, δA_V is the difference in extinction between the $S(\lambda)$ and $E(\lambda)$ regions. The values which minimise the residuals between $S(\lambda)$ and $S_m(\lambda)$ are $p = 0.23$, $\delta A_V = 2.2$ and $\alpha = 1.7$.

It should be noted we are over-simplifying by assuming that $S(\lambda)$ is the combination of $E(\lambda)$ and an FC, i.e. the stellar spectrum of both are the same. However, we argue this is just a method to get a data-based value for α, instead of just assuming a fixed value which is even less physically justified. Also, no further interpretation will be given in this regard besides the adoption of this α value to produce the FC base element[2].

3.2 Spatially Resolved Stellar Populations Synthesis

In order to perform the spatially resolved stellar synthesis with enough signal to noise ratio (S/N) we employed the Voronoi tessellation technique (Cappellari & Copin 2003) in our data cube, with a S/N target set to 20. Results from Cid Fernandes et al. (2005) show at this level STARLIGHT is able to reliably recover input parameters. Some spectra, however, failed to reach the desired S/N, even when combining several tens of spaxels, specifically those obscured by the galaxy's dust lane. Henceforward we will just analyse and show the results for those voronoi zones which the combined-spectra has $S/N \geq 10$, relying again on Cid Fernandes et al. (2005) tests that show it to be the minimum value to the reliability of the code. STARLIGHT measures the S/N as the ratio between the mean and the Root-Mean-Squared (RMS) flux in a user-selected region of the spectrum (which should be as featureless as possible), the range adopted here is a $\Delta\lambda = 20$ Å wide window around the normalisation wavelength as measured from the combined-spectra of the Voronoi zone.

In order to be able to explore both the effects of the FC component and the change of model/library, we run the STARLIGHT code in the spaxels of the binned cube using three distinct spectral bases:

- *BC03*: Only stellar SSP components from the BC03/STELIB models, see Table 1 for ages and metallicities.
- *BC03+FC*: Same as BC03 stellar SSPs, with the addition of an FC component ($F_\lambda \propto \lambda^{-1.7}$) to the spectral base.
- *M11+FC*: Stellar SSP components from M11/MILES, see Table 1 for ages and metallicities, in addition to the FC component.

Since the effects of the presence/absence of FC component can be tested comparing *BC03* with *BC03+FC*, and the change of model/library is explored comparing *BC03+FC* with *M11+FC*, we did not find necessary to test the synthesis using *M11* without FC, therefore we kept our analyse within these three configurations.

The FC component is available for STARLIGHT only in the spaxels of the inner 1.1 arcsec[3], which equals 3σ of the Gaussian point spread function. The reason for not allowing the FC to be used throughout the field is that there is a high level of degeneracy between the FC and a young reddened population (further discussion in Cid Fernandes & González Delgado (2010) and the next section), and also because there is no physical reason to have an FC emission outside the nucleus since it is emitted by the spatially unresolved accretion disk. We will call the percentage contribution of the FC to total light of a spaxel as x_{agn}. During the synthesis all the emission lines were masked (see Fig. 2), the mask is the same in all spaxels with exception to the central ones (r < 1.1″) where Hβ and [N II] +Hα masks are broader. The sum of x_Y, x_I, x_O, x_{agn} values is always 100 per cent for all spaxels.

The maps of the recovered properties from the three distinct bases are shown in Fig. A1, Fig. A2 and Fig. A3 at the Appendix A. These figures show the maps for x_Y, x_I, x_O, x_{agn}, A_V, the light-weighted stellar mean age $\langle log\ t_* \rangle$ defined as:

$$\langle log\ t_* \rangle = \frac{\sum_{j=1}^{N_*} x_j log(t_j)}{\sum_{j=1}^{N_*} x_j} \quad (2)$$

where x_j are the elements of the population vector $\vec{x}$, i.e. the fraction

[2] Further validation of this approximation will be presented throughout the paper, once the almost constant radial profiles shown in Fig. 3 is taken into account, and the inferred stellar A_V estimates, roughly consistent with those derived from the Balmer decrement (see also e.g. Fig. A.1 in Mingozzi et al. (2019) for consistent results) will be presented in appendixes A and B.

[3] The radius(r)= 0.0 is set as the peak of the continuum emission.

contribution of each component to the total light, t_j is the ages of j-th component, and N_* is the number of stellar spectra in the base (SSPs). The figures in Appendix A also shows the light-weighted stellar mean metallicity $\langle Z \rangle$ for each reduced population vector component x_Y, x_I and x_O, respectively $\langle Z \rangle_Y$, $\langle Z \rangle_I$ and $\langle Z \rangle_O$, defined as:

$$\langle Z \rangle = \frac{\sum_{j=t_0}^{t_f} x_j z_j}{\sum_{j=t_0}^{t_f} x_j} \quad (3)$$

where t_0 and t_f are respectively the lower and upper age limit of the reduced population vector components as defined in the previous section.

The upper panel of Fig. 2 shows an example fit for a spaxel at $r = 0.''6$, the residuals between the observed and the fitted spectra and the emission line mask. At the bottom panels the age/metallicity/FC decomposition for the three syntheses are shown as an example of the small differences resulting from the change of spectral base (see subsection 3.3 and subsection 3.4).

In Fig. 3 we show the radial profiles of x_Y, x_I, x_O, x_{agn} and $\langle log\ t_* \rangle$, in bins of $0.''45$ ($\approx$ 70 pc), with points representing the median, and the coloured region represents the 25 and 75 percentiles of the azimuthal distribution for the given radial bin. In Fig. 4 we show the values of $\langle Z \rangle$ for each one of the bases integrated over the entire FoV.

In general terms the presence of a large contribution of old metal-rich SSPs and a smaller, but significant, contribution of young metal-poor stars seems to be independent of the presence of an FC component, or the change of model/library. The detailed analyses of the differences caused by the distinct spectral bases available to the code will be better explored in the sections below.

3.3 The FC Component Usage: Comparing BC03 and BC03+FC

As shown by Fig. 3, the differences in the *BC03* and *BC03+FC* synthesis are seen only at the inner spaxels and are linked to the presence of the FC component in the spectral base. For the external spaxels ($r > 1.''1$), where only BC03 stellar components are used in both synthesis, the recovered properties are identical, as one would expect. In the external spaxels, the x_O values range between 75 per cent and 85 per cent, with all spaxels having super-solar mean metallicity, $\langle Z \rangle_O > 1.5\ Z_\odot$, and the majority of them being close to the upper limit of the models, $\langle Z \rangle_O \approx 2.5\ Z_\odot$. The x_Y values are between 15 per cent and 25 per cent, with most spaxels having a sub-solar mean metallicity, $\langle Z \rangle_Y \leq 1.0\ Z_\odot$, with a considerable portion of them at the lower limit of the model, i.e. $\langle Z \rangle_Y = 0.2\ Z_\odot$. Some properties are identical in all runs even at the inner spaxels, A_V is very high in the innermost spaxels ($A_V > 3$ mag) declining rapidly to $A_V \approx 2.5$ mag and reaching 1.5 mag at the border spaxels (A_V map shown at Appendix A). Similarly, the contribution from intermediate SSPs, x_I, is null at most spaxels and reaches a maximum value between 10 and 20 per cent in very few regions.

Comparing the inner spaxels of *BC03* and *BC03+FC*, we see that the presence of an FC component in the base causes a decrease in x_O by just a few per cent. Larger differences, however, are seen in the contribution from young stars, especially where an FC component is not available (*BC03*). In this case, there is a sharp increase in x_Y from a steady 20 per cent at $r > 1''$ to more than 40 per cent at the centre. On the other hand, the (*BC03+FC*) base produces a roughly constant x_Y at $r < 1.0''$, while x_{agn} increases from ~0 per cent at $1.0''$ to ~20 per cent in the innermost spaxels. This effect is caused by the above-mentioned degeneracy between an FC spectrum and a young-reddened SSP (Cid Fernandes et al. 2004; Cid Fernandes & González Delgado 2010). As shown by Cardoso et al. (2017), fitting a spectrum that contains an AGN power law-like continuum with only stellar components causes the solution to have an excess of young populations, which leads to a drop in the $\langle log\ t_* \rangle$ (see the bottom panel of Fig. 3). Although such degeneracy can cast some doubts in the exact values of the x_Y and x_{agn} decomposition in *BC03+FC*, the fact that the solution at the centre has x_Y values compatible with the ones of the external regions of the FoV, and that the FC component contribution follows a radial profile compatible with an unresolved source (i.e increasing from $x_{agn} \approx 0$ per cent to $x_{agn} \approx 20$ per cent at the continuum peak) is strong evidence in favour of the existence of an FC emission in NGC 2992.

3.4 Decomposition Stability: Comparing BC03/STELIB and M11/MILES

In this section we discuss differences in the recovered properties between *BC03+FC* and *M11+FC* bases and their derivations. We do not intend to make a detailed analysis of the models and its derivations, nor to suggest one is a better choice than the other for use with this type of data. Such discussions can be found in other studies, e.g. Baldwin et al. (2018); Ge et al. (2019). Instead, we merely want to test the stability of the inferred stellar properties with changes in models.

Besides the distinct stellar libraries used in these model libraries, they also employ different evolutionary prescriptions (see Conroy 2013, for a review on stellar evolutionary models). BC03 is constructed using the isochrone synthesis approach, while M11 uses the fuel consumption theory. The treatment of the thermally pulsing asymptotic giant branch (TP-AGB) phase is also a major topic of disagreement between different models. For example, Dametto et al. (2019) found a relative excess of young populations and lack of intermediate-age components when Near-Infrared (NIR) stellar populations synthesis are performed with BC03 SSPs, favouring results achieved with the M11 models. Nevertheless, these effects are much more important when modelling stellar populations in the NIR, being significantly less relevant in the optical.

Both x_{agn} and A_V are very similar to those obtained with *BC03+FC*, but the population vectors have notable differences. For instance, x_O values for *M11+FC* are systematically lower by ~5 to 10 per cent than those recovered with *BC03+FC*, while at the same time both x_Y and x_I are conversely higher for *M11+FC*. Given the increase of both x_Y and x_I and the decrease in x_O, the light-weighted mean stellar age $\langle log\ t_* \rangle$ for *M11+FC* is systematically lower than for *BC03+FC* by ~ 0.5 to 0.1 dex, as show in the bottom panel of Fig. 3.

Although there are small differences in age decomposition, the metallicity general pattern seems to be maintained. As can be seen in Fig. 4, the old populations have a super-solar mean metallicity, close to the upper limit of the model ($1.5\ Z_\odot < \langle Z \rangle_O \leq 2.0\ Z_\odot$) and the young populations have a solar to sub-solar mean metallicity ($\langle Z \rangle_Y \leq 1.0\ Z_\odot$), as shown in the middle panels of Fig. 4. However, while the values of $\langle Z \rangle_Y$ in *BC03+FC* are mostly sub-solar ($\langle Z \rangle_Y < 1.0\ Z_\odot$) the values in *M11+FC* are all solar ($\langle Z \rangle_Y = 1.0\ Z_\odot$). This discrepancy is probably caused by the fact that the MILES library does not contain SSPs with a sub-solar metallicity younger than 55 Myr (see Table 1). For instance, in the example of Fig. 2, while *BC03* and *BC03+FC* recover its young populations as a combination of three SSPs with ages of 1 Myr, 5 Myr and 10 Myr, the two first with sub-solar metallicity ($Z = 0.2\ Z_\odot$) and the later with solar

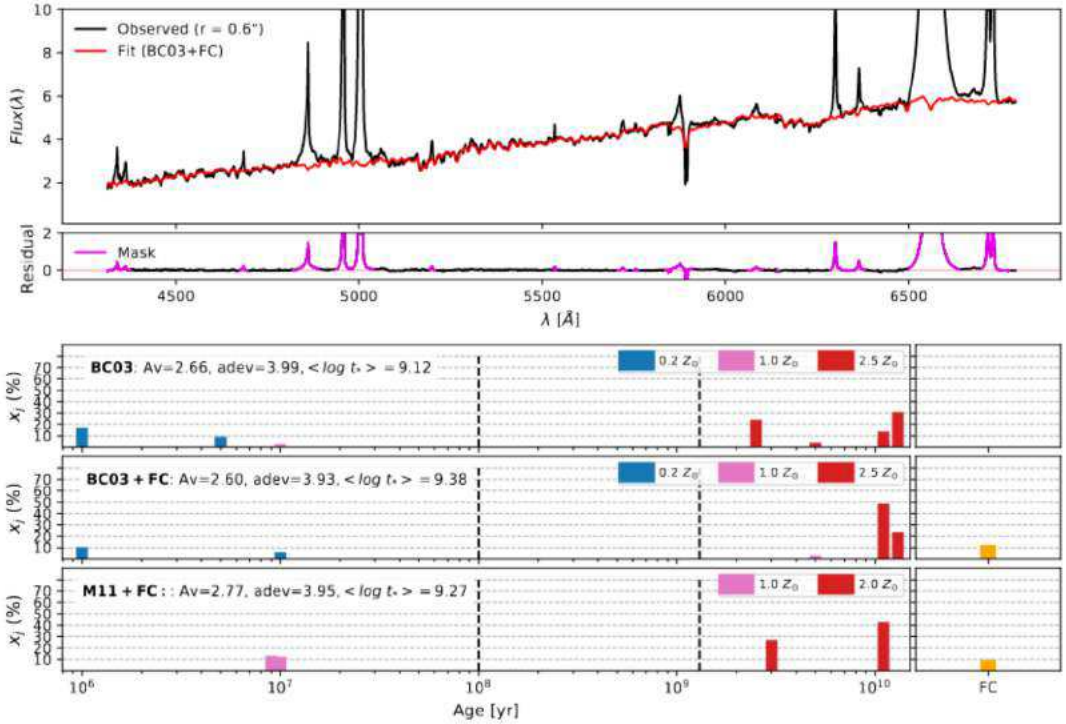

Figure 2. Example of stellar population synthesis fit. Top: Observed (black) and synthetic (red) spectra both in units of 10^{-15} erg s^{-1} cm^{-2} Å^{-1}in a spaxel at radius equal to 0.″6. Middle: Residual between the observed and synthetic spectra, masked emission lines are shown in purple. Bottom: Age/metallicity and FC decomposition for the three synthesis, *BC03*, *BC03+FC* and *M11+FC*. The dashed lines show the division between x_Y, x_I and x_O SSPs.

metallicity ($Z = 1.0$ Z$_\odot$), the *M11+FC* recovers it as both 9 Myr and 10 yr solar metallicity SSPs, and the fitting code would not be able to fit such a young component with lower metallicity precisely because MILES library does not provide an SSPs with $Z = 0.5$ Z$_\odot$ younger than 55 Myr. Therefore, we can see these $\langle Z \rangle_Y = 1.0$ Z$_\odot$ values in the synthesis using *M11+FC* base as an upper limit for the young population metallicity.

As mentioned, above, we do not claim any of the three syntheses to be the one that better describes the data. In fact, there are no significant differences in the *adev* parameters among the bases: *adev* values range from 3 per cent at the inner spaxels up to 8 per cent at larger radius. Recovered properties produced with the distinct models present the same general trend (see subsection 3.2). However, we argue the bases which include an FC component are more physically justified. Both the large decrease in $\langle log\, t_* \rangle$ in the inner spaxels, when this component is ignored, and the fact that the FC components fluxes have a spatial profile characteristic of a point-like source (FWHM $\approx$ 0.″8, see Fig. 7) are strong evidence of the existence of an FC like emission in NGC 2992. It is worth mentioning even though we are not discussing results for the stellar kinematics, we have made sure all the three decompositions were kinematically consistent with each other, and no non-physical value was fitted to v_*, σ_* parameters, which would cause an incorrect subtraction of the continuum used in emission line fitting procedures of the next sections.

4 GAS KINEMATICS

Emission line structure of the central regions of AGN is very complex, often possessing multiple velocity components along the line of sight (e.g. Villar-Martín et al. 2011; Veilleux et al. 2013; McElroy et al. 2015). For the type-1 and intermediate-type AGNs, the presence of both narrow and broad emission lines are seen; these emission lines are believed to come from two distinct parts of the AGN. The first is named the "Broad Line Region" (BLR). Its typical size, as deduced from the broad line variability, is 10-100 light-days, therefore it is spatially unresolved by current observations, meaning that its spatial profile is the same as the point spread function (PSF) of the observation. BLR emission is characterised by very broad (1000 km s^{-1}< FWHM < 10000 km s^{-1}) Balmer lines and the absence of forbidden lines (Peterson 1997). In most cases, the line profiles strongly deviate from a Gaussian profile, e.g. NGC 1097 (Schimoia et al. 2015). The second region is the "Narrow Line Region" (NLR) which is much larger than the BLR since no clear variation of the narrow emission lines is observed in objects undergoing large variations of the AGN's featureless continuum on timescales shorter than several years. The NLR is resolved by ground-based observations showing dimensions of 100-1000 pc in most nearby AGNs and up to several kpc's in higher redshift quasars (Bennert et al. 2006; Sun et al. 2017; Storchi-Bergmann et al. 2018). The NLR emission is characterised by both permitted and forbidden lines with lower velocity dispersion (FWHM < 1000 km s^{-1}), but still broader than emission lines of normal star forming galaxies. Even the NLR emission lines are some times not well fitted by a simple Gaussian profile, given the presence of multiple kinematical components in the line of sight, e.g. gaseous disk rotation, gas outflows and inflows (e.g. Zakamska et al. 2016; Schnorr-Müller et al. 2017).

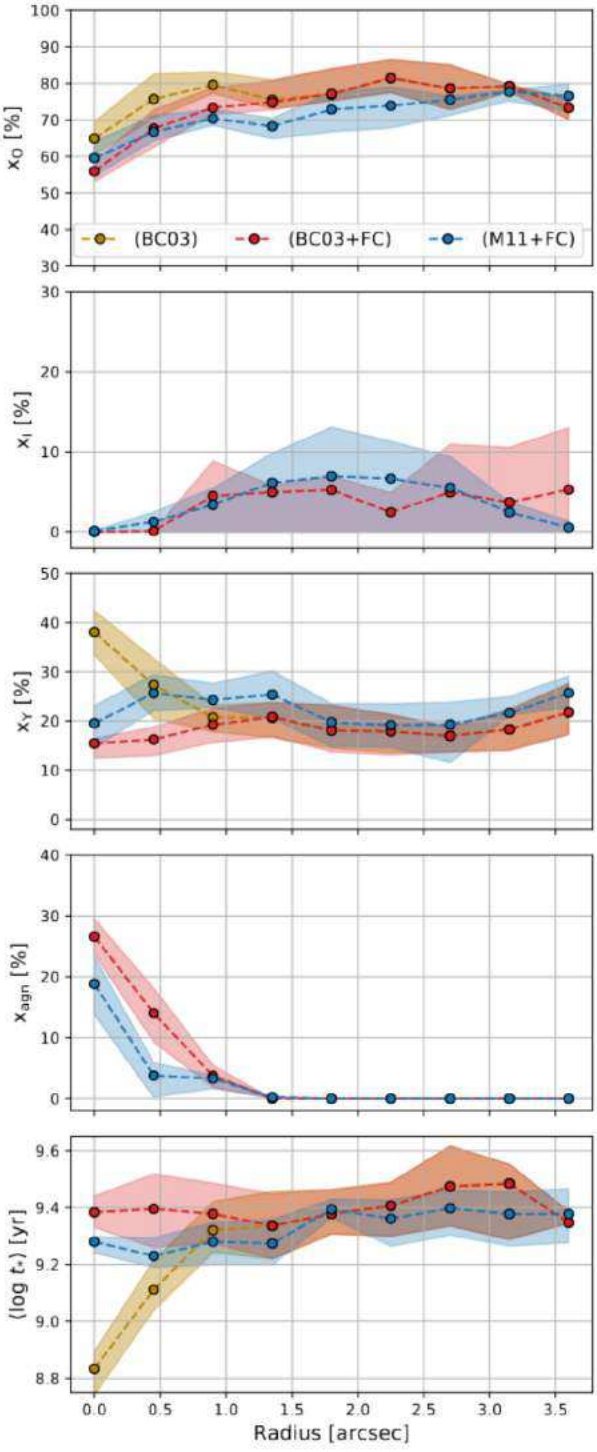

Figure 3. Radial profiles of the recovered properties for *BC03* (gold), *BC03+FC* (red) and *M11+FC* (blue) in bins of 0.″45 (~ 70 pc). From top to bottom: Per cent contribution to the total light from young (x_O), intermediate (x_I) and old (x_Y) SSPs, from the FC (x_{agn}) and the light-weighed mean stellar age ($\langle log\ t_* \rangle$). x_{agn} is null for *BC03* by definition. The x_I values for *BC03* are not shown, however they are exactly the same as *BC03+FC*.

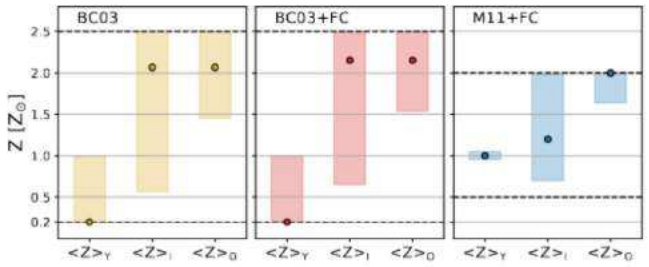

Figure 4. Values of $\langle Z \rangle_Y$, $\langle Z \rangle_I$ and $\langle Z \rangle_O$ integrated over the entire FoV for each base, from left to right, respectively, *BC03*, *BC03+FC* and *M11+FC*. Points are the median values, and the coloureds bars are the 25 and 75 percentiles. The dashed black lines show the metallicity limit for each of the models.

4.1 Emission line fitting

In order to fit the emission lines in NGC 2992 we use the IFSCube package[4] (Ruschel-Dutra 2020). IFSCube is a python based software package designed to perform analysis tasks in data cubes of integral field spectroscopy, mainly focused on the fitting of spectral features, such as atomic lines. It allows for multiple combinations of Gaussian and Gauss-Hermite functions, with or without constraints to its parameters. Stellar continuum subtraction, as well as pseudo continuum fitting if necessary, are performed internally, and in this case, we used the residual spectra from the stellar population synthesis performed with STARLIGHT. Initial guesses for the parameters are set for the first spaxel, usually, the one with the highest S/N, and all subsequent spectra use the output of neighbouring successful fits as the initial guess.

When dealing with complex emission, the standard approach is to model the line profile with a combination of Gaussian functions. Visual inspection of our IFU shows distinct velocity components, evidenced by large asymmetries in the line profiles, are present in over one-third of the spectra in the FoV. As a result, we decided to model these components separately and to investigate whether they possessed any meaningful physical information, following previous works (e.g. Villar-Martín et al. 2011; McElroy et al. 2015; Fischer et al. 2018).

For every fitted emission line, we determined if the multi-component model was statistically justified, and not a better fit purely by virtue of the extra model parameters, by performing a series of f-tests. The f-test is a standard statistical test to gauge whether a higher order model is preferable to a simpler model when fitting a particular data set. We set the false rejection probability for the lower order model to 10^{-5}. The higher this threshold is set, the harder it is to justify a more complex model and the more likely it is to be over-fitting noise. The reader interested in more detailed analyses and a step-by-step deduction of the application of f-test in astrophysics emission line fitting is referred to Freund (1992) and statistical references therein.

As an Intermediate-type Seyfert nucleus, NGC 2992 presents both BLR and NLR emission. The BLR emission lines (Hα and Hβ) are blended with some NLR emission lines (Hα, [N II]λ6548, [N II]λ6583 and Hβ), leading to degeneracies if both NLR and BLR emission lines are fitted, spaxel by spaxel, at the same time with all parameters free. Fortunately, the fact that the BLR is not resolved, i.e. its kinematics and its Balmer decrement (Hα/Hβ) can not

[4] http://github.com/danielrd6/ifscube

vary spatially, can be used to decrease this degeneracy. Our chosen methodology consists on first fitting an integrated spectrum to fix the BLR emission line profile (kinematics and Balmer decrement), and later using this BLR spectrum as a fixed component, except for the flux, on the spatially resolved NLR fits.

We extracted a spectrum centred at the continuum peak, using a virtual aperture of $3\sigma = 1\farcs1$ (σ refers to the Gaussian point spread function). In this spectrum we fitted [N II]λ6548, [N II]λ6583, Hα (both BLR and NLR) and Hβ (both BLR and NLR), adding Gaussian components to the emission lines until the addition of a new component does not increase the fitting quality, as measured by the f-test described above. The final fit has shown that two Gaussians are necessary to fit each one of the BLR Balmer emission lines. This resulting profile, meaning the superposition of two Gaussian functions, hereafter called as BLR Component, can be seen in panel (1) of Fig. 5, and is characterised by a $\mathrm{FWHM_{BLR}} = 2010$ km s^{-1} and a Balmer decrement of $(\mathrm{H}\alpha/\mathrm{H}\beta)_{\mathrm{BLR}} = 24.2$. These values are in considerable agreement with the ones fitted by Schnorr-Müller et al. (2016), $\mathrm{FWHM_{BLR}} = 2192$ km s^{-1} and $(\mathrm{H}\alpha/\mathrm{H}\beta)_{\mathrm{BLR}} = 19.2$, considering these authors used three Gaussian functions to model the profile and the BLR of NGC 2992 has been shown to vary in a few years period (L. Trippe et al. 2008).

In order to resolve the kinematics of the NLR and obtain maps of emission line ratios, we fitted the following eight strongest emission lines present in the data cube: Hβ, [O III]λ4959, λ5007, Hα, [N II]λ6548, λ6583 and [S II]λ6716, λ6731. Each emission line was modelled with a set of Gaussian functions. The central wavelength of the Gaussian functions was allowed to vary by up to $\pm$400 km s^{-1} and the velocity dispersion up to 400 km s^{-1} (FWHM $\approx$ 1000 km s^{-1}). We added one more set of Gaussians to the fit, meaning that each emission line is modelled by up to two Gaussian components. To reduce the number of free parameters, each set of Gaussians was required to have the same velocity and velocity dispersion (meaning their relative wavelengths were fixed), while their fluxes were allowed to vary. The reason for this is each component represents a kinematically distinct part of the gas, meaning that they may have different ionisation states determined by their relative fluxes. This means that, for example, the single-component set of Gaussians fit to the eight emission lines instead of having twenty four (eight lines $\times$ three parameters) free parameters, only had nine (a single velocity, v, and velocity dispersion, σ, amplitudes of Hα, Hβ, the two [S II] and the stronger [N II] and [O III], while the amplitudes of the weaker [N II] and [O III] were set fixed as 1/3 of the stronger ones, as given by their Quantum Mechanics' probabilities (hereafter we call [O III]λ5007 as [O III], [N II]λ6583 as [N II], and the [S II]λ6716, λ6731 as [S II]). As described in the previous paragraph, the BLR Component was also included in the fit with only the amplitude as free parameter.

To estimate the uncertainties in the parameters, we performed Monte Carlo simulations, in which Gaussian noise was added to the observed spectrum. One hundred iterations were performed and the estimated uncertainty in each parameter was derived from the standard deviation in all the iterations. The uncertainty maps are presented in Appendix B.

We then applied the f-test to each one of the NLR emission lines, spaxel by spaxel, in order to assess if the simple model (single-Gaussian) is enough to fit the data or the more complex model (two Gaussians) is required. The f-test results in spatially contiguous regions of the required number of components for each emission line. The maps for [N II] and [O III] emission lines are shown in Fig. 5 and Fig. 6. The figures also show spectral and emission line fits in selected regions of the FoV.

The maps are not exactly equal for all emission lines, the size of the region in which two components are needed depends on the line S/N[5], therefore the size is maximum for [O III] (Fig. 6) and Hα (Fig. 11), a little bit smaller for [N II] (Fig. 5) and the [S II] doublets (not shown) and much smaller for the low S/N line, Hβ (not shown). However, the general pattern is the same for all emission lines: the data are well fitted by a single-Gaussian in most of the FoV, but in a region, from the nucleus to the end of the FoV in the northwest (NW) direction two Gaussians are needed.

As can be seen in both figures, for those spaxels in which the emission lines are well behaved and symmetric, a single-Gaussian function, which we will call Component 1, is enough to fit the data. However, in the spaxels where two components were statistically significant, the profiles show an asymmetry in the form of a blueshifted wing (see panels (1) and (2) in Fig. 5 and Fig. 6) requiring the addition of a second Gaussian, which we will call Component 2.

In Fig. 7 we show the spatial and radial profile of the BLR Component. As expected for an unresolved structure, this component is detected just in the innermost spaxels, with a spatial distribution of a point-like source, equal to that of the stars in the acquisition image (FWHM $\approx 0\farcs8$, see section 2); at radii larger than 3σ (1.1 arcsec) it is almost undetectable.

4.2 Rotational and Non-Rotational Components in the NLR

Let us now discuss the spatially resolved properties of the NLR Components 1 and 2 and their possible physical interpretation. Component 1 is present in the entire FoV. In the top panels of Fig. 8 we show, from left to right, [O III] flux, velocity dispersion (σ), already corrected by instrumental dispersion. In the middle left panel, we present the radial velocity (v). We show the [O III] flux as an example of the morphology of this component, which is similar to the continuum morphology, with the peak of the emission shifted by only $\sim 0\farcs2$ to southwest (SW), with a steep decrease (up to 2 *dex*) towards the dust lane region. The σ values range from 50-100 km s^{-1} and show a very disturbed pattern. The v map shows values from -130 to 120 km s^{-1} and although it presents some disturbance, a rotation pattern is clearly discernible, with the SW portion receding and the north-eastern (NE) approaching. We have considered the west side of the galaxy is the near one, following the literature (e.g. Marquez et al. 1998; Veilleux et al. 2001); this explains why the emission is seen mainly to the east and less to the west where it is attenuated by the dust lane in the line-of-sight.

In order to quantify how much the velocity field deviates from a pure rotation and to derive both the major axis PA and the inclination of disk we fit the Bertola et al. (1991) model. The model assumes a spherical potential with pure circular orbits, in which the observed radial velocity at a position (R, ψ) in the plane of the sky given by the relation:

$$v(R,\psi) = v_{\mathrm{sys}} + \frac{AR\cos(\psi-\psi_0)\sin\theta\cos^p i}{\left\{R^2\left[\sin^2(\psi-\psi_0)+\cos^2(\psi-\psi_0)\right]+c_0^2 cos^2 i\right\}^{p/2}} \quad (4)$$

where v_{sys} is the systemic velocity, i the inclination of the disk (with $i = 0$ for a face-on disk), A is the amplitude of the curve, c_0 is the concentration parameter and ψ_0 the line of nodes PA. The parameter

[5] Because the f-test detection is sensible to how much the second component, the more complex model, stands out from the noise. Therefore in low S/N lines, it is less likely the f-test will require a complex model.

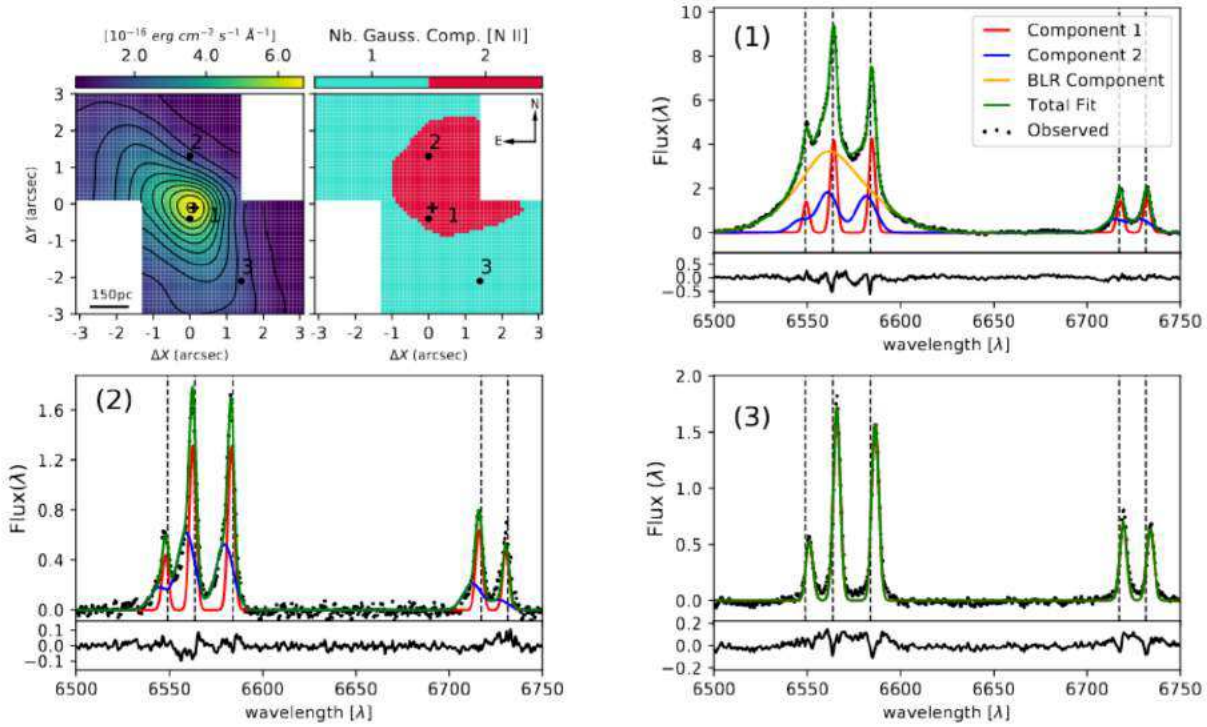

Figure 5. Top left: Map of the continuum emission at $\lambda = 5500$ Å and map of the preferred number of Gaussian components to the [N II] emission-lines. Top right and bottom: Examples of the Hα, [N II]λ6548, λ6583 and [S II]λ6716, λ6930 emission lines fitting and their residual in distinctly regions of the FoV marked in the maps. The vertical axis units in the panels showing the emission-line profiles are 10^{-15} erg s^{-1} cm^{-2} Å^{-1} and the dashed vertical lines show rest-frame wavelength of the lines.

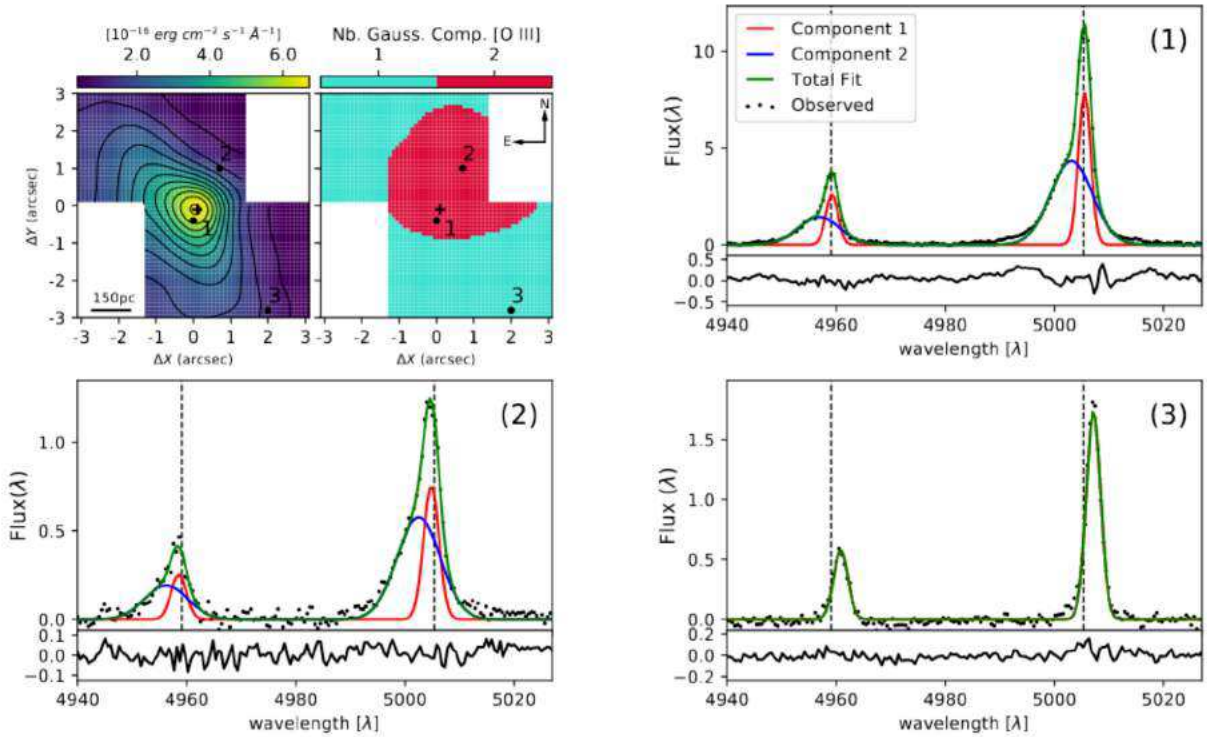

Figure 6. Same as Fig. 5 but for [O III] emission lines.

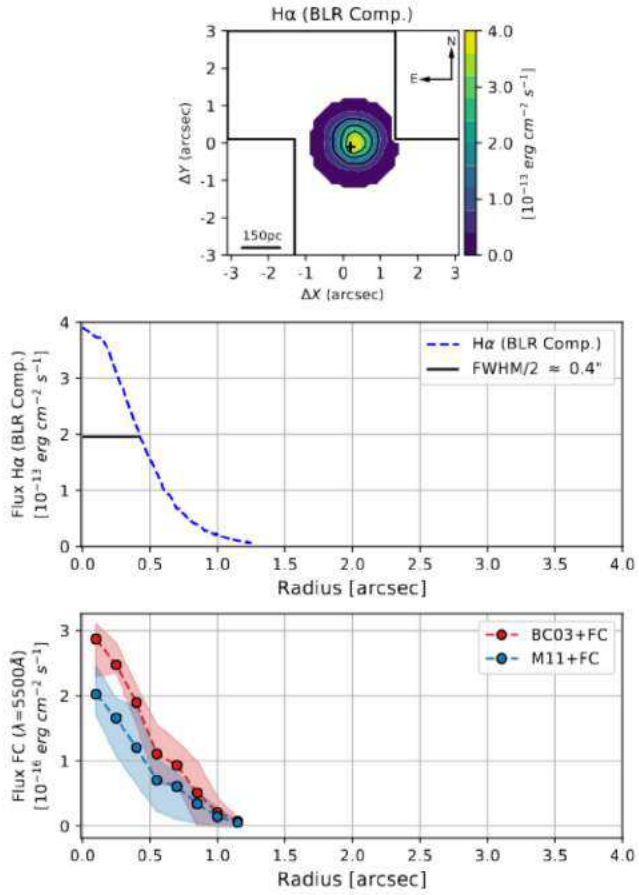

Figure 7. Top: Spatial distribution of the BLR Component. Middle: Radial projection of the BLR Component profile, vertical axis units of 10^{-13} erg s^{-1} cm^{-2}. Both show the point-like source emission of the BLR, with a FWHM ≈ 0.″8 given by the spatial resolution of the observation. Bottom: Radial projection of the FC components fluxes (see section 3), also presenting a point-like source emission.

p defines the form of the rotation curve, varying in the range between 1 (logarithm potential) and 1.5 (Keplerian potential). To avoid the degeneracy between the parameters, we restricted the disk inclination to have values of $i = 70 \pm 10$ (based on Duc et al. 2000, photometric analyses) and we assumed the kinematical centre to be co-spatial with the peak of the continuum emission. A Levenberg-Marquardt least-squares minimisation was performed to determine the best fitting parameters and the uncertainties were obtained by making one hundred Monte Carlo iterations. We show the best parameters and their uncertainties in Table 2.

The PA of the line of nodes was measured as 32±1°, in agreement with previous values from the literature: PA = 32° (Veilleux et al. 2001, hereafter V01), PA= 30° (Marquez et al. 1998, hereafter M98). V_{sys} and i are also in reasonable agreement with other studies of the galaxy: V01 found, respectively, 2335 ± 20 km s^{-1} and 68°, while M98 found 2330 km s^{-1} and 70°. The velocity field amplitude (A = 132±4 km s^{-1}), though, is much lower than the ones found by both V01 and M98 (225±20 km s^{-1} and 250 km s^{-1}). This discrepancy is probably due to the fact that both have used long-slit data in their studies, therefore being able to map the velocity field up to several kpc. Thus having a better constraint in the behaviour of the field at a larger radius, while our data can only recover the internal portion of the velocity field.

Table 2. Best Fitting Parameters Bertola et al. (1991) Model.

Parameters	Values
v_{sys}	2345 ± 5 [km s^{-1}]
A	132 ± 4 [km s^{-1}]
p	1^a
c_0	3.5 ± 0.1 [arcsec]
ψ_0	$32° \pm 1°$
i	$70° \pm 1°$

[a] In the model the parameters p is allowed to vary between 1 and 1.5, the fitted value was equals to 1 in all the Monte Carlo iterations.

The modelled velocity field is shown in the middle right panel of Fig. 8, and the residuals between the observed field and model are shown in the bottom left panel of the same figure. The uncertainty map for the Comp. 1 v field, as measured by the Monte Carlo simulations described in the subsection 4.1, is shown in the bottom right of Fig. 8. While most of the field is well represented by the disk rotation model ($|v - v_{Model}| < 20$ km s^{-1}), there is one region at the eastern border with residuals up to 40 km s^{-1}. Since the maximum uncertainty in v is 15 km s^{-1}, this deviation from pure rotation is probably real. The same seems to be true for the σ field, shown in Fig. 9. The uncertainties in the Component 1 σ are of ~5 km s^{-1} in the central region, and up to 15 km s^{-1} at the borders, as shown in Fig. B1. Therefore, the lack of structure in the σ map is, in fact, real and not due to observational artefacts[6].

These types of disturbances, in the both v and σ, are predicted by simulations (Kronberger et al. 2007; Bois et al. 2011) and observed (Torres-Flores et al. 2014; Hung et al. 2016; Bloom et al. 2018) in galaxies which are, or recently were, undergoing merging processes, as is the case of NGC 2992, and are attributed to perturbations in the gravitational potential due to tidal forces. In Paper II we will investigate whether these disturbances are also present in the velocity field of NGC 2993.

The fainter component of the NLR (Component 2) is detected in a smaller region, originating near the continuum peak and extending towards the NW. For the brightest line, [O III]λ5007, the emission extends up to ~ 3″, as shown by both the flux map, top left panel of Fig. 9 and the P-V plot in Fig. 10. In Fig. 9, we show the maps of equivalent width (EW) of [O III], σ and v for the Component 2. The v map shows only blueshifted velocities, with values ranging from -250 to -200 km s^{-1}. The velocity dispersion is higher than that of Comp. 1, ranging from 200 to 215 km s^{-1}. We also show in all the panels, the contours of the 8-shaped region detected in the 6 cm radio emission (in grey) in which the smaller loop seems to be co-spatial with Component 2.

The position-velocity plot along the major kinematical axis (PA = 32°) and the major axis of the Radio emission (PA = -26°) of NGC 2992 are shown in Fig. 10. It is clear that while Comp. 1 has a

[6] There is no clear evidence of the "Beam Smearing" effect too, given that there is no increase in velocity dispersion values of Comp.1 in the central regions, where the gradient of the velocity field is maximum. The high values of velocity dispersion in Comp. 2, also cannot be purely due to this effect, because it is not co-spatial with the galactic centre and shows very blueshifted velocities from -250 to -200 km s^{-1}, as can be seen Fig. 9. Furthermore when σ of both Comp. 2 and Comp. 1 are taken into account their values are in agreement with the ones measured from Brγ IR lines by Friedrich et al. (2010).

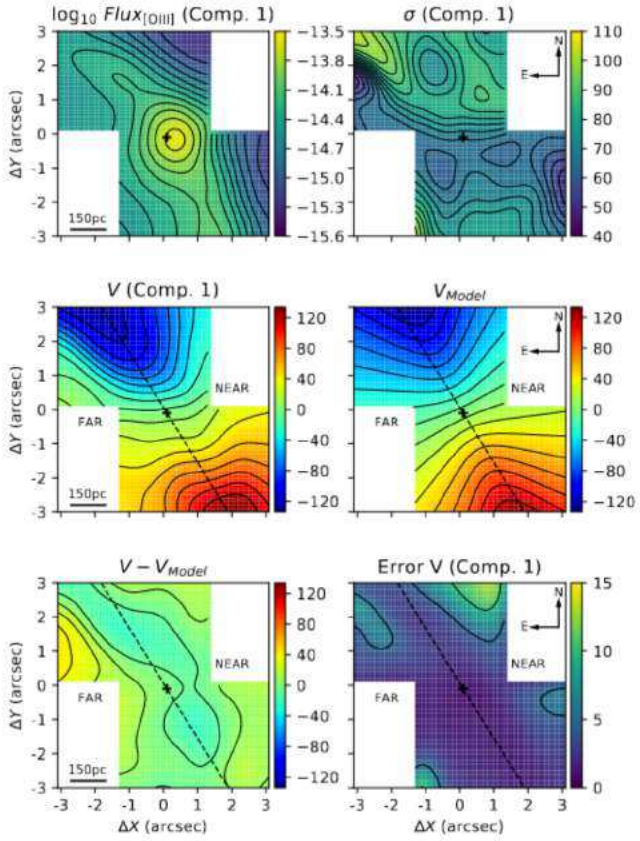

Figure 8. Component 1 properties. Top left: Log_{10} Flux [O III] λ5007 ($\mathrm{erg\,s^{-1}\,cm^{-2}}$). Top right: Velocity dispersion σ ($\mathrm{km\,s^{-1}}$). Middle left: Radial velocity v ($\mathrm{km\,s^{-1}}$). Middle right: Modelled radial velocity ($\mathrm{km\,s^{-1}}$), from the Bertola et al. (1991) rotation model fitting. Bottom left: Residual between the measured and the modelled velocity field. Bottom right: Uncertainties in the radial velocity v ($\mathrm{km\,s^{-1}}$). Black cross is the continuum peak and the dashed black line is the fitted major axis PA.

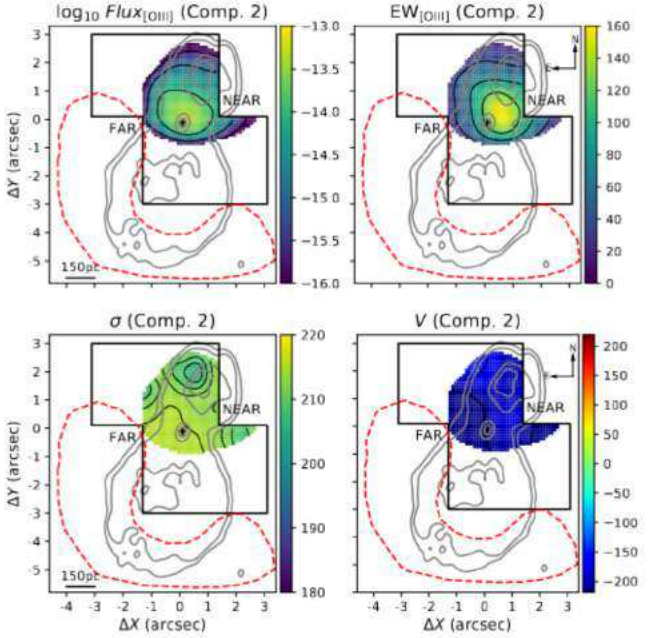

Figure 9. Component 2 properties. Top left: Log_{10} Flux [O III] λ5007 ($\mathrm{erg\,s^{-1}\,cm^{-2}}$). Top right: Equivalent Width of [O III] λ5007 (Å). Bottom left: Velocity dispersion, σ ($\mathrm{km\,s^{-1}}$). Bottom right: Radial velocity, v ($\mathrm{km\,s^{-1}}$). Solid black lines represent our FoV. Black cross is the continuum peak. Grey contours are the 6cm radio emission (Ulvestad & Wilson 1984). Red dashed line is the contour of the redshifted structure found by García-Lorenzo et al. (2001), at the farthest part of the radio emission major loop, taken from Fig. 9 of their paper.

rotational pattern, Comp. 2 deviates considerably from this pattern. Considering:

- Component 2 is not following the galaxy's rotation;
- It is co-spatial with the radio emission;
- It has higher velocity dispersion values than those of Comp. 1, $\sigma > 200\ \mathrm{km\,s^{-1}}$;
- It has blueshifted velocities in the near side of the galaxy;

we are led to the conclusion that it is tracing a radio-jet driven gas outflow since all these are well-known characteristics of this type of phenomena. In fact, this ionised gas outflow was already reported by other IFU studies, e.g. García-Lorenzo et al. (2001), Friedrich et al. (2010) and Mingozzi et al. (2019). Particularly, García-Lorenzo et al. (2001) interpreted this blueshifted structure as the interaction of the minor loop of the radio-jet with the interstellar medium (ISM). García-Lorenzo et al. (2001) also found a similar, however redshifted, structure in the far side of the galaxy, co-spatial with the farthest part of the radio emission major loop, which is mostly not visible in our FoV. We have extracted the contours of this structure from Figure 9 of their paper and show it as the red dashed line in Fig. 9. This finding supports the scenario in which a bipolar over-pressure relativistic plasma is expanding, accelerating and compressing the ISM gas in its path (Chapman et al. 2000). Interestingly, the only

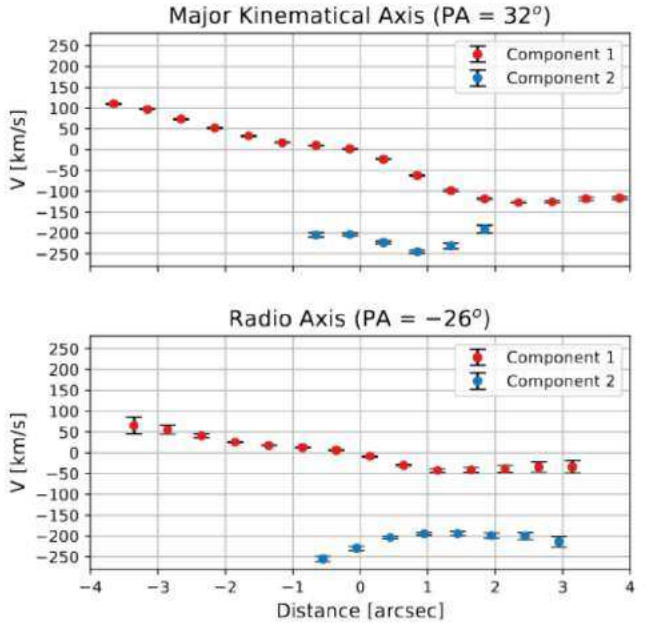

Figure 10. Position-Velocity plot in virtual slits with 0.″4 width. In the top panel the slit is at the PA of the major kinematical axis, in the bottom the slit is at the PA of 8-shaped radio emission major axis. Points are the measured velocity values, and the error bars are the uncertainties in the velocities. Red points are the velocities of Component 1 and blue points the Component 2 ones.

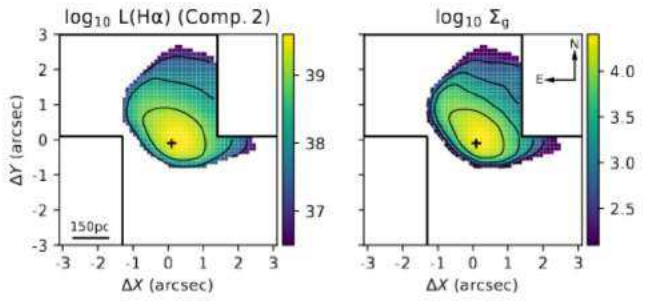

Figure 11. Left: Logarithm of Component 2 dereddened Hα luminosity in erg s^{-1}. Right: Logarithm of Component 2 surface mass density in units of $M_\odot$ (0.″1)$^{-2}$. Black cross is the peak of the continuum emission.

portion of this structure which falls within our FoV is co-spatial with the largest velocity residuals seen in figure Fig. 8. Although our statistical analysis does not indicate the necessity of a separate component, the large residuals clearly indicate a perturbation in the velocity field.

A very similar geometry was found by Riffel & Storchi-Bergmann (2011) in the galaxy Mrk 1157, in which non-rotational blueshifted and redshifted structures are present and co-spatial to the two loops of a very similar nuclear 8-shaped radio emission. The authors also interpreted these structures as the effect of the expanding radio-emitting gas into the ionised ISM.

4.3 Outflow Properties

If we consider Component 2 as ionised outflowing gas, we can measure its properties such as mass, mass outflow rate and kinetic power. We followed the prescriptions described in Lena et al. (2015), in which a biconical outflow geometry is assumed, even though in our case we can see only one of the cones.

The mass outflow rate can be estimated as the ratio between the mass of the outflowing gas and the dynamical time (time for the gas to reach the present distance from the nucleus), M_g/t_d. The mass of the gas in outflow (Component 2) is estimated as:

$$M_g = n_e m_p V f \tag{5}$$

where m_p is the proton mass, n_e and V are the electron density and the volume of the region where the component is detected, f is the filling factor. The filling factor and volume are eliminated by combining Equation 5 with the following expression for the Hα luminosity:

$$L(H\alpha) \approx f n_e^2 j_{H\alpha} V \tag{6}$$

with $j_{H\alpha} = 3.534 \times 10^{-25}$ erg cm^3 s^{-1} at $T = 10000$K (Osterbrock & Ferland 2006). Therefore, the gas mass can be written as:

$$M_g = \frac{m_p L(H\alpha)}{n_e j_{H\alpha}} \tag{7}$$

Our estimates for n_e are based on the flux ratio between [S II] lines, as described in Appendix C. Please note the $L(H\alpha)$ used here is based on the flux of Comp. 2 Hα emission only, corrected by extinction as described in Appendix C. The spatially resolved $L(H\alpha)$ and M_g (i.e. gas mass surface density, Σ_g) are shown in Fig. 11.

The integrated gas mass is $M_g = 3.6 \pm 0.6 \times 10^6 M_\odot$. The t_d was estimated as the ratio between the maximum extension of the outflow ~ 3 arcsec ≈ 450 pc (see Fig. 10) to its mean velocity, $\langle v_{out} \rangle \approx 210$ km s^{-1}, which gives $t_d \approx 2.2 \times 10^6$ yr. Combining these values we estimated an outflow mass rate of $\dot{M}_{out} \approx 1.6 \pm 0.6$ $M_\odot$.

We also estimated the outflow kinetic power as:

$$\dot{E}_{out} = \frac{\dot{M}_{out} v_{out}^2}{2} \tag{8}$$

where v_{out} is the radial velocity of Component 2 (Fig. 9). Integrating the entire outflow we obtained a total outflow kinetic power $\dot{E}_{out} \approx 2.2 \pm 0.3 \times 10^{40}$ erg s^{-1}. In subsection 6.3, we compare these values with the ones found in the literature and those expected by outflow-AGN relations.

5 IONISATION MECHANISMS

Given the presence of young stars discussed in section 3, X-ray (section 1) and BLR emission (section 4) which indicate AGN excitation, and the presence of radio emission that can drive shocks (Dopita 2002; Allen et al. 2008), we used the [N II]/Hα vs. [O III]/Hβ and [S II]/Hα vs. [O III]/Hβ Baldwin et al. (1981, BPT) diagnostic diagrams to investigate which of these excitation mechanisms are dominant in the innermost region of the galaxy.

In the bottom panels of Fig. 12, we show the maps of [O III]/Hβ, [N II]/Hα and [S II]/Hα line ratios for the entire line profile (by summing the kinematical components; we do that to increase the precision in the flux measurement and to avoid regions where a second component is detected in high S/N lines, like [O III], but not detected in lower S/N ones, like Hβ.) We excluded the regions where uncertainties in the total flux, as shown in Appendix B, are higher than 30 per cent. The [O III]/Hβ shows a clear AGN signature, with its peak, up to [O III]/H$\beta \approx 25$, at the centre of the FoV and decreasing radially down to [O III]/H$\beta \approx 2$ at SW corner of the FoV. The [N II]/Hα and [S II]/Hα, however, do not show the same pattern: their maximum values are off-nuclear, and they do not present a radial decrease as in the [O III]/Hβ one. This indicates a lower energy mechanism (lower than an AGN, but higher than H II regions) can be ionising the gas too. In fact, shock ionised regions are characterised by having smaller [O III]/Hβ ratios and larger [S II] ([N II])/Hα than those ionised by AGN (Veilleux & Osterbrock 1987; Kewley et al. 2006; Allen et al. 2008).

We selected limiting regions in the line ratio maps and shown it in the respectively BPT diagrams in the top panels of Fig. 12. We also show some division lines: the solid black curves on both diagnostic diagrams trace the Kewley et al. (2001) theoretical upper limit of regions ionised by pure star formation (K01 line). All spectra lying above the K01 line are dominated by ionisation mechanisms more energetic than star formation. Several excitation mechanisms can increase the collisional excitation rate, enhancing the ratios of the forbidden to recombination lines, among them energetic photons from a power law-like emission (AGN); shock excitation and evolved stellar populations (pos-AGB) can also produce line ratios along this branch of the diagram. The latter case does not apply to the nuclear region of NGC 2992 given that it requires EW(Hα) < 3 Å (Stasinska et al. 2008; Cid Fernandes et al. 2011) and our entire FoV has EW(Hα) > 10 Å. We also show the dashed black curve on the [N II]/Hα vs. [O III]/Hβ diagnostic diagram: the Kauffmann et al. (2003) empirical classification line (Ka03 line), which traces the upper boundary of the Sloan Digital Sky Survey Strauss et al. (SDSS 2002) star formation sequence. All spectra lying below the Ka03 line are dominated

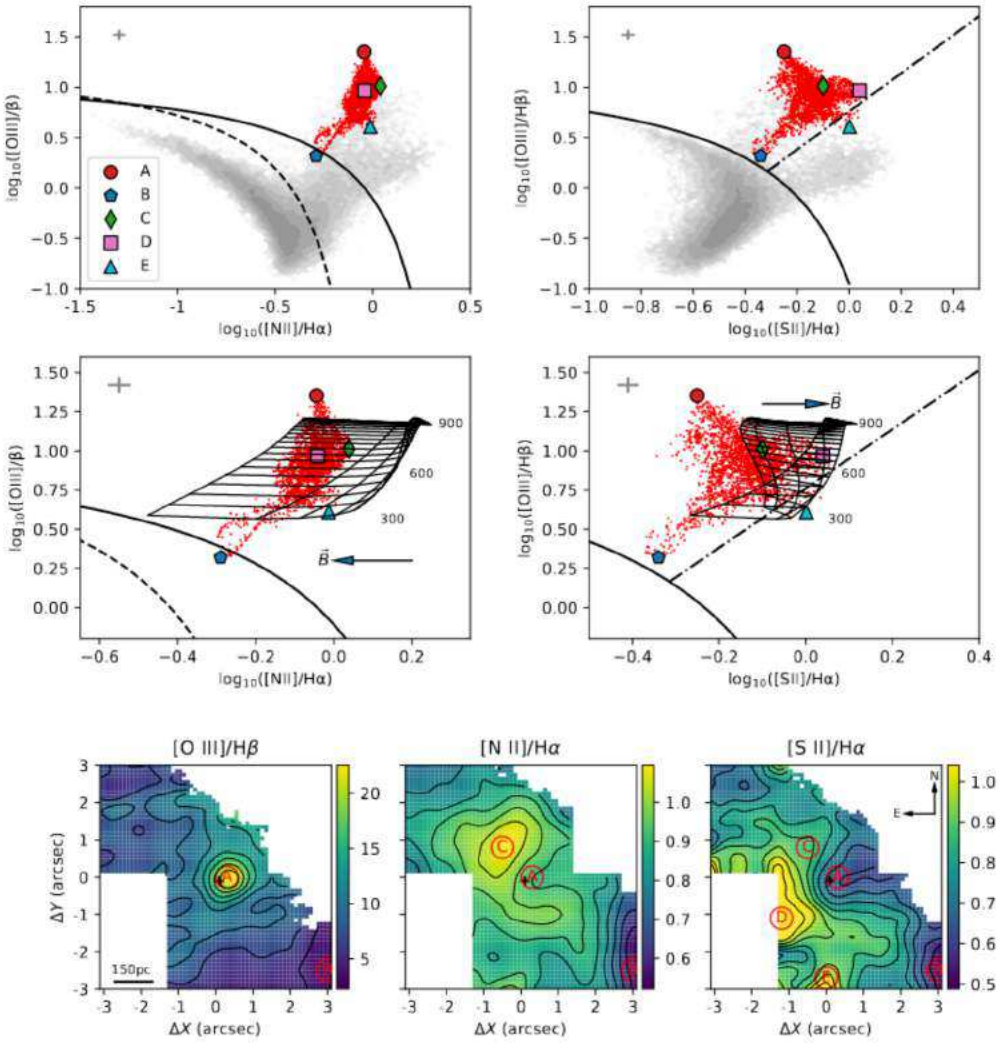

Figure 12. Top: [N II]/Hα vs. [O III]/Hβ and [S II]/Hα vs. [O III]/Hβ BPT diagrams; grey countours are galaxies from the SDSS main galaxy sample. red points are the spaxel of NGC 2992. Colored markers are the selected regions of NGC 2992, as shown in the bottom panels, representing: red (Region A), blue (B), green (C), pink (D) and cyan (E). Middle: Zoomed BPT diagrams with shock+precursor grid models as measured with MAPPINGS V code (Sutherland et al. 2018); the $\vec{B}$ indicates increasing magnetic field of the model (from 0.01 to 4 μG); the black numbers indicates the velocities of the shocks, ranging from 300 to 900 km s^{-1}. Bottom: Respectively, from left to right, [O III]/Hβ, [N II]/Hα, and [S II]/Hα emission lines ratio maps; red circles show the selected regions shown in the upper panels. In BPT diagrams the grey crosses are the typical errors in the emission line ratios; the solid black lines are Kewley et al. (2001) theoretical upper limits for pure star forming galaxies. In the [N II]/Hα vs. [O III]/Hβ diagram the dashed black line represents Kauffmann et al. (2003) line which traces the upper boundary of the SDSS star formation sequence. In the [S II]/Hα vs. [O III]/Hβ diagram the dashed-dotted black line represents the empirical division between AGN like and low-ionisation nuclear emission-line region (LINER) (Kewley et al. 2006).

by star formation. The dashed-dotted black curve on the [S II]/Hα vs. [O III]/Hβ diagnostic diagram traces the Kewley et al. (2006) empirical classification line (K06 line), which separates high ionisation spectra associated with Seyfert (AGN) and other intermediary ionisation mechanisms including shock excitation. We also show as grey points in the top BPT diagrams a collection of single-fibre emission line measurement from SDSS main galaxy sample by Kewley et al. (2006).

Region A is the peak of the [O III]/Hβ map, it shows clear AGN-like ratios, with an upper [O III]/Hβ value higher than any SDSS AGN, which corresponds to a 3″diameter aperture, and therefore has a diluted AGN/host-galaxy emission line ratio. Region B has the lowest value in all the maps; it lies below K01, showing the radial decrease in the AGN contribution to the emission lines and significant contributions from both star formation and AGN excitation. Regions C, D, and E display the highest values in the [S II]/Hα and [N II]/Hα maps; however, they have lower [O III]/Hβ values than region A. Region E, in fact, crosses the K06 line in the [S II]/Hα diagram, which again indicates the presence of another ionisation mechanism.

In order to search for an explanation to the increase in this intermediary ionisation energy lines ([N II] and [S II]) we used the MAPPINGS V shock models by Sutherland et al. (2018). We explored the parameter space in the pure shock and shock+precursor grids of the models. None of the pure shock models could explain these line ratios, given the high [O III]/Hβ values. However shock+precursor (Shock ionisation in a medium already ionised by power-law like emission) with shock velocities between 300 km s^{-1}and 900 km s^{-1}and magnetic field ($\vec{B}$) between 0.01μG and 4μG, with a two-solar metallicity and a pre-shock density of 1 cm^{-3}, successfully reproduce the line ratios of regions C, D and E. In the

middle panels of Fig. 12 we show the grid models in these shock velocity and magnetic field ranges superimposed with the emission line ratios of the regions. The shocks in NGC 2992 have been extensively studied by Allen et al. (1999), who conclude that shocks are the predominant ionisation mechanism in the extended NLR cones at a distance of several kpc from the nucleus.

We can conclude that a more simple Starburst-AGN mixture (e.g. Davies et al. 2014a,b; D'Agostino et al. 2018) in which the maximum values of all [O III]/Hβ, [N II]/Hα and [S II]/Hα are located in the innermost spaxel (location of the AGN), and all decrease radially towards the H II ionisation region of the BPT in a straight line (see for example figure 1 in Davies et al. 2014b), cannot describe the ionisation at the circumnuclear region of NGC 2992. Instead, a more complex Starburst-AGN-Shocks mixture is responsible for its ionisation. However, the very high values of [O III]/Hβ indicate the most important among these three mechanisms is AGN ionisation, at least in the innermost portion (see further discussion in subsection 6.4).

6 DISCUSSION

6.1 Interaction-Driven Circumnuclear Star formation

In general terms, the stellar population synthesis discussed in section 3 shows that stellar content in the inner 1.1 kpc of NGC 2992 is mainly composed by an old metal-rich population, with a smaller but considerable contribution from young metal-poor stars. The presence of the latter is supported by other studies, for instance, using the Bica & Alloin (1986) base of star clusters for stellar population synthesis, Storchi Bergmann et al. (1990) found a predominance of old stellar populations (10^{10} yr) and a small contribution of at least 5 per cent by recent star formation in the inner 5″. Moreover, Friedrich et al. (2010) find that 10-20 per cent of the IR flux is attributable to a starburst, based on the emission from polycyclic aromatic hydrocarbon (PAH) molecules. Additionally, these authors estimate the starburst to have occurred between 40-50 Myr, based on the equivalent width of the Brγ line.

Major merger processes are known to be responsible for gas inflow towards the central regions of galaxies enhancing circumnuclear star formation and possibly triggering nuclear activity. Merger galaxies have an increase in the SFR, mainly at the nuclear regions (Ellison et al. 2013; Pan et al. 2019). Thus, these sources have younger nuclear populations than those found in isolated galaxies, in which most of their recent formed stars are concentrated at the spiral arms. Moreover, major mergers are also able to modify the metallicity gradients of galaxies (Barrera-Ballesteros et al. 2015). Galaxy simulations show that the gas, originally located at external portions of the isolated galaxy (metal-poor regions), moves towards internal regions (metal-rich regions) of the companion galaxy during the encounter and is capable of cooling and forming stars.. Such processes are able to explain both the increase in the SFR and the modifications in the metallicity gradient (Dalcanton 2007; Torrey et al. 2012; Sillero et al. 2017). In fact, the pericentre passage between NGC 2992 and its companion NGC 2993 is estimated to have occurred ~ 100 Myr ago (Duc et al. 2000). Thus, a possible scenario is that metal-poor gas inflow has led to interaction-driven circumnuclear star formation which can explain the presence of such young metal-poor stellar population in the nucleus. Such inflows could also be responsible for triggering NGC 2992's nuclear activity, a scenario which will be further explored using numerical simulations in Paper III.

6.2 Feeding vs Feedback

We can compare the mass outflow rate, estimated in subsection 4.3, with the accretion rate necessary to power the AGN at the nucleus of NGC 2992, calculated as follows:

$$\dot{M}_{\rm BH} = \frac{L_{bol}}{c^2 \eta} \tag{9}$$

where η is the mass-energy conversion efficiency, which for Seyfert galaxies is usually assumed to be $\eta = 0.1$ (Frank et al. 2002), L_{bol} is the bolometric luminosity of the AGN, and c is the speed of light. To measure L_{bol} we applied the bolometric correction by Marconi et al. (2004) on the most recent X-ray luminosity measurement of NGC 2992 made by Marinucci et al. (2018). The author used a 2015 *NuSTAR* observation and obtained an absorption corrected 2-10 Kev Luminosity of $7.6 \pm 0.1 \times 10^{42}$ ergs^{-1} that translates to $L_{bol} = 9.1 \pm 0.2 \times 10^{43}$ ergs^{-1}. We use these values to derive an accretion rate of $\dot{M}_{\rm BH} \approx 0.02$ M$_\odot yr^{-1}$.

The nuclear accretion rate is two orders of magnitude smaller than the mass outflow rate ($\dot{M}_{out} \approx 1.6 \pm 0.6$ M$_\odot$ yr^{-1}, see subsection 4.3). This implies that most of the outflowing gas does not originate in the AGN, but in the surrounding ISM, and this result supports the scenario in which the plasma bubbles (radio loops) are expanding, pushing gas away from the nuclear region. However, the ratio between the kinetic power of this blueshifted outflow loop and the bolometric luminosity is ~ 0.002, which means only 0.2 per cent of the AGN radiative power is in this outflow. Many authors argue that such a low value is not enough to have the feedback effects expected by cosmological simulations (Springel et al. 2005; Silk & Mamon 2012; Bullock & Boylan-Kolchin 2017), stating that $\dot{E}_{out}/L_{bol}$ should be closer to 5 per cent or above in order to effectively suppress growth in the most massive galaxies. However, some models show that coupling efficiencies of $\dot{E}_{out}/L_{bol} \approx 0.5$ per cent (Hopkins & Elvis 2010), and even 0.1 per cent (Costa et al. 2018) could successfully prevent star formation.

6.3 AGN-Wind Scaling Relations

Comparing our outflow measurements with those from the literature we noted ours results disagree with those presented in Müller-Sánchez et al. (2011), who reported $\dot{M}_{out} = 120$ M$_\odot$ yr^{-1} and $\dot{E}_{out} = 2.5\times10^{42}$ erg s^{-1}, both almost one hundred times greater than ours. We attribute this difference to two factors: **i)** they assumed the filling factor f to be constant equal to 0.001, while we have measured the filling factor from L(Hα) and n_e (see Equation 6). This assumption makes their M$_g$ proportional to n_e, and not inversely proportional (as in Equation 7); **ii)** they assume an electronic density of $n_e = 5000$ cm^{-3}, a value more than 5 times larger than the maximum value we measured in the nuclear region of the galaxy. These two factors combined explain their overestimation of both $\dot{M}_{out}$ and $\dot{E}_{out}$. We also argue these differences cannot be due to a larger coverage of the outflow by a larger field of view, in the sense of seeing the farthest part of the radio emission major loop and its redshifted outflow structure, given the authors have used the OSIRIS/VLT instrument, which has an even smaller FoV than GMOS.

We can compare our values to the properties of outflows found in other precious papers across the literature. In Fig. 11, we show the Fiore et al. (2017) compilation of a set of outflow energetics from various studies over the years spanning a large range of AGN luminosity ($L_{bol} \geq 10^{44}$), which they use to establish AGN wind scaling relations, mass outflow rate and outflow power as a function of bolometric luminosity, together with several measurements of nearby

galaxies from individual studies compiled by us from the literature or obtained by our collaborators: NGC 1068, NGC 3783, NGC 6814, NGC 7469 (Müller-Sánchez et al. 2011), NGC 4151 (Crenshaw et al. 2015), Mrk 573 (Revalski et al. 2018), Mrk 34 (Revalski et al. 2018), NGC 7582 (Riffel et al. 2009), Mrk 1066 (Riffel et al. 2010b), Mrk 1157 (Riffel & Storchi-Bergmann 2011), Mrk 79 (Riffel et al. 2013a), NGC 5929 (Riffel et al. 2013b), NGC 5728 (Shimizu et al. 2019), and NGC 3081 (Schnorr-Müller et al. 2014), ESO 362-G18 (Humire et al. 2018), NGC 1386 (Lena et al. 2015), ESO 153-G20 (Soto-Pinto et al. 2019), 3C 33 (Couto et al. 2017), including NGC 2992 measurement by Müller-Sánchez et al. (2011). Although these estimates are made using different recipes, leading to differences between methods, they are generally similar to the one adopted here. Therefore, this comparison with the literature may be useful at least as an order of magnitude approximation.

As we can see, the overestimated previous measurement of NGC 2992's outflow made this source to be an outlier in the Fiore et al. (2017) relations, while our values make the galaxy more likely to be explained by these relations. However, the other measurements in nearby Seyfert galaxies support the existence of a larger scatter of these relations, both in $\dot{E}_{out}$ and $\dot{M}_{out}$, at lower luminosities. To confirm whether this extension is valid or not, more detailed studies like this, mainly using IFU, are needed so that outflow properties can be properly and systematically measured, without assuming fixed values of n_e and f.

6.4 Multiple Ionisation Mechanisms

In section 5 we showed that despite being dominated by AGN excitation, star formation and shocks cannot be excluded as ionisation mechanisms in the nuclear region of the galaxy. The existence of star formation ionisation in the nucleus is confirmed by Friedrich et al. (2010) IR emission line analyses, as mentioned in subsection 6.1. The presence of shocks is also supported by Allen et al. (1999) using long-slit spectroscopy. The authors also argue the dominance of shocks increases, compared to ionisation by the central source, at larger radius.

Galaxies undergoing rapid phases of evolution (through processes such as galaxy-galaxy interactions, gas outflows and radio jets) often have multiple ionisation mechanisms contributing to their optical line emission (e.g. Rich et al. 2011; Lanz et al. 2015; Rich et al. 2015; Davies et al. 2017). These multiple ionisation mechanisms are also in agreement with evolutionary scenarios in which gas inflows (driven either by secular mechanisms, like nuclear bars or nuclear spiral arms, or environmental ones, like minor and major mergers) triggers nuclear star formation and nuclear activity (feeding process) and then the active nucleus can drive both ionising photons from the accretion disk and radio jets (feedback process) that impacts the ISM physical conditions (Hopkins et al. 2008; Hopkins & Quataert 2010).

7 SUMMARY AND CONCLUSIONS

We have analysed the stellar population, the ionisation mechanism and kinematics of the ionised gas in the inner 1.1 kpc of the interacting Seyfert galaxy NGC 2992, using optical spectra obtained with the GMOS integral field spectrograph on the Gemini South telescope, with a spatial resolution of $\approx$ 120 pc and spectral resolution $\approx$ 40 km s^{-1}. The main results are:

- The stellar population in the nuclear region of the galaxy is mainly composed (60 per cent$\leq x_O \leq$ 80 per cent) by an old (t > 1.4 Gyr) metal-rich ($\langle Z \rangle_O \geq 2.0\ Z_\odot$) population with a smaller, but considerable contribution (10 per cent $\leq x_Y \leq$ 30 per cent) of an young (t < 100 Myr) metal-poor ($\langle Z \rangle_Y \leq 1.0\ Z_\odot$) population. A possible scenario is that metal-poor gas inflow during the pericentre passage of NGC 2993 has led to interaction-driven circumnuclear star formation, which can explain the presence of such young metal-poor stellar population in the nuclear region;
- The emission line analyses show the presence of both BLR and NLR emission, confirming its classification as an intermediate-type Seyfert galaxy. The BLR emission profile has a velocity dispersion of FWHM$_{BLR}$ = 2010 km s^{-1} and a Balmer decrement of (Hα/Hβ)$_{BLR}$ = 24.2. The NLR presents two distinctly kinematical components: one that although disturbed is well fitted by a disk model, and therefore can be identified as gas in orbit in the galaxy disk, with radial velocities ranging from -130 to 130 km s^{-1}; another that we interpreted as an outflow associated with the radio emission, with blueshifted velocities of $\sim$ 200 km s^{-1}, a mass outflow rate of $\dot{M}_{out} \approx 1.6 \pm 0.6$ M$_\odot$ and a kinematic power of $\dot{E}_{out} \approx 2.2 \pm 0.3 \times 10^{40}$ erg s^{-1};
- The BPT diagnostic diagrams show the galaxy posses multiple ionisation mechanisms: a mixture of AGN, star-formation and shocks, the former being the dominant one. The [O III]/Hβ ratio peaks at the innermost spaxels, and is located in the upper region

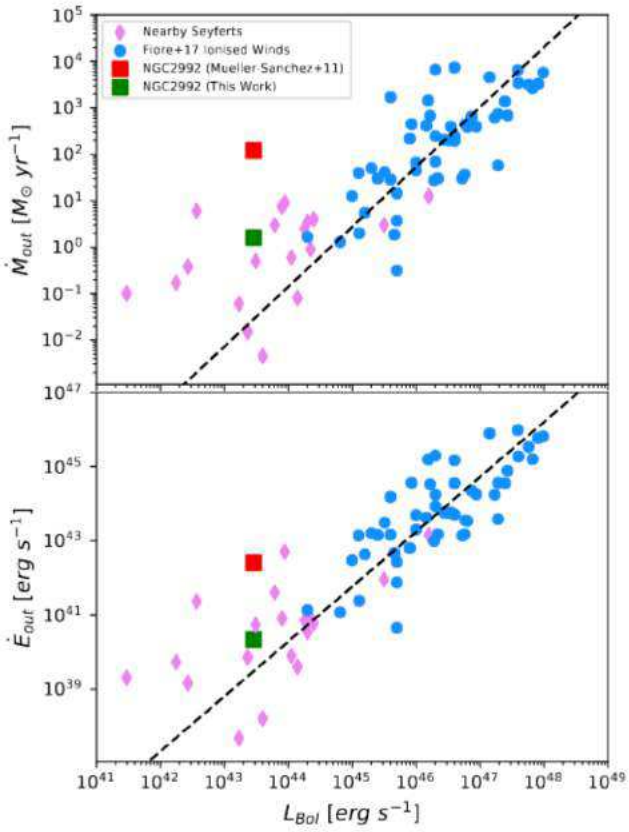

Figure 13. Correlations between the mass outflow rate ($\dot{M}_{out}$, Top Panel) and kinetic outflow power ($\dot{E}_{out}$, Bottom Panel). Blue points are the data compiled by Fiore et al. (2017) and the black dashed lines show the best fit correlations for these points. Red Squares are the previous measurement of NGC 2992 by Müller-Sánchez et al. (2011), and green ones are the results of this work. Violet diamonds are compiled from various literature sources for more modest AGN luminosities.

of the BPT diagram. The lower values, located at the border of the FoV, decreases down to below the Kewley et al. (2001) line, showing an increase in the star-formation ionisation compared to the AGN ionisation at larger radius. Off-nuclear peaks in the [N II]/Hα and [S II]/Hα maps indicate the presence of another mechanism and are successfully explained by Sutherland et al. (2018) shock+precursor models.

ACKNOWLEDGMENTS

We thank the anonymous referee whose comments helped us improve the methodology and the clarity of this work. G-P, M. thanks the Brazilian National Council for Scientific and Technological Development (CNPq) for his Master Scholarship and Taro Shimizu for providing a collection of data points for Fig. 13. G. C. acknowledges the support by the Comité Mixto ESO-Chile and the DGI at University of Antofagasta. J. A. H. J. thanks to Chilean institution CONICYT, Programa de Astronomía, Fondo ALMA-CONICYT 2017, Código de proyecto 31170038. N.Z.D. acknowledges partial support from FONDECYT through project 3190769. This work is based on observations obtained at the Gemini Observatory, which is operated by the Association of Universities for Research in Astronomy, Inc., under a cooperative agreement with the NSF on behalf of the Gemini partnership: the National Science Foundation (United States), the Science and Technology Facilities Council (United Kingdom), the National Research Council (Canada), CONICYT (Chile), the Australian Research Council (Australia), Ministério da Ciência e Técnologia (Brazil) and south-eastCYT (Argentina).

DATA AVAILABILITY

The data underlying this article will be shared on reasonable request to the corresponding author.

REFERENCES

Allen M. G., Dopita M. A., Tsvetanov Z. I., Sutherland R. S., 1999, ApJ, 511, 686
Allen M. G., Groves B. A., Dopita M. A., Sutherland R. S., Kewley L. J., 2008, ApJS, 178, 20
Alloin D., Collin-Souffrin S., Joly M., Vigroux L., 1979, A&A, 78, 200
Bacon R., et al., 2010, in McLean I. S., Ramsay S. K., Takami H., eds, Society of Photo-Optical Instrumentation Engineers (SPIE) Conference Series Vol. 7735, Ground-based and Airborne Instrumentation for Astronomy III. p. 773508, doi:10.1117/12.856027
Baldwin J. A., Phillips M. M., Terlevich R., 1981, PASP, 93, 5
Baldwin C., McDermid R. M., Kuntschner H., Maraston C., Conroy C., 2018, MNRAS, 473, 4698
Barrera-Ballesteros J. K., et al., 2015, A&A, 579, A45
Begelman M. C., Blandford R. D., Rees M. J., 1984, Reviews of Modern Physics, 56, 255
Bennert N., Jungwiert B., Komossa S., Haas M., Chini R., 2006, Astronomy & Astrophysics, 456, 953–966
Bertola F., Bettoni D., Danziger J., Sadler E., Sparke L., de Zeeuw T., 1991, ApJ, 373, 369
Bica E., Alloin D., 1986, A&A, 162, 21
Block A., 2011, Caelum-Observatory:NGC2992. `http://www.caelumobservatory.com/gallery/n2992.shtml`
Bloom J. V., et al., 2018, Monthly Notices of the Royal Astronomical Society, 476, 2339–2351
Blumenthal K. A., Barnes J. E., 2018, MNRAS, 479, 3952
Bois M., et al., 2011, MNRAS, 416, 1654
Bruzual G., Charlot S., 2003, MNRAS, 344, 1000
Bullock J. S., Boylan-Kolchin M., 2017, ARA&A, 55, 343
Calzetti D., Armus L., Bohlin R. C., Kinney A. L., Koornneef J., Storchi-Bergmann T., 2000, ApJ, 533, 682
Cappellari M., Copin Y., 2003, MNRAS, 342, 345
Cardelli J. A., Clayton G. C., Mathis J. S., 1989, ApJ, 345, 245
Cardoso L. S. M., Gomes J. M., Papaderos P., 2017, A&A, 604, A99
Chabrier G., 2003, PASP, 115, 763
Chapman S. C., Morris S. L., Alonso-Herrero A., Falcke H., 2000, MNRAS, 314, 263
Chen X. Y., Liang Y. C., Hammer F., Prugniel P., Zhong G. H., Rodrigues M., Zhao Y. H., Flores H., 2010, Astronomy and Astrophysics, 515, A101
Cid Fernandes R., 2018, MNRAS, 480, 4480
Cid Fernandes R., González Delgado R. M., 2010, Monthly Notices of the Royal Astronomical Society, 403, 780
Cid Fernandes R., Gu Q., Melnick J., Terlevich E., Terlevich R., Kunth D., Rodrigues Lacerda R., Joguet B., 2004, MNRAS, 355, 273
Cid Fernandes R., Mateus A., Sodré L., Stasińska G., Gomes J. M., 2005, MNRAS, 358, 363
Cid Fernandes R., Stasińska G., Mateus A., Vale Asari N., 2011, Monthly Notices of the Royal Astronomical Society, 413, 1687–1699
Cid Fernandes R., et al., 2013, A&A, 557, A86
Colina L., Fricke K. J., Kollatschny W., Perryman M. A. C., 1987, A&A, 178, 51
Conroy C., 2013, Annual Review of Astronomy and Astrophysics, 51, 393–455
Costa T., Rosdahl J., Sijacki D., Haehnelt M. G., 2018, MNRAS, 479, 2079
Couto G. S., Storchi-Bergmann T., Schnorr-Müller A., 2017, MNRAS, 469, 1573
Crenshaw D. M., Fischer T. C., Kraemer S. B., Schmitt H. R., 2015, ApJ, 799, 83
Croton D. J., et al., 2006, MNRAS, 365, 11
D'Agostino J. J., Poetrodjojo H., Ho I.-T., Groves B., Kewley L., Madore B. F., Rich J., Seibert M., 2018, Monthly Notices of the Royal Astronomical Society, 479, 4907–4935
Dalcanton J. J., 2007, The Astrophysical Journal, 658, 941
Dametto N. Z., et al., 2019, MNRAS, 482, 4437
Davies R. L., Rich J. A., Kewley L. J., Dopita M. A., 2014a, MNRAS, 439, 3835
Davies R. L., Kewley L. J., Ho I. T., Dopita M. A., 2014b, MNRAS, 444, 3961
Davies R. L., et al., 2017, Monthly Notices of the Royal Astronomical Society, 470, 4974–4988
Di Matteo T., Springel V., Hernquist L., 2005, Nature, 433, 604
Dopita M. A., 2002, in Henney W. J., Steffen W., Binette L., Raga A., eds, Revista Mexicana de Astronomia y Astrofisica Conference Series Vol. 13, Revista Mexicana de Astronomia y Astrofisica Conference Series. pp 177–182
Duc P.-A., Brinks E., Springel V., Pichardo B., Weilbacher P., Mirabel I. F., 2000, The Astronomical Journal, 120, 1238
Ellison S. L., Patton D. R., Mendel J. T., Scudder J. M., 2011, MNRAS, 418, 2043
Ellison S. L., Mendel J. T., Patton D. R., Scudder J. M., 2013, MNRAS, 435, 3627
Event Horizon Telescope Collaboration et al., 2019, ApJ, 875, L1
Fan L., et al., 2016, ApJ, 822, L32
Ferrarese L., Merritt D., 2000, ApJ, 539, L9
Ferré-Mateu A., Vazdekis A., Trujillo I., Sánchez-Blázquez P., Ricciardelli E., de la Rosa I. G., 2012, MNRAS, 423, 632
Fiore F., et al., 2017, A&A, 601, A143
Fischer T. C., et al., 2018, ApJ, 856, 102
Frank J., King A., Raine D. J., 2002, Accretion Power in Astrophysics: Third Edition
Freund J., 1992, Annalen Der Physik - ANN PHYS-BERLIN, 504, 380
Friedrich S., Davies R. I., Hicks E. K. S., Engel H., Müller-Sánchez F., Genzel R., Tacconi L. J., 2010, A&A, 519, A79
García-Bernete I., et al., 2015, MNRAS, 449, 1309
García-Lorenzo B., Arribas S., Mediavilla E., 2001, A&A, 378, 787

Ge J., Mao S., Lu Y., Cappellari M., Yan R., 2019, Monthly Notices of the Royal Astronomical Society, 485, 1675–1693
Gilli R., Maiolino R., Marconi A., Risaliti G., Dadina M., Weaver K. A., Colbert E. J. M., 2000, A&A, 355, 485
Glikman E., Simmons B., Mailly M., Schawinski K., Urry C. M., Lacy M., 2015, Major Mergers Host the Most Luminous Red Quasars at z 2: A Hubble Space Telescope WFC3/IR Study (arXiv:1504.02111)
González Delgado R. M., et al., 2015, A&A, 581, A103
Greene J. E., Zakamska N. L., Smith P. S., 2012, ApJ, 746, 86
Hopkins P. F., Elvis M., 2010, MNRAS, 401, 7
Hopkins P. F., Quataert E., 2010, MNRAS, 407, 1529
Hopkins P. F., Hernquist L., Cox T. J., Kereš D., 2008, ApJS, 175, 356
Humire P. K., et al., 2018, A&A, 614, A94
Hung C.-L., Hayward C. C., Smith H. A., Ashby M. L. N., Lanz L., Martínez-Galarza J. R., Sanders D. B., Zezas A., 2016, ApJ, 816, 99
Irwin J. A., et al., 2017, MNRAS, 464, 1333
Kauffmann G., et al., 2003, MNRAS, 346, 1055
Kennicutt Robert C. J., 1998, ApJ, 498, 541
Kewley L. J., Dopita M. A., Sutherland R. S., Heisler C. A., Trevena J., 2001, ApJ, 556, 121
Kewley L. J., Groves B., Kauffmann G., Heckman T., 2006, MNRAS, 372, 961
Koleva M., Prugniel P., Ocvirk P., Le Borgne D., Soubiran C., 2008, MNRAS, 385, 1998
Kormendy J., Ho L. C., 2013, ARA&A, 51, 511
Koski A. T., 1978, ApJ, 223, 56
Koss M., Mushotzky R., Veilleux S., Winter L., 2010, ApJ, 716, L125
Kronberger T., Kapferer W., Schindler S., Ziegler B. L., 2007, Astronomy & Astrophysics, 473, 761–770
L. Trippe M., Crenshaw D., R. P. D., Dietrich M., 2008, AJ, 135
Lanz L., Ogle P. M., Evans D., Appleton P. N., Guillard P., Emonts B., 2015, The Astrophysical Journal, 801, 17
Le Borgne J.-F., et al., 2003, A&A, 402, 433
Lena D., et al., 2015, ApJ, 806, 84
Madau P., Dickinson M., 2014, ARA&A, 52, 415
Maksym W. P., Ulmer M. P., Roth K. C., Irwin J. A., Dupke R., Ho L. C., Keel W. C., Adami C., 2014, MNRAS, 444, 866
Mallmann N. D., et al., 2018, MNRAS, 478, 5491
Maraston C., Strömbäck G., 2011, MNRAS, 418, 2785
Marconi A., Risaliti G., Gilli R., Hunt L. K., Maiolino R., Salvati M., 2004, MNRAS, 351, 169
Marinucci A., Bianchi S., Braito V., Matt G., Nardini E., Reeves J., 2018, MNRAS, 478, 5638
Marquez I., Boisson C., Durret F., Petitjean P., 1998, A&A, 333, 459
McElroy R., Croom S. M., Pracy M., Sharp R., Ho I. T., Medling A. M., 2015, MNRAS, 446, 2186
Menci N., Gatti M., Fiore F., Lamastra A., 2014, A&A, 569, A37
Menezes R. B., Steiner J. E., Ricci T. V., 2014, MNRAS, 438, 2597
Mentz J. J., et al., 2016, MNRAS, 463, 2819
Mingozzi M., et al., 2019, A&A, 622, A146
Müller-Sánchez F., Prieto M. A., Hicks E. K. S., Vives-Arias H., Davies R. I., Malkan M., Tacconi L. J., Genzel R., 2011, ApJ, 739, 69
Osterbrock D. E., Ferland G. J., 2006, Astrophysics of gaseous nebulae and active galactic nuclei
Pan H.-A., et al., 2019, ApJ, 881, 119
Peterson B. M., 1997, An Introduction to Active Galactic Nuclei
Peterson B. M., Wanders I., Bertram R., Hunley J. F., Pogge R. W., Wagner R. M., 1998, ApJ, 501, 82
Pettini M., Pagel B. E. J., 2004, MNRAS, 348, L59
Proxauf B., Öttl S., Kimeswenger S., 2014, A&A, 561, A10
Raimann D., Storchi-Bergmann T., González Delgado R. M., Cid Fernandes R., Heckman T., Leitherer C., Schmitt H., 2003, MNRAS, 339, 772
Revalski M., Crenshaw D. M., Kraemer S. B., Fischer T. C., Schmitt H. R., Machuca C., 2018, ApJ, 856, 46
Rich J. A., Kewley L. J., Dopita M. A., 2011, ApJ, 734, 87
Rich J. A., Kewley L. J., Dopita M. A., 2015, The Astrophysical Journal Supplement Series, 221, 28
Riffel R. A., Storchi-Bergmann T., 2011, Monthly Notices of the Royal Astronomical Society, 417, 2752–2769
Riffel R. A., Storchi-Bergmann T., Dors O. L., Winge C., 2009, MNRAS, 393, 783
Riffel R., Pastoriza M. G., Rodríguez-Ardila A., Bonatto C., 2010a, in Stellar Populations - Planning for the Next Decade.
Riffel R. A., Storchi-Bergmann T., Nagar N. M., 2010b, MNRAS, 404, 166
Riffel R. A., Storchi-Bergmann T., Winge C., 2013a, MNRAS, 430, 2249
Riffel R. A., Storchi-Bergmann T., Riffel R., 2013b, The Astrophysical Journal, 780, L24
Rupke D. S. N., Veilleux S., 2011, The Astrophysical Journal, 729, L27
Ruschel-Dutra D., 2020, danielrd6/ifscube v1.0, doi:10.5281/zenodo.3945237, https://doi.org/10.5281/zenodo.3945237
Sánchez-Blázquez P., et al., 2006, MNRAS, 371, 703
Satyapal S., Ellison S. L., McAlpine W., Hickox R. C., Patton D. R., Mendel J. T., 2014, MNRAS, 441, 1297
Schawinski K., Dowlin N., Thomas D., Urry C. M., Edmondson E., 2010, The Astrophysical Journal, 714, L108
Schimoia J. S., Storchi-Bergmann T., Grupe D., Eracleous M., Peterson B. M., Baldwin J. A., Nemmen R. S., Winge C., 2015, ApJ, 800, 63
Schlafly E. F., Finkbeiner D. P., 2011, ApJ, 737, 103
Schnorr-Müller A., Storchi-Bergmann T., Nagar N. M., Robinson A., Lena D., Riffel R. A., Couto G. S., 2014, MNRAS, 437, 1708
Schnorr-Müller A., et al., 2016, MNRAS, 462, 3570
Schnorr-Müller A., Storchi-Bergmann T., Nagar N. M., Robinson A., Lena D., 2017, MNRAS, 471, 3888
Shimizu T. T., et al., 2019, Monthly Notices of the Royal Astronomical Society
Shuder J. M., 1980, ApJ, 240, 32
Silk J., Mamon G. A., 2012, Research in Astronomy and Astrophysics, 12, 917
Sillero E., Tissera P. B., Lambas D. G., Michel-Dansac L., 2017, Monthly Notices of the Royal Astronomical Society, 472, 4404–4413
Silverman J. D., et al., 2008, ApJ, 679, 118
Soto-Pinto P., et al., 2019, MNRAS, 489, 4111
Springel V., et al., 2005, Nature, 435, 629
Stasinska G., Asari N. V., Fernandes R. C., Gomes J. M., Schlickmann M., Mateus A., Schoenell W., Sodré Jr L., 2008, Monthly Notices of the Royal Astronomical Society: Letters
Storchi Bergmann T., Bica E., Pastoriza M. G., 1990, MNRAS, 245, 749
Storchi-Bergmann T., Raimann D. I., González Delgado R. M., Schmitt H. R., Cid Fernandes R., Heckman T., Leitherer C., 2003, in Perez E., Gonzalez Delgado R. M., Tenorio-Tagle G., eds, Astronomical Society of the Pacific Conference Series Vol. 297, Star Formation Through Time. p. 363 (arXiv:astro-ph/0211474)
Storchi-Bergmann T., et al., 2018, ApJ, 868, 14
Strauss M. A., et al., 2002, AJ, 124, 1810
Sun A.-L., Greene J. E., Zakamska N. L., 2017, The Astrophysical Journal, 835, 222
Sutherland R., Dopita M., Binette L., Groves B., 2018, MAPPINGS V: Astrophysical plasma modeling code (ascl:1807.005)
Theureau G., Hanski M. O., Coudreau N., Hallet N., Martin J. M., 2007, A&A, 465, 71
Torres-Flores S., Amram P., Mendes de Oliveira C., Plana H., Balkowski C., Marcelin M., Olave-Rojas D., 2014, MNRAS, 442, 2188
Torrey P., Cox T. J., Kewley L., Hernquist L., 2012, The Astrophysical Journal, 746, 108
Treister E., Schawinski K., Urry C. M., Simmons B. D., 2012, The Astrophysical Journal, 758, L39
Trippe M. L., Crenshaw D. M., Deo R., Dietrich M., 2008, AJ, 135, 2048
Ulvestad J. S., Wilson A. S., 1984, ApJ, 285, 439
Veilleux S., Osterbrock D. E., 1987, ApJS, 63, 295
Veilleux S., Shopbell P. L., Miller S. T., 2001, AJ, 121, 198
Veilleux S., et al., 2013, ApJ, 776, 27
Veron P., Lindblad P. O., Zuiderwijk E. J., Veron M. P., Adam G., 1980, A&A, 87, 245
Villar-Martín M., Humphrey A., Delgado R. G., Colina L., Arribas S., 2011, MNRAS, 418, 2032

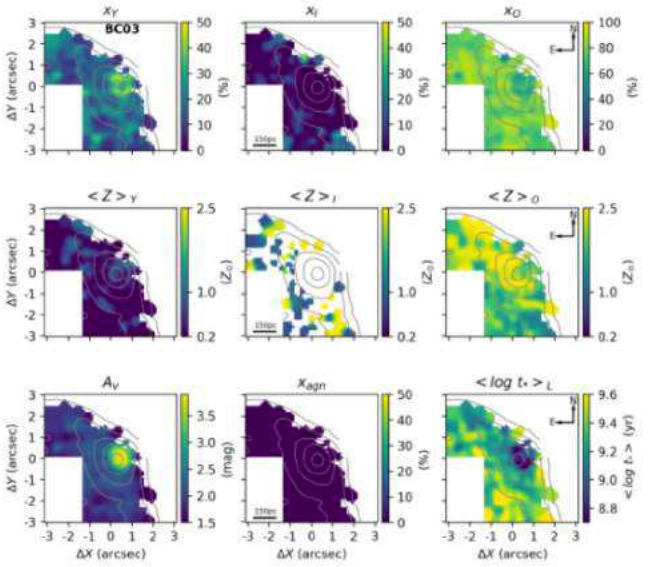

Figure A1. Maps of the recovered properties from the *BC03* synthesis. Top: from left to right, percentage contribution to the total light from young, intermediate and old SSPs (x_Y, x_I and x_O). Middle: from left to right, light-weighted mean stellar metallicity for the three SSP age groups, $\langle Z \rangle_Y$, $\langle Z \rangle_I$ and $\langle Z \rangle_O$. Bottom left: A_V extinction parameter. Bottom middle: Featureless continuum (FC) component percentage contribution to the total light (x_{agn}). Bottom Right: Light-weighted mean stellar age, $\langle log\ t_* \rangle$. The grey contour in all the maps is the continuum emission, left panel of Fig. 1. The x_{agn} is null in all points by definition, because there is no FC component in *BC03* synthesis spectra base.

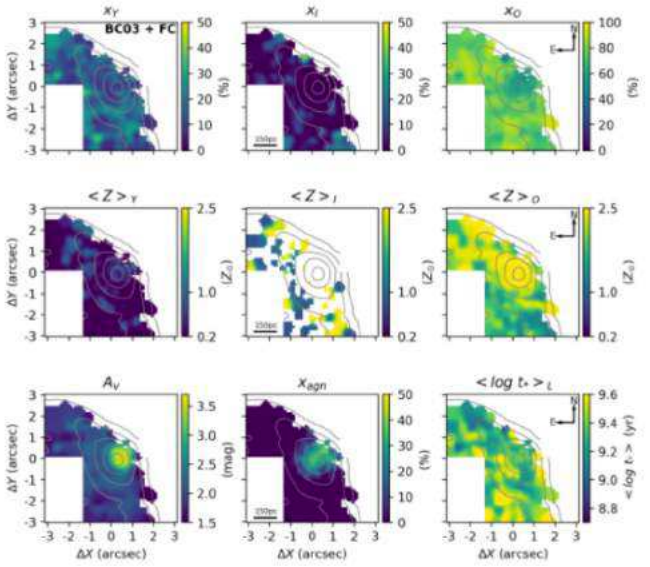

Figure A2. Same as Fig. A1for *BC03+FC*.

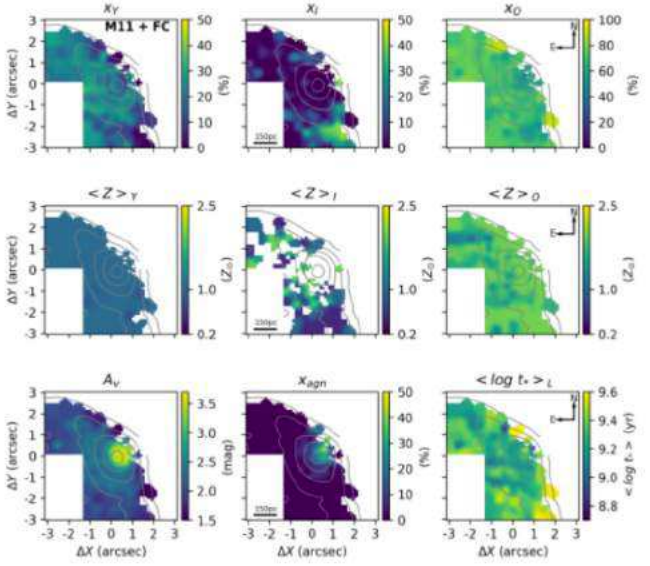

Figure A3. Same as Fig. A1 for *M11+FC*.

Ward M., Penston M. V., Blades J. C., Turtle A. J., 1980, MNRAS, 193, 563
Wilkinson D. M., Maraston C., Goddard D., Thomas D., Parikh T., 2017, MNRAS, 472, 4297
Zakamska N. L., et al., 2016, MNRAS, 459, 3144

APPENDIX A: STELLAR POPULATIONS SYNTHESIS MAPS

We show the maps of the recovered properties from three spatially resolved STARLIGHT synthesis we have performed, namely *BC03*, *BC03+FC* and *M11+FC*. The top panels show, from left to right, the per cent contribution to the total light for young, intermediate and old SSPs (x_Y, x_I and x_O). In the middle panels the light-weighted mean stellar metallicity for the three age groups, from left to right, $\langle Z \rangle_Y$, $\langle Z \rangle_I$ and $\langle Z \rangle_O$. In the bottom panel the V-Band extinction (A_V), the per cent contribution to the total light from the FC component (x_{agn}) and the light-weighted mean stellar age, $\langle log\ t_* \rangle$, are shown, respectively, from left to right.

APPENDIX B: EMISSION LINE FITTING UNCERTAINTIES

We present here the uncertainties in the parameters of the emission lines fitting described in subsection 4.1. The uncertainties are the standard deviation over the one hundred Monte Carlo iterations. The uncertainties in the radial velocity (V) of Component 1 was already presented in Fig. 8. In Fig. B1 we show the uncertainties in the velocity dispersion (σ) of Component 1, the values are mostly smaller than 5 km s^{-1}, reaching a maximum value of 15 km s^{-1}.

In the top panel we also show the uncertainties of v and σ of Component 2, values are less than 10 km s^{-1} in most the region, reaching up to 30 km s^{-1} in a very small region, the σ values are less then 10 km s^{-1} in the peak of component emission and up to 30 km s^{-1} in the borders of the detection region. In the middle and bottom panels the percentile uncertainties in the integrated flux (Component 1 + Component 2) of Hβ, [O III] λ5007, Hα, [N II] λ6583, and [S II] λ6716,6731 are shown.

The Hβ line uncertainties range from 10 per cent at the centre of the FoV, up to 45 per cent in the dust lane region. [O III] and Hα values range from less than 5 per cent up to 25 per cent at the dust lane region. [S II] and [N II] values range from less than 10 per cent up to 35 per cent at the dust lane region.

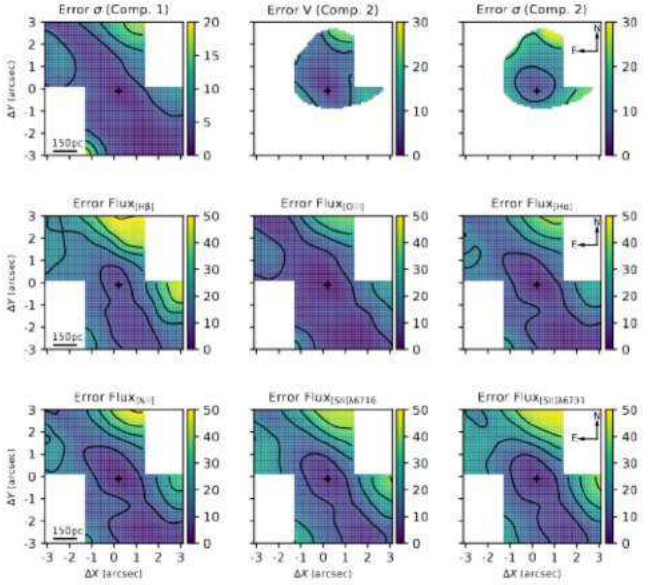

Figure B1. Emission line fitting uncertainties. Top: from right to left, velocity dispersion of Component 1 ($\mathrm{km\,s^{-1}}$), radial velocity of Component 2 ($\mathrm{km\,s^{-1}}$), velocity dispersion of Component 2 ($\mathrm{km\,s^{-1}}$). Middle and Bottom: percentage uncertainties in the integrated flux (Component 1 + Component) of Hβ, [O III] λ5007, Hα, [N II] λ6583, and [S II] λ6716,6731 (%). The black cross shows the peak of the continuum emission. Each contour in the maps means a 10% variation in the uncertainties.

APPENDIX C: NEBULAR EXTINCTION AND ELECTRON DENSITY

In order to measure the extinction in the NLR, we adopt the Calzetti et al. (2000) extinction law, and assume the case B recombination and the intrinsic Hα/Hβ value for the NLR (Osterbrock & Ferland 2006), which combined leads to the following expression to the V-band extinction:

$$A_\mathrm{v} = 7.95 \times \log_{10}\left(\frac{\mathrm{H}\alpha/\mathrm{H}\beta}{3.1}\right) \quad \text{(C1)}$$

In order to improve the S/N and given the fact that Hβ Component 2 is detected in a very small region, we used the integrated flux (Component 1 + Component 2) of the NLR Hα and Hβ lines. The A_v map is presented in the top left panel of Fig. C1, and its uncertainty in the bottom left panel. The A_v peak at ~ 4.5 mag at the peak of the emission lines emission, and has values > 3.5 mag in the dust lane portion of the FoV. However, this value may be even higher as the uncertainties are up to 2 mag in this region, caused by high impression on the Hβ flux measurement, as seen in Fig. B1. Although the A_v are not the same in the continuum Appendix A and in the NLR, the spatial patterns are similar: the higher values are found the central spaxels and towards the dust lane, and the lower towards the SE direction.

The electron density (n_e) of the ionised gas in the NLR can be obtained from the ratio between the [S II] lines, [S II]λ6716/λ6731 (Osterbrock & Ferland 2006). We applied the solution of the collisional equilibrium equations given by Proxauf et al. (2014) to obtain the n_e values, as follows:

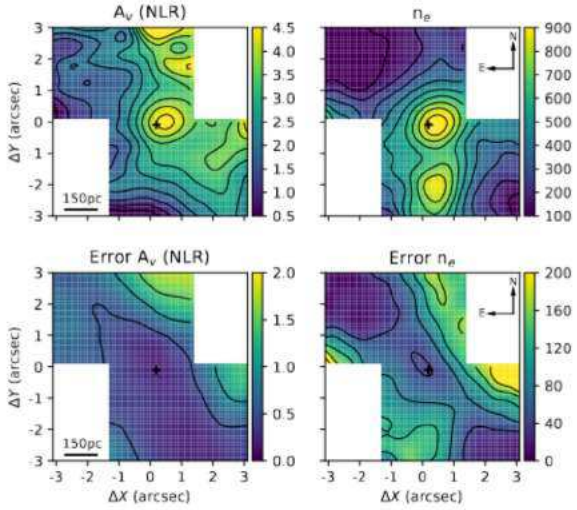

Figure C1. Top left and bottom left panels, shows, respectively the V-band extinction A_v map and its uncertainties, both in units of magnitudes. Top right and bottom right panel show, respectively, the electron density (n_e) and its uncertainties both in $\mathrm{cm^{-3}}$ units. The black cross shows the peak of the continuum emission.

$$\log_{10}(n_e\ [cm^3]) = 0.0543\tan(-3.0553R + 2.8506) + 6.98 - 10.6905R + 9.9186R^2 - 3.5442R^3 \quad \text{(C2)}$$

with R = F_{6716}/F_{6731}, the ratio between the [S II] lines. The n_e map in its uncertainties are presented, respectively, in the top right and bottom right panel of Fig. C1. The maximum value of n_e is 950 cm^{-3} reached at the peak of the emission lines, decreasing radially down to 100 cm^{-3}, another high ($\sim$ 800 cm^{-3}) density knot is present at the south of the nucleus. Both the values as well as the spatial profiles of both A_v and n_e measured here are in agreement with the recent published analyses by Mingozzi et al. (2019) using MUSE instrument, see their Figures A1 and B1.

This paper has been typeset from a TEX/LATEX file prepared by the author.

MNRAS **000**, 1–12 (2020) Preprint 17 May 2021 Compiled using MNRAS LATEX style file v3.0

The Eddington ratio-dependent multiple changing look events in NGC 2992

Muryel Guolo-Pereira[1]★, Daniel Ruschel-Dutra[1], Jaderson Schimoia[2], Dirk Grupe[3], Bradley M. Peterson[4,5,6], Rodrigo Nemmen[7], Thaisa Storchi-Bergmann[8], Andrew Robinson[9]

[1]*Departamento de Física - CFM - Universidade Federal de Santa Catarina, 476, 88040-900 Florianópolis, SC, Brazil*
[2]*Departamento de Física - CCNE - Universidade Federal de Santa Maria, 97105-90, Santa Maria, RS, Brazil*
[3]*Space Science Center, Morehead State University, 235 Martindale Drive, Morehead, KY 40351, USA*
[4] *Department of Astronomy, The Ohio State University, 140 W 18th Ave, Columbus, OH 43210, USA*
[5] *Center for Cosmology and AstroParticle Physics, 191 Woodruff Ave., Columbus, OH 43210, USA*
[6] *Space Telescope Science Institute, 3700 San Martin Drive, Baltimore, MD 21218, USA*
[7] *Instituto de Astronomia, Geofísica e Ciências Atmosféricas, Universidade de São Paulo, São Paulo, SP 05508-090, Brazil*
[8] *Departamento de Astronomia, Universidade Federal do Rio Grande do Sul. Av. Bento Goncalves 9500, 91501-970 Porto Alegre, RS, Brazil*
[9] *School of Physics and Astronomy, Rochester Institute of Technology, 84 Lomb Memorial Drive, Rochester, NY 14623, USA*

Accepted XXX. Received YYY; in original form ZZZ

ABSTRACT

We present the analyses of the historical X-rays and optical spectra of the 'changing look' active galactic nucleus (AGN) NGC 2992, ranging from 1978 to 2019. The galaxy presents multiple Seyfert type transitions from type 2 to intermediate-type losing and regaining its Hα Broad Emission Line (BEL) recurrently. In X-rays, the source shows intrinsic variability with the absorption corrected luminosity varying by a factor of ~ 35. We rule-out tidal disruption events or variable obscuration as causes of the type transitions, and show that the presence (and flux) of the broad Hα emission line is directly correlated with the 2-10 keV X-ray luminosity (L_{2-10}): a minimum value of $L_{2-10} \approx 4 \times 10^{42}$ erg s^{-1} is necessary for its appearance, this value translates to a Eddington ratio ($\lambda_{Edd} = L_{Bol}/L_{Edd}$) of $2.0^{+2.0}_{-1.3}$% for the assumed black hole mass. The detection of the Hβ BEL is only possible at even higher accretion rates of $\sim$ 5–8%. We find a correlation between the narrow Fe Kα flux and λ_{Edd}, and an anti-correlations between full width at half maximum of Hα BEL and λ_{Edd}. Two possible scenarios for type transitions are compatible with our results: either the dimming (brightening) of the AGN continuum, which reduces (increases) the supply of ionising photons available to excite the gas in the vicinity of the black hole, or the fading of the Broad Line Region (BLR) structure itself occurs as the low accretion rate is not able to sustain the required cloud flow rate in a disk-wind BLR model.

Key words: galaxies: Seyfert – galaxies: nuclei – X-rays: galaxies – optical: galaxies

1 INTRODUCTION

Supermassive black holes (SMBH) at the centre of galaxies can become active by the accretion of surrounding matter (see Storchi-Bergmann & Schnorr-Müller 2019, for a review on the feeding mechanism). Such active galactic nuclei (AGN) can be identified by features in their optical spectra - such as broad emission lines (BEL) and/or narrow high ionisation emission lines due to the non-stellar ionising continuum - or by their nuclear X-ray emission. Emission lines produced by the gas orbiting in the vicinity of the SMBH are Doppler broadener, forming the broad-line region (BLR), while the narrow-line region (NLR) extends from a few parsecs to hundreds of parsecs beyond the accretion disk. Historically, Type 1 AGNs are those showing both broad ($> 10^3$, $< 10^4$ km s^{-1}) and narrow ($< 10^3$ km s^{-1}) permitted emission lines and narrow forbidden lines in their optical spectra; while Type 2 AGNs lack BELs. Intermediate AGN types were added by Osterbrock (1981), including types 1.8 and 1.9, classified, respectively, according to the presence of a weak, or absent, Hβ BEL, while retaining an Hα BEL.

AGN unification models attribute differences in AGN type to the viewing angle toward an axisymmetric, parsec scale obscuring structure, which can block our direct view of the AGN central engine (Antonucci 1993; Urry & Padovani 1995) and is responsible for the lack of BEL in Type 2 AGNs. However, a relatively small number of AGN show transitions from one type to another in a few years; these objects are known as "changing look" (CL) AGNs. CL-AGNs

★ E-mail:muryel@astro.ufsc.br

have changed the widely accepted AGN paradigm, not only in the orientation-based unified model but also standard accretion disk models (see Lawrence 2018, for a review of the so-called Quasar Viscosity Crisis). Their extreme and fast variability has motivated alternatives and/or modifications for both the AGN Unified Model (e.g. Nicastro 2000; Elitzur & Shlosman 2006; Elitzur et al. 2014) and for the standard Shakura & Sunyaev (1973) accretion disk model (e.g. Sniegowska et al. 2020; Jiang & Blaes 2020)

Until recently there were only a handful of CL events reported, including NGC 3516 (Andrillat & Souffrin 1971), NGC 1566 (Pastoriza & Gerola 1970; Oknyansky et al. 2019), Mrk 590 (Denney et al. 2014), NGC 2617 (Shappee et al. 2014), NGC 7603 (Tohline & Osterbrock 1976), Mrk 1018 (Cohen et al. 1986), NGC 1097 (Storchi-Bergmann et al. 1993), NGC 3065 (Eracleous & Halpern 2001) and NGC 7582 (Aretxaga et al. 1999). In 2015 LaMassa et al. discovered the first CL Quasar and since then the number of known CL-AGNs has increased rapidly (e.g. MacLeod et al. 2016; McElroy et al. 2016; Runnoe et al. 2016; Yang et al. 2018; Ruan et al. 2016; Sheng et al. 2017; Kollatschny et al. 2018; Guo et al. 2019; Wang et al. 2019; Graham et al. 2019; Kollatschny et al. 2020); however, the number is still fewer than a hundred.

Some of these CL might be successfully explained via variable obscuration (e.g., Matt et al. 2003; Puccetti et al. 2007; Risaliti et al. 2010; Marinucci et al. 2013; Marchese et al. 2012): in models where the obscuring material has a patchy distribution (e.g. Nenkova et al. 2008; Elitzur 2012), the dynamical movement of the dust clouds could result in a change of classification. Transient events such as tidal disruption events (TDE) of a star by the SMBH were also claimed as possible drivers of CL events (Eracleous et al. 1995); however, this scenario does not apply to sources presenting multiple (and quasi-periodic) CL events.

In a third scenario, it has been argued that changes in type are expected with variations in accretion rate. In this scenario either the BELs disappear (reappear) due to the reduction (increase) of ionising photons available to excite the gas in the vicinity of the black hole (e.g. Storchi-Bergmann et al. 2003; LaMassa et al. 2015) or the BLR itself disappears, given that in disk-wind BLR models (e.g. Nicastro 2000; Elitzur & Shlosman 2006; Elitzur & Ho 2009) the broad line emission region follows an evolutionary sequence that is directly related to the accretion rate of the compact source. In such disk-wind BLR models, a low accretion efficiency is not able to sustain the required cloud flow rate responsible for the formation of the BLR clouds which gives origin to the distinct (intrinsic) AGN types, as proposed by Elitzur et al. (2014).

NGC 2992 is a highly inclined, $i \sim 70°$, nearby (z = 0.00771, Keel 1996) Seyfert galaxy. The galaxy was the subject of several studies and target of all major X-ray missions due to its variability. In the X-rays, it steadily declined in observed flux from 1978, when it was observed by *HEAO1* (Mushotzky 1982) at a flux level of about 8×10^{-11} erg cm^{-2} s^{-1}until 1994 when it was observed by *ASCA* (Weaver et al. 1996) at a flux level by about a factor 20 fainter. Then it underwent a rapid recovery: in 1997 it was observed by *BeppoSAX* at a flux level somewhat higher than in 1994, while in 1998 the source fully recovered its *HEAO1* brightness (Gilli et al. 2000). In 2003, when observed by *XMM-Newton*, the flux was even higher, about 10^{-10} erg cm^{-2} s^{-1}(Shu et al. 2010). The source was then observed by *Suzaku* on November/December 2005, and found in a much fainter state, almost an order of magnitude fainter than in the *XMM-Newton* observation.

The Rossi X-ray Timing Explorer (RXTE, Swank 2006) monitoring campaign between early March 2005 and late January 2006 found large amplitude (almost an order of magnitude) variability, indicating that apart from the long-term variability of the source, it also presents short-term outbursts with variations in the order of days, while no significant variation of the primary power-law index was found (Murphy et al. 2007); at the end of the campaign the source was again at a low flux state, confirmed by *Suzaku*, at a flux level of $\sim 1 \times 10^{-11}$ erg cm^{-2} s^{-1}(Ptak et al. 2007; Yaqoob et al. 2007) and *Chandra*, at flux level of $\sim 0.3 \times 10^{-11}$ erg cm^{-2} s^{-1}(its historical minimum flux, Murphy et al. 2017). In 2010, NGC 2992 was observed eight times for $\sim$ 40 ks by *XMM-Newton* with a 2–10 keV flux ranging from 0.3×10^{-11} erg cm^{-2} s^{-1}to 1.3×10^{-11} erg cm^{-2} s^{-1}. A further 2013 *XMM-Newton* observation caught the source in a higher but still low flux state (1.6×10^{-11} erg cm^{-2} s^{-1}). In 2015, observations performed simultaneously with *Swift* and *NuSTAR* found a 2-10 keV flux of 6×10^{-11} erg cm^{-2} s^{-1}(Marinucci et al. 2018). The most recent observations were performed again with *XMM-Newton* in May 2019, when the flux was again at the highest levels seen, ranging from 6.8 to 10×10^{-11} erg cm^{-2} s^{-1}(Marinucci et al. 2020).

The optical variability of the source was first explored by Gilli et al. (2000) who noticed that in 1999 the Hα BEL was present again, as it was in early observations of the galaxy by Veron et al. (1980) at the end of the 1970s which led to its first classification as a Seyfert 1.9, in contrast to the Type 2 spectra seen in 1994 by Allen et al. (1999). Later, Trippe et al. (2008) showed that from the beginning of 2006 to the middle of 2007 the source had lost its BEL. Recently Schnorr-Müller et al. (2016) and Guolo-Pereira et al. (2021) not only showed that the Hα BEL was detectable again but also, for the first time, a very faint Hβ BEL was claimed to be present.

Besides being a very well studied galaxy, to the best of our knowledge no study has yet explored the entire X-ray and optical historical emission of NGC 2992, nor attempted to link the behaviour in the two wavelength bands. These are our goals in this paper. The paper is organised as follow: in section 2 we describe the data collection. The analysis of the data is described in section 3, while the results are discussed in section 4. Our conclusions appear in section 5.

2 DATA COLLECTION

This paper results from a careful re-examination of the entire literature on NGC 2992, both X-rays and optical spectra, from its discovery as an X-ray source (Cooke et al. 1978; Ward et al. 1980) and classification as a Seyfert galaxy (Osmer et al. 1974) to the most recent optical and X-ray spectra published to date (Marinucci et al. 2020; Guolo-Pereira et al. 2021).

2.1 X-ray Spectra

The X-ray spectrum of NGC 2992 is very well fitted by an absorbed power-law which accounts for most of the X-ray emission. However, the spectrum also presents a narrow iron Kα component **at 6.4 kev**, which becomes more intense at high flux levels (Yaqoob et al. 2007; Marinucci et al. 2018; Marinucci et al. 2020, see also section 3.1), We collected the fluxes in the 2-10 keV X-ray band (F_{2-10}) and the best-fitting parameters for the absorbed continuum model, namely the power-law continuum photon indexes (Γ)[1] and the absorbed material column densities (N_H), as reported by the

[1] The power law index in the continuum model: $F(E) \propto E^{-\Gamma}$.

authors throughout the literature on the source. For the more recent spectra, where the narrow Fe Kα is detected we also collected their measured fluxes, F(Fe Kα). In the top panel of Fig. 1, we show the historical 2-10 keV light curve. In Table 1, we show the best-fitting continuum model parameters, the Fe Kα fluxes, the observation dates, and references. The $N_{\rm H}$ are only accounting for the absorption at the redshift of the source therefore not including Galactic absorption, $N_{\rm H\ Gal} \approx 5.5{\times}10^{20}$ cm^{-2} (Kalberla et al. 2005). Errors in the X-rays parameters correspond to the 90% confidence level for the parameter of interest ($\Delta\chi^2 = 2.7$), as reported by the authors. For the papers in which the authors reported their uncertainties in another scale, e.g., $\Delta\chi^2 = 4.6$, the errors were re-scaled using a Python package (`asymmetric_uncertainties`) for treatment of asymmetric statistical errors derived from confidence levels, which employs a combination of the methods proposed by Barlow (2004) and Possolo et al. (2019). The method and a brief discussion on uncertainties can be found in Appendix A. The propagation of the uncertainties for the X-ray derived quantities (see section 3.1 and Table 1) is also performed with this same method, see appendix A.

2.2 Historical Optical Spectra

To access the historical presence or absence of Hα BEL and the galaxy optical classification, we reviewed all papers that report optical spectra of the galaxy. As most of these spectra are not available to allow inter-calibration and measurement of the BELs flux variability, we restrict ourselves to a binary classification of the Hα BEL, i.e., whether the component was undoubtedly detected (D) or not-detected (N-D) by the authors. We do so by searching for a detection/non-detection claim in the original text and by visually inspecting the published spectra. In the middle panel of Fig. 1, we show the Hα BEL detection history. In Table 2, we show the observation dates, the references and the Seyfert type at the time.

In summary: the first spectra of the galaxy in the '70s (Ward et al. 1980; Veron et al. 1980; Shuder 1980; Durret & Bergeron 1988) detected only Hα broad components, with no counterpart in Hβ, resulting in its original classification as a Seyfert 1.9 galaxy. Throughout mid '80s to the mid '90s several authors have reported that the BEL Hα was not detectable anymore (Busko & Steiner 1990; Allen et al. 1999; Marquez et al. 1998; Veilleux et al. 2001), changing its classification to Seyfert 2 Type. However the broad component was detected again from the end of the '90s to the beginning of the 2000s (Gilli et al. 2000; García-Lorenzo et al. 2001; Stoklasová et al. 2009). Later, Trippe et al. (2008) performed an 18 months long monitoring campaign from the beginning of 2006 to mid 2007 that revealed the Hα BEL component was missing again, throughout the entire campaign. More recent observations have shown that the galaxy has regained the broad Hα component (Dopita et al. 2015; Schnorr-Müller et al. 2016; Mingozzi et al. 2019), and for the first time, an Hβ BEL was unambiguously detected, in late 2018, by Guolo-Pereira et al. (2021), therefore changing its classification to a 1.8 Type Seyfert galaxy.

It is important to note the large number of data points collected: 40 in the X-rays (33 with reported $N_{\rm H}$ and Γ values) and 18 in the optical; which allow us to have a quasi-contemporaneous X-ray measurement for each optical spectrum, within less than one year for most, and less than two years for all of them, see Fig. 1.

2.3 Modern Optical Spectra

For four of the six recent spectra of NGC 2992, we were able to apply methods of flux intercalibration that have been developed for reverberation mapping studies (Peterson 1993; van Groninge & Wanders 1992; Peterson et al. 1995; Fausnaugh 2017) and measure the intrinsic flux variability of the BELs. The spectra are from:

- Trippe et al. (2008) and taken in December of 2006 in the Cerro Tololo Inter-American Observatory; the spectrum was obtained by private communication with one of the authors;
- Dopita et al. (2015) as part of the Siding Spring Southern Seyfert Spectroscopic Snapshot Survey (S7), taken in April of 2014 and publicly available at the S7 survey website;
- Mingozzi et al. (2019) as part of the Measuring Active Galactic Nuclei Under MUSE Microscope (MAGNUM) survey using the Multi-Unit Spectroscopic Explorer (MUSE) at the Very Large Telescope (VLT) and taken in February of 2015; the spectral data cube is public available at the VLT archive;
- A paper recently published by our group (Guolo-Pereira et al. 2021). The spectral data cube was taken using the Gemini Multi-Object Spectrographs (GMOS) at the Gemini South Telescope in February of 2018.

The inter-calibration, aperture/seeing corrections, and the process for emission line fitting of these spectra will be presented in section 3.2.

2.4 Estimates of the Black Hole Mass and Luminosity Distance

Precise black hole mass and luminosity distance measurements are essential for the energetic calibrations and scaling to come. Using stellar velocity dispersion measurements of σ_* = 158 km s^{-1}, Woo & Urry (2002) estimated the black hole mass of NGC 2992 to be 5.2×10^7 M$_\odot$ by applying the Tremaine et al. (2002) M$_{\rm BH}$- σ_* relation. The value obtained from Gültekin et al. (2009) M$_{\rm BH}$- σ_* relation is M$_{\rm BH}$ = $4.8^{+3.9}_{-2.4} \times 10^7$ M$_\odot$, using a bulge stellar velocity dispersion σ_* = 158 ± 13 km s^{-1} (Nelson & Whittle 1995). From the normalised excess variance σ^2_{rms} in the 2-10 keV band and assuming the σ^2_{rms}- M$_{\rm BH}$ correlation from Ponti et al. (2012), Marinucci et al. (2020) reported a M$_{\rm BH}$ = $3.0^{+5.5}_{-1.5} \times 10^7$ M$_\odot$. Furthermore, we also estimate the SMBH mass using the emission line measurements, to be described in section 3.2.2, by using single-epoch (SE) M$_{\rm BH}$ estimates. We applied Dalla Bontà et al. (2020) M$_{\rm SE}(\sigma_{H\beta}, L_{H\beta})$ relation in all the four modern spectra (section 2.3). We corrected extinction effects using the measured Balmer decrements and assuming Calzetti et al. (2000) extinction law. We obtained the following values for M$_{\rm BH}$: $1.3^{+2.8}_{-0.9}{\times}10^7$ M$_\odot$, $3.5^{+7.4}_{-2.4}{\times}10^7$ M$_\odot$ and $2.4^{+5.1}_{-1.4}\times 10^7$ M$_\odot$, respectively for 2014, 2015 and 2018 spectra. For 2006 spectrum, as the the Hβ BEL was not detected we use the Hα BEL, assuming a Balmer decrement of 9 (see section 3.2.3), we obtained M$_{\rm BH}$ = $0.5^{+1.5}_{-0.4} \times 10^7$ M$_\odot$. In summary, although the distinct methods results in distinct M$_{\rm BH}$ values, they are all within the $0.5 - 5.5 \times 10^7$ M$_\odot$ range.

Theureau et al. (2007) found a recession velocity of 2657 km s^{-1} for NGC 2992 (already corrected for peculiar motions), which assuming a cosmology with H_0 = 70 km s^{-1}Mpc^{-1}, translates to a luminosity distance to NGC 2992 equals to 38 Mpc.

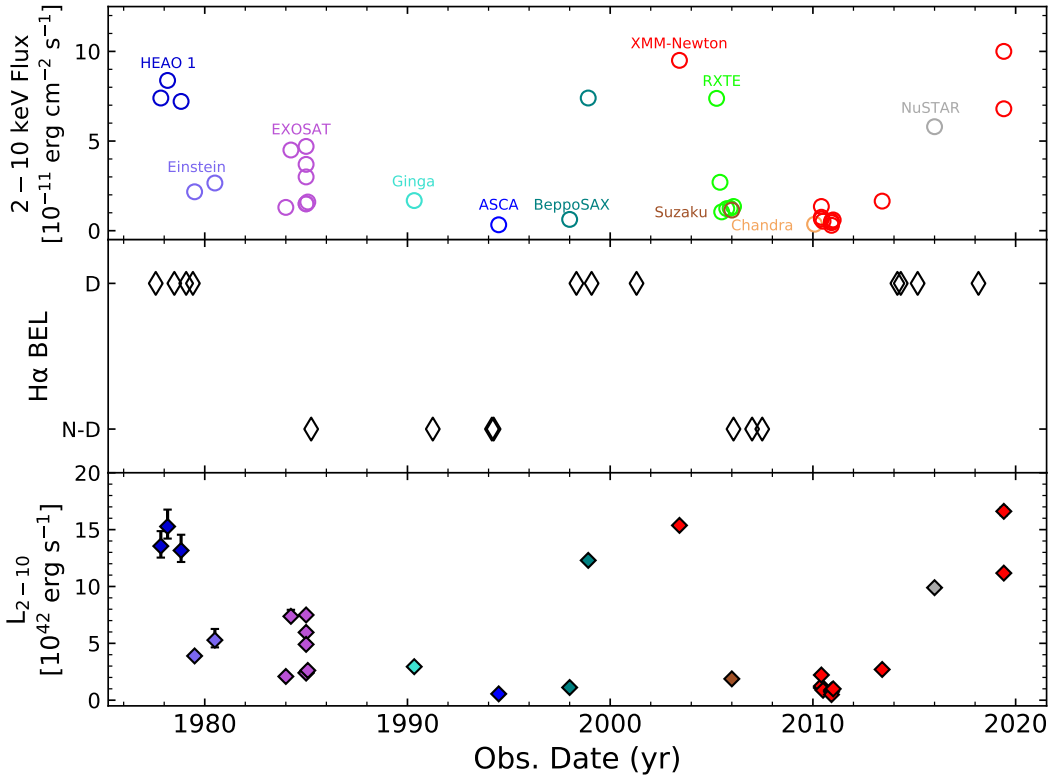

Figure 1. Top: Historical 2-10 keV light curve of the source. Middle: Historical detections (D) and non-detections (N-D) of the broad Hα emission line. **Bottom: Intrinsic (absorption corrected) 2-10 keV Luminosity (L_{2-10}) light curve. Each colour represents a distinct X-ray mission, and will be maintained throughout the entire paper. In the L_{2-10} panel, the points without error bars have errors smaller then 3×10^{41} erg s^{-1}, see Table 1 for the exact values.**

3 DATA ANALYSES

3.1 X-ray Variability

In the scenario where the CL events are caused by variable absorption, two natural consequences are an anti-correlation between the N_H and F_{2-10} and a constant intrinsic (absorption corrected) luminosity. In the top panel of Fig. 2 we show log N_H as function of F_{2-10}: no clear anti-correlation can be seen. The Spearman rank correlation coefficient (r_s) for the two variables and its correspondent p_{value} are $r_s = 0.19^{+0.15}_{-0.14}$ and $p_{value} = 0.22^{+0.45}_{-0.17}$, while the best-fitting constant value is $N_H = 22.01^{+0.03}_{-0.03}$, where the errors correspond to 90% confidence level measured by performing a thousand Monte Carlo iterations (see details in appendix A).

We can therefore conclude that although there were some variations in the column density it is not anti-correlated with the X-ray flux as seen in variable absorption CL-AGNs (e.g. Puccetti et al. 2007; Bianchi et al. 2009). **A further confirmation that the absorption is not the main factor responsible for the behaviour of the source can be seen by the intrinsic (i.e. absorption corrected) rest-frame luminosity (L_{2-10}). The measured L_{2-10} values, for each observation in which a N_H value is provided, are presented in Table 1. The values range from 4.9×10^{41} erg s^{-1} to $\sim 1.7\times10^{43}$ erg s^{-1}. The L_{2-10} light curve is shown in the bottom panel of Fig. 1, and it has the same behaviour as the F_{2-10} and this indicates/confirms that the variations are intrinsic and not due to changes in absorption.**

The Sperman rank correlation test shows that there is no monotonic correlation between the photon index Γ and the X-rays flux (or luminosity) for NGC 2992 (bottom panel of Fig. 2). The values found were $r_s = 0.15^{+0.12}_{-0.12}$ and $p_{value} = 0.27^{+0.55}_{-0.23}$. The existence of a correlation between luminosity and photon index is in fact debatable, and several contradictory results have been presented in the last years. While Dai et al. (2004) reported the existence of a positive correlation, other works found none (e.g. Winter et al. 2009) or a negative correlation (e.g. Corral et al. 2011). A 'V' shape for the Γ versus L_{Edd} relation for NGC 2992 was claimed by Liu et al. (2019); the authors interpreted this as a change in accretion mode, similar to the ones that occur in stellar-mass X-ray binaries, e.g. Qiao & Liu (2013), in the AGN. We argue here that their finding is due to selection effects, as the authors only used data from 2003 to 2013. When the entire historical data of the source is shown (Fig. 2), this effect is not seen. However, there is a positive correlation between F_{2-10} and the flux of the Fe Kα, with $r_s = 0.69^{+0.07}_{-0.11}$ and $p_{value} = 0.01^{+0.03}_{-0.01}$. Fitting the data by assuming a relation of the type:

$$\log F(\text{Fe K}\alpha) = \alpha + \beta \log F_{2-10} \quad (1)$$

we obtained a slope of $\beta = 0.39 \pm 0.04$. As the iron Kα line is created by reprocessing of the primary X-ray continuum, a tight correlation between the flux of the line and that of the continuum is expected. For large samples of galaxies Ricci et al. (2014), found $\beta = 0.89 \pm 0.04$, while Shu et al. (2010) found $\beta = 0.86 \pm 0.01$. However, NGC 2992 seems to be one of a few objects where this correlation is found in a single object, though with a lower slope than the ones found in the general AGN population.

Table 1. Historical X-ray data for NGC 2992.

Obs. Date[(a)]	Satellite	$F_{2-10}^{(b)}$	$N_H^{(c)}$	Γ	F(Fe Kα)[(d)]	Reference	$L_{2-10}^{(e)}$
10/1977		7.40			–		$13.48^{+1.40}_{-0.99}$
02/1978	HEAO 1	8.38	$16.0^{+8.0}_{-6.0}$	$1.79^{+0.09}_{-0.07}$	–	Mushotzky (1982)	$15.30^{+1.52}_{-1.13}$
10/1978		7.21			–		$13.09^{+1.34}_{-0.85}$
06/1979	Einstein	2.17	$14.3^{+6.0}_{-4.0}$	$1.82^{+0.14}_{-0.14}$	–	Maccacaro et al. (1982)	$3.89^{+0.30}_{-0.20}$
06/1980		2.66	$22.3^{+15.2}_{-10.7}$	$1.92^{+0.47}_{-0.47}$	–		$5.25^{+1.01}_{-0.64}$
12/1983	EXOSAT	1.30	$7.0^{+3.5}_{-1.2}$	$1.46^{+0.23}_{-0.16}$	–	Turner & Pounds (1989)	$2.09^{+0.10}_{-0.03}$
03/1984		4.50	$7.8^{+6.2}_{-1.6}$	$1.68^{+0.31}_{-0.22}$	–		$7.37^{+0.59}_{-0.17}$
12/1984		4.70	$6.0^{+1.7}_{-0.6}$	$1.64^{+0.07}_{-0.09}$	–		$7.50^{+0.18}_{-0.07}$
12/1984		3.70	$7.0^{+1.2}_{-0.3}$	$1.56^{+0.10}_{-0.06}$	–		$5.96^{+0.12}_{-0.03}$
12/1984		3.00	$8.6^{+2.6}_{-0.3}$	$1.48^{+0.15}_{-0.11}$	–		$4.91^{+0.27}_{-0.03}$
12/1984		1.50	$6.9^{+7.1}_{-1.8}$	$1.49^{+0.46}_{-0.27}$	–		$2.42^{+0.23}_{-0.07}$
12/1984		1.50	$5.6^{+5.2}_{-1.2}$	$1.58^{+0.39}_{-0.20}$	–		$2.39^{+0.19}_{-0.05}$
01/1985		1.60	$7.4^{+4.7}_{-1.2}$	$1.67^{+0.31}_{-0.17}$	–		$2.61^{+0.18}_{-0.05}$
04/1990	GINGA	1.68	$13.6^{+3.3}_{-3.3}$	$1.64^{+0.08}_{-0.08}$	–	Nandra & Pounds (1994)	$2.94^{+0.12}_{-0.12}$
06/1994	ASCA	0.33	$10.1^{+2.7}_{-2.3}$	1.70[(f)]	–	Weaver et al. (1996)	$0.56^{+0.02}_{-0.02}$
12/1997	BeppoSAX	0.63	$14.0^{+5.0}_{-4.0}$	$1.72^{+0.13}_{-0.12}$	–	Gilli et al. (2000)	$1.12^{+0.07}_{-0.06}$
11/1998		7.40	$9.0^{+0.3}_{-0.3}$	$1.70^{+0.02}_{-0.02}$	–		$12.29^{+0.05}_{-0.05}$
05/2003	XMM-Newton	9.50	$6.5^{+0.3}_{-0.2}$	$1.83^{+0.06}_{-0.04}$	–	Shu et al. (2010)	$15.37^{+0.07}_{-0.05}$
03/2005	RXTE	7.38	–(g)	$1.71^{+0.03}_{-0.03}$	–	Murphy et al. (2007)	–
05/2005		2.70	–	$1.72^{+0.04}_{-0.04}$	–		–
06/2005		1.05	–	$1.75^{+0.10}_{-0.10}$	–		–
09/2005		1.23	–	$1.85^{+0.13}_{-0.12}$	–		–
11/2005		1.25	–	$1.96^{+0.12}_{-0.11}$	–		–
01/2006		1.35	–	$1.76^{+0.08}_{-0.08}$	–		–
12/2005	SUZAKU	1.15	$8.0^{+0.6}_{-0.4}$	$1.57^{+0.05}_{-0.03}$	$3.99^{+0.80}_{-0.80}$	Yaqoob et al. (2007)	$1.88^{+0.01}_{-0.01}$
01/2010	CHANDRA	0.36	–	–	–	Murphy et al. (2017)	–
05/2010	XMM-Newton	0.65	$9.2^{+1.0}_{-1.0}$	$1.67^{+0.05}_{-0.05}$	$3.51^{+0.35}_{-0.35}$	Marinucci et al. (2018)	$1.08^{+0.01}_{-0.01}$
05/2010		0.75	$8.6^{+1.0}_{-1.0}$	$1.64^{+0.04}_{-0.04}$	$2.96^{+0.42}_{-0.42}$		$1.24^{+0.02}_{-0.01}$
05/2010		1.35	$8.4^{+1.0}_{-1.0}$	$1.61^{+0.04}_{-0.04}$	$4.49^{+0.48}_{-0.48}$		$2.22^{+0.03}_{-0.03}$
06/2010		0.53	$8.5^{+1.0}_{-1.0}$	$1.67^{+0.05}_{-0.05}$	$3.69^{+0.32}_{-0.32}$		$0.87^{+0.01}_{-0.01}$
11/2010		0.54	$8.0^{+1.0}_{-1.0}$	$1.67^{+0.05}_{-0.05}$	$3.64^{+0.34}_{-0.34}$		$0.88^{+0.01}_{-0.01}$
11/2010		0.45	$8.0^{+1.0}_{-1.0}$	$1.70^{+0.06}_{-0.06}$	$3.70^{+0.35}_{-0.35}$		$0.74^{+0.01}_{-0.01}$
11/2010		0.30	$8.1^{+1.0}_{-1.0}$	$1.71^{+0.09}_{-0.09}$	$3.19^{+0.32}_{-0.32}$		$0.49^{+0.01}_{-0.01}$
12/2010		0.60	$9.0^{+1.0}_{-1.0}$	$1.68^{+0.04}_{-0.04}$	$3.00^{+0.37}_{-0.37}$		$1.00^{+0.01}_{-0.01}$
05/2013		1.65	$8.1^{+1.0}_{-1.0}$	$1.63^{+0.06}_{-0.06}$	$5.66^{+1.12}_{-1.12}$		$2.70^{+0.03}_{-0.03}$
12/2015	NuSTAR	5.80	$11.0^{+2.0}_{-2.0}$	$1.72^{+0.03}_{-0.03}$	$8.68^{+1.92}_{-1.92}$		$9.89^{+0.26}_{-0.24}$
05/2019	XMM-Newton	10.00	$9.0^{+1.6}_{-1.6}$	$1.68^{+0.10}_{-0.10}$	$12.96^{+1.60}_{-1.60}$	Marinucci et al. (2020)	$16.59^{+0.34}_{-0.34}$
05/2019		6.80	$8.5^{+1.6}_{-1.6}$	$1.63^{+0.06}_{-0.06}$	$12.96^{+1.60}_{-1.60}$		$11.18^{+0.23}_{-0.22}$

(a) mm/yyyy. (b) in units of 10^{-11} erg cm^{-2} s^{-1}. (c) in units of 10^{21} cm^{-2}. (d) in units of 10×10^{-14} erg cm^{-2} s^{-1} (e) Absorption corrected, in units of 10^{42} erg s^{-1}. (f) The value was frozen in the model fitting, therefore it was excluded in the analyses of the Γ parameter variability of section 3.1. (g) Values not provided by the authors.

3.2 Modern Optical Spectra Analyses

In this section, we explore the flux variability of the BELs using four of the six most recent spectra, namely from 12/2006, 04/2014, 02/2015 and 02/2018 (see Table 2).

3.2.1 Absolute calibration of the spectra

Even under the best conditions, which are not often realized, flux calibration of ground-based spectrophotometry is no better than ≈5%, which is insufficient for detailed comparisons of variable spectra. Thus the standard technique of flux calibration, through comparison with stars of known spectral energy distribution, is not good enough for the study of AGN variability. Instead, we use the fluxes of the narrow emission lines known to be non-variable on time scales of tens of years in most AGN. Consequently, the bright narrow emission lines can be adopted as internal calibrators for scaling AGN spectra (Peterson 1993). We assume that the flux of the [O III] λ5007 line remains constant during the interval covered by these spectra.

We extracted the spectra using virtual apertures from the original data, making them as similar as possible to each other in the data cubes, as shown in Table 3. The scaling of the extracted spectra was carried out using a refinement of the method of van Groningen & Wanders (1992), employed as a Python package (`mapspec`) by Fausnaugh (2017). This method allows us to obtain a homogeneous

Table 2. Historical broad Hα line and Seyfert Type classification for NGC 2992.

Obs. Date[(a)]	Hα BEL[(b)]	Reference	Seyfert Type
07/1977	D	Ward et al. (1980)	1.9
< 1978	D	Veron et al. (1980)	1.9
01/1979	D	Shuder (1980)	1.9
05/1979	D	Durret & Bergeron (1988)	1.9
03/1985	N-D	Busko & Steiner (1990)	2
03/1991	N-D	Marquez et al. (1998)	2
02/1994	N-D	Veilleux et al. (2001)	2
03/1994	N-D	Allen et al. (1999)	2
04/1998	D	García-Lorenzo et al. (2001)	1.9
01/1999	D	Gilli et al. (2000)	1.9
03/2001	D	Stoklasová et al. (2009)	1.9
01/2006	N-D		2
12/2006	N-D	Trippe et al. (2008)	2
06/2007	N-D		2
02/2014	D	Schnorr-Müller et al. (2016)	1.8/1.9
04/2014	D	Dopita et al. (2015)	1.9
02/2015	D	Mingozzi et al. (2019)	1.8/1.9
02/2018	D	Guolo-Pereira et al. (in prep)	1.8

(a) mm/yyyy. (b) Whether the Hα BEL was Detected (D) or Non-Detected (N-D).

set of spectra with the same wavelength solution, same spectral resolution (at ~ 6300Å), and the same [O III]λ5007 flux value.

3.2.2 *Stellar component subtraction and emission-line fitting*

We subtracted the host galaxy stellar continuum fitted using the STARLIGHT (Cid Fernandes et al. 2005) full spectra fitting code, using a base of 45 Simple Stellar Population (SSP) spectra, with 15 ages (from 1 Myr to 13 Gyr) and 3 metallicities (0.2, 1.0 and 2.5 $Z_\odot$). The emission line fitting was performed using the IFSCUBE package[2] (Ruschel-Dutra 2020). The code employs Sequential Least Square Programming and allows multiple components with physically motivated constraints. In order to measure the BEL fluxes, the narrow emission components must be separated from the broad components. This process is not straightforward due to the fact the BELs are blended with the narrow lines, for both Hα and Hβ.

The narrow line subtraction was performed in two steps. First we fitted the narrow and broad Hα and Hβ simultaneously. For the narrow lines, we created a template comprised of two Gaussian components that were based on the [S II]λ6716 profile. This template was used to fit the [N II] and narrow Hα and Hβ lines by adjusting its flux scaling factor only. The fits to the broad lines were subtracted from the spectra, isolating the narrow emission; we then re-fitted the narrow lines assuming the H I and [N II] lines have the same velocity dispersion and redshift and we set the flux of [N II]λ6583 line as 2.96 times that of the [N II]λ6548 line, in accordance with the ratio of their transition probabilities (Osterbrock & Ferland 2006), while the Hα and [N II]λ6583 fluxes were free parameters in the fit. Finally, we subtracted the resulting narrow lines from the original spectrum and re-fit only broad lines using three Gaussian components, in order to account for the known non-Gaussian profiles of the BEL. The errors were taken as the standard deviations of one hundred Monte Carlo iterations. The resulting fits for the four spectra are shown in Fig. 3.

[2] http://github.com/danielrd6/ifscube

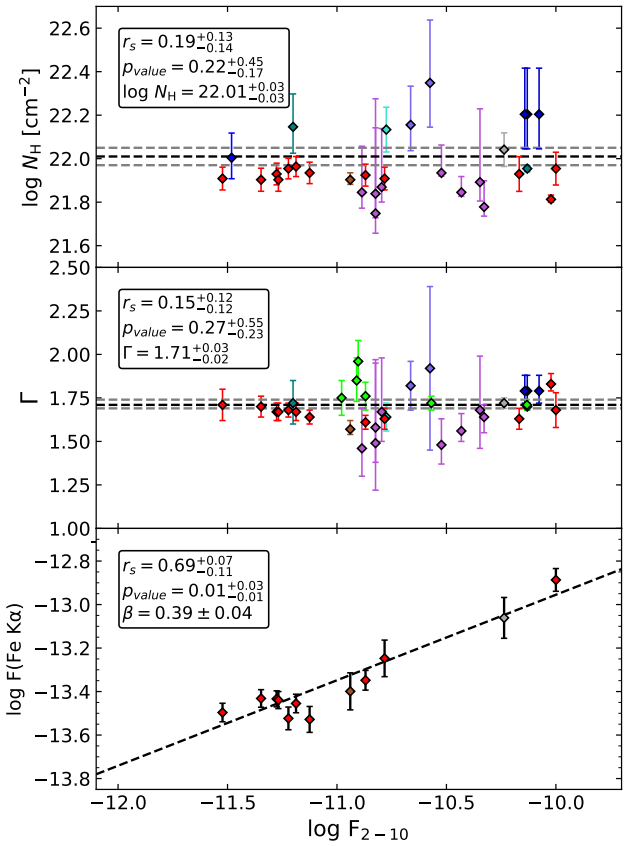

Figure 2. Best-fitting parameters N_H (top panel) and Γ (middle panel) for an absorbed power-law continuum model as function of the 2-10 keV Flux. The left top boxes show the Spearman rank correlation coefficient (r_s) for the two variables and its corresponding $p_{\rm value}$, as well as the best-fitting constant values. Fe Kα flux as function as function of the 2-10 keV flux. The left top box show the Spearman rank correlation coefficient (r_s) for the two variables and its corresponding $p_{\rm value}$, β is the slope of the best fitting line (see Equation 1).

3.2.3 *Inter-calibration of the spectral data*

The fluxes measured in the scaled spectrum described in the previous sections were corrected for aperture and distinct seeing effects, because while the BLR is effectively a point-like source, the NLR is an extended one. Consequently, the measured NLR flux depends on the size of the spectrograph's entrance aperture and the observations seeing (see Peterson et al. 1995, for a detailed discussion). In order to correct our fluxes for these effects, we determined a point-source correction factor (φ), which was measured using the procedure described in Peterson et al. (1995). The φ value represents the differences in the amount of light from the NLR with respect to the amount of light from the BLR for each observation, it is normalised using the largest aperture ($\varphi = 1.0$, for 04/2015 spectrum). Then the scaled inter-calibrated and aperture/seeing corrected BEL fluxes were measured as follows:

$$F(H\alpha) = \varphi \cdot F_{\lambda 5007} \left[\frac{F(H\alpha)}{F([\mathrm{O\,III}]\lambda 5007)} \right]_{\rm obs} \quad (2)$$

where $F_{\lambda 5007}$ is the scaling absolute flux in the [O III]λ5007 line, described in section 3.2.1, and the value in brackets is the broad Hα to [O III]λ5007 measured flux ratio for each spectrum as described in section 3.2.2. The same procedure was applied to Hβ BEL.

Table 3. Modern Optical Spectra. Point-Source Scale Factor (φ) is measured using Peterson et al. (1995) algorithm, the errors in φ represents the uncertainty in the centring of the virtual apertures.

Obs. Date (mm/yyyy)	Aperture	Point-Source Scale Factor φ	F(Hα) (10^{-13} erg cm^{-2} s^{-1})	FWHM(Hα) (km s^{-1})	F(Hβ) (10^{-13} erg cm^{-2} s^{-1})	F(Hα)/F(Hβ)
12/2006	Slit (width = 2.0″)	0.734 ± 0.063	≤ 4.4	2733 ± 55	–	–
04/2014	Circular (radius = 2.8″)	0.972 ± 0.025	27.5 ± 1.4	2002 ± 28	3.6 ± 2.6	7.6 ± 2.8
02/2015	Circular (radius = 3.0″)	1.000 ± 0.011	33.8 ± 1.5	2313 ± 17	3.3 ± 2.2	10.1 ± 3.3
02/2018	Circular (radius = 3.0″)	0.973 ± 0.013	43.8 ± 2.2	2016 ± 13	4.9 ± 1.4	8.8 ± 1.7

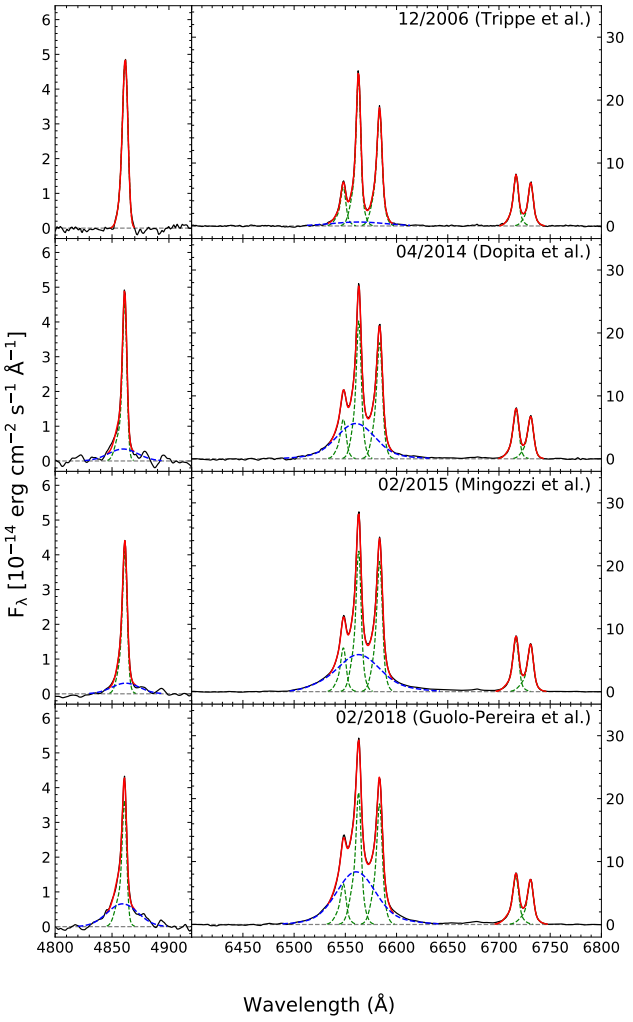

Figure 3. Fit of the emission lines for the modern optical spectra. From top to bottom: 12/2006 (Trippe et al. 2008), 04/2014 (Dopita et al. 2015), 02/2015 (Mingozzi et al. 2019) and 02/2018 (Guolo-Pereira et al. 2021). Scaled observed spectra (black), narrow components (green), broad components (blue) and total model (red) are shown. Left panels show the Hβ lines while right ones show the Hα, [N II] and [S II] lines.

The BEL Hα and Hβ fluxes and the Balmer decrements (Hα/Hβ) are shown in Table 3 and in the right panels of Fig. 4. In the 12/2006 spectrum, the Hα BEL is not unambiguously detected (which leads to its classification as a Seyfert 2), and if it is indeed present, it is very faint, with a maximum flux of 4.4×10^{-13} erg cm^{-2} s^{-1}. From 2014 to 2018 the broad Hα flux increases from $\sim 28 \times 10^{-13}$ erg cm^{-2} s^{-1} to $\sim 44 \times 10^{-13}$ erg cm^{-2} s^{-1}. The Hβ BEL flux, however, does not increase monotonically: in the 04/2014 spectrum it had a flux of 3.6×10^{-13} erg cm^{-2} s^{-1}, and a lower flux, 3.3×10^{-13} erg cm^{-2} s^{-1}, in 02/2015, while in 02/2018 it was measured as 4.9×10^{-13} erg cm^{-2} s^{-1}. In the middle right panel of Fig. 4 we also show an estimate of the detection limit for each spectrum. The broad Hβ is only well above this limit in the 02/2018 spectrum and possibly in 02/2015. Therefore, based on these spectra, the galaxy can be classified as a Seyfert 1.8. Within the uncertainties the Balmer decrements seems to be constant at a value of ∼ 9.

By using this reddening value of the BLR, Hα/Hβ ≈ 9 → A_V = 3.68 mag using (Calzetti et al. 2000) law, and the relation N_H= 1.68×10^{21} A_V cm^{-2} derived by van Steenberg & Shull (1988) for the local ISM, we estimate the column density absorbing the BLR to be $N_H \approx 6.2 \times 10^{21}$ cm^{-2}. Comparing this with the average value observed in the X-rays, $N_H \approx 10^{22}$, it may fit with a scenario where this constant extinction/absorption is mainly due to the host galaxy.

3.3 The Link Between the X-ray Luminosity and the BELs

Comparing the middle and bottom panels of Fig. 1, one can directly see a correlation between the intrinsic X-ray luminosity and the detection of the broad Hα component. The periods in which the broad component is detectable are the ones where L_{2-10} shows the highest values; the epochs when the galaxy is classified as a Seyfert 2 are those when closest available X-ray spectra show lower L_{2-10} values. Given that the X-ray and optical observations are not simultaneous, in order to quantify the correlation between the BELs and the X-ray luminosity we linearly interpolate the L_{2-10} curve (bottom panel of Fig. 1) and attribute a L_{2-10} value for each historical optical spectrum. In Fig. 5 we show the interpolated L_{2-10} value for each spectrum as function of the bi-modal Hα BEL detection.

From Fig. 5, the link between the BEL and the X-ray luminosity is clear: at all epochs when an Hα BEL is detected, $L_{2-10} > 4 \times 10^{42}$ erg s^{-1}; conversely, when a Seyfert 2 spectrum is observed, $L_{2-10} < 4 \times 10^{42}$ erg s^{-1};. Moreover, from Fig. 4 (top panels) and Fig. 6 (top panel) we can see that for the modern spectra (2006-2018) the Hα BEL flux increases with the increase in the L_{2-10}. From the same figures, we can see that the transitions between Type 1.9 to Type 1.8 (i.e., the clear detection of the Hβ BEL) occurs between 10 - 15 $\times 10^{42}$ erg s^{-1}. It is possible that the oldest high Eddington Ratio optical observations did not detect the broad Hβ due to its faintness or lower signal to noise ratio.

Under some assumptions we can convert the transitional X-

ray luminosity (4×10^{42} erg s^{-1}) into an Bolometric luminosity (L_{bol}) and than into Eddington ratio (λ_{Edd}), as follows:

$$\lambda_{Edd} = \frac{L_{Bol}}{L_{Edd}} = \frac{[K_X(L_{2-10}) \pm \Delta K_X] \times L_{2-10}}{1.3 \times 10^{38}\ M_{BH}} \quad (3)$$

where K_X is the bolometric correction and ΔK_X is uncertainty in the bolometric correction (the intrinsic spread of the AGN population dominates this uncertainty). We use Duras et al. (2020) correction, which assumes values of $K_X(L_{2-10} = 4{\times}10^{42}$ erg s^{-1}) = 15.64 and ΔK_X = 0.37 *dex*, we can estimate the Eddigton ratio in which the transitions occurs as:

$$\lambda_{Edd} \approx \frac{2.0^{+2.0}_{-1.3}}{\overline{M_{BH}}}\ \% \quad (4)$$

where $\overline{M_{BH}} = M_{BH}\ /3{\times}10^7\ M_\odot$ is written as a systematic scaling factor to take into account the uncertainties in the black hole mass and the distinct values that can be considered (see section 2.4), since if we would have propagated it would dominate the λ_{Edd} uncertainty.

In summary, this analysis strongly supports the hypothesis that the CL phenomenon in NGC 2992 is caused by variations in the accretion rate and not due to changes in absorption nor due to TDEs (which we discard due to the several repeated CL events).

In the last several years, the idea that the orientation-based Unification Models alone cannot explain the variety of AGNs (see Spinoglio & Fernández-Ontiveros 2019, for a review of challenges to the Unification Model), and that the specific accretion rate, as given by the Eddington ratio, is as essential as obscuration in the classification of the distinct AGN types, has been explored by several authors. For example, Trump et al. (2011) using a sample of 118 unobscured ($N_H < 10^{22}$ cm^{-2}) AGNs show that the BELs are present only at the highest accretion rates ($L_{bol}/L_{Edd} > 10^{-2}$).

Several authors have proposed models that posit different accretion rates as a cause of the differences between observed AGNs (see Ho 2008, for a review in the properties of low luminosity AGNs). Elitzur & Ho (2009) suggest that the BLR and "torus" are inner (ionized) and outer (clumpy and dusty) parts of the same disk-driven wind and that this wind is no longer supported at low accretion rates (Nicastro 2000; Elitzur & Shlosman 2006; Nenkova et al. 2008). Based on this disk-wind BLR model, Elitzur et al. (2014) proposed that the intrinsic spectral sequence S1 $\rightarrow$ S1.2/S1.5 $\rightarrow$ S1.8/S1.9 $\rightarrow$ S2[3] is a true evolutionary sequence, reflecting the evolution of the BLR structure with decreasing accretion rate onto the central black hole and that this evolution is regulated by the $L_{bol}/\ M_{BH}\ ^{2/3}$ variable (which behaves like λ_{Edd}). These models have been successfully used to explain the existence of "true" Type 2 Seyferts as shown by Marinucci et al. (2012) and are recently being invoked to explain CL-AGNs.

We have shown that the variability in NGC 2992 is intrinsically driven by changes in accretion rate, and not due to variable obscuration. In this scenario, the CL events (i.e., the disappearing and reappearing of the BELs) can be due to two distinct effects:

- Dimming/brightening of the AGN continuum, which changes the supply of ionising photons available to excite the gas in the immediate vicinity of the black hole and therefore the BLR. In this case, variations in the BEL fluxes are due to changes in the ionisation state of the BLR clouds and not to change in its geometry or structure (Storchi-Bergmann et al. 2003; Schimoia et al. 2012; LaMassa et al. 2015);
- The fading of the BLR structure itself as proposed by the disk-wind BLR models (Elitzur & Shlosman 2006; Elitzur & Ho 2009), in which a low accretion rate is not able to sustain the required cloud flow rate (Nicastro 2000; Trump et al. 2011; Elitzur et al. 2014), that makes up the BLR.

The first scenario is supported in the case of the double-peaked LINER/Seyfert 1 nucleus of NGC 1097, for which Storchi-Bergmann et al. (2003) and Schimoia et al. (2012) found an inverse correlation between the width of the Hα broad profile and the flux of the line, as well as for NGC 5548 by Peterson et al. (2002) and for the CL-Quasar SDSS J015957.64+003310.5 by LaMassa et al. (2015). The authors preferred explanation for this is the fact that, when the AGN is brightest, it ionises farther out in the BLR, reaching lower velocity clouds, and the profile becomes narrower. When the AGN is dimmer, it ionises only the closest regions, where the velocities are higher and the profile becomes wider, in agreement with a virialized BLR. In our data, there seems to be such a inverse correlation between FWHM(Hα) and F(Hα), in the modern optical spectra, as can be seen in the bottom panel of Fig. 6.

However, in the second scenario, where the BLR is described as a disk-driven wind and not as clouds orbiting in Keplerian-like orbits, this inverse correlation is also predicted. Using distinct, prescriptions both Nicastro (2000) and Elitzur et al. (2014) show that with increasing accretion rate (λ_{Edd}) (which increases Hα BEL flux) the FWHM in the BLR decreases. In the Nicastro (2000) model, the relation between the two parameters is written as:

$$\log(\lambda_{Edd}) = -3\log(\mathrm{FWHM}) + 9.86 + \log(\eta/\alpha) \quad (5)$$

where η/α is the ratio between the disk efficiency (η) and its viscosity (α), while Elitzur et al. (2014) use:

$$\log(\lambda_{Edd}) = -4\log(\mathrm{FWHM}) + 3.60 + \log(M_{BH}) + \log(\xi) \quad (6)$$

where ξ is the ratio between the BLR radius (r_{BLR}) and the dust sublimation radius (R_d) with $\xi < 1.0$. The reader is referred to the original papers as well as to Nicastro et al. (2018) for detailed explanation of the models and equations. **In the middle panel of Fig. 6, we show both models with best-fitting parameters (η/α = 0.04 and ξ = 0.42) for the measured Hα BEL FWHM and λ_{Edd}, measured from the interpolated L_{2-10} (Fig. 5) using the above prescription (equations 3 and 4).**

While we have successfully shown that the CL events in NGC 2992 are driven by changes in the accretion rate, we could not determine the true nature of the BEL variability, mainly because, as discussed, we still do not have a full understanding of the formation and evolution of the BLRs in AGNs. In the next section we discuss the overall state-of-art modelling of the innermost structure of active galaxies as well as a proposed technique to distinguish between the two above proposed scenario.

4 RESULTS AND DISCUSSION

In both the scenarios discussed in the previous section, quick ($\sim$ 10 years between the maximum and the minimum activity) and large (a factor of $\sim$ 35 in L_{2-10}) variations in the accretion rate are necessary. However, the standard Shakura & Sunyaev (1973)

[3] Referring here only to the "true" Type 2 Seyferts, meaning those which do not have BELs even in polarised light, therefore excluding those which have obscured Type 1 nucleus.

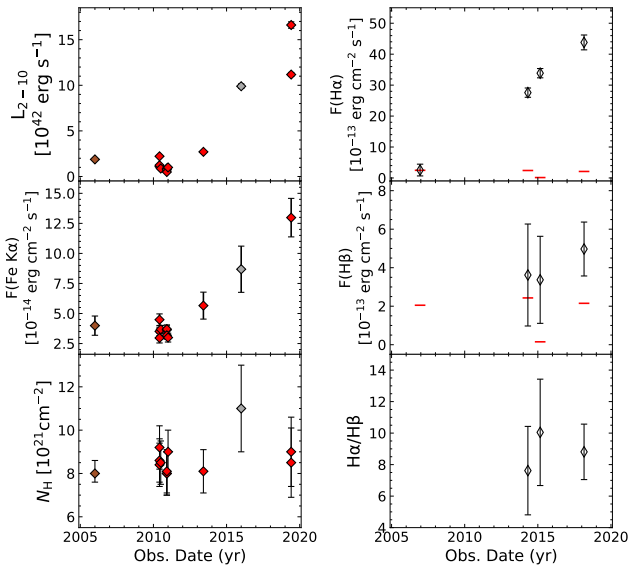

Figure 4. X-ray (left) and optical (right) properties from 2005 to 2020. From top to bottom in the X-ray panels: Intrinsic 2-10 keV Luminosity (L_{2-10}), narrow Fe Kα line flux, and the column density (N_H). From top to bottom in the optical panels: Flux of the Hα BEL, the flux of the Hβ BEL, and the Balmer decrement (Hα/Hβ). In the optical panels, the red lines represent a lower limit for the detection of the lines, being measured as the flux of a line with a signal to noise ratio equal to 3.

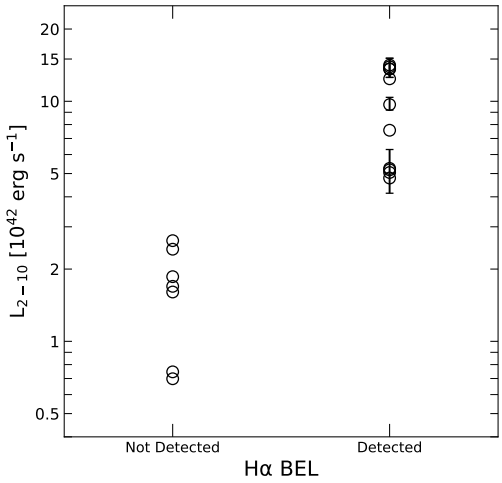

Figure 5. Interpolated intrinsic 2-10 keV x-ray luminosity (L_{2-10}) for each optical spectrum as function of the detection or non-detection of the Hα BEL. Showing a clear lower boundary of $L_{2-10} \approx 4 \times 10^{42}$ erg s^{-1} for the detection of the component.

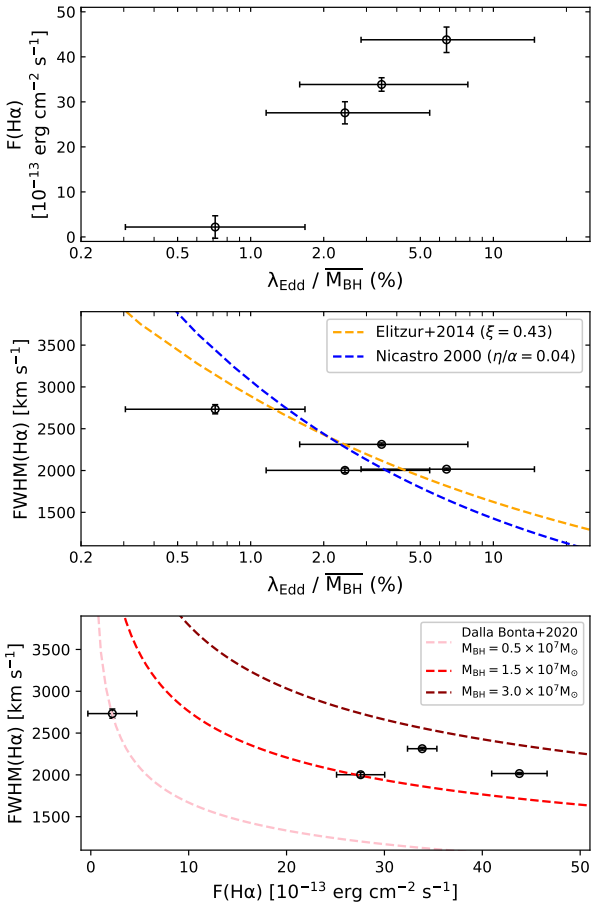

Figure 6. Top: flux of Hα BEL as function of Eddington Ratio (λ_{Edd}), measured using equations 3 and 4, for each modern optical spectrum. Middle: FHWM of Hα BEL as function of λ_{Edd} for each modern optical spectrum. Blue and orange dashed lines are, respectively, are the best-fitting Nicastro (2000) and Elitzur et al. (2014) disk-wind models (see section 3.3 and equations 5 and 6). $\overline{M_{BH}} = M_{BH}/3 \times 10^7$ $M_\odot$ is written as a systematic scaling factor to take into account the uncertainties in the black hole mass and the distinct values that can be considered (see section 2.4). Bottom: FHWM of Hα broad as function of Hα BEL flux for for each modern optical spectrum. Each dashed line represent the Dalla Bontà et al. (2020) relation between the two parameters, assuming a constant Balmer decrement of 9 and Calzetti et al. (2000) extinction law, for distinct supermassive black hole masses (M_{BH}) in the range discussed in section 2.4.

accretion disk model does not support such variations, given that for AGN scales (where the model still predicts the existence of a geometrically thin disk, H $\ll$ R) the viscous time scale of the disk is in the order of 10^4 to 10^5 years, greatly exceeding the timescales over which CL transitions are known to occur. This incompatibility was noticed long ago (e.g. Koratkar & Blaes 1999; Antonucci 2013), but just recently some modification or alternatives to the application of Shakura & Sunyaev (1973) model to AGNs have been proposed in order to explain the increasing number of the discovery of these CL sources.

The Eddington ratio in which the BEL transitions occurs in NGC 2992 contains the critical value at which there is a state transition between a radiatively inefficient accretion flow (RIAF) and a thin accretion disk ($\lambda_{Edd} \sim 0.01$; e.g. Xie & Yuan 2012). The similarity between these values suggests that NGC 2992 is operating at the threshold mass accretion rate between the two accretion modes. Indeed, Sniegowska et al. (2020) proposed an explanation for the sources displaying multiple quasi-periodic CL phenomena according to which they would be operating at a few per cent of the Eddington limit. They argue that the outbursts are caused by the radiation pressure instability operating in the narrow ring between the standard (Shakura & Sunyaev 1973) thin pressure dominated outer disk and the hot optically thin inner RIAF (Yuan & Narayan 2014). The corresponding limit cycle is responsible for periodic outbursts, and the timescales are therefore much shorter than the

standard viscous timescale due to the narrowness of the unstable radial zone.

Dexter & Begelman (2018) propose that alternatively AGN accretion discs are vertically supported by magnetic pressure which makes it geometrically thick (H/R between 0.1 and 1.0) at all luminosities. Jiang & Blaes (2020) show, for a 5×10^8 $M_\odot$ mass black hole, using three dimensional radiation magneto-hydrodynamic simulations, that under this assumption the Rosseland mean opacity is expected to be larger than the electron scattering value, and the iron opacity bump then causes the disk to be convectively unstable. This results in strong fluctuations in surface density and heating of the disk. The opacity drops with increasing temperature and convection is suppressed. The disk cools down and the whole process repeats. This causes strong oscillations of the disk scale height and luminosity variations by more than a factor of $\approx 3 - 6$ over timescales of few years. They argue that since the iron opacity bump will move to different locations of the disk for black holes with different masses and accretion rates, this is a physical mechanism that can explain the accretion rate variability of AGN with a wide range of amplitudes over a time scale of years to decades.

Even with the possibility of such rapid variability in the accretion rate (given some of these alternatives to the classical accretion disk) the cause of the type transition remains uncertain, dimming of the ionising source or fading of the BLR structure itself. By using radiative transfer Monte Carlo simulations to test the multiple causes of the CL phenomenon, Marin (2017) argues that the differences between these two scenarios can only be observable in polarised light: in the ionising source dimming scenario the polarisation properties between the high and low flux state should be the same, while that for the BLR fading a decrease in the degree of polarisation and a rotation in the polarization angle are expected in the low flux state. We had access to a spectropolarimetric observation of NGC 2992 obtained in 2006 (Robinson et al., in prep), when the galaxy was at a dim state (see Fig. 1). It shows no signs of BEL in the polarimetric spectrum (as well as in normal flux). In order to test Marin (2017) predictions we would need a recent (with the AGN at its bright state) observations as well. As this data is not available to us now, the exact intrinsic cause of the CL-AGN events in NGC 2992 is still an open question. We join these authors in advocating for systematic polarimetric observations of CL-AGN in order to fully understand their true nature. In this sense, follow up observations (polarimetric or not) of NGC 2992 in the next decades will continue to help constrain the physics of AGNs. Furthermore, this source joins several others in the literature that show that the accretion rate is a fundamental variable for any model that tries to unify the AGN zoology, and that viewing angle or obscuration effects alone cannot fully explain differences seen in SMBH activity in galaxies.

5 CONCLUSIONS

We have analysed the historical X-ray and optical observations of the Seyfert galaxy NGC 2992, from 1978 to 2019, focusing on its CL events. The main results are:

- The source presents large intrinsic X-ray luminosity variability ranging from 4.9×10^{41} erg s^{-1} up to 1.7×10^{43} erg s^{-1};
- The source presents several transitions between type 2 Seyfert to intermediate-type spectrum, losing and regaining its Hα BEL on timescales of several years;
- We ruled out TDEs or variable obscuration as causes of the type transitions. We show that the presence (and the flux) of the Hα BEL is directly correlated with the 2-10 keV X-ray luminosity: a minimum value of $L_{2-10} \approx 4 \times 10^{42}$ erg s^{-1} is necessary for its appearance. This value translates to a Eddington ratio of $2.0^{+2.0}_{-1.3}$%, if we assume $M_{BH} = 3 \times 10^7$ $M_\odot$. Due to its faintness, the unambiguously detection of the Hβ BEL was only possible in the most recent spectrum, at even higher accretion rates of $\lambda_{Edd} \approx 5$–8%;
- We find a correlation between the narrow Fe Kα flux and λ_{Edd}, and an anti-correlation between full width at half maximum of Hα BEL and λ_{Edd}, as predicted by the disk-wind BLR models.
- Two possible scenarios for type transitions are still open: either the dimming (brightening) of the AGN continuum luminosity, which reduces (increases) the supply of ionising photons available to excite the gas in the immediate vicinity of the black hole (LaMassa et al. 2015) or the disappearance of the BLR structure itself occurs as the low accretion efficiency is not able to sustain the required cloud flow rate in a disk-wind BLR model (Elitzur & Shlosman 2006; Trump et al. 2011; Elitzur et al. 2014). Multi-epoch polarimetric observations may distinguish between the two scenarios.
- This study supports the idea that the accretion rate is a fundamental variable in determining the observed AGN type, and therefore should be included in a more complete model to unify the AGN zoology.

ACKNOWLEGMENTS

We would like to thank all those authors and observatories that made public their data making this work possible, specially Michael Crenshaw for providing the Trippe et al. (2008) spectrum and Adam Thomas for helping us access the S7 survey (Dopita et al. 2015) data. MGP also would like to thanks Michael Fausnaugh for making `mapspec` public available as well as for his comments and suggestions on the paper.

DATA AVAILABILITY

The GMOS and MUSE spectral data cubes are public available at the Gemini and ESO archive web pages, respectively. The other data underlying this article will be shared on reasonable request to the corresponding author.

REFERENCES

Allen M. G., Dopita M. A., Tsvetanov Z. I., Sutherland R. S., 1999, ApJ, 511, 686
Andrillat Y., Souffrin S., 1971, A&A, 11, 286
Antonucci R., 1993, ARA&A, 31, 473
Antonucci R., 2013, Nature, 495, 165
Aretxaga I., Joguet B., Kunth D., Melnick J., Terlevich R. J., 1999, The Astrophysical Journal, 519, L123–L126
Avni Y., 1976, ApJ, 210, 642
Barlow R., 2003a, in Lyons L., Mount R., Reitmeyer R., eds, Statistical Problems in Particle Physics, Astrophysics, and Cosmology. p. 250 (arXiv:physics/0401042)
Barlow R., 2003b, arXiv e-prints, p. physics/0306138
Barlow R., 2004, Asymmetric Statistical Errors (arXiv:physics/0406120)
Bianchi S., Piconcelli E., Chiaberge M., Bailón E. J., Matt G., Fiore F., 2009, ApJ, 695, 781
Busko I. C., Steiner J. E., 1990, MNRAS, 245, 470
Calzetti D., Armus L., Bohlin R. C., Kinney A. L., Koornneef J., Storchi-Bergmann T., 2000, ApJ, 533, 682

Cid Fernandes R., Mateus A., Sodré L., Stasińska G., Gomes J. M., 2005, MNRAS, 358, 363

Cohen R. D., Rudy R. J., Puetter R. C., Ake T. B., Foltz C. B., 1986, ApJ, 311, 135

Cooke B. A., et al., 1978, MNRAS, 182, 489

Corral A., Della Ceca R., Caccianiga A., Severgnini P., Brunner H., Carrera F. J., Page M. J., Schwope A. D., 2011, A&A, 530, A42

Dai X., Chartas G., Eracleous M., Garmire G. P., 2004, The Astrophysical Journal, 605, 45–57

Dalla Bontà E., et al., 2020, The Astrophysical Journal, 903, 112

Denney K. D., et al., 2014, The Astrophysical Journal, 796, 134

Dexter J., Begelman M. C., 2018, Monthly Notices of the Royal Astronomical Society: Letters, 483, L17–L21

Dopita M. A., et al., 2015, ApJS, 217, 12

Duras F., et al., 2020, Astronomy & Astrophysics, 636, A73

Durret F., Bergeron J., 1988, A&AS, 75, 273

Elitzur M., 2012, The Astrophysical Journal, 747, L33

Elitzur M., Ho L. C., 2009, The Astrophysical Journal, 701, L91–L94

Elitzur M., Shlosman I., 2006, ApJ, 648, L101

Elitzur M., Ho L. C., Trump J. R., 2014, MNRAS, 438, 3340

Eracleous M., Halpern J. P., 2001, The Astrophysical Journal, 554, 240

Eracleous M., Livio M., Halpern J. P., Storchi-Bergmann T., 1995, ApJ, 438, 610

Fausnaugh M. M., 2017, Publications of the Astronomical Society of the Pacific, 129, 024007

García-Lorenzo B., Arribas S., Mediavilla E., 2001, A&A, 378, 787

Gilli R., Maiolino R., Marconi A., Risaliti G., Dadina M., Weaver K. A., Colbert E. J. M., 2000, A&A, 355, 485

Graham M. J., et al., 2019, Monthly Notices of the Royal Astronomical Society

Gültekin K., et al., 2009, ApJ, 698, 198

Guo H., Sun M., Liu X., Wang T., Kong M., Wang S., Sheng Z., He Z., 2019, ApJ, 883, L44

Guolo-Pereira M., Ruschel-Dutra D., Storchi-Bergmann T., Schnorr-Müller A., Cid Fernandes R., Couto G., Dametto N., Hernandez-Jimenez J. A., 2021, MNRAS, 502, 3618

Ho L. C., 2008, Annual Review of Astronomy and Astrophysics, 46, 475

Jiang Y.-F., Blaes O., 2020, The Astrophysical Journal, 900, 25

Kalberla P. M. W., Burton W. B., Hartmann D., Arnal E. M., Bajaja E., Morras R., Pöppel W. G. L., 2005, A&A, 440, 775

Keel W. C., 1996, ApJS, 106, 27

Kollatschny W., Ochmann M. W., Zetzl M., Haas M., Chelouche D., Kaspi S., Pozo Nuñez F., Grupe D., 2018, Astronomy & Astrophysics, 619, A168

Kollatschny W., et al., 2020, Astronomy & Astrophysics, 638, A91

Koratkar A., Blaes O., 1999, Publications of the Astronomical Society of the Pacific, 111, 1

LaMassa S. M., et al., 2015, Astrophysical Journal, 800, 144

Lampton M., Margon B., Bowyer S., 1976, ApJ, 208, 177

Lawrence A., 2018, Nature Astronomy, 2, 102

Liu H., Wu Q., Lyu B., Yan Z., 2019, Evidence for changing-look AGNs is caused by change of accretion mode (arXiv:1912.03972)

MacLeod C. L., et al., 2016, MNRAS, 457, 389

Maccacaro T., Perola G. C., Elvis M., 1982, ApJ, 257, 47

Marchese E., Braito V., Della Ceca R., Caccianiga A., Severgnini P., 2012, MNRAS, 421, 1803

Marin F., 2017, Astronomy & Astrophysics, 607, A40

Marinucci A., Bianchi S., Nicastro F., Matt G., Goulding A. D., 2012, The Astrophysical Journal, 748, 130

Marinucci A., Risaliti G., Wang J., Bianchi S., Elvis M., Matt G., Nardini E., Braito V., 2013, Monthly Notices of the Royal Astronomical Society, 429, 2581–2586

Marinucci A., Bianchi S., Braito V., Matt G., Nardini E., Reeves J., 2018, MNRAS, 478, 5638

Marinucci A., Bianchi S., Braito V., De Marco B., Matt G., Middei R., Nardini E., Reeves J. N., 2020, Monthly Notices of the Royal Astronomical Society, p. staa1683

Marquez I., Boisson C., Durret F., Petitjean P., 1998, A&A, 333, 459

Matt G., Guainazzi M., Maiolino R., 2003, Monthly Notices of the Royal Astronomical Society, 342, 422–426

McElroy R. E., et al., 2016, A&A, 593, L8

Mingozzi M., et al., 2019, A&A, 622, A146

Murphy K. D., Yaqoob T., Terashima Y., 2007, The Astrophysical Journal, 666, 96–108

Murphy K. D., Nowak M. A., Marshall H. L., 2017, ApJ, 840, 120

Mushotzky R. F., 1982, ApJ, 256, 92

Nandra K., Pounds K. A., 1994, MNRAS, 268, 405

Nelson C. H., Whittle M., 1995, ApJS, 99, 67

Nenkova M., Sirocky M. M., Nikutta R., Ivezić Ž., Elitzur M., 2008, ApJ, 685, 160

Nicastro F., 2000, The Astrophysical Journal, 530, L65–L68

Nicastro F., Mathur S., Krongold Y., 2018, When a Seyfert... ...has a Crash on a Model, doi:10.5281/zenodo.1473677, https://doi.org/10.5281/zenodo.1473677

Oknyansky V. L., Winkler H., Tsygankov S. S., Lipunov V. M., Gorbovskoy E. S., van Wyk F., Buckley D. A. H., Tyurina N. V., 2019, MNRAS, 483, 558

Osmer P. S., Smith M. G., Weedman D. W., 1974, ApJ, 192, 279

Osterbrock D. E., 1981, ApJ, 249, 462

Osterbrock D. E., Ferland G. J., 2006, Astrophysics of gaseous nebulae and active galactic nuclei

Pastoriza M., Gerola H., 1970, Astrophys. Lett., 6, 155

Peterson B. M., 1993, PASP, 105, 247

Peterson B. M., Pogge R. W., Wanders I., Smith S. M., Romanishin W., 1995, Publications of the Astronomical Society of the Pacific, 107, 579

Peterson B. M., et al., 2002, The Astrophysical Journal, 581

Ponti G., Papadakis I., Bianchi S., Guainazzi M., Matt G., Uttley P., Bonilla N. F., 2012, A&A, 542, A83

Possolo A., Merkatas C., Bodnar O., 2019, Metrologia, 56, 045009

Ptak A., Yaqoob T., Murphy K., Suzaku Ngc 2992 Team 2007, Progress of Theoretical Physics Supplement, 169, 252

Puccetti S., Fiore F., Risaliti G., Capalbi M., Elvis M., Nicastro F., 2007, MNRAS, 377, 607

Qiao E., Liu B. F., 2013, The Astrophysical Journal, 764, 2

Ricci C., Ueda Y., Paltani S., Ichikawa K., Gand hi P., Awaki H., 2014, MNRAS, 441, 3622

Risaliti G., Elvis M., Bianchi S., Matt G., 2010, Monthly Notices of the Royal Astronomical Society: Letters, p. no–no

Ruan J. J., et al., 2016, The Astrophysical Journal, 826, 188

Runnoe J. C., et al., 2016, MNRAS, 455, 1691

Ruschel-Dutra D., 2020, danielrd6/ifscube v1.0, doi:10.5281/zenodo.3945237, https://doi.org/10.5281/zenodo.3945237

Schimoia J. S., Storchi-Bergmann T., Nemmen R. S., Winge C., Eracleous M., 2012, ApJ, 748, 145

Schnorr-Müller A., et al., 2016, MNRAS, 462, 3570

Shakura N. I., Sunyaev R. A., 1973, A&A, 500, 33

Shappee B. J., et al., 2014, ApJ, 788, 48

Sheng Z., Wang T., Jiang N., Yang C., Yan L., Dou L., Peng B., 2017, The Astrophysical Journal, 846, L7

Shu X. W., Yaqoob T., Murphy K. D., Braito V., Wang J. X., Zheng W., 2010, The Astrophysical Journal, 713, 1256–1265

Shuder J. M., 1980, ApJ, 240, 32

Sniegowska M., Czerny B., Bon E., Bon N., 2020, A possible mechanism for multiple changing look phenomenon in Active Galactic Nuclei (arXiv:2007.06441)

Spinoglio L., Fernández-Ontiveros J. A., 2019, AGN types and unification model (arXiv:1911.12176)

Stoklasová I., Ferruit P., Emsellem E., Jungwiert B., Pécontal E., Sánchez S. F., 2009, Astronomy & Astrophysics, 500, 1287–1325

Storchi-Bergmann T., Schnorr-Müller A., 2019, Nature Astronomy, 3, 48

Storchi-Bergmann T., Baldwin J. A., Wilson A. S., 1993, ApJ, 410, L11

Storchi-Bergmann T., et al., 2003, ApJ, 598, 956

Swank J. H., 2006, Advances in Space Research, 38, 2959

Theureau G., Hanski M. O., Coudreau N., Hallet N., Martin J.-M., 2007, A&A, 465, 71

Tohline J. E., Osterbrock D. E., 1976, ApJ, 210, L117
Tremaine S., et al., 2002, ApJ, 574, 740
Trippe M. L., Crenshaw D. M., Deo R., Dietrich M., 2008, AJ, 135, 2048
Trump J. R., et al., 2011, The Astrophysical Journal, 733, 60
Turner T. J., Pounds K. A., 1989, MNRAS, 240, 833
Urry C. M., Padovani P., 1995, PASP, 107, 803
Veilleux S., Shopbell P. L., Miller S. T., 2001, AJ, 121, 198
Veron P., Lindblad P. O., Zuiderwijk E. J., Veron M. P., Adam G., 1980, A&A, 87, 245
Wang J., Xu D. W., Wang Y., Zhang J. B., Zheng J., Wei J. Y., 2019, The Astrophysical Journal, 887, 15
Ward M., Penston M. V., Blades J. C., Turtle A. J., 1980, MNRAS, 193, 563
Weaver K. A., Nousek J., Yaqoob T., Mushotzky R. F., Makino F., Otani C., 1996, ApJ, 458, 160
Winter L. M., Mushotzky R. F., Reynolds C. S., Tueller J., 2009, ApJ, 690, 1322
Woo J.-H., Urry C. M., 2002, ApJ, 579, 530
Xie F.-G., Yuan F., 2012, MNRAS, 427, 1580
Yang Q., et al., 2018, ApJ, 862, 109
Yaqoob T., 1998, ApJ, 500, 893
Yaqoob T., et al., 2007, PASJ, 59, 283
Yuan F., Narayan R., 2014, ARA&A, 52, 529
van Groninge E., Wanders I., 1992, PASP, 104, 700
van Groningen E., Wanders I., 1992, PASP, 104, 700
van Steenberg M. E., Shull J. M., 1988, ApJS, 67, 225

During this research we faced the problem that even with numerous of uncertainties propagation tools publicly-available (e.g. `astropy.uncertainty`, `uncertainties`) none of them are able to handle asymmetric uncertainties as we needed, due to the assumptions stated above. We therefore created the `asymmetric_uncertainties` Python package, the main idea of the code is to generate a random sample from the likelihood function and use this sample in other calculations (Possolo et al. 2019). The code assumes a "Variable Width Gaussian" likelihood, which, as shown by Barlow (2004), reproduces very well the underlying likelihood of low counting measurements, and, in contrast to, for example, a "Generalised Poisson" distribution, has a unique and analytical solution for given values of $\hat{x}$, $u_{\rm l}$ and $u_{\rm r}$ at a given confidence level ($\Delta\chi^2$). From this likelihood the code generates a random sample of data, that can be passed as parameters for any type of function. Simple operations are deal internally by the code and the more sophisticated ones can be easy performed by the user, for example: L_{2-10} values in Table 1 whose uncertainties were propagated from Γ and $N_{\rm H}$ uncertainties; as well as the statistical tests (r_s and $p_{\rm value}$) in Fig. 2. The resulting sample is then fitted by the code returning the nominal value and the propagated uncertainties. The code is publicly-available at github[4] where examples in how to use the code are also presented.

This paper has been typeset from a TEX/LATEX file prepared by the author.

APPENDIX A: PROPAGATION OF ASYMMETRIC UNCERTAINTIES

When the underlying likelihood function of a parameter is not symmetric, the error distribution will also be asymmetric. Different origins of asymmetry are discussed in detail by Barlow (2003a,b) and Barlow (2004). In high-energy astrophysics it is related to the low photon counting. In this case, the estimated parameters are usually reported in a form like $\hat{x}^{+u_{\rm r}}_{-u_{\rm l}}$. Where $\hat{x}$ is the best-fitting parameter (minimum χ^2) and $u_{\rm l}$ and $u_{\rm r}$ are the draw where the $\Delta\chi^2$ curve reaches some value, for classical 1σ (68%) confidence level $\Delta\chi^2 = 1.0$, however the 90% confidence level ($\Delta\chi^2 = 2.7$) is the most employed in X-ray astronomy (Avni 1976; Lampton et al. 1976; Yaqoob 1998).

Usually, one needs to calculate a function of one or more quantities, and propagate its uncertainties. In most circumstances, well known "Error Propagation" formulas are adequate. But there are some assumptions and approximations under the Error Propagation, and if they fail, the method is invalid. These assumptions can be summarised as: the errors are Normally distributed (Gaussian errors) and they are relatively small. For asymmetric errors in astronomy any of these assumptions can be made; if the asymmetry is really small, rounding/averaging the negative and the positive errors into a single value and making the distribution symmetric does not change the result much. But when the values are not appropriate to do that, researchers often tend to put two error values into quadrature separately and combine them in the result. Actually this is not a valid method due to violation of the Central Limit Theorem (Barlow 2003b). Eventually more sophisticated methods are needed to use: we present here a Python-based Monte Carlo solution for this problem, based in a combination of Barlow (2004) and Possolo et al. (2019) derivations.

[4] https://github.com/muryelgp/asymmetric_uncertainties